

Thesis/ Thèse

University of Kent, School of Chemistry and Forensic Science
L'Université de Lille, École Doctorale des Sciences de la Matière, du
Rayonnement et de l'Environnement

Jessica Mariah Dawber

Submitted for the degree of *Doctor of Philosophy*
En vue d'obtenir le grade de *Docteur*

Chemistry/ Chimie des Matériaux

**Unveiling the structure and dynamics of treated
methyl-ammonium lead iodide: insights from
scattering and magnetic resonance techniques**

**Etude des traitements post-synthétiques sur la
structure et la dynamique de l'iodure de plomb
méthylammonium**

Defense scheduled for 11th December 2024
Soutenance prévue le 11 Décembre 2024

Co-Supervisors / Co-Directeurs de thèse:

Mark Green, Professeur, University of Kent, MEE
Olivier Lafon, Professeur, Université de Lille, UCCS

Examiners/ Rapporteurs.trices:

Karen Johnston, Professeur, University of Durham, Department of Chemistry
Frédéric Sauvage (*Président du jury*), Directeur de Recherche, Université de Picardie
Jules Verne,

Laboratoire de réactivité et chimie des solides

Dedicated to my late grandfather, Professor John Graham Dawber. Though he passed in 2018, before he could see me complete my undergraduate degree and embark on this journey in chemistry, his spirit and passion live on in every step I take in this field.

From a young age, he filled my world with wonder, laughter, and the marvels of magnets, instilling a worldly curiosity that has only deepened with time. His love for science, his joy in sharing it and inspiring others set me on this path, and it is with immense gratitude that I walk in his footsteps today.

Declaration

This work, except where specific references are made to the work of others, has not been submitted, in whole or in part, for any degree or qualification at any institution other than the University of Kent and Université de Lille under the cotutelle agreement. This dissertation represents my independent work, conducted under the joint supervision of Professor Mark Green and Professor Olivier Lafon, except where collaborations are noted in the text and acknowledgments.

Chapter 3 The Quasi Elastic Neutron Scattering experiment on OSIRIS at the ISIS Neutron and Muon Source was carried out by Dr. Jake Minns, with assistance from Dr. Victoria Garcia Sakai. Sample synthesis for this experiment was performed by Dr. Jake Minns and Rhianna Day. The variable-temperature synchrotron powder diffraction experiments were conducted with the assistance of Dr. Charles McMonogale at the Swiss-Norwegian Beamline (SNBL) at the ESRF, and Dr. Sarah Day and Dr. Lucy Saunders at the I11 beamline at Diamond Light Source.

Chapters 4 and 5 The NMR and NQR experiments were performed with assistance from Dr. Bertrand Doumert and Dr. Julien Trébosc at Université de Lille.

Jessica Mariah Dawber

2024

Acknowledgements

As I bring this chapter of my life to a close with the completion of this thesis, I am reminded at every turn that none of this would have been possible without the support, collaboration, and guidance of so many. This research, and the journey it has taken me on, has profoundly shaped both my work and the person I am today.

First and foremost, my gratitude goes to Professor Mark A. Green for his supervision, expertise, and understanding, which made this unique research project a reality. Equally, I would like to thank Professor Olivier Lafon, whose immense knowledge of NMR, along with unwavering dedication and support - both during my time in Lille and beyond - were pivotal to my progress. Their continuous encouragement has been a guiding force; without it, I would not have come this far.

I am also grateful to the past and present members of my research groups at both universities. At Kent, I am indebted to Jake and Rhianna, whose work sparked this project, as well as to Anna and Ane for their support and camaraderie in our beloved lab 124. I thank the MEE group researchers for their insights during meetings, and my PhD cohort, who made the journey through a pandemic not only bearable but meaningful, with many of them now becoming dear friends. In Lille, I am deeply grateful to the entire RM2I research team. To my PhD colleagues Jennifer, Racha, Diane, Parth, Andrew, Lama, and Guillaume, along with many others, thank you for

welcoming me so warmly - both into the group and into France - with open hearts and an abundance of cherry-red beers.

My gratitude extends to those who helped with experiments and analyses throughout this research. My sincere thanks to the resilience and commitment of Dr. Julien Trébosc, without whom I would have struggled to make sense of all this NMR, and to both Dr. Bertrand Doumert and Bertrand Revel, who patiently guided me through spectrometer issues and tolerated my attempts at French. I am also grateful to Dr. Charles McMonagle at the Swiss-Norwegian beamline, ESRF, Dr. Sarah Day, and Dr. Lucy Saunders on the I11 beamline, Diamond Light Source for their assistance with synchrotron powder diffraction experiments, as well as their advice on how not to break the instruments. I would also like to thank the cotutelle scholarship, organised between the University of Kent and Université de Lille, which made this unique research opportunity possible.

To my friends, who have been my lifeline throughout this journey, I offer my deepest gratitude. A special thanks to Jess and Kallum, who held me up during the toughest times, helped me rediscover my spark, and kept me moving forward to the very end.

There have been a few extraordinary influences who first inspired this journey into chemistry. I thank my secondary school chemistry teacher, Mr. Donovan — whom I am now perhaps finally grown enough to call Alan. Your passion for chemistry and inventive teaching left a lasting mark. I fondly remember our talks about Joy Division and all of my tests marked with RTQ (read the question) or even RTFQ for particularly creative answers. Most importantly, I am eternally grateful to my grandfather, to whom this thesis is dedicated. I hope to have made him as immensely proud as my grandmother assures me he would be.

Finally, I owe everything to the unwavering support of my family. Each of them has patiently endured my practice presentations, often bewildered but always encouraging. Thank you for not asking, “So what is it you actually do?” too many times! To my siblings, Ella, Bradley, and Amelie, who provided a much-needed escape and a reminder of home — I hope to show you that anything is possible. To my father and stepmother, John and Karen, thank you for your love and support; your work ethic and drive for personal excellence have motivated me every step of the way. To my mother and stepfather, Claire and Wayne, thank you for filling our home with laughter, unconditional love, and being the steady foundation on which I could stand. A special dedication goes to my mother, who has been the most devoted, hardworking, and inspiring role model I could ask for. I feel incredibly lucky to have even a fraction of her character.

Thank you, all of you.

Abstract

This doctoral thesis examines the structure and dynamics of methyl-ammonium lead iodide (MAPI), a prominent hybrid perovskite material, through advanced scattering and magnetic resonance techniques. With its high power conversion efficiencies and cost-effective fabrication, MAPI is a promising candidate for photovoltaic technology. However, its stability under environmental stressors, such as moisture and heat, poses significant challenges to commercial deployment.

This research investigates the influence of various post-synthetic treatments, including vacuum and iodine annealing, on MAPI's structural integrity and phase transitions. Through techniques such as X-ray diffraction (XRD), quasi-elastic neutron scattering (QENS), and nuclear magnetic resonance (NMR), this study provides insights into the flexible nature of the perovskite lattice and the dynamic behavior of the methyl-ammonium cation, highlighting critical aspects of cation mobility and phase stability. Additionally, the thesis addresses the formation of impurity phases, notably NH_4PbI_3 , during post-synthetic treatments and explores the potential mechanisms driving their formation. This work also advances the application of nuclear quadrupole resonance (NQR) for halide perovskites, demonstrating the possibility to use numerical simulations to optimise NQR experiments for the observation of ^{127}I nuclei.

By refining annealing parameters, this research demonstrates a method of post-

synthetically altering the structure and dynamics in MAPI, contributing valuable insights to the development of perovskite-based solar cells. The findings offer promising pathways to enhance the stability and efficiency of these materials, reinforcing their potential for next-generation photovoltaic applications.

Résumé

Cette thèse de doctorat porte sur l'étude des traitements post-synthétiques sur la structure et la dynamique à l'échelle atomique de l'iodure de plomb méthylammonium (MAPI) en combinant des techniques avancées de diffraction et de résonance magnétique. De part son rendement élevé et son faible coût de fabrication, le MAPI est un matériau prometteur pour l'énergie photovoltaïque. Toutefois, lorsqu'il est exposé aux conditions environnementales réelles, tels que l'humidité et la chaleur, son manque de stabilité pose des problèmes importants pour son déploiement commercial.

Ces travaux de recherche ont visé à étudier l'influence de divers traitements post-synthétiques, y compris le recuit sous vide et en présence d'iode, sur l'intégrité structurale et les transitions de phase du MAPI. Nous avons utilisé des techniques complémentaires telles que la diffraction des rayons X (DRX), la diffusion quasi-élastique des neutrons et la résonance magnétique nucléaire (RMN). Cette étude permet de mieux comprendre la nature flexible du réseau pérovskite et le comportement dynamique du cation méthyl-ammonium, et leurs influences sur de la mobilité du cation et de la stabilité des phases cristallines. En outre, la thèse montre la formation d'impureté, notamment de cristaux de NH_4PbI_3 , au cours des traitements post-synthétiques et explore les mécanismes potentiels de leur formation. Ce travail fait également progresser l'application de la résonance quadrupolaire nucléaire (RQN) pour les pérovskites d'halogénure, en démontrant la possibilité d'utiliser des simulations de dynamique de

spin pour optimiser les expériences RQN pour observer les noyaux ^{127}I .

Cette recherche démontre une méthode de modification post-synthétique de la structure et de la dynamique de ces matériaux, renforçant ainsi leur potentiel pour les dispositifs photovoltaïques de la prochaine génération.

"Among those whom I like or admire, I can find no common denominator, but among those whom I love, I can; all of them make me laugh."

- W. H. Auden

Table of contents

List of figures	xxiv
List of tables	xxxviii
1 Introduction	1
1.1 Current world energy crisis	1
1.2 Renewable energy sources	3
1.2.1 Hydroelectric Power	5
1.2.2 Wind Energy	7
1.2.3 Bioenergy (Biofuel)	8
1.2.4 Solar Power	9
1.3 Solar cells	12
1.3.1 First Generation Solar Cells	15
1.3.2 Second Generation Solar Cells	17

Table of contents

1.3.3	Third Generation Solar Cells	20
1.4	Perovskites	25
1.4.1	Perovskite Cells as Emerging PVs	25
1.4.2	Architecture of Perovskite PV Devices	25
1.4.3	The Perovskite Structure	28
1.4.4	Goldschmidt's Tolerance Factor	29
1.4.5	Phase transitions of MAPI	30
1.4.6	The MA ⁺ Cation	31
1.5	Challenges of Perovskite PVs	34
1.5.1	Stability	34
1.5.2	Stability in Humidity	35
1.5.3	Thermal and Photo-Stability	38
1.5.4	Further Environmental Challenges	39
1.6	Enhancing perovskites through compositional engineering	39
1.6.1	A-site Cation Engineering	40
1.6.2	B-site Cation Engineering	40
1.6.3	X-site Anion Engineering	41
1.7	Aims of the Thesis	42

References	43
2 Characterisation Techniques	49
2.1 Scattering and Diffraction	50
2.2 X-ray Diffraction	52
2.2.1 X-ray Generation	53
2.2.2 Reciprocal Space	55
2.2.3 Bragg's Law	55
2.2.4 The Ewald Sphere	57
2.2.5 Powder X-ray Diffraction	57
2.2.6 Rietveld Refinement	59
2.3 Quasi Elastic Neutron Scattering (QENS)	62
2.3.1 Elastic vs. Inelastic Scattering	63
2.3.2 Coherent vs. Incoherent Scattering	64
2.4 Nuclear Magnetic Resonance	65
2.4.1 Zeeman Interaction	67
2.4.2 Chemical Shielding Interaction	68
2.4.3 Dipolar Interaction	68
2.4.4 J-Coupling	69

2.4.5	Quadrupolar Interaction	69
2.5	Nuclear Quadrupole Resonance	72
2.5.1	General background of NQR	72
2.5.2	Basic NQR Theory	73
2.5.3	Further complexities in NQR detection	76
References		78
3	Probing the Influence of Post-Synthetic Treatments on MAPI Structures through Scattering and Diffraction Techniques	80
3.1	Introduction	80
3.1.1	Thin Film Deposition	82
3.1.2	Role of Thermal Annealing	83
3.1.3	Addressing Inconsistencies in Annealing Parameters for Optimal Perovskite Performance	84
3.1.4	Purpose of this Chapter	85
3.2	Experimental	85
3.2.1	Precursor Synthesis	85
3.2.2	Solution Synthesis of $\text{CH}_3\text{NH}_3\text{PbI}_3$	86
3.2.3	Solution Synthesis of NH_4PbI_3	86

Table of contents

3.2.4	Quasi Elastic Neutron Scattering Measurements	87
3.2.5	Synchrotron Powder Diffraction	87
3.3	Probing cation dynamics with Quasi-elastic Neutron Scattering	88
3.4	Optimising Vacuum Annealing through Variable Temperature and Time	98
3.4.1	Purpose of this study	98
3.4.2	Initial Investigation into Reproducibility of Variable Temperature Annealing	99
3.4.3	Further Investigating the Impact of Annealing Time	101
3.5	Attempt to optimise Iodine Annealing post synthetic treatment	113
3.6	Addressing Impurity Phase Formation in the Optimisation of MAPI Treatments	125
3.6.1	Synthesis and determination of NH_4PbI_3	128
3.7	NH_4PbI_3 as a Decomposition Product in the Annealing of MAPbI_3 . . .	133
3.7.1	Thermal Decomposition of MAPbI_3	135
3.7.2	Formation of NH_4PbI_3 During Annealing	136
3.7.3	Impact on Material Properties and Challenges	136
3.8	Final Discussion	137
	References	140

4 Investigating Cation Dynamics in MAPI Using Solid-State NMR Techniques	143
4.1 Introduction	143
4.2 Experimental	144
4.2.1 Solid-state ^1H NMR Spectroscopy	144
4.2.2 Solid-state ^{13}C NMR Spectroscopy	145
4.2.3 Solid-state ^{14}N NMR Spectroscopy	146
4.3 Investigation of MA^+ Cation Dynamics and Impurities in Post-Synthetically Treated MAPI via ^1H NMR	147
4.3.1 Results from ^1H NMR	148
4.4 Analysing Carbon Environments in Treated MAPI Using ^{13}C NMR	154
4.5 Structural and Dynamic Insights from Variable Temperature ^{14}N NMR	157
4.5.1 Temperature Dependent Variations in Quadrupolar Coupling Constant (C_Q) and Their Implications for Phase Transitions in MAPI	162
4.6 Summary of Structural and Dynamic Insights from Solid-State NMR	171
4.7 Overview on the Impact of Phase Transition Behaviour of Post-synthetic treatments	172
4.8 MAPI and the Magic Angle	174

References		179
5	Optimisation of NQR echo for MAPbI₃	181
5.1	The Application of Halide NMR and NQR to Study Hybrid Perovskites	181
5.2	Current Status of NQR Optimisation	185
5.3	Purpose of Present Study	188
5.4	Experimental Section	189
5.4.1	Material Synthesis	189
5.4.2	Characterisation	189
5.5	Results and Discussion	191
5.5.1	Initial RF calibration with 400 MHz NMR Spectrometer	191
5.5.2	Experimental NQR Measurements	193
5.5.3	Investigating the effect of shorter second pulse	198
5.5.4	Spinach Simulations of echo pulse nutations	203
5.6	Conclusions and Outlook	204
References		209
6	Final Conclusions and Outlook	212
6.1	Conclusions	212

6.2 Outlook 214

List of figures

1.1	Comparison of LCOE across various technologies, utilising data from references.[8, 9] IRENA data is illustrated with colored circles, while the maximum and minimum LCOE values from Lazard are depicted with lighter-shaded rectangles. Notably, Lazard’s report does not provide information on hydroelectric power or bioenergy, which have therefore been excluded from this comparison.	4
1.2	Global renewable electricity generation from 1965 to 2023. The graph illustrates the significant growth of renewable energy sources, particularly hydropower, wind, and solar energy. Hydropower remains the dominant contributor, though wind and solar have experienced rapid expansion in recent decades. The category "Other renewables" includes energy sources such as geothermal, biomass, and wave energy. Reproduced from reference [10].	6

1.3	Percentage share of cumulative installed power generation capacity across all technologies from 2010 to 2027, based on re-plotted data from reference [13]. The forecast remains consistent with Figure 1.2, indicating that hydropower is expected to continue as the leading source of renewable electricity generation throughout the forecast period, even though its capacity is projected to grow at a slower rate compared to wind and solar PV technologies. Data was not reported at the source for nuclear energy.	10
1.4	NREL Best Research-Cell Efficiency Chart of emerging PV technologies from 1975 to 2025.[19] Highlighting advancements in dye-sensitised (open circles), perovskite yellow filled circles), organic (filled circles), quantum dot (open diamonds), and CZTS (filled diamonds) solar cells, illustrating the rapid efficiency gains in next-generation PV materials.	14
1.5	Schematic diagram of a silicon solar cell structure and operation. Demonstrating the photovoltaic effect in a silicon solar cell, where light energy generates electron-hole pairs in the N-type and P-type silicon layers, producing voltage (top). The atomic structure of pure silicon, N-type silicon (with an extra electron), and P-type silicon (with a missing electron or hole), highlighting the role of doping in charge carrier movement (bottom).	16

1.6	The four most common perovskite solar cell architectures including a transparent conducting oxide (TCO) layer, electron transport layer (ETL), and a hole transport layer (HTL). a) planar cell, b) planar inverted cell, c) mesoporous cell and d) mesoporous carbon cell. The beige coloured spheres represent mesoporous titania, the small yellow spheres represent a mesoporous zirconia layer and the black spheres are mesoporous carbon.	26
1.7	Structures of spiro-OMeTAD (top), PCBM (bottom left), and PE-DOT:PSS (bottom right).	27
1.8	Generic ABX_3 structure of a perovskite	28
1.9	The three temperature-dependent phases of $MAPbI_3$	31
1.10	Temperature-dependent transitions between the polymorphic phases (α , β , γ , and δ) of $CsPbI_3$. The photoactive phases are illustrated in dark gray, while the non-photoactive phase is shown in yellow. Adapted from [71].	36
2.1	Demonstration of where each technique can probe the organic-inorganic halide perovskites, showcasing multi-technique characterisation to investigate structural changes in the inorganic lattice and alterations in the dynamics of the organic cation.	50
2.2	A plot illustrating various characterisation techniques and their positions on a graph of timescale vs momentum, exemplifying the range of information each technique can capture. This diagram visualises comparisons between the techniques. The diagram is taken from [1]. . .	51

2.3	Schematic of the different energy level transitions and the corresponding generated characteristic X-ray	54
2.4	Illustration of Bragg diffraction, where incident waves reflect off atomic planes in a crystal with spacing, d . Waves 1 and 2, initially in phase, remain in phase after reflection if the path difference CBD is an integer multiple of the wavelength λ , satisfying Bragg's Law (2.1) The reflected angle θ equals the incident angle, and diffraction occurs at specific angles corresponding to different reflection orders ($n = 1,2,3$, etc.). At non-integer n , destructive interference eliminates the reflected waves.	56
2.5	The Ewald sphere represents the reciprocal space construction for X-ray diffraction. The intersection of the scattering vector k with a reciprocal lattice point (hkl) satisfies Bragg's condition, resulting in diffraction from the real lattice planes with spacing d_{hkl} . A shorter incident X-ray wavelength increases the radius of the Ewald sphere ($r = 1/\lambda$), leading to more crossing points and additional Bragg reflections.	58
2.6	Schematic of the different spin interactions within a nucleus	67
2.7	Diagram displaying the effect of quadrupolar splitting for an $I = 5/2$ nucleus upon application of a magnetic field.	71
2.8	Energy level splitting and allowed transitions for a spin-5/2 nucleus in NQR. The six m_I sublevels ($\pm 5/2, \pm 3/2, \pm 1/2$) are split by quadrupolar interactions. Dashed lines indicate allowed transitions ($\Delta m_I = \pm 1$), corresponding to measurable NQR frequencies.	74

3.1	Photograph of the SNBL based diffractometer during a powder diffraction experiment. Photo captured by Dr Charlie McMonagle for purpose of this thesis.	89
3.2	Representative QENS measurements of pristine MAPI indicating scattering intensity against energy transfer ω (meV) measured at 270 K plotted for groups of 7 detectors corresponding to different momentum transfers, Q . Values are 0.24354, 0.40552, 0.63719, 0.96461, 1.23083, 1.52726, and 1.7197 \AA^{-1}	90
3.3	Representative QENS spectrum of pristine MAPI corresponding to $Q = 1.72 \text{\AA}^{-1}$ measured at 270 K. Experimental data are represented by hollow circles with associated error bars. The solid red curve corresponds to the fit of $S(Q, \omega)$ model. The elastic part is simulated with a delta function (green) and the quasielastic part is simulated with a single Lorentzian function (purple).	91
3.4	FWHM of Lorentzian <i>vs.</i> momentum transfer (Q^2) for QENS data ranging from 365 to 160 K for pristine MAPI.	93
3.5	FWHM of Lorentzian <i>vs</i> Q for QENS data ranging from 365 to 160 K for vacuum-annealed MAPI.	95
3.6	FWHM of Lorentzian <i>vs</i> Q for QENS data ranging from 365 to 160 K for MAPI exposed to I_2 vapour in the post-synthetic annealing treatment.	97
3.7	Powder X-ray diffraction patterns for MAPI samples annealed under vacuum at various temperatures for 90 minutes. (b) Expanded view of the tetragonal phase reflections at [211] and [022].	100

3.8	X-ray powder diffraction profile from Rietveld refinement for the MAPI samples annealed under vacuum at temperatures ranging from 280 to 320 K. Measurements were collected at room temperature. (a) Pristine MAPI $R_p = 4.32\%$ and $R_{wp} = 6.42\%$, (b) Vac280 $R_p = 4.32\%$ and $R_{wp} = 6.42\%$, (c) Vac290 $R_p = 5.22\%$ and $R_{wp} = 7.54\%$, (d) Vac300 $R_p = 6.30\%$ and $R_{wp} = 9.19\%$, (e) Vac310 $R_p = 5.62\%$ and $R_{wp} = 7.79\%$ and (f) Vac320 $R_p = 5.04\%$ and $R_{wp} = 7.25\%$	102
3.9	X-ray powder diffraction profile from Rietveld refinement for the MAPI samples annealed under vacuum at temperatures ranging from 320 to 360 K. The measurements were collected at room temperature. (a) Vac330 $R_p = 4.45\%$ and $R_{wp} = 6.03\%$, (b) Vac340 $R_p = 6.55\%$ and $R_{wp} = 9.37\%$, (c) Vac350 $R_p = 5.19\%$ and $R_{wp} = 7.38\%$, (d) Vac360 $R_p = 5.44\%$ and $R_{wp} = 7.66\%$	103
3.10	Powder X-ray diffraction patterns for MAPI samples annealed under vacuum at 340 °C for various lengths of time. (b) Magnified view of the tetragonal phase reflections at (211) and (022). (c) The ratio of the intensity of these two peaks as a function of annealing time.	105
3.11	X-ray powder diffraction profile from Rietveld refinement for the samples performed at room temperature. (a) Vac 0h30 $R_p = 6.31\%$ and $R_{wp} = 8.22\%$, (b) Vac 1 h $R_p = 5.51\%$ and $R_{wp} = 8.38\%$, (c) Vac 1 h 30 $R_p = 6.09\%$ and $R_{wp} = 8.50\%$, (d) Vac 2 h $R_p = 6.03\%$ and $R_{wp} = 9.26\%$	106
3.12	I11 synchrotron powder diffraction profile of Pristine MAPI measured at 297 K.	107

3.13 I11 synchrotron powder diffraction profile of Vacuum Annealed 1 h measured at 297 K.	108
3.14 I11 synchrotron powder diffraction profile of Vacuum Annealed 2 h measured at 297 K.	108
3.15 The ratio of a and c lattice parameters $(c/a)\sqrt{2}$ plotted as a function of temperature for pristine MAPI, Vac 1 h, and Vac 2 h.	110
3.16 Unit cell volume for the Pristine, Vac 1 h, and Vac 2 h MAPI samples de- rived from Rietveld refinement of powder X-ray diffraction measurements performed at variable temperature.	112
3.17 P–I–Pb bond angle for the Pristine, Vac 1 h, and Vac 2 h MAPI samples derived from Rietveld refinement of powder X-ray diffraction measurements performed at variable temperature.	114
3.18 Powder X-ray diffraction patterns for MAPI samples annealed with 0.025 g of iodine at various temperatures for 90 min.	115
3.19 Powder X-ray diffraction patterns for MAPI samples annealed with 0.05 g of iodine at various temperatures for 90 minutes.	117
3.20 Powder X-ray diffraction patterns for MAPI samples annealed with 0.1 g of iodine at various temperatures for 90 minutes.	118
3.21 Powder X-ray diffraction patterns for MAPI samples annealed with variable amounts of iodine at 290 °C for 90 minutes.	119

-
- 3.22 X-ray powder diffraction profile from Rietveld refinement for I₂-Annealed performed at room temperature using I/4mcm space group. Lattice parameters were refined to $a = 8.9096(3) \text{ \AA}$, $b = 8.9096(3) \text{ \AA}$, $c = 12.5989(2) \text{ \AA}$. $R_p = 6.06\%$ and $R_{wp} = 8.69\%$ 120
- 3.23 X-ray powder diffraction profile from Rietveld refinement for I₂-Annealed performed at room temperature using Pm-3m space group. Lattice parameters were refined to $a = 6.3005(0) \text{ \AA}$, $b = 6.3005(0) \text{ \AA}$, $c = 6.3005(0) \text{ \AA}$. $R_p = 6.38\%$ and $R_{wp} = 8.63\%$ 121
- 3.24 Synchrotron powder diffraction profile from Rietveld refinement for I₂-Annealed performed at 297 K. Lattice parameters were refined to $a = 8.8909(3) \text{ \AA}$, $b = 8.8909(3) \text{ \AA}$, $c = 12.6457(5) \text{ \AA}$. $R_p = 8.98\%$ and $R_{wp} = 10.6\%$ 123
- 3.25 (a) Structural model for pristine MAPI with lattice parameter $a = 8.8696 \text{ \AA}$ and $c = 12.6685 \text{ \AA}$, and a cell volume of 996.621 \AA^3 . (b) Structural model for iodine treated MAPI with lattice parameter $a = 8.8909 \text{ \AA}$ and $c = 12.6458 \text{ \AA}$, and a cell volume of 999.626 \AA^3 124
- 3.26 Very small presence of secondary phase reflections in vacuum-annealed 2 h sample, indicated by asterisks. Diffraction pattern was collected on the I11 beamline. 126
- 3.27 Pattern matching of MAPI annealed with iodine was performed using the Diffrac.Eva software. The green reflections correspond to the main phase of pristine MAPI, the blue reflections match those of $\text{NH}_4\text{PbI}_3(\text{H}_2\text{O})_2$, and the pink reflections are consistent with PbI_2 127

3.28 Schematic of solution synthesis protocol for preparation of NH_4PbI_3 . . .	128
3.29 Comparison of synthesised NH_4PbI_3 with simulated diffraction pattern from CIF available in literature from reference [39].	129
3.30 Comparison of synthesised $\text{NH}_4\text{PbI}_3(\text{H}_2\text{O})_2$ with simulated diffraction pattern from CIF available in literature from reference [40].	130
3.31 X-ray powder diffraction profile from Rietveld refinement for $\text{NH}_4\text{PbI}_3(\text{H}_2\text{O})_2$ performed at room temperature. $R_p = 4.96\%$ and $R_{wp} = 7.06\%$	131
3.32 Different views of the refined crystal structure of $\text{NH}_4\text{PbI}_3(\text{H}_2\text{O})_2$ using the space group Pnma. The unit cell is described with a black cuboid. .	132
3.33 Comparison of the simulated diffraction pattern of $\text{NH}_4\text{PbI}_3(\text{H}_2\text{O})_2$ with experimental diffraction patterns of MAPI subjected to extended post-synthesis vacuum-annealing for 6 h (red) and 7 h (blue), highlighting the increased presence of secondary phases for comparison with observed reflections. Dotted lines are used to guide the eye towards matching reflections.	134
4.1 Experimental (black) and simulated (red) ^1H MAS NMR spectra at 9.4 T with a MAS frequency of 25 kHz for (a) MAI precursor, (b) pristine MAPbI_3 , (d) vacuum-annealed for 1 h, (e) vacuum-annealed for 2 h, and (f) iodine-annealed samples. Spectra were collected at room temperature and simulated as the sum of the signals of three species: CH_3 (blue), NH_3^+ (orange) and NH_4^+ (purple). Panel (c) shows an overlay of the four spectra to highlight the broadening of the NH_3 signal.	149

4.2	Experimental (black) and simulated (red) 1D ^1H MAS NMR spectra of MAPbI_3 , vacuum-annealed during 1 h or 2 h, or annealed in the presence of iodine acquired at 18.8 T with a MAS frequency of 40 kHz. Spectra were collected at room temperature simulated as the sum of the signals of three species: CH_3 (blue), NH_3^+ (orange), and NH_4^+ (purple). 151	151
4.3	Room temperature T_1 relaxation times of CH_3 , NH_3^+ , and NH_4^+ protons for each material measured at 18.8 T with a MAS frequency of 40 kHz. 153	153
4.4	Room temperature 1D ^{13}C MAS NMR spectra of pristine and post-synthetically treated MAPI at 9.4 T with a MAS frequency of 25 kHz. 155	155
4.5	1D ^{14}N NMR spectra of pristine and post-synthetically treated MAPI collected at 297 (top) and 350 K (bottom) using a 9.4 T magnetic field and a MAS frequency of 5 kHz. 159	159
4.6	1D variable temperature ^1H -decoupled ^{14}N NMR spectra of pristine and post-synthetically treated MAPI collected using a 9.4 T magnetic field and a MAS frequency of 5 kHz. 161	161
4.7	1D ^1H -decoupled ^{14}N MAS NMR experimental spectrum of pristine MAPI (black) compared with a spectral simulation (red dashed). The experimental spectrum was recorded at 295 K using a 9.4 T magnetic field and a MAS frequency of 5 kHz. The simulation, generated using the Topspin sola QUADALL model, represents the spectrum as a sum of the centreband (isotropic component) and a series of spinning sidebands (anisotropic component). 163	163

-
- 4.8 Plot of C_Q versus temperature for pristine MAPI (black), vac 1 h (orange), vac 2 h (blue), and I₂-annealed (purple) samples, illustrating the evolution of the ¹⁴N nucleus interaction with the EFG as a function of temperature. The differences in C_Q reflect variations in local symmetry and cation dynamics across the samples due to different post-synthetic treatments. 165
- 4.9 Plot of relative intensity of the centreband versus temperature for pristine MAPI (black), vac 1 h (orange), vac 2 h (blue), and I₂ annealed (purple) samples. 167
- 4.10 Plot of relative intensity of the second spinning sideband versus temperature for pristine MAPI (black), vac 1 h (orange), vac 2 h (blue), and I₂-annealed (purple) samples. 168
- 4.11 Plot of relative intensity of the second spinning sideband versus temperature for pristine MAPI (black), vac 1 h (orange), vac 2 h (blue), and I₂-annealed (purple) samples. Dashed lines serve only as a guide for the eyes. 173
- 4.12 1D ¹⁴N NMR spectrum with ¹H decoupling of pristine MAPI obtained at room temperature at 9.4 T with a MAS frequency of 5 kHz. The overall spectrum (black) is presented alongside expanded views of the centreband and various lineshapes of the spinning sidebands (red), offering detailed insight into the spectral characteristics. The asterisk indicates a contamination of NH₄Cl reference in the sample. 175

4.13 (a) ^2H signal of PMMA before (black) and after (orange) magic angle adjustment. (b) 1D ^{14}N NMR spectra of pristine MAPI recorded at room temperature using a 18.8 T magnetic field and a MAS frequency of 5 kHz. The spectrum includes the initial centreband signal without magic angle adjustment (black), the signal after adjustment using PMMA (orange), and the final resulting signal after applying magic angle adjustment directly to the MAPI sample (red).	176
4.14 Spectral simulations aimed at determining the effect of deviations in the magic angle on the lineshape distortion observed in MAPI. These simulations illustrate how variations in the magic angle influence the spectral characteristics, providing insights into the underlying causes of the observed lineshape alterations. Chosen spinning sideband is denoted with † on full spectra.	177
4.15 Simulations of the initially acquired spectra, facilitating the back calculation of the magic angle, enabling a more accurate understanding of its influence on the spectral lineshape of MAPI.	178
5.1 Simulation of ^{127}I NMR spectrum of MAPI at 28.2 T	183
5.2 (a) The evolution of the NQR signal as a function of RF pulse length for one resonance frequency of sodium nitrate. Below the nutation curve is the observed signal. Figure adapted from reference [33] and reprinted with permission. (b) Nutation curves for NQR signal of ^{14}N nucleus with $\eta_Q = 0$ (solid line) and $\eta_Q \neq 0$ (dashed line). Figure adapted from reference [33] and reprinted with permission.	187

5.3	Pulse sequence utilised to measure the Bloch-Siegert shift of protons for the calibration of rf field strength	191
5.4	Example of a 1D spectrum of silicon acquired (top). An example of a ^1H -detected Bloch-Siegert shift nutation spectrum depicted as a function of the pulse length τ_p (bottom).	192
5.5	QUEST simulation [17] of NQR spectra of tetragonal MAPbI_3 using C_Q and η_Q values reported in reference [24]. An expansion of the spectra corresponding to $3/2 \leftrightarrow 5/2$ and $1/2 \leftrightarrow 3/2$ transitions are provided above.	194
5.6	Illustration of the Hahn echo pulse sequence and corresponding coherence pathway for NQR experiments.	195
5.7	Influence of RF field amplitude on NQR transitions of MAPI resonating at (a, c, e) 83.45 and (b, d, f) 169.91 MHz detected using Hahn echo experiment and (a, b) 4 and (c, d) 2.5 mm MAS probes. For each RF field amplitude, the lengths of the first and second pulses were optimised. Panels (e, f) displays a comparison of the transitions at (e) 83.45 and (f) 169.91 MHz detected using 2.5 (red) and 4 (black) mm MAS probes.	197

5.8	Comparison of excitation bandwidth of each probe at various carrier frequencies. (a) 4 mm probe, 74 kHz RF field amplitude, (b) 2.5 mm probe, 125 kHz RF field amplitude, (c) 4 mm probe, 160 kHz RF field amplitude, and (d) 2.5 mm probe, 251 kHz RF field amplitude. Each experimentally measured signal is fitted with a Gaussian function (red) and plotted relative to the carrier frequency offset. The maximum intensity of each peak is depicted as a function of the offset and fitted with a smooth spline function (blue) to aid in overall comparisons. . . .	199
5.9	NQR excitation profile at 83.45 MHz using both shortened (a) and optimised (b) pulse 2 lengths with 4 mm probe.	201
5.10	NQR excitation profiles at 166.9 MHz using both shortened (a) and optimised (b) pulse 2 lengths with 4 mm probe.	202
5.11	Simulated nutation during (a, b) first and (c, d) second pulses of Hahn echo experiment along with (e, f) excitation profiles for the detection of NQR transition at 83.45 MHz using RF field amplitude of 50 (a, c, e) and 100 (b, d, f) kHz.	205
5.12	Simulated nutation during (a, b) first and (c, d) second pulses of Hahn echo experiment along with (e, f) excitation profiles for the detection of NQR transition at 166.90 MHz using RF field amplitude of 50 (a, c, e) and 100 (b, d, f) kHz.	206

List of tables

1.1	Tabulated data concerning the lattice parameters, space group, and temperature dependence of the three phases of MAPbI ₃	30
1.2	Conditions and parameters for the IEC 612215:1016 Damp Heat and Humidity Freeze tests[69].	35
2.1	Neutron scattering lengths and incoherent cross-sections for elements present in MAPI. Data sourced from.[6]	63
3.1	Comparing the reported PCE's and thermal treatment undertaken for several different studies of MAPI. Solvents are GBL (γ -butyrolactone), DMF (dimethylformamide), and DMSO (dimethyl sulfoxide).	84
3.2	Vacuum annealing conditions applied post-synthesis to a series of samples, each annealed for 90 minutes and identified by a unique ID indicating the annealing temperature.	99
3.3	Room temperature refined lattice parameters for variable temperature vacuum-annealed samples.	101

3.4	Post synthesis vacuum annealing conditions undertaken for a range of samples annealed at 340 °C identified by a unique ID, specifying the annealing time.	104
3.5	Refined structural parameters for Pristine MAPI derived from Rietveld refinement of synchrotron powder diffraction data measured at 297 K. Lattice parameters $a = 8.8705 \text{ \AA}$, $b = 8.8705 \text{ \AA}$, $c = 12.6678 \text{ \AA}$ and a cell volume of 996.771 \AA^3	109
3.6	Refined structural parameters and occupancies for Vac 1 h derived from Rietveld refinement of synchrotron powder diffraction data measured at 297 K. Lattice parameters $a = 8.8817 \text{ \AA}$, $b = 8.8817 \text{ \AA}$, $c = 12.6493 \text{ \AA}$ and a cell volume of 997.820 \AA^3	109
3.7	Refined structural parameters and occupancies for Vac 2 h derived from Rietveld refinement of synchrotron powder diffraction data measured at 297 K. Lattice parameters $a = 8.8926 \text{ \AA}$, $b = 8.8926 \text{ \AA}$, $c = 12.6238 \text{ \AA}$ and a cell volume of 998.274 \AA^3	109
3.8	Refined structural parameters for I ₂ -Annealed derived from Rietveld refinement of synchrotron powder diffraction data measured at 297 K. .	122
3.9	Refined structural parameters for NH ₄ PbI ₃ derived from Rietveld refinement of in-house powder diffraction data measured at room temperature. Lattice parameters $a = 10.2266(2) \text{ \AA}$, $b = 4.6049(1) \text{ \AA}$, $c = 22.6850(4) \text{ \AA}$ and a cell volume of 1068.286 \AA^3	130

4.1	Isotropic chemical shift (δ_{iso}) and FWHM values for different proton environments in pristine MAPI, obtained from ^1H NMR measurements at 18.8 T.	151
4.2	Isotropic chemical shift (δ_{iso}) and FWHM values for different proton environments in Vac 1 h, obtained from ^1H NMR measurements at 18.8 T.	152
4.3	Isotropic chemical shift (δ_{iso}) and FWHM values for different proton environments in Vac 2 h, obtained from ^1H NMR measurements at 18.8 T.	152
4.4	Isotropic chemical shift (δ_{iso}) and FWHM values for different proton environments in I ₂ -Annealed, obtained from ^1H NMR measurements at 18.8 T.	152
4.5	Summary of ^{13}C isotropic chemical shifts, FWHM, and relative intensities for pristine and post-synthetically treated MAPI	156
4.6	Comparison of phase transition temperatures for different MAPI samples as determined by diffraction and solid-state NMR techniques. Variations in transition temperatures highlight the impact of vacuum and iodine annealing on structural stability and phase behaviour.	174
5.1	NMR properties of the half-integer-spin quadrupolar halogen nuclei, adapted from Szell <i>et al.</i> (2020).[16]	182
5.2	Parameters for Bloch-Siegert experiments used to calibrate the RF field at relevant carrier frequencies for MAPI. Here, ν_{R} denotes the MAS frequency, $\nu_{0\text{X}}$ represents the carrier frequency, $\nu_{1\text{X}}$ indicates the RF field amplitude, and p_{90} is the pulse length.	193

5.3	Optimal experimental parameters for the observation of NQR transitions of MAPI at 83.45 and 166.91 MHz using 2.5 and 4.0 mm probes.	196
5.4	Optimised pulse lengths and FWHM from NQR simulations	203
5.5	Optimised pulse lengths for Hahn echo experiment to detect NQR transitions of MAPI resonating at 83.45 and 166.90 MHz	204

Chapter 1

Introduction

1.1 Current world energy crisis

The world stands on the brink of a profound energy crisis, exacerbated by rapid and uneven population growth, increasing per capita energy consumption, and declining global accessibility to fossil fuels.[1, 2] This looming crisis threatens not only energy supply but also the stability of economies, societies, and the environment. The "World Energy Trilemma," as described by the World Energy Council, underscores the critical challenge of achieving energy security, equity, and sustainability. The Trilemma framework acknowledges that each nation faces unique difficulties, with global and local crises further compounding these challenges. Events such as the COVID-19 pandemic and geopolitical conflicts like the Russian invasion of Ukraine have intensified imbalances in energy supply and demand, amplifying the urgency for solutions.[3]

In 2021, global primary energy consumption surged by 31 exajoules, marking the largest recorded increase in history. Despite growing recognition of the need for

1.1 Current world energy crisis

cleaner energy, fossil fuels - responsible for around 82% of the world's energy supply - remain dominant.[4, 5] This dependency is deeply problematic, as fossil fuels are the primary source of greenhouse gas (GHG) emissions, which are driving global warming and accelerating climate change. The world is now facing the so-called "*terawatt challenge*": the need to generate vast amounts of energy to sustain human activities while simultaneously cutting GHG emissions to mitigate the environmental damage caused by continued fossil fuel use.[5]

Despite heightened societal awareness, fueled by activism from groups like Extinction Rebellion, and the clear warnings from the scientific community, progress remains sluggish. While renewable energy resources are gaining ground, the global energy mix has seen little significant change in the past two decades, with fossil fuels maintaining a dominant share.[6] This persistent reliance on carbon-intensive fuels underscores the urgent need for a more decisive shift toward renewable energy.

Global initiatives, such as the European Union's 2030 targets, aim to reduce GHG emissions by 40% and generate 32% of energy from renewable sources.[7] However, achieving these targets requires not only advancements in the efficiency of renewable technologies but also substantial reductions in their costs. Without affordable and scalable renewable alternatives, economically and politically unstable regions may struggle to transition away from fossil fuels, deepening the global disparity in energy equity and sustainability.

The current energy crisis is not just a technological problem but a multifaceted challenge that intertwines environmental, economic, and social issues. Urgent and coordinated global action is required to accelerate the transition to cleaner energy systems, reduce reliance on fossil fuels, and avert the worst impacts of climate change. This chapter will explore the role of emerging energy technologies, including advanced

solar materials, in addressing this complex and urgent challenge.

1.2 Renewable energy sources

To serve as a viable alternative to fossil fuels, any renewable energy source must meet key criteria: it must be efficient, affordable, and have a long operational life. Renewable energy stands out due to its immense potential to fulfill global energy demands, provided it can be effectively harnessed. The leading renewable energy technologies include hydroelectric power, solar photovoltaic (PV), wind energy, geothermal power, and bioenergy. Over the past decade, significant cost reductions in these technologies have accelerated the transition towards a more sustainable energy system. This is reflected in the decreasing levelised cost of electricity (LCOE) for various renewable sources, as depicted in Figure 1.1. Since 2010, the LCOE for onshore wind has dropped by 69%, solar PV by 89%, and offshore wind by 59%, underscoring the increasing affordability of renewable energy. This downward trend in costs is expected to continue, further promoting the adoption of clean energy technologies.

The LCOE is a key metric in assessing the cost-effectiveness of electricity generation technologies, as it encompasses all relevant costs, including construction, installation, financing, and operation, alongside maintenance expenses. The LCOE influences the competitiveness of different energy sources and plays a critical role in their widespread deployment. As renewable technologies mature, improvements in efficiency, economies of scale, and technological advancements lead to further reductions in their LCOE, making them increasingly competitive with fossil fuel-based systems.

For fossil fuel-based technologies, the LCOE is influenced by fluctuating fuel prices and, for carbon-emitting technologies, the costs associated with carbon emissions.

1.2 Renewable energy sources

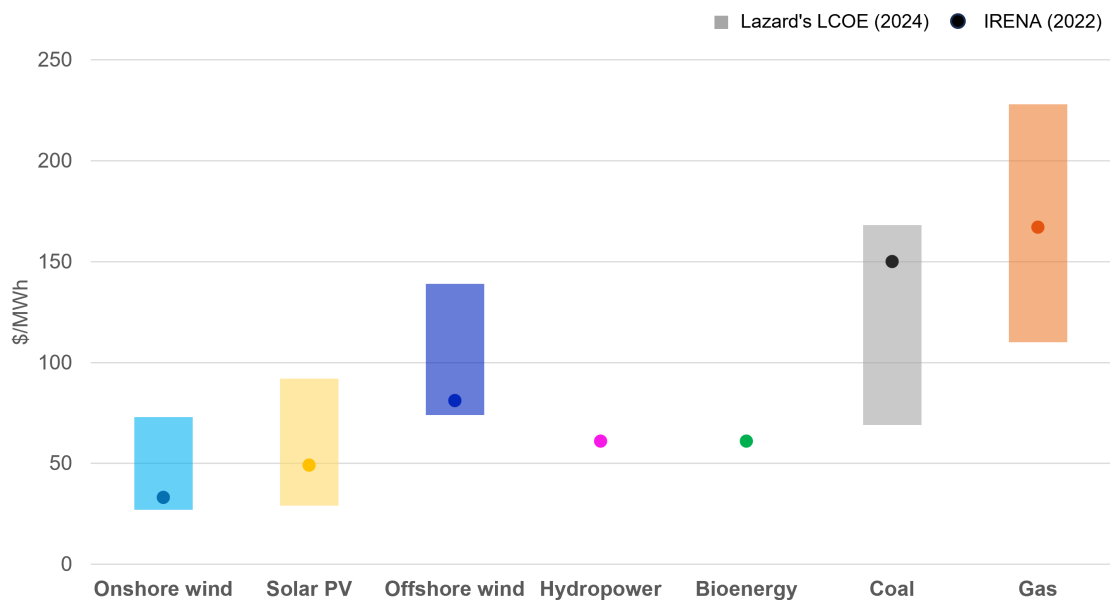


Figure 1.1 Comparison of LCOE across various technologies, utilising data from references.[8, 9] IRENA data is illustrated with colored circles, while the maximum and minimum LCOE values from Lazard are depicted with lighter-shaded rectangles. Notably, Lazard’s report does not provide information on hydroelectric power or bioenergy, which have therefore been excluded from this comparison.

Historically, more efficient and cost-effective technologies have replaced older, more expensive systems as they became obsolete. Today, a global shift towards renewable energy is driving the energy transition, as renewables become more affordable and accessible.

The data presented here draws from two primary sources: Lazard’s 2023 LCOE analysis (version 16.0) and the International Renewable Energy Agency’s (IRENA) cost assessments up to 2022.[8, 9] While Lazard’s analysis focuses primarily on U.S. projects, it is widely used as a global benchmark. In contrast, IRENA calculates global weighted averages for each technology. Despite these differences in scope, both sources show consistent trends in the declining LCOE of renewable technologies, emphasising their growing role in the future energy landscape.

In the subsequent section, each major renewable energy technology - hydroelectric power, solar PV , wind energy (both onshore and offshore), geothermal energy, and bioenergy - will be discussed in further detail. Their respective advantages, disadvantages, and costs will be compared to feasibility as alternatives to fossil fuels.

1.2.1 Hydroelectric Power

Hydroelectric power currently stands as the dominant source of renewable energy generation worldwide, as illustrated in Figure 1.2. It provides a cost-effective and reliable means of electricity production, with the added benefit of energy storage and the sustainability of water resources. However, its deployment faces significant regional variability. The high upfront capital costs, complex infrastructure requirements, and the necessity of access to abundant water sources limit its feasibility to specific geographic locations. This is reasonably reflected with an LCOE of \$61 per MWh.[8] Countries

Renewable electricity generation, World

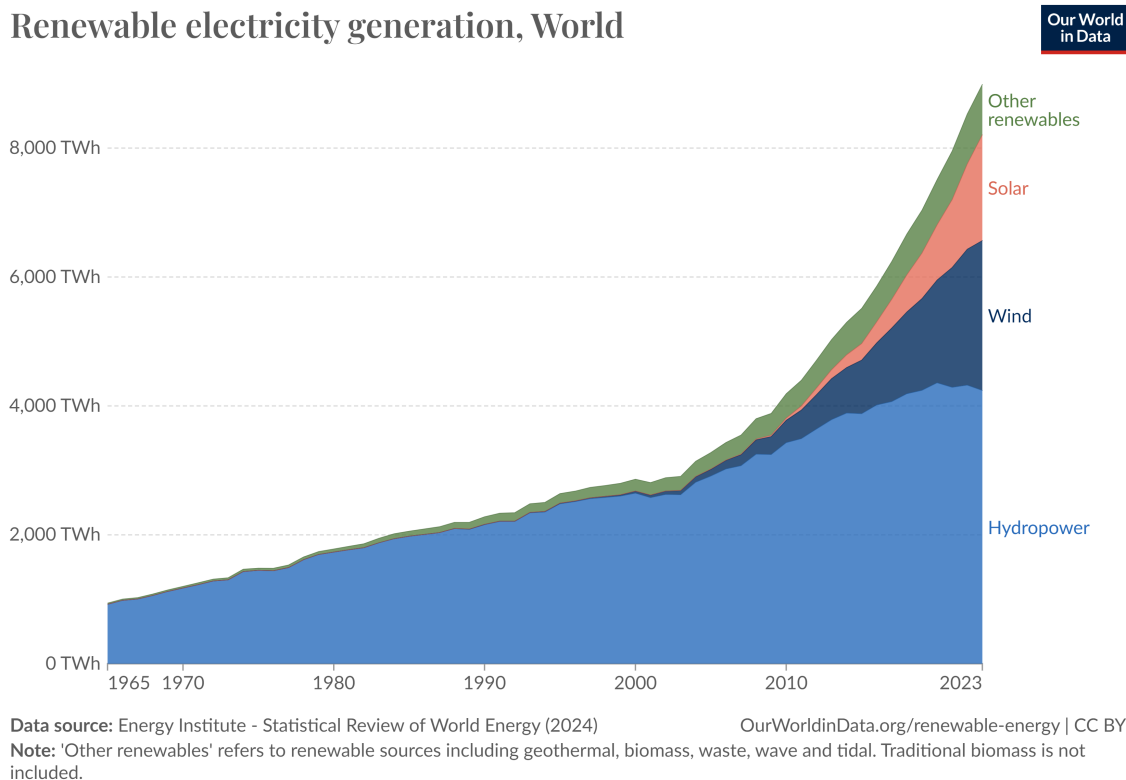


Figure 1.2 Global renewable electricity generation from 1965 to 2023. The graph illustrates the significant growth of renewable energy sources, particularly hydropower, wind, and solar energy. Hydropower remains the dominant contributor, though wind and solar have experienced rapid expansion in recent decades. The category "Other renewables" includes energy sources such as geothermal, biomass, and wave energy. Reproduced from reference [10].

experiencing water scarcity or lacking suitable natural water bodies are unable to fully harness the potential of hydroelectric power. Moreover, the ecological consequences of large-scale hydroelectric projects often raise concerns, particularly in regions where they disrupt sensitive river ecosystems.

A prominent example of these challenges can be observed in China's Three Gorges Dam, the largest hydroelectric project in the world. Although the dam has significantly increased China's renewable energy capacity, contributing to the country's energy security, it has also raised concerns about its environmental and social impacts. The

dam has altered natural water flow patterns, resulting in the displacement of millions of people and threatening the biodiversity of the Yangtze River. In addition, altered river flow has led to soil erosion and increased the risk of landslides in surrounding areas, raising questions about the long-term sustainability of such large hydroelectric projects.

This example highlights the delicate balance between the benefits of renewable energy generation through hydropower and the potential ecological and social costs, particularly when implemented on a large scale. Although hydroelectric power remains a critical component of the global energy mix, these concerns underscore the need for careful planning and environmental consideration in its expansion.

1.2.2 Wind Energy

Wind energy represents another eco-friendly alternative, characterised by relatively low startup costs compared to other renewable resources. Wind farms can be constructed onshore and offshore, providing flexibility in site selection and contributing significantly to the global renewable energy supply. Offshore wind farms, in particular, benefit from stronger and more consistent wind patterns, potentially increasing energy output. With advances in turbine efficiency, the LCOE for wind energy has decreased significantly. Onshore wind projects now deliver energy at an average cost of approximately \$27 to \$73 per MWh, making them one of the most cost-effective renewable options. Offshore wind, while more expensive due to higher installation and maintenance costs, is estimated to range from \$74 to \$139 per MWh.

However, the deployment of wind turbines has sparked debates, particularly with regard to their visual impact on natural landscapes and perceived disruption to rural

environments. In many regions, communities express concerns about the aesthetic changes caused by large wind turbine installations, as well as the noise pollution they may generate. Another critical issue is the potential occupation of arable land, which could conflict with agricultural activities in densely farmed regions.[11]

Despite these concerns, emerging research suggests that wind farms and agriculture can co-exist in a mutually beneficial relationship. Studies have shown that wind turbines can create microclimates that improve air circulation and reduce crop water stress, which could enhance crop growth in some cases. This concept, known as "agrivoltaics," highlights the possibility of synergising renewable energy generation with food production, turning wind farms into dual-purpose landscapes.[12] While more research is needed to confirm these findings across different environments, this approach could present a solution to one of the major criticisms of wind energy and further enhance its sustainability.

1.2.3 Bioenergy (Biofuel)

Bioenergy, encompassing biofuels and biomass, offers a promising and locally distributed alternative to conventional fossil fuels, enhancing energy security and supporting rural economies. Biofuels like bioethanol and biodiesel play a significant role in transportation, providing a renewable source of energy. However, they face challenges related to energy conversion efficiency, as they generally produce less energy compared to traditional diesel and petrol fuels. This efficiency gap can limit their adoption in sectors where high energy density is crucial, such as heavy-duty transportation. Despite this, biofuels can contribute to a diversified energy portfolio, reducing reliance on fossil fuels and mitigating greenhouse gas emissions.

Biomass-based energy production, which involves burning organic materials like waste or fresh feedstocks such as sugarcane, corn, and soybeans, offers a dual benefit by simultaneously managing waste and generating electricity. By utilising organic waste, biomass energy can help divert materials from landfills while generating renewable energy. However, this method is not without its environmental concerns. Large-scale bioenergy farming can lead to deforestation and a reduction in biodiversity as natural habitats are converted into monoculture crops for biofuel production. Additionally, the combustion of biomass, while renewable, releases pollutants that can contribute to air quality issues similar to those caused by fossil fuel combustion. These complexities highlight the need for careful consideration of land use and emissions when integrating bioenergy into the broader energy landscape.[12]

The current LCOE for bioenergy ranges from \$61 per MWh, positioning it as a competitive renewable energy source. However, this cost reflects the environmental challenges associated with its production and utilisation and limited power capacity. As the energy market evolves, it is crucial to balance economic viability with sustainability, ensuring that bioenergy can fulfill its potential as a clean energy alternative without compromising ecological integrity. Advancements in technology, such as improved biomass conversion methods and sustainable farming practices, may help address these challenges, making bioenergy a more attractive option in the transition toward a sustainable energy future.

1.2.4 Solar Power

Solar power stands as a potentially boundless and pollution-free energy source, offering vast opportunities for sustainable development. The Earth receives a staggering influx of 96,000 terawatts of solar energy, which far exceeds current global energy consumption

1.2 Renewable energy sources

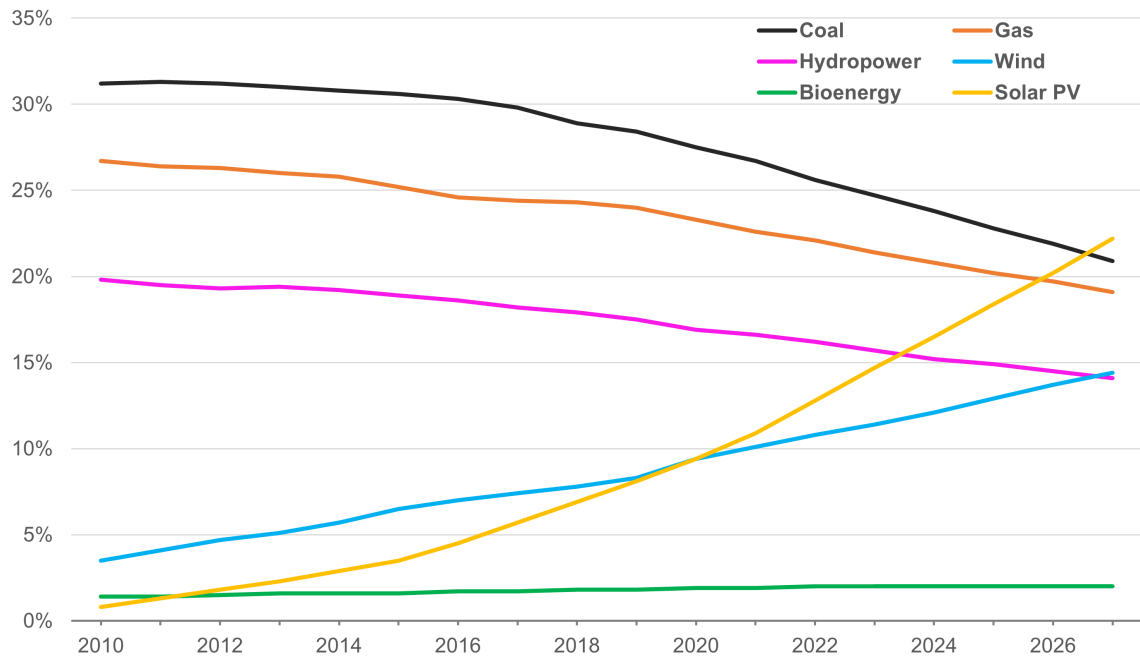


Figure 1.3 Percentage share of cumulative installed power generation capacity across all technologies from 2010 to 2027, based on re-plotted data from reference [13]. The forecast remains consistent with Figure 1.2, indicating that hydropower is expected to continue as the leading source of renewable electricity generation throughout the forecast period, even though its capacity is projected to grow at a slower rate compared to wind and solar PV technologies. Data was not reported at the source for nuclear energy.

demands. Although capturing all this solar energy is not feasible, estimates suggest that utilising just 2% of the Earth's land area with PV panels - operating at an average conversion efficiency of around 12% - could produce more than twice the energy required to meet global needs.[14] However, the inherent variability of sunlight presents limitations, particularly in regions like the Arctic. To harness the full potential of solar energy, the development of reliable energy storage and backup systems is crucial to mitigate these challenges.

While renewable resources offer cleaner and virtually limitless energy supplies, a significant barrier to widespread adoption remains the substantial upfront implementation costs. These costs often deter governments and major industries from investing heavily in renewable technologies. Furthermore, it is essential to recognize that there is no one-size-fits-all solution in the realm of renewable energy; each nation has unique energy demands and geographical characteristics that influence the feasibility of specific renewable methods. To advance the transition towards renewable energy, it is vital to diversify the energy supply portfolio, allowing for a more resilient and sustainable energy infrastructure that meets diverse energy needs without over-reliance on any single source.

Currently, solar PV power is expected to have the largest growth in terms of installation capacity, having surpassed that of all other renewable sources.[13] According to forecasts from the International Energy Agency (IEA), solar PV is projected to grow to over 2350 GW, exceeding natural gas in cumulative capacity by 2026 and coal by 2027. Despite challenges posed by rising investment costs driven by elevated commodity prices, utility-scale solar PV remains the most economically favorable option for new electricity generation in most countries, with a LCOE that is increasingly competitive between \$29 to \$92 per MWh. Additionally, the growth of distributed

solar PV, including rooftop installations, is buoyed by rising retail electricity prices and supportive policies aimed at helping consumers reduce energy costs. With these trends in mind, the future of energy generation appears to be firmly rooted in solar technology, marking a pivotal shift towards cleaner and more sustainable energy solutions.

1.3 Solar cells

The scientific exploration of solar energy can be traced back to the discovery of the photovoltaic effect by Henri Becquerel in 1837, marking a pivotal moment in our understanding of this renewable resource.[15, 16] However, the utilisation of solar energy predates this scientific discovery by millennia. Historical evidence suggests that as early as the 7th century BC, humans employed magnifying glasses and mirrors to concentrate sunlight and ignite fires. This primitive use of solar energy laid the groundwork for subsequent technological advancements in harnessing solar power for practical applications.

Significant milestones in solar energy technology occurred over the following centuries. In 1883, Charles Fritts created the first solar cells using selenium wafers, which achieved an efficiency of approximately 1%. This early innovation, while rudimentary, set the stage for further developments in solar technology. The field experienced a transformative leap in 1953 when researchers at Bell Labs advanced the design, utilising crystalline silicon to produce solar cells with a solar-to-electrical power conversion efficiency (PCE) of up to 6%.[17] This development catalysed subsequent innovations, leading to remarkable advancements in solar cell technology. Today, silicon-based solar cells boast PCEs exceeding 26%.[18]

The evolution of solar cells can be categorised into three additional generational

developments, each contributing to improved efficiency and broader applicability. These advancements are crucial for addressing the growing demand for sustainable energy solutions and mitigating the impacts of climate change.

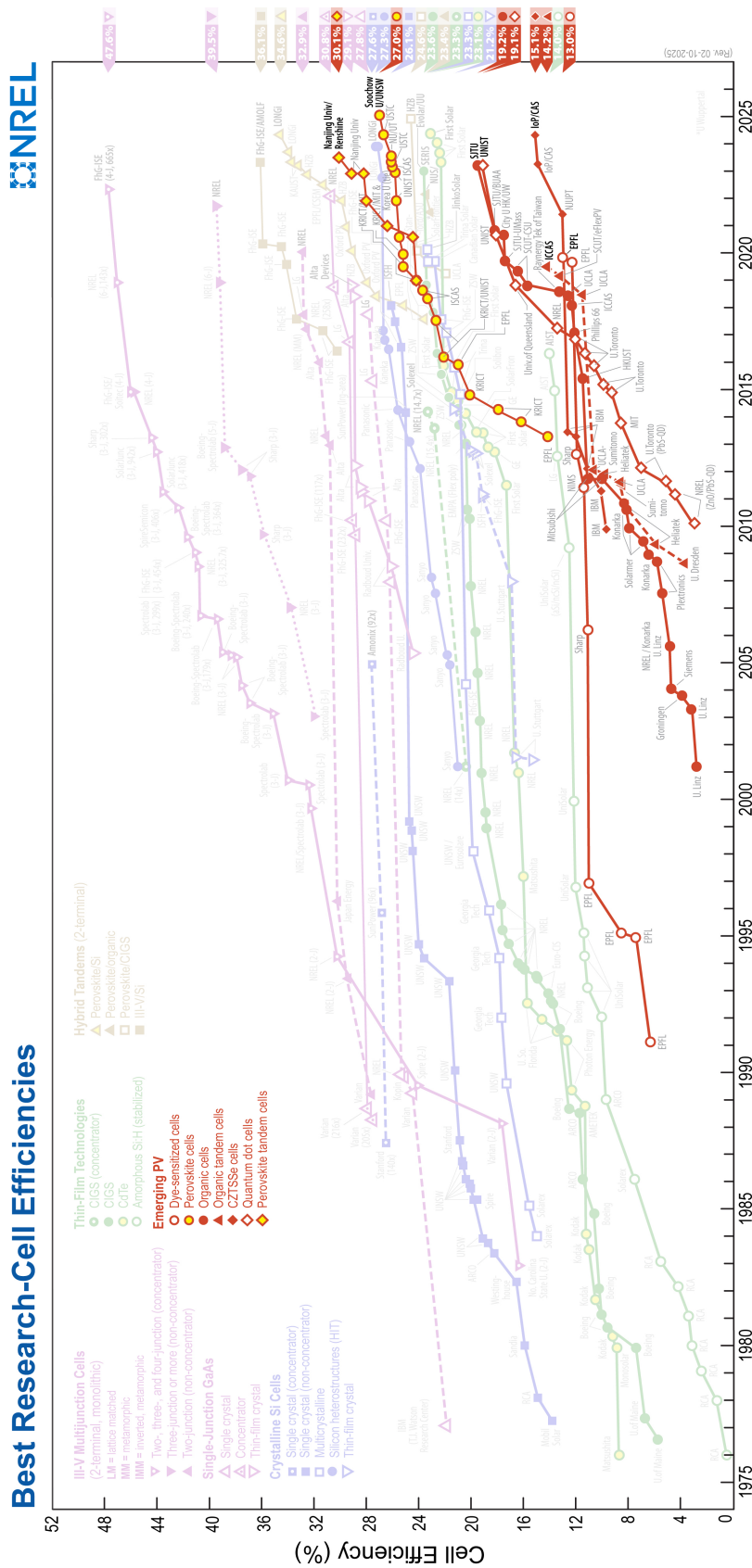


Figure 1.4 NREL Best Research-Cell Efficiency Chart of emerging PV technologies from 1975 to 2025.[19] Highlighting advancements in dye-sensitized (open circles), perovskite yellow filled circles), organic (filled circles), quantum dot (open diamonds), and CZTS (filled diamonds) solar cells, illustrating the rapid efficiency gains in next-generation PV materials.

1.3.1 First Generation Solar Cells

Initially introduced by Ohl in 1941,[20] crystalline silicon solar cells, structured as wafers, have risen to prominence due to their stable photo-conversion efficiency and non-toxic nature. They have asserted their dominance in the global solar cell market, accounting for approximately 90% of total production.[21]

Within this predominance, about one-third of these cells employ mono-crystalline silicon, while the remaining two-thirds utilise multi-crystalline silicon. Both variants operate on the principle of a p-n junction system, wherein p and n-doped wafers are nestled between two contacts, facilitating the movement of electrons between these regions as shown in Figure 1.5. Silicon's widespread adoption is attributed to its status as the Earth's second most abundant material in the crust, ensuring ample supply for both current and future requirements when compared to the rare metals used in other types of solar cells. Furthermore, silicon cells seamlessly integrate with the well-established silicon-based microelectronics industry, enabling the utilisation of mature technologies in cell manufacturing.

Mono-crystalline solar cell systems have achieved remarkable efficiencies of approximately 27%, while their multi-crystalline counterparts have reached efficiencies around 24%.[19] The primary trade-off between these two types lies in their manufacturing costs. Mono-crystalline silicon cells are produced through the energy-intensive Czochralski process, which requires high-purity silicon, precise temperature control, and extended production times.[22] Additionally, it is important to note that mono-crystalline silicon (mono-Si) cells often exhibit reduced conversion efficiency at elevated temperatures, necessitating careful consideration of cooling solutions during installation to maintain optimal performance.

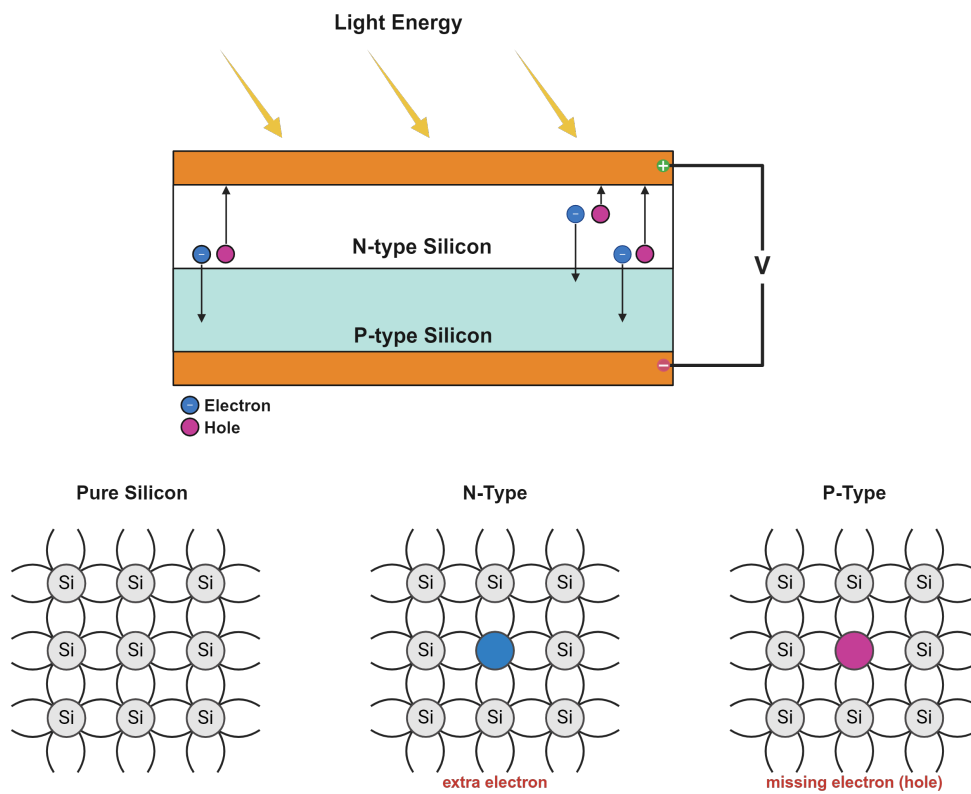


Figure 1.5 Schematic diagram of a silicon solar cell structure and operation. Demonstrating the photovoltaic effect in a silicon solar cell, where light energy generates electron-hole pairs in the N-type and P-type silicon layers, producing voltage (top). The atomic structure of pure silicon, N-type silicon (with an extra electron), and P-type silicon (with a missing electron or hole), highlighting the role of doping in charge carrier movement (bottom).

In contrast, multi-crystalline silicon cells utilise randomly oriented crystals, which results in lower production and energy costs, reduced greenhouse gas emissions, and mitigated temperature-related efficiency challenges. However, the inherent defects and higher impurity concentrations in multi-crystalline silicon can lead to increased recombination rates and subsequently lower voltage output, which contributes to their comparatively lower efficiency.

In summary, while silicon remains the predominant material used in PV cells, it does not represent the ideal photovoltaic material. The bandgap of silicon, at 1.1 eV at room temperature, is suboptimal compared to the ideal bandgap of 1.34 eV, as defined by the Shockley-Queisser limit.[23] This limitation necessitates the use of thick and brittle wafers to enhance sunlight absorption, which restricts design flexibility and increases the need for costly purification processes, thereby extending manufacturing times.

1.3.2 Second Generation Solar Cells

Building on the principles established by first-generation PV technologies, second-generation solar cells have emerged by utilising thin films of the active layer to significantly reduce material and manufacturing costs. These thin film cells typically possess a maximum thickness of just a few micrometers, allowing for a more economical approach to production. Despite their reduced material usage, second-generation PV cells have demonstrated competitive efficiencies in research settings when compared to traditional crystalline silicon cells. Thin film solar cells are predominantly composed of one of three key materials: amorphous silicon (a-Si), copper indium gallium selenide (CIGS), and cadmium telluride (CdTe). Amorphous silicon, for instance, is non-crystalline and can be deposited on a variety of substrates, making it versatile for

different applications.

Amorphous Silicon

a-Si shares several advantages with first-generation crystalline silicon, notably its reliance on abundant and non-toxic raw materials. Additionally, a-Si benefits from low-temperature manufacturing processes, which allow for the use of cost-effective substrates and contribute to a reduced material requirement per cell due to its thinner profile. The fundamental distinction between amorphous silicon and traditional crystalline silicon lies in their atomic structure. In a-Si, silicon atoms are arranged more randomly, and have short ranged order as opposed to long ranged like in its crystalline counterparts. This random atomic arrangement leads to an increased band gap of 1.7 eV, which is closer to the ideal band gap for photovoltaic applications.[23]

Despite these promising attributes, it is important to recognize that the maximum recorded efficiency of an a-Si cell remains limited to approximately 14%.[19] Furthermore, the operational lifespan of amorphous silicon cells is notably shorter compared to their crystalline counterparts. This reduced longevity is primarily due to the formation of hole-electron recombination centres and complications arising from doping treatments, which often require the introduction of hydrogen to create hydrogenated amorphous silicon. However, hydrogen doping can introduce operational challenges, as this material is more susceptible to degradation when exposed to sunlight. Consequently, the effective layer thickness diminishes over time, leading to the necessity of thicker layers for sustained cell operation[24]. Ultimately, it is these performance limitations inherent in a-Si cells that hinder their ability to effectively compete with crystalline silicon technologies in the solar energy market.

Cadmium Telluride

CdTe, a semiconductor with a band gap of 1.45 eV, is a promising material for single-junction solar cells. Laboratory efficiencies of CdTe solar cells have reached an impressive approximately 23%. [19] This high efficiency positions CdTe cells in direct competition with first-generation silicon cells, enabling them to capture a substantial market share, accounting for roughly half of the thin film solar technology sector.

CdTe offers several advantages over crystalline silicon, notably its ability to withstand high temperatures and its superior performance in capturing radiation in humid environments. These characteristics make CdTe a viable option for diverse applications and geographical settings. However, significant challenges are associated with CdTe's constituent elements that hinder large-scale production of solar cells. A primary concern is the toxicity of cadmium, which necessitates the implementation of sealed production environments to prevent human exposure, thereby increasing manufacturing costs and disposal at end of life. Moreover, the use of tellurium presents another critical limitation due to its low abundance. This scarcity complicates efforts to mass-produce solar cells, potentially constraining scalability and sustainability initiatives in the solar energy sector. [25] As such, while CdTe solar cells demonstrate considerable potential, addressing these challenges will be essential for realising their full market impact and long-term viability in the renewable energy landscape.

Copper Indium Gallium Di-Selenide

CIGS, represented by the general formula $\text{Cu}(\text{In}_x\text{Ga}_{1-x}\text{Se}_2)$, is a quaternary semiconductor material that incorporates elements from groups I, III, and VI of the periodic table. These elements are selected for their advantageous properties, including high

optical absorption coefficients and favorable electrical characteristics that enable effective device optimisation.[22] Similar to cadmium telluride (CdTe), CIGS features a direct band gap that ranges from 1.0 to 1.7 eV, depending on its specific composition. Laboratory PCEs for CIGS have reached approximately 23%.[19] However, achieving these efficiencies in scaled-up manufacturing remains a significant challenge.

While CIGS does not contain cadmium, its typical device architecture includes a cadmium sulfide (CdS) layer, which raises toxicity concerns similar to those associated with CdTe production.[26] More critically, the primary challenge facing CIGS cells stems from their reliance on indium, a rare metal that limits the scalability of manufacturing processes. This dependence places CIGS production in direct competition with other industries, such as electronics for phone screens and liquid crystal displays (LCDs), which also heavily utilise indium. Consequently, the high demand for indium leads to significant price fluctuations, ultimately increasing production costs that are transferred to consumers.[27] As such, while CIGS technology holds considerable promise for the solar energy market, addressing these supply chain challenges is essential for enhancing its commercial viability and sustainability.

1.3.3 Third Generation Solar Cells

The development of third-generation solar cells aims to achieve the high PCEs characteristic of first-generation cells while simultaneously reducing manufacturing costs through innovative deposition techniques inspired by second-generation technologies. Although many of these advanced materials and technologies are still in the research and development phase, as of 2024, several small startups are actively working to bring these promising devices to the commercial market. Third-generation solar materials include a range of innovative options such as copper zinc tin sulfide (CZTS), organic

photovoltaics (OPVs), quantum dots (QDs), dye-sensitised solar cells (DSSCs), and perovskite solar cells (PSCs).[25]

Copper Zinc Tin Sulfide (CZTS)

CZTS is a promising semiconductor material that has garnered significant attention in the field of PV research and development. With the general formula $\text{Cu}_2\text{ZnSnS}_4$, CZTS consists of abundant and non-toxic elements, making it an environmentally friendly alternative to traditional solar materials such as cadmium CdTe and CIGS. The ideal bandgap of CZTS is approximately 1.5 eV, which aligns well with the Shockley-Queisser limit for optimal solar energy conversion, providing a strong foundation for its use in solar cells.[28]

One of the most notable advantages of CZTS is its earth-abundant and non-toxic constituent elements: copper, zinc, tin, and sulfur. This characteristic not only contributes to lower production costs but also mitigates environmental concerns associated with the mining and disposal of rare and toxic materials commonly used in conventional PV technologies.[29] The synthesis of CZTS can be achieved through various methods of thin film deposition techniques, which enable the production of high-quality films at lower temperatures. CZTS solar cells have demonstrated promising laboratory efficiencies, reaching around 15% in research settings. However, the path to commercialisation has faced challenges, including issues related to grain boundary defects and sub-optimal charge carrier mobilities, which can hinder overall efficiency.

Organic Photovoltaics (OPVs)

OPVs present a promising long-term alternative in the field of PV technology, particularly for large-scale applications. These solar cells are typically composed of thin films of organic semiconductors, including conjugated polymers and small molecule compounds such as pentacene, polyphenylene vinylene, and various carbon nanostructures. The intriguing aspect of these materials lies in their flexibility and disposability; OPVs can be easily printed onto flexible, semi-transparent substrates at a low cost. This adaptability allows for tailoring to specific market needs or environmental conditions as required.[22]

Organic semiconductors are significantly more cost-effective to produce than traditional silicon or inorganic semiconductors. Moreover, straightforward processing techniques can be applied to organic molecules, enabling high-volume manufacturing that is not as suitable for inorganic crystalline materials.

The PCE of single-junction organic cells has recently reached around 19%, which, while relatively low, is considered promising compared to other emerging PV materials.[19] However, the main challenges with OPVs revolve around the long-term stability of organic components when exposed to sunlight over the lifespan of PV systems. These reactions can have a detrimental impact on device performance.[30] Additionally, as more complex active layer materials are developed to mitigate potential photo-chemical reactions, the increased molecular complexity introduces synthetic challenges and higher production costs, ultimately raising the overall price of organic cells.

Quantum Dots (QDs)

QDs represent a cutting-edge technology in the field of PV systems, offering a novel approach to harnessing solar energy. These nanoscale semiconductor particles exhibit unique optical and electronic properties due to quantum confinement effects, allowing for tailored energy bandgaps that can be adjusted based on their size and composition.[31] This tunability enables quantum dots to absorb light across a broad spectrum, including ultraviolet and infrared wavelengths, thereby enhancing their potential efficiency in converting solar energy into electricity.

A significant recognition of the importance of quantum dots came in 2023, when the Nobel Prize in Chemistry was awarded to researchers who contributed to the development of these materials.[32] One of the most compelling advantages of quantum dot solar cells is their potential for low-cost manufacturing. Similar to organic photovoltaics, QDs can be processed using solution-based techniques, such as inkjet printing and spray coating. This flexibility in fabrication allows for the integration of QDs into various substrates, including flexible and lightweight materials, which can lead to diverse applications in both traditional and emerging markets.

Despite their promising attributes, quantum dot solar cells face challenges, including stability issues and relatively lower PCEs compared to established technologies like silicon-based solar cells.[19] However, ongoing research is addressing these concerns through advancements in materials science and device engineering.

Dye-Sensitised Solar Cells (DSSCs)

The pioneering DSSC was developed by O'Regan and Grätzel in the 1990s, employing nanoparticle TiO_2 sensitised by a ruthenium complex.[33] These cells represent a hybrid

design, combining both organic and inorganic components. Typically, DSSCs comprise a semiconductor and a liquid electrolyte. The semiconductor and electrolyte collaborate to efficiently separate the electron-hole pairs generated when sunlight strikes the cell. The use of a photosensitive dye, commonly iodine, serves as the source of photo-induced charge carriers, giving the technology its name of "dye sensitised".[34]

In line with Grätzel's research, TiO_2 is frequently employed to immobilise the dye molecules, offering a more cost-effective alternative to silicon used in conventional solar cells. DSSCs employing the original ruthenium complex dyes have consistently demonstrated respectable efficiencies, around 11%, since the early 2000's.[19] However, the high cost, scarcity, and purification challenges associated with ruthenium have impeded their widespread adoption in the commercial market.[22]

Efforts have been made to develop dyes based on more abundant metal complexes and organic compounds for DSSCs. Researchers have explored a variety of alternatives to ruthenium-based dyes, aiming to enhance the sustainability and cost-effectiveness of these solar cells. While some progress has been made in improving the stability and absorption properties of these alternative dyes, none have yet managed to surpass the performance of ruthenium-based counterparts. Consequently, classic DSSCs still struggle to compete with the PCEs achieved by silicon solar cells, which dominate the market, as well as other emerging technologies like perovskites, which have demonstrated remarkable efficiencies in recent years.

1.4 Perovskites

1.4.1 Perovskite Cells as Emerging PVs

The focus of this project is on perovskite materials for solar cells. These cells are derived from O'Regan and Grätzel's DSSC as discussed in Section 1.3.3, where in 2009,[35] perovskites were used as the active semiconductor layer and reported an initial PCE of 3.8% and have since led to the steepest curve in reported efficiencies over the last 10 years as seen in Figure 1.4.[19] Lead halide perovskites have narrow band gaps and high absorption coefficients that are suitable for DSSC solar cells but lack the scale-up technologies, high efficiency and long-term stability required to become a competitor in the PV market.

1.4.2 Architecture of Perovskite PV Devices

The first hybrid perovskite materials were used in DSSC like devices, replacing the liquid electrolyte dye sensitiser by a perovskite layer. In a typical DSSC, a thick layer of porous TiO_2 collects and transports electrons, while the electrolyte acts as a hole conductor. Figure 1.6 displays the most common types of perovskite PV architectures which function in a similar manner to solid state p-n junction solar cells. The glass substrate is coated in a transparent conductive oxide, usually fluorine doped tin oxide (FTO) or indium tin oxide (ITO).

The perovskite is the active layer acting as an intrinsic absorber sandwiched between a n-type electron transporting material (ETM) and p-type hole transporting material (HTM). The ETM is commonly composed of TiO_2 or PCBM while the HTM can be made of spiro-OMeTAD or PEDOT:PSS depending on the device architecture

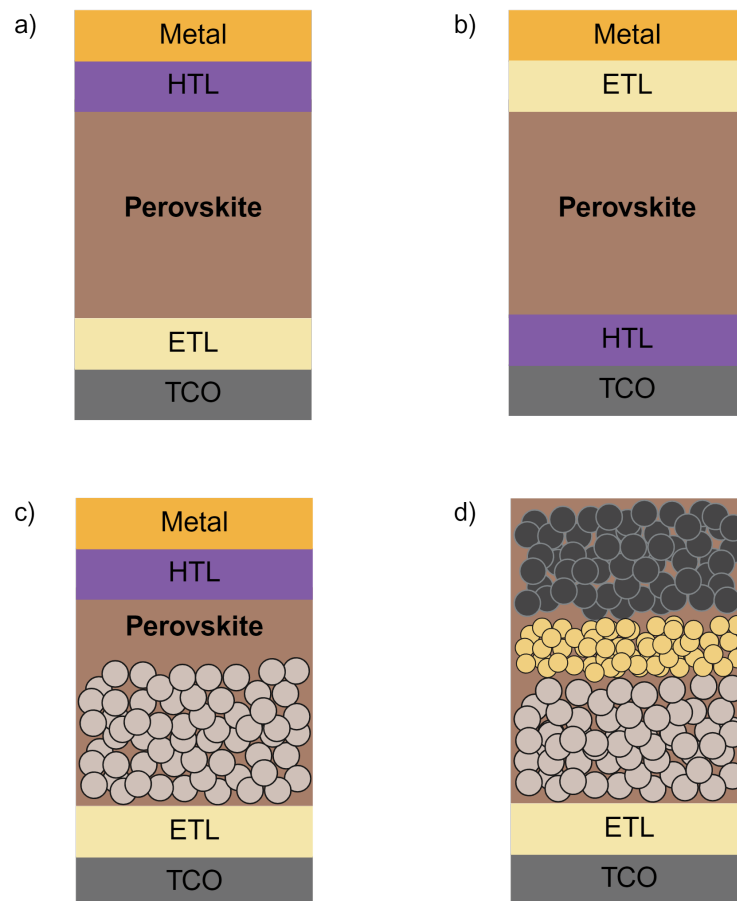


Figure 1.6 The four most common perovskite solar cell architectures including a transparent conducting oxide (TCO) layer, electron transport layer (ETL), and a hole transport layer (HTL). a) planar cell, b) planar inverted cell, c) mesoporous cell and d) mesoporous carbon cell. The beige coloured spheres represent mesoporous titania, the small yellow spheres represent a mesoporous zirconia layer and the black spheres are mesoporous carbon.

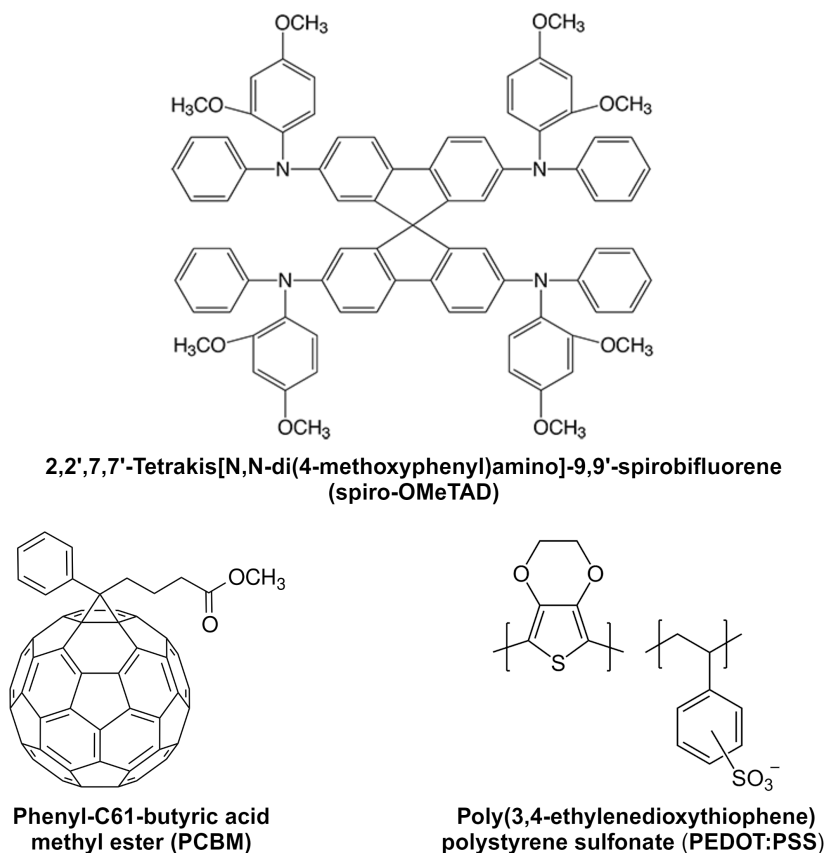


Figure 1.7 Structures of spiro-OMeTAD (top), PCBM (bottom left), and PEDOT:PSS (bottom right).

(structures shown in Figure 1.7). Mesoscopic devices also include a perovskite-filled mesoporous layer of metal oxide, such as TiO_2 or Al_2O_3 which decrease the carrier transport distances and enhances charge collection.[36–39] The basic function of these cells is as follows: when sunlight hits the top of the device, the perovskite layer absorbs the light and generates electrons and holes. The ETM layer then selectively collects the electrons while the HTM layer collects the holes. From here, the electrons are allowed to flow to the HTM layer via the external circuit at which point they combine with the available holes.[40]

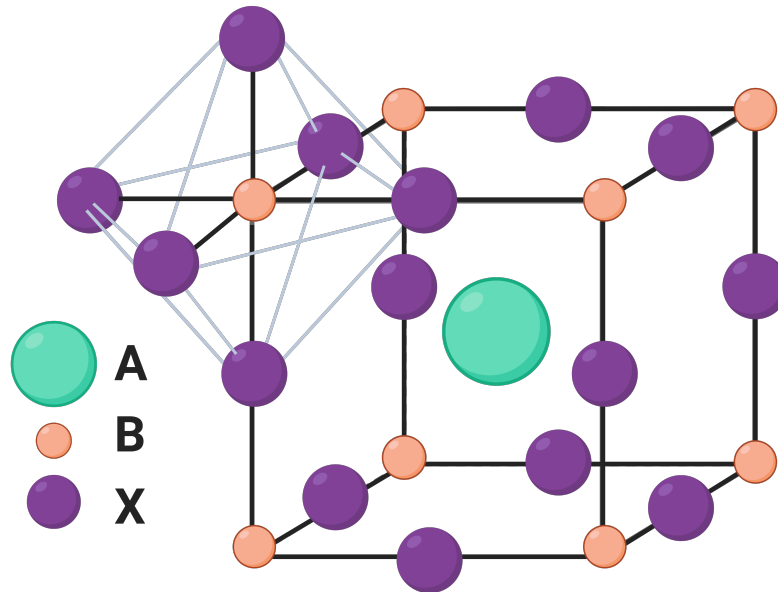


Figure 1.8 Generic ABX₃ structure of a perovskite

1.4.3 The Perovskite Structure

Perovskite refers to the mineral CaTiO₃, first discovered in 1839 by Lev Perovski. The term now broadly describes materials that share the same crystal structure as CaTiO₃. Due to their versatile properties, perovskite compounds are employed in a range of applications beyond PVs, such as sensors, memory devices, and solid oxide fuel cells.[41]

Perovskite compounds follow the general formula ABX₃ with the valency of the ions either being A²⁺B⁴⁺X²⁻ like in CaTiO₃ or A⁺B²⁺X⁻ like in CsPbI₃. Many perovskites experience structural distortions or formations of different structures due to the differences in sizes between the A, B, and X ions. For PVs, the perovskites tend to contain either a Pb²⁺ or Sn²⁺ B site and a single or mixture of halides; Cl⁻, Br⁻, I⁻ as the X site. The A cation can either be inorganic like Cs⁺ or Rb⁺ or have an organic molecule such as methylammonium (CH₃NH₃⁺, MA), formamidinium [(NH₂)₂CH]⁺,

FA)) or even butylammonium ($\text{C}_4\text{H}_9\text{NH}_3^+$, BA). The most widely studied perovskite for PV applications is methylammonium lead iodide (MAPI) and which is the focus of this work.

MAPI was first characterised by Weber in 1978, though research in the field slowed until the early 2000s, when interest revived due to its potential use in light-emitting diodes (LEDs) and thin film transistors.[42–44] In 2009, Kojima synthesised a perovskite-based dye-sensitised solar cell (DSSC), which marked the beginning of intensive research into perovskites for solar cell applications.[35]

1.4.4 Goldschmidt’s Tolerance Factor

During early work on synthetic perovskites a principle, known as Goldschmidt’s tolerance factor, t , was introduced.[45] The tolerance factor uses ionic radii, to estimate how suitable combinations of ions are to fit the perovskite structure and is a real measure of the degree of distortion from the ideal cubic structure. Equation 1.1 demonstrates the proposed relationship between these ionic radii where r_A , r_B and r_X relate to the ionic radii of the A, B, and X-site ions, respectively.

$$t = (r_A + r_X) / \sqrt{(r_B + r_X)} \quad (1.1)$$

From this, the value of t will decrease when r_A decreases and/or r_B increases.[46] Generally, if t is between 0.8 to 0.1, the perovskite will form. For $0.9 < t < 1.0$ the structure is cubic, for $0.7 < t < 0.9$ the structure will adopt a distorted cubic phase due to a mismatch in the relative sizes of the ions. A value below 0.7 tends to lead to an orthorhombic structure being adopted.

Table 1.1 Tabulated data concerning the lattice parameters, space group, and temperature dependence of the three phases of MAPbI₃.

Phase	Temperature (K)	Lattice Parameters (Å)	Space Group	Reference
Orthorhombic	$T < 162$	8.8657, 12.6293, 8.5768	Pmna	[51]
Tetragonal	$162 > T > 326$	8.8789, 8.8789, 12.6887	I4/mcm	[52]
Cubic	$T > 326$	6.3115, 6.3115, 6.3115	Pm-3m	[53]

Calculating tolerance factors for lead halide perovskites with an organic A site cation, such as methylammonium (MA), is increasingly complex due to challenges in estimating the ionic radius of molecular ions. As a result of this ambiguity in the effective radius of the non-centrosymmetric molecule, it tends to be that the values of t range between 0.83 to 0.95.[47] There has been research into alternative or extended models of Goldschmidt’s tolerance factor which revise the calculated values of cationic radii to ideally reveal t values that more accurately describe the perovskite behaviour exhibited by MAPI experimentally.[48–50]

1.4.5 Phase transitions of MAPI

MAPI exists as three temperature dependent phases which are depicted in Figure 1.9. At temperatures above 327 K the perovskite exists in the cubic phase (a), below this the structure adopts the tetragonal phase which is characterised by the tilting of the PbI₆ octahedra (b). The final transition exhibited by MAPbI₃ is to the orthorhombic phase (c) which exists below 162 K, with a further tilting of the octahedra.

For inorganic lead halide compounds, these distortions are accurately explained by steric effects in the perovskite structure, which arise due to a mismatch in the relative sizes of the ions. As a result, the octahedra rotate to accommodate the local

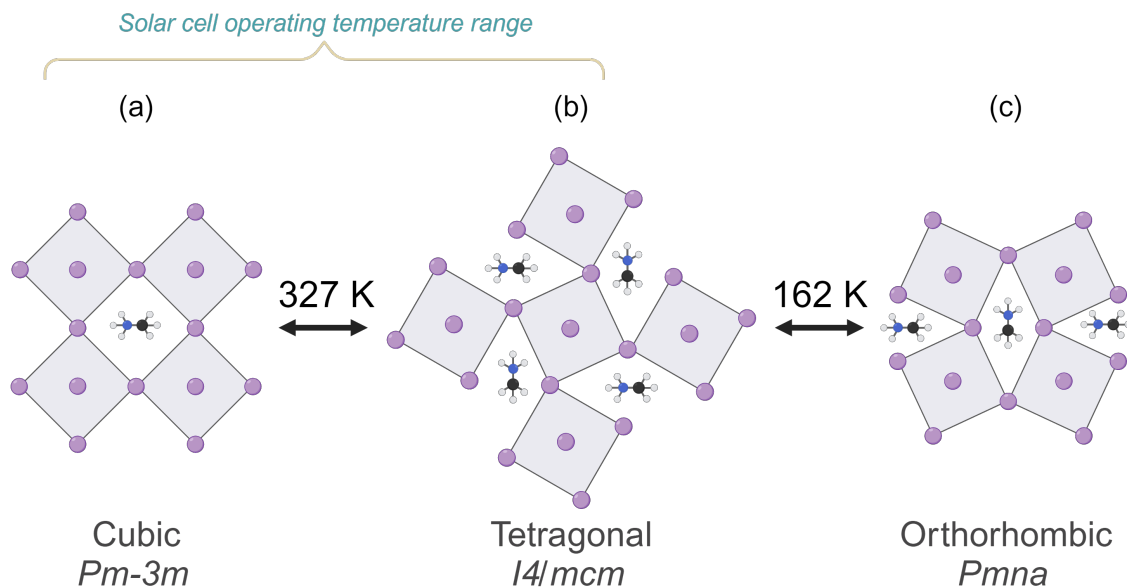


Figure 1.9 The three temperature-dependent polymorphs of MAPbI₃. Pb–I–Pb bond angles decrease from cubic (a) to tetragonal (b) to orthorhombic (c) with decreasing temperature.

environment, and this behaviour can be quantified using Goldschmidt’s tolerance factor (described in Section 1.4.4). However, in hybrid perovskites, while the general structure of corner-sharing octahedra is preserved, the organic cation exhibits different mobility characteristics. Hydrogen bonding between the organic cation and the halide anion also plays a role in determining the observed octahedral tilting.[54, 55]

1.4.6 The MA⁺ Cation

Although the methylammonium cation (MA) constitutes over half of the atomic composition in MAPI, its role in the structure and its contribution to PV performance remain subjects of ongoing debate and are not yet fully understood. Despite the rapid improvement in perovskite solar cell efficiency, the fundamental physical properties of perovskite materials—particularly molecular motion and ionic diffusion—are still not entirely clear. It is widely accepted that both electronic and ionic processes occur within

these materials.[56, 57] Several computational and experimental studies have indicated that the MA⁺ cation plays a critical role in the temperature-dependent phase transitions of MAPI.[52, 58] As the material progresses from the low-temperature orthorhombic phase to the high-temperature cubic phase, increased disorder and displacement of the MA⁺ cation are observed, highlighting its influence on the material's structural dynamics.

The MA⁺ cation disorder also contributes to the observed octahedral tilting, as determined from computational studies. When in the cubic phase, the MA⁺ cation contains the greatest amount of rotation and disorder as the Pb–I–Pb bond angle becomes 180°.[59] The free rotation of the cation allows for this high symmetry structure to be stabilised at high temperature. In the tetragonal phase where tilting is observed, the MA⁺ cation gets partially trapped which allows for stronger hydrogen bonding which in turn drives the octahedral tilt. When lowering the temperature further, the MA⁺ cation becomes increasingly ordered, adopting a staggered conformation, and less dynamic rotation is observed, along with stronger hydrogen bonding allowing for a more extreme tilt in the orthorhombic phase, which in turn, reduces the capacity of the cavity size.[60] It is clear that although the MA⁺ cation may drive this temperature dependent tilting, it is a synergistic movement of all the structure which drives the overall symmetry.

However, there is conflicting evidence regarding the specific motions and orientations of the cation, along with disputes on the order of the activation energy relating to the hydrogen bonding experienced between the cation and inorganic cage. For instance, several different Quasi-elastic neutron scattering studies using a variety of beamline instruments have been published, but there is differing evidence on the cation motions within MAPI. Leguy *et al.* describe an ordering of the cation existing throughout the

phase transitions, where the cation 'jumps' between preferential orientations, which disputes thoughts of a random disordering of the cation at high temperature.[61] However QENS measurements by Chen *et al.* partly contradicts this idea of similar ordering throughout the phase transition, and instead shows increasing disorder with increasing temperature.[62, 63] Several QENS studies attempt to demonstrate the type of rotation of the MA⁺ cation in that whether a 3 and/or 4-fold rotation occurs while in each of its three different morphologies. Further discussion on this is provided by Sharma.[64] Overall, it is difficult to describe MA⁺ cation dynamics from QENS alone, due to the large differing in timescales on each available spectrometer, and how initial synthesis can also play a part in the observed hydrogen dynamics.[61]

More studies using a combination of QENS, vibrational spectroscopy, and molecular dynamics allow for other possible rotational models to come to light, while also offering additional information on the ion migration and contribution the cation makes towards the dielectric response.[65, 66] It is undisputed that the ordering, orientation, and overall dynamics of the MA⁺ cation all make contributions to the optoelectronic properties of MAPbI₃. Features such as high charge mobility, long carrier lifetimes, and low binding energy all have an influence on the PV properties of the material and hence affect the overall performance of the solar cell. Thus, it is crucial to gain a full understanding of the cation dynamics in this system and other similar materials in order to better tune its properties and resolve higher power conversion efficiencies.

1.5 Challenges of Perovskite PVs

1.5.1 Stability

One of the greatest issues that face the development of perovskites for PV applications is its stability under solar cell operating conditions, which will vary depending on location. Generally, when a solar cell operates under direct sunlight, device temperatures can reach over 45 °C higher than normal room temperature, meaning a cell must be able to withstand this heat without changing or degrading over time.[67, 68] The International Electrotechnical Commission (IEC) 61215 is a standard of certification that a PV module must endure and pass in order to be considered as successful for manufacturing. The 61215:2021 Damp Heat and Humidity Freeze tests[69] are used to determine whether a PV module can withstand the effect of outdoor operating conditions by exposing them to a repeated temperature cycling of extreme conditions, as shown in Table 1.2. In order to pass, a cell must complete 10 cycles without: delamination of the encapsulant and backsheet, backsheet cracking, failures in edge sealing, and corrosion at the front surface interconnects. Meanwhile, the device must go through internal temperature, and current and voltage monitoring while maintaining a good and consistent PCE.

In research, most perovskite PV technologies typically can be stable from a matter of hours to months, one group was able to maintain an efficiency between 13-15% by using a multi-dimensional junction consisting of 2D/3D perovskites that was then stable for up to a year.[70] Despite this progress made towards perovskite PVs reaching the commercial market, the issues of stability remain. Most halide perovskite materials suffer from degradation caused by several parameters: moisture, light, and heat being the most prevalent. These are individually discussed below.

Table 1.2 Conditions and parameters for the IEC 612215:1016 Damp Heat and Humidity Freeze tests[69].

Test Condition	Parameters
Temperature Range	−40 °C to 85 °C
Rate of temp change	< 100 °C/h
Dwell time at −40 °C	> 30 min
Dwell time at 85 °C	> 20 hours
Humidity	85% (±5%) at 85 °C
Cycle Time	24 hours per cycle
No. of Cycles	10

1.5.2 Stability in Humidity

Hybrid perovskites are well known to degrade immediately over time due to their sensitivity when exposed to air and water vapour. The full pathway of degradation in perovskites such as MAPbI₃ is still to be fully elucidated under humidity but a summary of the general features can be made. The majority of halide perovskite materials are hygroscopic in nature. However, the pathway and effect of degradation is majorly dependent on the identity of the A site cation. For instance, as shown in Figure 1.10, when an inorganic perovskite such as CsPbI₃ comes into contact with relative humidity, it can catalyse a phase transition from the black-coloured α phase, which has been shown to be ideal for PV applications, through its β and γ phases and back to the most stable but least desired yellow orthorhombic δ phase. From here, further moisture contact can degrade the perovskite further into its inorganic salts of CsI and PbI₂. [71, 72]

Despite this, all inorganic perovskite materials are seen to be superior in moisture stability compared to their organic-inorganic A site counterparts. One such study revealed that when measuring the PCE values of CsPbI₃ and MAPbI₃ while each were exposed to moisture, the PCE of the MAPbI₃ solar cell dropped dramatically to 70%

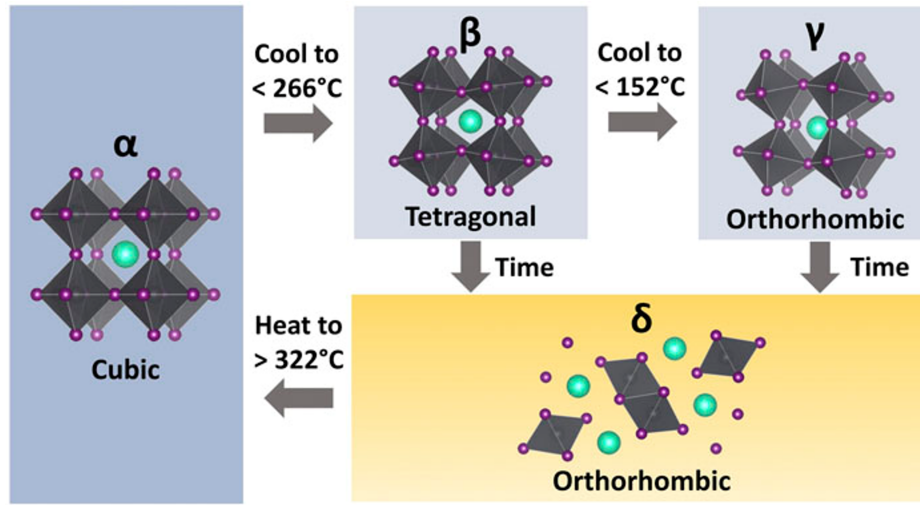


Figure 1.10 Temperature-dependent transitions between the polymorphic phases (α , β , γ , and δ) of CsPbI_3 . The photoactive phases are illustrated in dark gray, while the non-photoactive phase is shown in yellow. Adapted from [71].

of the initial efficiency after 500 h of exposure. Meanwhile the corresponding CsPbI_3 solar cell lost just 25% of its initial efficiency within the same time period, therefore indicating that CsPbI_3 has relatively better stability under humid conditions. [73]

Furthering this, it can be agreed that the moisture induced changes seen in organic-inorganic perovskites largely differ. Due to its hydrogen-bonded organic MA^+ cation, MAPI, is extremely hygroscopic and its degradation pathway involves the formation of intermediate hydrated phases. [74–76]



Equations 1.2 and 1.3 demonstrate how the initial intermediate phase is formed, followed by its successive degradation into the precursors of MAPI. Interestingly, Leguy *et al.* were able to support this theory of a new monohydrate intermediate phase

formation through using ellipsometry measurements. Here, they demonstrate the fact that the band gap of MAPbI₃ doubles when exposed to a high moisture environment for a length of time.[77] This intermediate formation is also seen to be a reversible process, and with a sufficiently dry atmosphere, the MAPI can be fully recovered.[77, 78] However, when MAPbI₃ is exposed to water vapour directly and/or for long periods of time, results showed the pathway does not involve a hydrated intermediate species, and instead, as demonstrated by Equations 1.4 and 1.5, directly and irreversibly decomposes into its organic constituents and PbI₂. [77, 79]



The mechanistic pathway in which this degradation occurs is still largely debated [80–82]. However, most suggestions involve the intercalation of polar water molecules into the perovskite lattice due to their ability to form strong hydrogen bonds with the iodides and, to a lesser extent, the methylammonium cations. [83, 84] This then can weaken the CH₃NH₃⁺-X⁻ hydrogen interaction while also possibly causing a hydrolysis of the C-N bond within the cation, generating ammonia and hydrogen iodide as described in Equation 1.4. [79] Meanwhile, others argue decomposition follows through a route involving the loss of a small amount of MA⁺ which destabilises the structure and leads to the formation of lead iodide and methylammonium iodide as shown in Equation 1.5. [79, 85] It has been proposed that this pathway is then accompanied by an ammonia gas release via sublimation or assisted chemical reaction under sunlight where methyl iodide is formed, as shown in Equation 1.6. [82]

1.5.3 Thermal and Photo-Stability

One of the key characteristics of solar cells is the ability to operate in direct sunlight, and be stable under moderately high temperature ($>85\text{ }^{\circ}\text{C}$).^[69] Geography and climate also need to be considered in regional solar installations, as the natural environment fluctuates more rapidly across the globe. As shown earlier in Figure 1.9, MAPI, like some other perovskites, undergoes a phase transition over the existing operating temperature range of a device. Hence, it is imperative to assure that thermal stability can be guaranteed with materials possessing structural variability. Although not completely resolved, the degradation pathway for MAPI and its counterparts under light are very similar to those described in Equations 1.4, 1.5 and 1.6. Once again, it is the organic cation that is responsible for initiating the photo-degradation process,^[86] which can then lead to the formation of both PbI_2 and iodine gas.^[87]

Using alternative available halide systems (Br, Cl) has been shown to increase stability due to shorter and stronger $\text{Pb}-\text{X}$ bonds. Using other organic cations such as FA or switching to an inorganic cation like Cs^+ has also been shown to improve thermal and photochemical stability. It was later shown that FA decomposition leads to the formation of other undesirable organic species such as hydrogen cyanide and ammonia.^[82, 88] Caesium on the other hand, either through partial or complete substitution, showed much greater thermal and photochemical stability.^[86, 88] It is also a difficult feat to separate moisture, thermal, and photo-degradation in operational solar cells, as once one has triggered the degradation of the perovskite, all other forms can follow quickly in sequence leading to a rapid degradation and loss of PCE. Resistance to this occurring can be done by employing a moisture-resistant layer or coatings of carbon nanotubes or graphite. Further encapsulation techniques employ plastic films to improve device stability with little effect on operating efficiency.^[89, 90]

1.5.4 Further Environmental Challenges

Throughout solar perovskite research, it is still the case that the most promising cells in terms of stability and efficiency have been lead based. However, commercialisation of these devices is hindered due to the toxicity, carcinogenicity, and concerning environmental impact of lead.[91, 92] Because of this, there has been a drive towards lead-free devices, utilising Sn or Bi as alternative B site cations. However, success in producing efficient and stable solar cells with these materials is somewhat limited.[93, 94] Alternatively, recent life cycle and environmental impact assessments show that lead bears but a small proportion on the overall environmental impact during manufacturing.[95] This potential hazard has also developed research opportunities in recycling lead waste from batteries or spent solar cells, to be recrystallised into new perovskite thin film devices which have competitive efficiencies to freshly made cells.[96]

1.6 Enhancing perovskites through compositional engineering

Compositional engineering in hybrid perovskite systems has emerged as a primary strategy to enhance PCE, stability, and reduce environmental toxicity in perovskite solar cells. The approach involves manipulating the chemical composition of the A, B, and X sites in the perovskite structure, aiming to overcome challenges related to material degradation, performance under operational conditions, and toxicity, particularly due to lead content.[97] As described in Section 1.4.4, the Goldschmidt tolerance factor has traditionally been used to predict the structural stability of perovskites, with an ideal value between 0.8 and 1.0. However, for halide-based perovskites, this predictor has

1.6 Enhancing perovskites through compositional engineering

proven unreliable, particularly in photovoltaic applications. Consequently, the range of atomic substitutions in compositional engineering has been relatively narrow, but focused adjustments are yielding significant improvements.

1.6.1 A-site Cation Engineering

The A-site cation, typically methylammonium (MA) or formamidinium (FA), directly influences both stability and electronic properties. FA has a larger ionic radius than MA, favoring a cubic perovskite structure that enhances stability and thermal properties. For instance, FAPbI₃ has a more favorable bandgap (1.47 eV) than MAPbI₃ (1.57 eV), closer to the Shockley-Queisser limit.[98, 99] However, difficulties in achieving highly crystalline photoactive thin films of FAPbI₃ have led to mixed cation approaches, such as incorporating small amounts of Cs⁺ to stabilise the perovskite phase. The triple-cation system (MA_xFA_{0.95-x}Cs_{0.05}Pb(I_{1-y}Br_y)₃) has achieved record efficiencies while maintaining greater phase stability.[100, 101]

1.6.2 B-site Cation Engineering

Lead (Pb²⁺) toxicity has driven research into alternative B-site cations, such as tin (Sn²⁺) and germanium (Ge²⁺). Substitution with Sn²⁺ narrows the bandgap, which is advantageous for solar spectrum absorption.[102] However, Sn²⁺ oxidizes to Sn⁴⁺, leading to rapid degradation.[103] Efforts to partially substitute Pb with Sn (e.g., MAPb_{0.9}Sn_{0.1}I₃) have shown promise, maintaining 90% of initial PCE after 500 hours of light exposure.[104] Ge-based systems have received less attention due to poor stability, but substitution by both Sn²⁺ and Ge²⁺ cations remain vital avenues for reducing toxicity.

1.6.3 X-site Anion Engineering

The choice of halide ($X = \text{I}^-$, Br^- , Cl^-) strongly influences both the bandgap and material stability. Iodide-rich perovskites exhibit strong light absorption and efficient charge transport but suffer from poor stability and relatively low open-circuit voltage. Substituting iodide with bromide (Br^-) increases the bandgap, improving open-circuit voltage and structural stability, though at the cost of reduced light absorption.[105] Chloride-based perovskites have even larger bandgaps (around 3.1 eV), making them unsuitable for light absorption but valuable for enhancing grain size and structural robustness when used as additives.[106] Mixed halide perovskites, such as $\text{MAPb}(\text{I}_x\text{Br}_{3-x})$, allow fine-tuning of the bandgap and enhance moisture resistance, though phase segregation under operating conditions remains a challenge.[107, 108] Small amounts of chlorine have also been incorporated to improve grain size and reduce defects, contributing to material stabilisation.

Compositional engineering across the A, B, and X sites has enabled significant improvements in PSC performance. The introduction of mixed cation and halide systems has driven PCE to new heights while addressing stability concerns. B-site substitution for lead remains critical for environmental concerns, though stability issues persist with alternatives like Sn^{2+} . Ultimately, continued refinement of compositional strategies, including the combination of organic and inorganic components, could hold the key to the future commercialisation and environmental sustainability of hybrid perovskite solar cells.

1.7 Aims of the Thesis

The aim of this thesis is to investigate the structural and dynamic behavior of methylammonium lead iodide perovskites in the bulk, with a particular focus on the effects of post-synthetic treatments on their stability and potential impact on their optoelectronic properties. While MAPI has demonstrated exceptional efficiency in photovoltaic applications, its long-term commercial viability is hindered by environmental instability, particularly in response to moisture, heat, and oxygen exposure. To address these challenges, this research systematically examines the impact of vacuum and iodine annealing treatments on MAPI's phase transitions, lattice integrity, and cation dynamics, utilising advanced characterisation techniques such as X-ray diffraction, quasi-elastic neutron scattering, and nuclear magnetic resonance.

A key objective is to refine annealing conditions that enhance material stability while preserving or improving its photovoltaic performance. Furthermore, this work investigates the formation of secondary phases, notably NH_4PbI_3 , as an unintended byproduct of post-synthetic treatments, assessing its influence on the structural and electronic properties of MAPI. To further advance the understanding of perovskite materials, this thesis also explores the application of nuclear quadrupole resonance as a tool for monitoring halide distribution and structural defects, incorporating numerical simulations to optimise experimental parameters. By addressing these fundamental aspects, this research aims to contribute to the ongoing development of stable, high-performance perovskite materials for next-generation photovoltaic applications.

References

- [1] UN Department of Economics and Social Affairs, Population Division, *World Population Prospects 2022: Summary of Results*, tech. rep., United Nations, New York, 2022.
- [2] UN Department of Economics and Social Affairs, Population Division, *World Urbanization Prospects: The 2018 Revision*, tech. rep., United Nations, New York, 2018.
- [3] W. E. Council, *World Energy Trilemma Index*, tech. rep., World Energy Council, London, 2013.
- [4] W. E. Council, *World Energy Resources*, tech. rep., World Energy Council, London, 2013.
- [5] U.S. Energy Information, *International Energy Outlook 2019*, tech. rep., The United States Energy Information Administration, Washington D.C., 2019.
- [6] BP, *Statistical Review of World Energy 71st Edition*, tech. rep., British Petroleum, London, 2022.
- [7] EU, *2030 Energy Strategy*, tech. rep., European Union, Brussels, 2014.
- [8] International Renewable Energy Agency (IRENA), *Renewable Power Generation Costs in 2022*, tech. rep., International Renewable Energy Agency, 2023.
- [9] Lazard, *Lazard's Levelized Cost of Energy+ (LCOE+) Report – 2024*, tech. rep., Lazard, 2024.
- [10] H. Ritchie, M. Roser and P. Rosado, *Our World in Data*, 2020, Accessed: 2024-08-26.
- [11] F. Love, *Wind turbines may have beneficial effects for crops, according to Iowa State University Research*, <https://www.news.iastate.edu/news/2016/12/09/windturbulence>, 2016.
- [12] O. Ellabban, H. Abu-Rub and F. Blaabjerg, *Renewable Sustainable Energy Rev.*, 2014, **39**, 748–764.
- [13] IEA, *Renewables 2022*, tech. rep., International Energy Association, Paris, 2022.

- [14] D. M. Chapin, C. S. Fuller and G. L. Pearson, *J. Appl. Phys.*, 1954, **25**, 676–677.
- [15] A. E. Becquerel, *C. R. Acad. Sci.*, 1839, **9**, 145–149.
- [16] A. E. Becquerel, *Ann. Phys. Chem.*, 1841, **54**, 35–42.
- [17] M. A. Green, *Prog. Photovolt Res. Appl.*, 2009, **17**, 183–189.
- [18] F. I. for Solar Energy Systems, *Photovoltaics Report*, tech. rep., Fraunhofer Institute for Solar Energy Systems, Freiburg, 2017.
- [19] National Renewable Energy Laboratory (NREL), *Best Research-Cell Efficiency Chart*, <https://www.nrel.gov/pv/cell-efficiency.html>, Accessed: 2024-07-19, 2024.
- [20] R. S. Ohl, US2481602A, Filed on 1946-06-06, issued on 1949-06-14, 1948.
- [21] T. Ibn-Mohammed, S. C. L. Koh, I. M. Reaney, A. Acquaye, G. Schileo, K. B. Mustapha and R. Greenough, *Renew. Sustain. Energy Rev.*, 2017, **80**, 1321–1344.
- [22] P. G. V. Sampaio and M. O. A. González, *Renew. Sustain. Energy Rev.*, 2017, **74**, 590–601.
- [23] S. Ruhle, *Sol. Energy*, 2016, **130**, 139–147.
- [24] J. A. Luceño-Sánchez, A. M. Díez-Pascual and R. Peña Capilla, *Int. J. Mol. Sci.*, 2019, **20**.
- [25] M. A. Contreras, B. Egaas, K. Ramanathan, J. Hiltner, A. Swartzlander, F. Hasoon and R. Noufi, *Prog. Photovoltaics Res. Appl.*, 1999, **7**, 311–316.
- [26] P. Jackson, D. Hariskos, E. Lotter, S. Paetel, R. Wuerz, R. Menner, W. Wischmann and M. Powalla, *Prog. Photovoltaics Res. Appl.*, 2011, **19**, 894–897.
- [27] C. Candelise, M. Winkler and R. Gross, *Prog. Photovoltaics Res. Appl.*, 2012, **20**, 816–831.
- [28] H. Katagiri, K. Saitoh, T. Washio, H. Shinohara, T. Kurumadani and S. Miyajima, *Solar Energy Mater. Solar Cells*, 2001, **65**, 141–148.
- [29] C. Wadia, A. P. Alivisatos and D. M. Kammen, *Environ. Sci. Technol.*, 2009, **43**, 2072–2077.
- [30] M. Jorgensen, K. Norrman, S. A. Gevorgyan, T. Tromholt, B. Andreasen and F. C. Krebs, *Adv. Mater.*, 2012, **24**, 580–612.
- [31] S. Shishodia, B. Chouchene, T. Gries and R. Schneider, *Nanomaterials*, 2023, **13**, 2889.
- [32] *Nobel Prize in Chemistry*, <https://www.nobelprize.org/prizes/chemistry/>, Accessed: 2024-08-26, 2024.
- [33] M. J. Grätzel, *J. Am. Ceram. Soc.*, 1997, **80**, 3157–3171.
- [34] L. A. L. L. El Chaar and N. E. Zein, *Renew. Sustain. Energy Rev.*, 2011, **15**, 2165–2175.

- [35] A. Kojima, K. Teshima, Y. Shirai and T. Miyasaka, *J. Am. Chem. Soc.*, 2009, **131**, 6050–6051.
- [36] A. K. Jena, A. Kulkarni and T. Miyasaka, *Chem. Rev.*, 2019, **119**, 3036–3103.
- [37] M. Liu, M. B. Johnston and H. J. Snaith, *Nature*, 2013, **501**, 395–398.
- [38] M. M. Lee, J. Teuscher, T. Miyasaka, T. N. Murakami and H. J. Snaith, *Science*, 2012, **338**, 643–647.
- [39] M. Hu, L. Liu, A. Mei, Y. Yang, T. Liu and H. Han, *J. Mater. Chem. A*, 2014, **2**, 17115–17121.
- [40] J. L. Minns, P. Zajdel, D. Chernyshov, W. Van Beek and M. A. Green, *Nat. Commun.*, 2017, **8**, 1–5.
- [41] N. S. Kumar and K. C. B. Naidu, *J. Materiomics*, 2021, **7**, 940–956.
- [42] D. Weber, *Z. Naturforsch. B*, 1978, **33**, 1443–1445.
- [43] D. B. Mitzi, K. Chondroudis and C. R. Kagan, *IBM J. Res. Dev.*, 2001, **45**, 29–45.
- [44] C. R. Kagan, D. B. Mitzi and C. D. Dimitrakopoulos, *Science*, 1999, **286**, 945–947.
- [45] V. M. Goldschmidt, *Naturwissenschaften*, 1926, **21**, 477–485.
- [46] T. Sato, S. Takagi, S. Deledda, B. C. Hauback and S. I. Orimo, *Sci. Rep.*, 2016, **6**, 1–10.
- [47] A. S. Thind, X. Huang, J. Sun and R. Mishra, *Chem. Mater.*, 2017, **29**, 6003–6011.
- [48] G. Kieslich, S. Sun and A. K. Cheetham, *Chem. Sci.*, 2014, **5**, 4712–4715.
- [49] C. J. Bartel, C. Sutton, B. R. Goldsmith, R. Ouyang, C. B. Musgrave, L. M. Ghiringhelli and M. Scheffler, *Sci. Adv.*, 2019, **5**, 1–10.
- [50] W. Travis, E. N. K. Glover, H. Bronstein, D. O. Scanlon and R. G. Palgrave, *Chem. Sci.*, 2016, **7**, 4548–4556.
- [51] A. Franz, D. M. Többens and S. Schorr, *Cryst. Res. Technol.*, 2016, **51**, 534–540.
- [52] M. T. Weller, O. J. Weber, P. F. Henry, A. M. Di Pumpo and T. C. Hansen, *Chem. Commun.*, 2015, **51**, 4180–4183.
- [53] C. C. Stoumpos, C. D. Malliakas and M. G. Kanatzidis, *Inorg. Chem.*, 2013, **52**, 9019–9038.
- [54] J. H. Lee, N. C. Bristowe, J. H. Lee, S. H. Lee, P. D. Bristowe, A. K. Cheetham and H. M. Jang, *Chem. Mater.*, 2016, **28**, 4259–4266.
- [55] P. S. Whitfield, N. Herron, W. E. Guise, K. Page, Y. Q. Cheng, I. Milas and M. K. Crawford, *Sci. Rep.*, 2016, **6**, 1–16.
- [56] J. M. Frost and A. Walsh, *Acc. Chem. Res.*, 2016, **49**, 528–535.

- [57] O. Almora, C. Aranda, I. Zarazua, A. Guerrero and G. Garcia-Belmonte, *ACS Energy Lett.*, 2016, **1**, 209–215.
- [58] J. Li and P. Rinke, *Phys. Rev. B*, 2016, **94**, 1–12.
- [59] J. Li, M. Bouchard, P. Reiss, D. Aldakov, S. Pouget, R. Demadrille, C. Aumaitre, B. Frick, D. Djurado, M. Rossi and P. Rinke, *J. Phys. Chem. Lett.*, 2018, **9**, 3969–3977.
- [60] J.-H. Lee, N. C. Bristowe, P. D. Bristowe and A. K. Cheetham, *Chem. Commun.*, 2015, **51**, 6434–6437.
- [61] A. M. A. Leguy, J. M. Frost, A. P. McMahon, V. G. Sakai, W. Kochelmann, C. Law, X. Li, F. Foglia, A. Walsh, B. C. O’Regan, J. Nelson, J. T. Cabral and P. R. F. Barnes, *Nat. Commun.*, 2019, **6**, 7124.
- [62] T. Chen, B. J. Foley, B. Ipek, M. Tyagi, J. R. D. Copley, C. M. Brown, J. J. Choi and S. H. Lee, *Phys. Chem. Chem. Phys.*, 2015, **17**, 31278–31286.
- [63] B. Li, Y. Kawakita, Y. Liu, M. Wang, M. Matsuura, K. Shibata, S. Ohira-Kawamura, T. Yamada, S. Lin, K. Nakajima and et al., *Nat. Commun.*, 2017, **8**.
- [64] V. K. Sharma, R. Mukhopadhyay, A. Mohanty, V. G. Sakai, M. Tyagi and D. D. Sarma, *J. Phys. Chem. C*, 2021, **125**, 13666–13676.
- [65] E. Mosconi and F. De Angelis, *ACS Energy Lett.*, 2016, **1**, 182–188.
- [66] A. A. Bakulin, O. Selig, H. J. Bakker and et al., *J. Phys. Chem. Lett.*, 2015, **6**, 3663–3669.
- [67] A. Mellor, D. Alonso Alvarez, I. Guarracino, A. Ramos, A. Riverola Lacasta, L. Ferre Llin, A. Murrell, D. Paul, D. Chemisana, C. Markides and N. Ekins-Daukes, *Sol. Energy*, 2018, **174**, 386–398.
- [68] R. Vaillon, S. Parola, C. Lamnatou and D. Chemisana, *Cell Rep. Phys. Sci.*, 2020, **1**, 100267.
- [69] IEC, *Terrestrial photovoltaic (PV) modules – Design qualification and type approval – Part 1: Test requirements*, International Electrotechnical Commission, Geneva, 2021.
- [70] G. Grancini, C. Roldán-Carmona, I. Zimmermann, E. Mosconi, D. M. X. Lee, S. Narbey, F. Oswald, F. D. Angelis, M. Graetzel and M. K. Nazeeruddin, *Nat. Commun.*, 2017, **8**.
- [71] A. B. Kaplan, Q. C. Burlingame, R. Holley and Y.-L. Loo, *APL Energy*, 2023, **1**, 010901.
- [72] A. Marronnier, G. Roma, S. Boyer-Richard, L. Pedesseau, J.-M. Jancu, Y. Bonnassieux, C. Katan, C. C. Stoumpos, M. G. Kanatzidis and J. Even, *ACS Nano*, 2018, **12**, 3477.
- [73] R. Chen, Y. Hui, B. Wu, Y. Wang, X. Huang, Z. Xu, P. Ruan, W. Zhang, F. Cheng, W. Zhang and et al., *J. Mater. Chem. A*, 2020, **8**, 9597–9606.

- [74] C. Wang, B. R. Ecker, H. Wei, J. Huang and Y. Gao, *J. Phys. Chem. C*, 2018, **122**, 3513–3522.
- [75] Y. Ouyang, Y. Li, P. Zhu, Q. Li, Y. Gao, J. Tong, L. Shi, Q. Zhou, C. Ling, Q. Chen and et al., *J. Mater. Chem. A*, 2019, **7**, 2275–2282.
- [76] M. A. Akhavan Kazemi, P. Raval, K. Cherednichekno, J.-N. Chotard, A. Krishna, A. Demortiere, G. N. M. Reddy and F. Sauvage, *Small Methods*, 2021, **5**.
- [77] A. M. Leguy, Y. Hu, M. Campoy-Quiles, M. I. Alonso, O. J. Weber, P. Azarhoosh, M. van Schilfgaarde, M. T. Weller, T. Bein, J. Nelson and et al., *Chem. Mater.*, 2015, **27**, 3397–3407.
- [78] J. Schlipf, L. Bießmann, L. Oesinghaus, E. Berger, E. Metwalli, J. A. Lercher, L. Porcar and P. Müller-Buschbaum, *J. Phys. Chem. Lett.*, 2018, **9**, 2015–2021.
- [79] C. Zheng and O. Rubel, *J. Phys. Chem. C*, 2019, **123**, 19385–19394.
- [80] W. J. Nimens, S. J. Lefave, L. Flannery, J. Ogle, D.-M. Smilgies, M. T. Kieber-Emmons and L. Whittaker-Brooks, *Angew. Chem. Int. Ed.*, 2019, **58**, 13912–13921.
- [81] B. Kim and S. I. Seok, *Energy Environ. Sci.*, 2020, **13**, 805–820.
- [82] E. J. Juarez-Perez, L. K. Ono, I. Uriarte, E. J. Cocinero and Y. Qi, *ACS Appl. Mater. Interfaces*, 2019, **11**, 12586–12593.
- [83] L. Zhang and P. H.-L. Sit, *J. Phys. Chem. C*, 2015, **119**, 22370–22378.
- [84] J. S. Manser, M. I. Saidaminov, J. A. Christians, O. M. Bakr and P. V. Kamat, *Acc. Chem. Res.*, 2016, **49**, 330–338.
- [85] J. Huang, S. Tan, P. D. Lund and H. Zhou, *Energy Environ. Sci.*, 2017, **10**, 2284–2311.
- [86] Z. Song and W. et al., *Sustainable Energy Fuels*, 2018, **2**, 2460–2467.
- [87] H. Wang, Y. Liu and M. L. et al., *Optoelectron. Adv. Mater.*, 2014, **2**, 705–710.
- [88] R. J. Sutton, G. E. Eperon, L. Miranda, E. S. Parrott, B. A. Kamino, J. B. Patel and H. J. Snaith, *Adv. Chem. Mater.*, 2016, **6**, 150–245.
- [89] Z. Song, S. C. Watthage, A. B. Phillips and M. J. Heben, *J. Photonics Energy*, 2016, **6**, 022001.
- [90] F. Palazon, D. Pérez-del-Rey, S. Marras, M. Prato, M. Sessolo, H. J. Bolink and L. Manna, *ACS Energy Lett.*, 2018, **3**, 835–839.
- [91] M. A. Mutalib, N. A. Ludin, N. A. A. N. Ruzalman, V. Barrioz, S. Sepeai, M. A. M. Teridi, M. S. Su'ait, M. A. Ibrahim and K. Sopian, *Mater. Renew. Sustain. Energy*, 2018, **7**, 1–13.
- [92] A. Babayigit, A. Ethirajan and M. Muller, *Nat. Mater.*, 2016, **15**, 247–251.
- [93] F. Giustino and H. J. Snaith, *ACS Energy Lett.*, 2016, **1**, 1233–1240.

- [94] A. E. Magdalin, P. D. Nixon, E. Jayaseelan, M. Sivakumar, S. K. N. Devi, M. Subathra, N. M. Kumar and N. Ananthi, *Results Eng.*, 2023, **20**, 101438.
- [95] J. Gong, S. B. Darling and F. You, *Energy Environ. Sci.*, 2015, **8**, 1953–1968.
- [96] A. Binek, M. L. Petrus, N. Huber, H. Bristow, Y. Hu, T. Bein and P. Docampo, *ACS Appl. Mater. Interfaces*, 2016, **8**, 12881–12886.
- [97] Q. Chen, H. Zhou, Y. Fang, A. Z. Stieg, T. B. Song, H. H. Wang, X. Xu, Y. Liu, S. Lu, J. You, P. Sun, J. McKay, M. S. Goorsky and Y. Yang, *Nat. Commun.*, 2015, **6**, 7269.
- [98] G. E. Eperon, S. D. Stranks, C. Menelaou, M. B. Johnston, L. M. Herz and H. J. Snaith, *Energy Environ. Sci.*, 2014, **7**, 982–988.
- [99] B. Slimi, M. Mollar, I. B. Assaker, I. Kriaa, R. Chtourou and B. Marà, *Energy Procedia*, 2016, **102**, 87–95.
- [100] M. Saliba, T. Matsui, J.-Y. Seo, K. Domanski, J.-P. Correa-Baena, M. K. Nazeeruddin, S. M. Zakeeruddin, W. Tress, A. Abate, A. Hagfeldt and M. Grätzel, *Energy Environ. Sci.*, 2016, **9**, 1989–1997.
- [101] K. Kranthiraja, M. Parashar, R. Mehta and et al., *Sci. Rep.*, 2022, **12**, 18574.
- [102] T. M. Koh, T. Krishnamoorthy, N. Yantara, C. Shi, W. L. Leong, P. P. Boix, A. C. Grimsdale, S. G. Mhaisalkar and N. Mathews, *J. Mater. Chem. A*, 2015, **3**, 14996–15000.
- [103] R. Lin, K. Xiao, Z. Qin, Q. Han, C. Zhang, M. Wei, M. I. Saidaminov, Y. Gao, J. Xu, M. Xiao, A. Li, J. Zhu, E. H. Sargent and H. Tan, *Nat. Energy*, 2019, **4**, 864–873.
- [104] Y. Yin, S. Fu, S. Zhou, Y. Song, L. Li, M. Zhang, J. Wang, P. Mariyappan, S. M. Alshehri, T. Ahamad and Y. Yamauchi, *Electron. Mater. Lett.*, 2020, **16**, 224–230.
- [105] S. A. Kulkarni, T. Baikie, P. P. Boix, N. Yantara, N. Mathews and S. Mhaisalkar, *J. Mater. Chem. A*, 2014, **2**, 9221–9225.
- [106] T. Baikie, N. S. Barrow, Y. Fang, P. J. Keenan, P. R. Slater, R. O. Piltz, M. Gutmann, S. G. Mhaisalkar and T. J. White, *J. Mater. Chem. A*, 2015, **3**, 9298–9307.
- [107] J. H. Noh, S. H. Im, J. H. Heo, T. N. Mandal and S. I. Seok, *Nano Lett.*, 2013, **13**, 1764–1769.
- [108] D. J. Slotcavage, H. I. Karunadasa and M. D. McGehee, *ACS Energy Lett.*, 2016, **1**, 1199–1205.

Chapter 2

Characterisation Techniques

This chapter covers a range of advanced characterisation techniques employed to study the structural and dynamic properties of hybrid halide perovskites. X-ray diffraction is utilised to analyse the crystal structure and identify phase transitions, providing critical insights into lattice parameters and symmetry changes. Quasi-elastic neutron scattering is applied to probe the molecular dynamics of organic cations within the perovskite framework, revealing information about the cation's mobility and reorientation processes. Solid-state nuclear magnetic resonance spectroscopy, including ^1H , ^{13}C , and ^{14}N NMR, offers detailed information on the local chemical environments of both organic and inorganic components. This technique is particularly valuable in studying the interactions and dynamics of methylammonium cations within the perovskite lattice. Finally, solid-state nuclear quadrupole resonance is employed to measure electric field gradients around ^{127}I nuclei, allowing for the investigation of quadrupolar interactions, which can provide insights into the local symmetry and disorder within the perovskite structure.

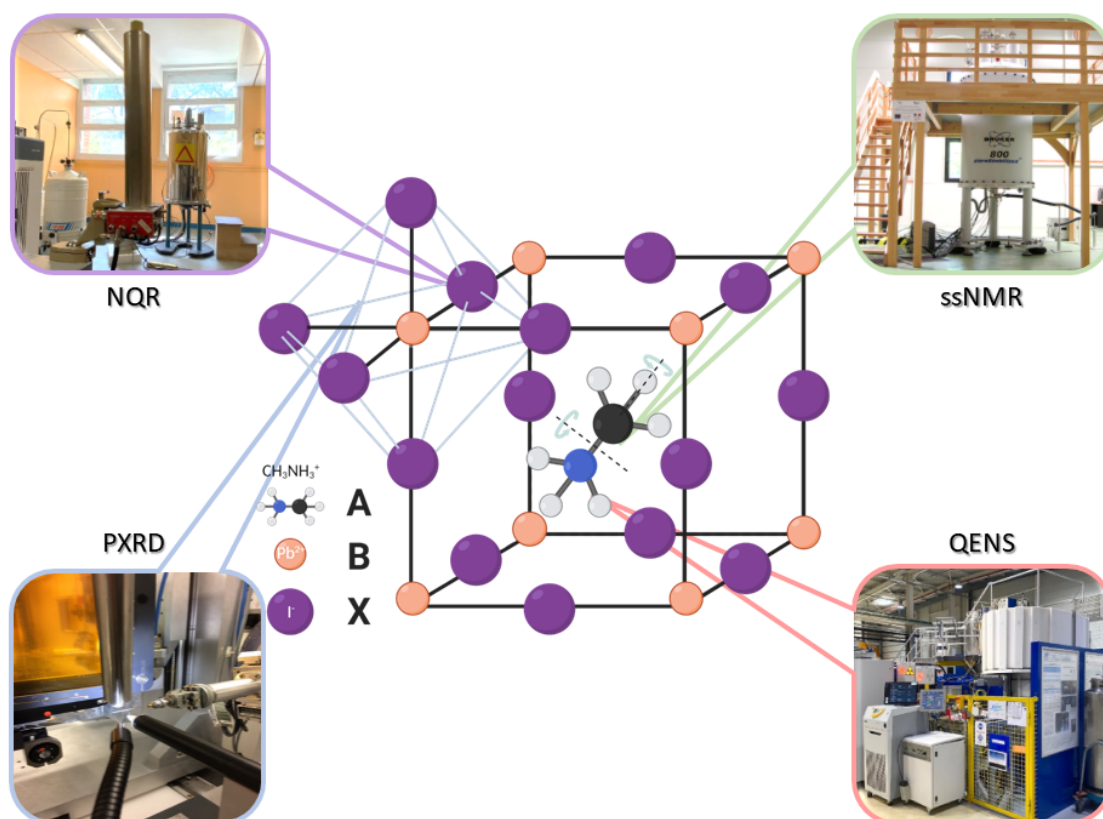


Figure 2.1 Demonstration of where each technique can probe the organic-inorganic halide perovskites, showcasing multi-technique characterisation to investigate structural changes in the inorganic lattice and alterations in the dynamics of the organic cation.

Together, these techniques offer a comprehensive understanding of the structural, dynamic, and electronic properties of hybrid halide perovskites (Figure 2.1) while also collecting information across a variety of timescales (as exemplified in Figure 2.2), contributing to the optimisation of their performance in real-world applications.

2.1 Scattering and Diffraction

In the pursuit of determining the crystal structure through characterisation, a fundamental consideration revolves around the choice of an appropriate radiation source.

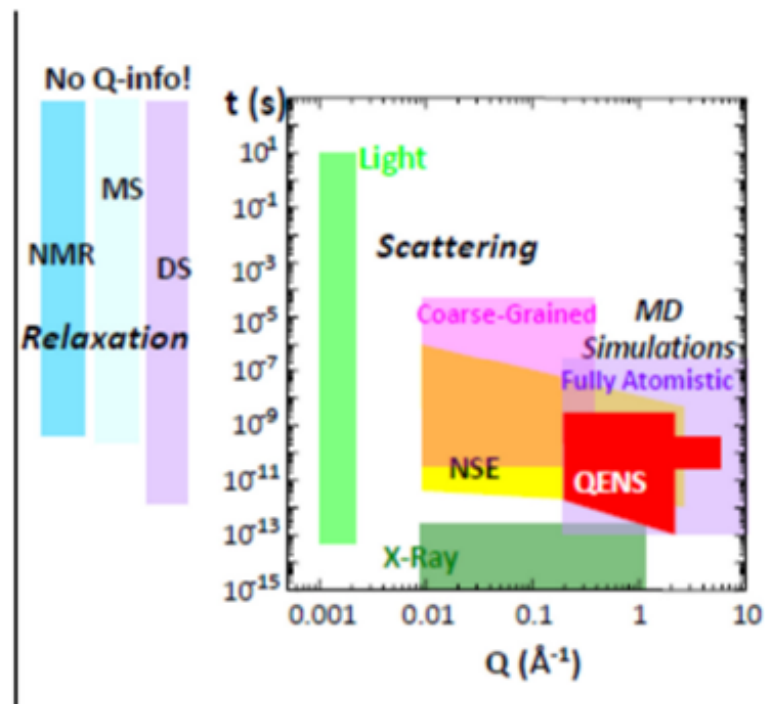


Figure 2.2 A plot illustrating various characterisation techniques and their positions on a graph of timescale vs momentum, exemplifying the range of information each technique can capture. This diagram visualises comparisons between the techniques. The diagram is taken from [1].

To obtain high-resolution images of the crystal atoms, it is imperative that the wavelength of the selected radiation is similar to the inter-atomic distances within the crystal. Several types of radiation fulfill this criterion, including electron, neutron, and electromagnetic radiation. Another critical factor in beam selection is ensuring that the radiation is not excessively absorbed by the material, as excessive absorption can damage the sample and/or give inaccurate results. Consequently, the use of protons or neutral atoms may be precluded, depending on the sample under investigation. While some degree of absorption is anticipated with all forms of radiation experiments, managing these effects is more feasible when employing neutrons, electrons, or X-rays.

Scattering phenomena encompass a range of modes, including both elastic and inelastic, as well as coherent and incoherent scattering. Explanations of these types of scattering are given further in this chapter in Section 2.3.1 and 2.3.2. Given this diversity in the information offered by the process of scattering, various techniques have been devised to customise data collection based on the specific information sought from the sample. Many of these techniques leverage diffraction, a process involving coherent elastic scattering that relies on the long-range order within a crystal structure.

2.2 X-ray Diffraction

X-ray diffraction (XRD) is an invaluable technique for the structural analysis and phase identification of crystalline materials. Its effectiveness arises from the X-ray wavelength, which falls within the range of a crystal's interatomic distances, typically around 1Å.

In most in-house X-ray diffractometers, a Bragg-Brentano configuration is employed. In this setup, a monochromatic X-ray beam is directed toward a sample at an angle θ .

The beam's divergence and collection angle are controlled by slits positioned after the X-ray source but before the detector.

2.2.1 X-ray Generation

Within laboratory settings, X-rays are generated when a beam of electrons is accelerated towards a metal target, with copper and molybdenum being the most commonly used metals. When an electron collides with the metal target, it displaces one of the metal's inner electrons. Subsequently, X-rays are emitted when an outer shell electron transitions into the vacant electron level, releasing its energy in the form of an X-ray photon with a characteristic energy. The emitted X-ray's energy depends on both the initial energy level of the electron filling the gap and the energy level of the displaced electron, as illustrated in Figure 2.3.

A notable example of such transitions is the movement from the L shell to the K shell, referred to as K_α . In fact, there are two K_α transitions, denoted as $K_{\alpha 1}$ and $K_{\alpha 2}$. While these transitions have similar energies, the $K_{\alpha 1}$ line exhibits twice the intensity of the $K_{\alpha 2}$ line. The $K_{\alpha 1}$ transition corresponds to the transition from the $2p_{3/2}$ orbital (where $3/2$ corresponds to the total angular momentum quantum number), to the $1s$ orbital, whereas the $K_{\alpha 2}$ line corresponds to the transition from the $2p_{1/2}$ orbital to the $1s$ orbital. Consequently, the $K_{\alpha 1}$ line is twice as intense as the $K_{\alpha 2}$ line because the $2p_{3/2}$ state has twice the number of available quantum states compared to the $2p_{1/2}$ state, resulting in a greater probability of the $K_{\alpha 1}$ transition occurring. Additionally, each material possesses characteristic X-ray wavelengths. For instance, copper (Cu) has characteristic K_α wavelengths measured at 1.54051 \AA for $K_{\alpha 1}$ and 1.54433 \AA for $K_{\alpha 2}$.^[2] In addition to laboratory-based X-ray source, synchrotron facilities offer alternative sources of X-ray radiation. These facilities provide high-intensity X-rays, tunable

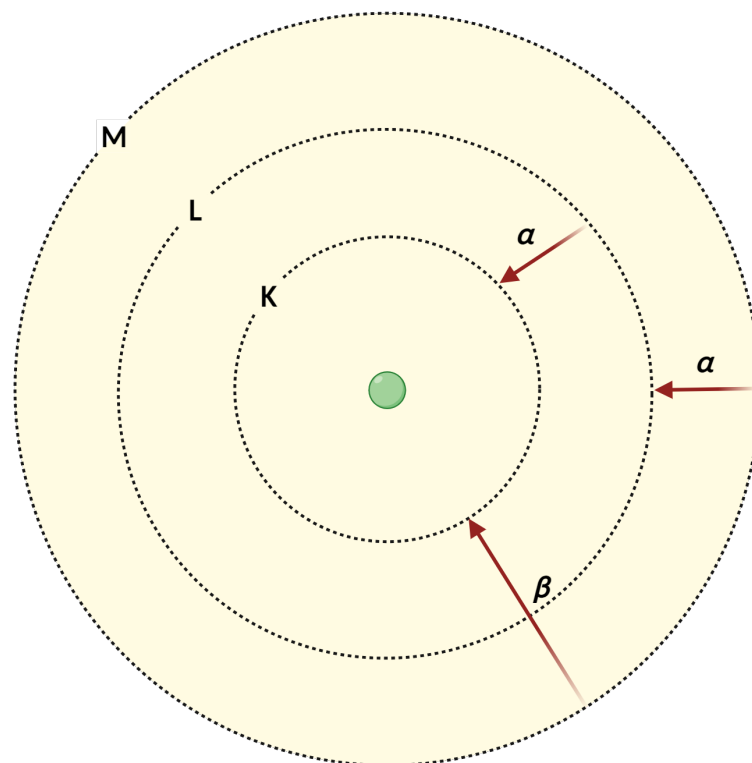


Figure 2.3 Schematic displaying the different energy level transitions and the corresponding characteristic X-ray generated

wavelengths, high polarisation, and low divergence, making them valuable resources for advanced XRD applications.

In a basic X-ray experiment, the X-ray beam interacts with a sample and is subsequently diffracted, reaching a detector at an angle of 2θ (where 2θ is angle between the incident and scattered X-ray beams), as seen in Figure 2.4, resulting in a diffraction pattern. To extract meaningful information from this pattern, it must be interpreted in the context of crystal structure properties, relying on fundamental principles like reciprocal space and Bragg's Law.

2.2.2 Reciprocal Space

A crystal lattice represents a regularly repeating three-dimensional arrangement of atoms or ions in real space. When transitioning into reciprocal space, a reciprocal lattice is constructed. This reciprocal lattice is defined by a set of vectors whose spacing and orientation mirror the periodicity and symmetry of the observed crystal lattice in real space. In real space, we use vectors a , b , and c to describe actual atomic positions, while in reciprocal space, these vectors become a^* , b^* , and c^* . In terms of diffraction, when X-ray radiation is scattered in any direction due to interactions with the crystal lattice, the direction in which this wave is scattered corresponds to the reciprocal of the shortest distance between the Miller (hkl) planes.

2.2.3 Bragg's Law

Bragg's Law articulates the connection between the angle of incidence (θ), the wavelength of the incident X-rays (λ), and the spacing between crystal planes (d).

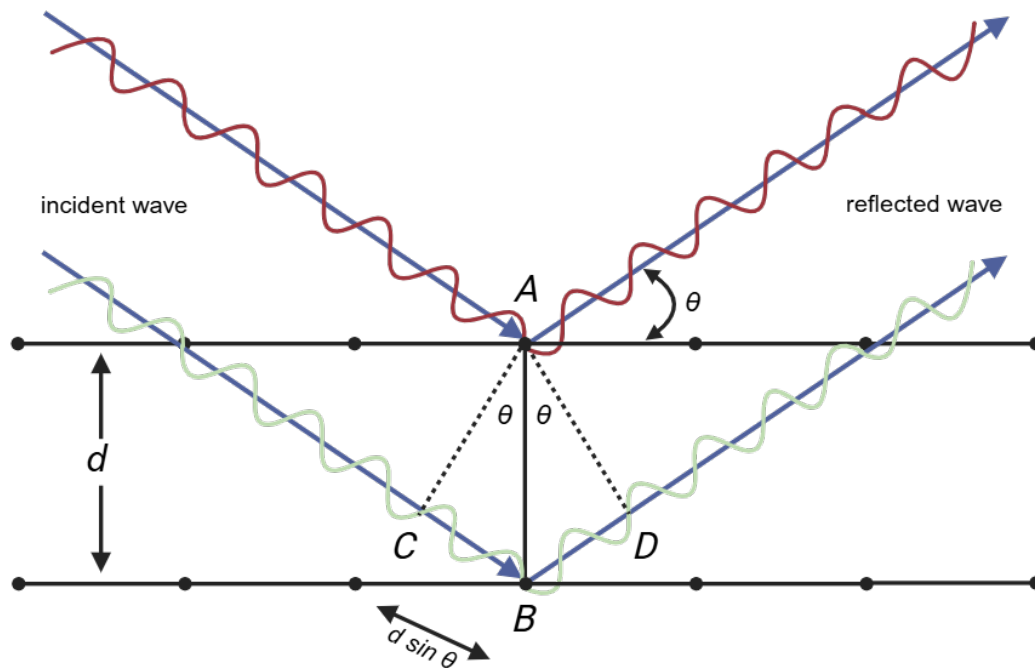


Figure 2.4 Illustration of Bragg diffraction, where incident waves reflect off atomic planes in a crystal with spacing, d . Waves 1 and 2, initially in phase, remain in phase after reflection if the path difference CBD is an integer multiple of the wavelength λ , satisfying Bragg's Law (2.1). The reflected angle θ equals the incident angle, and diffraction occurs at specific angles corresponding to different reflection orders ($n = 1, 2, 3$, etc.). At non-integer n , destructive interference eliminates the reflected waves.

$$n\lambda = 2d\sin(\theta) \quad (2.1)$$

To satisfy Bragg's Law, the angle between the incoming X-ray beam and the crystal lattice must be such that the path difference between X-rays scattered by different lattice planes equals an integer number of wavelengths. When Bragg's Law is fulfilled for a specific set of crystal planes, the X-rays undergo constructive interference, resulting in strong diffraction peaks in the X-ray diffraction pattern.

2.2.4 The Ewald Sphere

The Ewald sphere serves as a visual representation of diffraction conditions in relation to the reciprocal lattice within three dimensions. It aids in determining which points in the reciprocal lattice contribute to the diffraction pattern. The center of the Ewald sphere (corresponding to a 000 reflection) aligns with the incident X-ray wave vector (\mathbf{k}), and its radius is inversely proportional to the wavelength of the X-rays ($1/\lambda$). As the Ewald sphere is rotated in reciprocal space, it intersects various reciprocal lattice points, representing different sets of crystal planes. Bragg's Law is met if one or multiple lattice points interact with the sphere's surface, resulting in an angle of 2θ .

2.2.5 Powder X-ray Diffraction

Powder diffraction involves the analysis of patterns obtained from crystalline powders or thin film materials. While it may not be as favoured as single crystal diffraction in some cases, it offers the advantage of rapid phase identification. This is because diffraction patterns are distinct for each material, making it especially useful given the

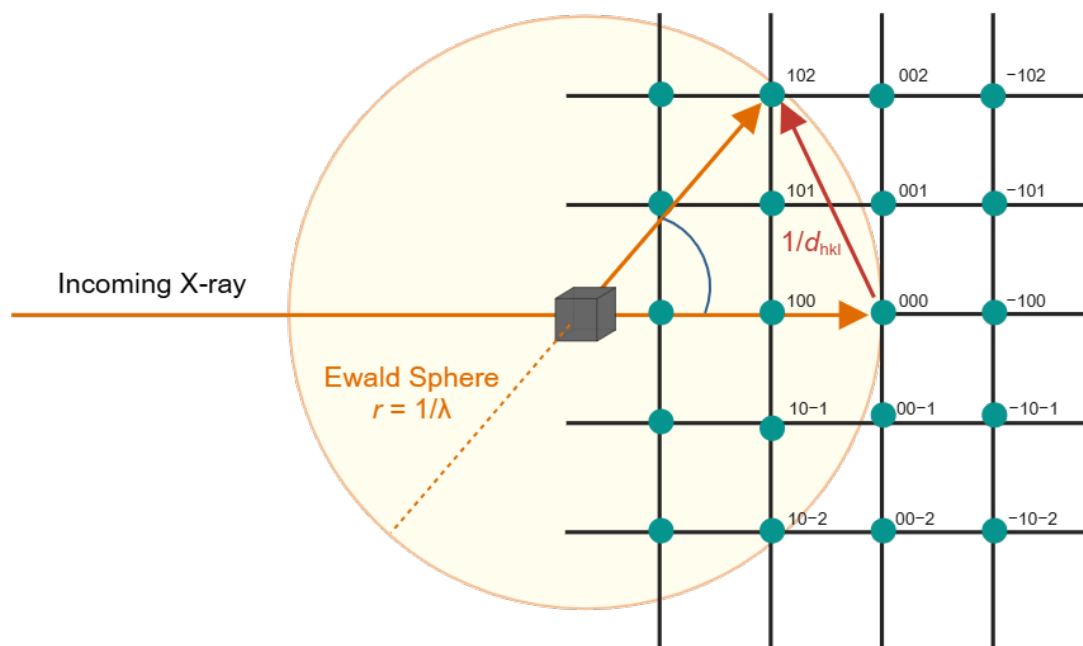


Figure 2.5 The Ewald sphere represents the reciprocal space construction for X-ray diffraction. The intersection of the scattering vector k with a reciprocal lattice point (hkl) satisfies Bragg's condition, resulting in diffraction from the real lattice planes with spacing d_{hkl} . A shorter incident X-ray wavelength increases the radius of the Ewald sphere ($r = 1/\lambda$), leading to more crossing points and additional Bragg reflections.

time-consuming process of growing single crystals and identifying suitable candidates.

In a typical XRD experiment, a single crystal would yield different diffraction patterns depending on the orientation of its planes. However, in the case of bulk powder, the orientation-specific diffraction can be effectively disregarded. This is because the crystals within the powder are randomly oriented. As a result, powder X-ray diffraction (PXRD) allows for quick identification of structures by comparing indexed peaks to a database of known compounds.

2.2.6 Rietveld Refinement

One of the primary challenges associated with powder diffraction lies in the random orientation of crystalline particles within the sample. This random orientation effectively collapses the structural information along three crystallographic axes into a single axis within the diffraction pattern, typically measured as 2θ . Consequently, this can result in the overlapping of diffraction peaks, particularly when the distances between Miller planes are similar. To address this issue, a significant advancement in the field was made by Hugo Rietveld, who developed a method of profile analysis. This method allows for the refinement of experimental diffraction patterns using an initial approximate structural model.[3] The fundamental goal of the Rietveld refinement method is to minimise the weighted difference in peak intensities between the observed experimental diffraction profile (Y_i^{obs}) and the corresponding profile calculated from the initial structural model (Y_i^{calc}). By iteratively adjusting the parameters of the structural model, such as atomic positions, thermal dependent parameters, and other crystallographic parameters, the Rietveld refinement method seeks to achieve the best possible agreement between the observed and calculated diffraction patterns. This process not only improves the accuracy of the structural model but also provides

valuable insights into the crystal structure, including atomic positions and unit cell parameters.

$$S_y = \sum_{i=1}^n w_i (Y_i^{\text{obs}} - Y_i^{\text{calc}})^2 \quad (2.2)$$

Equation 2.2 presents the concept of how each individual data point (n) is assigned a specific weight (w_i), and subsequently, a non-linear least squares optimisation technique is employed to minimise the disparity between observed and calculated values. This refinement process uses the initial structural model to generate a calculated profile that offers a representation of the crystal structure of the material under investigation.

The term Y_i^{obs} encompasses a multitude of reflections. On the other hand, the model used for Y_i^{calc} typically draws its foundation from a comprehensive crystal structure database, such as the Inorganic Crystal Structure Database (ICSD).[4] The model is subject to iterative adjustments that encompass a broad spectrum of parameters. These parameters include modifications to the structure factor, background coefficients, peak shape, instrument parameters, lattice parameters, thermal factors, and other pertinent variables. Equation 2.3 describes the peak intensity for a typical XRD experiment where:

$$Y_i^{\text{calc}} = s \sum_{hkl} m_{hkl} L_{hkl} (F_{hkl})^2 A_i G(2\theta_i - 2\theta_{hkl}) P_{hkl} T + b_i \quad (2.3)$$

- s describes the scale factor;
- m_{hkl} is the multiplicity factor;
- L_{hkl} is the Lorentz-polarisation factor for the reflection;
- F_{hkl} is the structure factor;

- A_i is the asymmetry parameter;
- $2\theta_{hkl}$ is the zero-point corrected calculated Bragg peak position;
- P_{hkl} denotes preferred orientation;
- T relates to absorption correction;
- b_i describes the background function which can be user-defined or entered as a polynomial.

While S_y in Equation 2.2 serves as a crucial component in assessing the goodness of fit through minimisation, it possesses limitations in evaluating the structural accuracy of the model. Consequently, various metrics, known as R -factors, are employed to gauge the quality of a given model. Among these metrics, two prominent ones are the R -profile (R_p) and the R -weighted profile (R_{wp}), which are defined in Equations 2.4 and 2.5 respectively. Profile weighting does not allow for preference to be given to highest intensity peaks, instead it attempts to fit all peaks equally.

$$R_p = \frac{\sum_i |Y_i^{\text{obs}} - Y_i^{\text{calc}}|}{\sum_i Y_i^{\text{obs}}} \quad (2.4)$$

$$R_{wp} = \frac{\sum_i w_i (Y_i^{\text{obs}} - Y_i^{\text{calc}})^2}{\sum_i w_i Y_i^2} \quad (2.5)$$

Indeed, an additional parameter that is widely employed to gauge the quality of a fit is χ^2 . As expressed in Equation 2.6, χ^2 takes into account the number of observations (N), the number of refined parameters (P), and the number of constraints (C) to provide a quantitative measure of the goodness of fit.

$$\chi^2 = \frac{\sum_i w_i (Y_i^{\text{obs}} - Y_i^{\text{calc}})^2}{N - P + C} \quad (2.6)$$

In the realm of crystallography, χ^2 serves as a valuable metric for assessing the quality of a model fit to experimental data. When χ^2 approaches a value of approximately 1, it signifies a remarkably good fit between the model and the observed data. In essence, χ^2 offers a statistical measure of how well the model aligns with the

2.3 Quasi Elastic Neutron Scattering (QENS)

experimental evidence. Researchers often strive to achieve χ^2 values as close to 1 as possible, indicating a high degree of fidelity between the proposed crystal structure and the actual diffraction pattern.

2.3 Quasi Elastic Neutron Scattering (QENS)

Neutrons have zero charge and negligible electric dipole moment, meaning they only interact with atoms through the nuclear force and the intrinsic magnetic moment of an atom. Therefore neutrons can penetrate deeper in samples than charged particles (for instance electrons for surface characterisation), which is ideal for studying the position of nuclei within a crystal structure. Neutrons are commonly used to determine crystal structures through diffraction, or to study molecular dynamics like in QENS. In order to probe dynamical information, the energy of the neutron needs to be in the same order of magnitude as intermolecular energies in materials of study ($E \sim 25$ meV).[5]

The neutron energy utilised in QENS measurements is too small to trigger any excitation of nuclei or electrons, and so the assumption is made that the small changes in neutron energies are only due to the motion of neighbouring nuclei. QENS analyses small energy and momentum exchanges between scattering nuclei. Neutrons are selective in that they interact with some nuclei more than others, and so scattering lengths are randomly assorted with no direct correlation to atomic number (Z) as shown in Table 2.1. This differs to X-rays where atomic scattering factor is proportional to Z . As the incoherent cross section of ^1H is much larger than that of ^{127}I or ^{207}Pb , this means QENS can be used in perovskites to probe the dynamics of the molecular moieties independently from the surrounding inorganic sub-lattice.

2.3 Quasi Elastic Neutron Scattering (QENS)

Table 2.1 Neutron scattering lengths and incoherent cross-sections for elements present in MAPI. Data sourced from.[6]

Element	Z	Neutron Scattering Length (fm)	Incoherent cross section (barn)
¹ H	1	-3.74	80.27
¹² C	6	6.65	0.0
¹⁴ N	7	9.37	0.50
¹²⁷ I	53	5.28	0.31
²⁰⁷ Pb	82	9.28	0.002

2.3.1 Elastic vs. Inelastic Scattering

Two categories of neutron-nuclei scattering processes can be defined.

Elastic scattering refers to an event where the total neutron energy and the sample remains conserved. In other words, the neutron loses no energy during the interaction, and only its momentum (Q) changes. Elastic scattering is typically associated with stationary or long-term average structures in a material, where no net energy transfer occurs between the neutron and the sample. This provides information on the static arrangement or slow dynamics of the atoms. In QENS, the elastic peak is observed at zero energy transfer and corresponds to components of the system that do not exhibit motion on the timescales probed.

$$\Delta E_{\text{initial}} = \Delta E_{\text{final}} \tag{2.7}$$

As the total initial energy ($\Delta E_{\text{initial}}$) is equal to the final energy (ΔE_{final}) (Equation 2.7), the overall energy transfer is zero ($\Delta E = 0$) and the scattering is characterised by only momentum transfer ($\Delta \vec{Q}$), but no energy exchange.

Inelastic scattering is where there is a change in the total energy between the neutron and the material. In this case, the neutron either loses or gains energy during

2.3 Quasi Elastic Neutron Scattering (QENS)

the interaction, depending on whether the system absorbs or releases energy. Inelastic scattering provides information on the dynamic properties of the material, such as vibrations, rotations, or other forms of atomic and molecular motion. The energy transferred between the neutron and the sample during inelastic scattering reflects these internal motions.

There is an energy transfer ($\Delta E \neq 0$), indicating that the neutron exchanges energy with the system (either gaining or losing energy).

$$\Delta E_{\text{initial}} \neq \Delta E_{\text{final}} \quad (2.8)$$

2.3.2 Coherent vs. Incoherent Scattering

In QENS, inelastic scattering refers to interactions in which atoms or molecules within a material undergo motion, resulting in energy transfers. These motions occur across a range of timescales, leading to small, but finite, changes in neutron energy. *Quasi-elastic scattering*, a specific form of inelastic scattering, occurs when the energy transfer is minimal, though not precisely zero. The small energy shift in quasi-elastic scattering is indicative of slower dynamic processes, such as molecular diffusion or reorientations. QENS targets these quasi-elastic processes to explore the slow dynamics in materials, as these involve minimal momentum transfer and reflect slower, diffusive movements. By analysing the quasi-elastic broadening of the elastic peak in the energy spectrum, researchers can extract valuable information about the timescales and mechanisms of diffusive behavior.

A key aspect of QENS analysis is the distinction between coherent and incoherent scattering, which affects the type of information obtained on atomic or molecular

dynamics. The type of scattering observed depends on the specific nuclei in the system. Coherent scattering occurs when neutrons scatter in such a way that interference effects arise between waves scattered by different atoms, yielding structural information about the material. It provides insight into collective motions and correlations between atoms, offering a picture of the material's overall structural behavior.

Conversely, incoherent scattering arises when neutrons scatter independently off individual atoms or molecules. This scattering process results from variations in the scattering lengths of isotopes, which reflect the dynamics of individual nuclei. For Hydrogen, the incoherent scattering cross-section is significantly larger than that of most other elements, meaning the incoherent signal often dominates. For example, in the study of hybrid perovskites, QENS data are primarily sensitive to the dynamics of hydrogen atoms, as their incoherent scattering cross-section vastly outweighs that of other atoms. This makes QENS an especially powerful tool for investigating hydrogen-related motions in complex materials.

2.4 Nuclear Magnetic Resonance

The principle behind NMR is many nuclei have spin and hence, are magnetic. It is this property of spin that dominates the fundamental understanding of NMR in physics. However, this is out of the scope of this thesis. Therefore, any interested reader is directed to NMR textbooks for a more comprehensive review of the topic.[7–9] Nevertheless, an attempt to explain the fundamentals of NMR spectroscopy required for the discussion of results in chapters 4 and 5 is made here.

NMR spectroscopy is a useful technique to explore the chemical environment of a specified nucleus that possesses a nuclear spin quantum number $I \geq \frac{1}{2}$. During an

2.4 Nuclear Magnetic Resonance

experiment, the application of an external stationary magnetic field (\mathbf{B}_0) is required to lift the degeneracy of the nuclear spin energy levels. From this, the nuclear spins orient and undergo precession about \mathbf{B}_0 , and an energy transfer is possible between consecutive energy levels. The energy transfer occurs at a wavelength that corresponds to radio frequencies (rf), typically between 10 MHz and 1 GHz, and when the spin returns to its ground state, energy is emitted at this same frequency also called Larmor frequency, ω_0 . The signal that matches this transfer is then measured and processed in order to yield an NMR spectrum. The Larmor frequency is unique for each nucleus and is dependent on the gyromagnetic ratio, γ , and the strength of \mathbf{B}_0 as shown in Equation 2.9.

$$\omega_0 = -\gamma B_0 \quad (2.9)$$

The gyromagnetic ratio is an intrinsic property of a nucleus and is related to its nuclear spin and magnetic moment (see Equation 2.10).

$$\boldsymbol{\mu} = \gamma \mathbf{I} \quad (2.10)$$

During nuclear spin precession, several perturbations occur which effect the precession of the nuclear spin. A total Hamiltonian can be written to describe these interactions (Equation 2.11).

$$\hat{H}_{\text{total}} = \hat{H}_Z + \hat{H}_{\text{CS}} + \hat{H}_{\text{DD}} + \hat{H}_J + \hat{H}_Q \quad (2.11)$$

Here \hat{H}_Z , \hat{H}_{CS} , \hat{H}_{DD} , \hat{H}_J , and \hat{H}_Q refer to the respective Hamiltonians of the

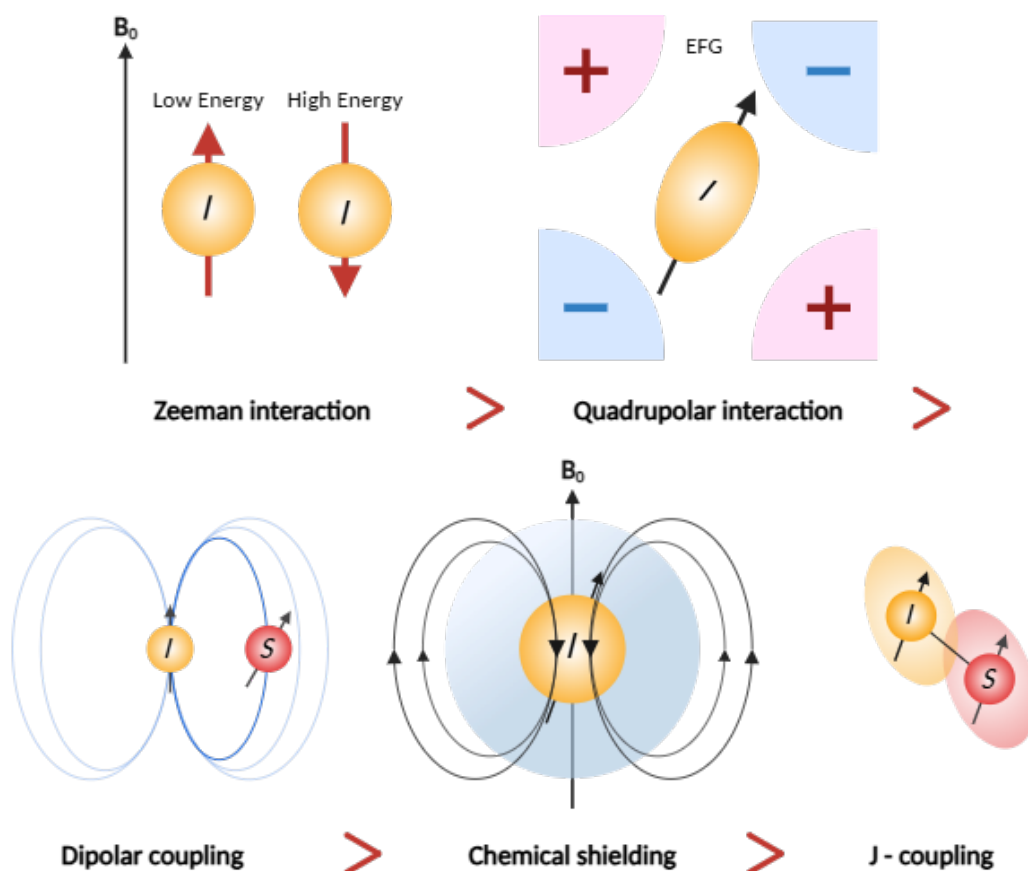


Figure 2.6 Schematic of the different spin interactions which are ranked, going from largest to smallest in terms of magnitude in solid state NMR for a typical quadrupolar nucleus

Zeeman interaction, chemical shielding, dipolar coupling, spin-spin (J) coupling, and quadrupolar coupling as seen in Figure 2.6. Each of these interactions influences the spin of the observed isotope, and therefore affects the resulting NMR signal acquired during an experiment. Each interaction is briefly discussed below.

2.4.1 Zeeman Interaction

A phenomenon that describes the coupling of a nucleus' magnetic moment to \mathbf{B}_0 . Here, the nuclear spins align either parallel or anti-parallel to the field, resulting in a splitting of the energy levels. The magnitude of this interaction is linear with B_0 , meaning that

higher magnetic fields induce larger separations of the energy levels and an increase in the signal-to-noise ratio of the spectrum.

2.4.2 Chemical Shielding Interaction

It arises from the shielding of the nucleus by the electrons surrounding it, which results in a small shift in its resonance frequency. The electrons in a molecule can shield/deshield the nucleus from the external magnetic field. This shielding/deshielding effect depends on the electron density and electronic structure. This shift in resonance frequency is directly proportional to the strength of the magnetic field and the electron density around the nucleus and depends on the local electronic environment of the nucleus. In the solid-state, this interaction is dependent on crystallite orientation (anisotropic), leading to broadening of a signal to create a “powder pattern” lineshape.

2.4.3 Dipolar Interaction

Dipole-dipole interactions are a type of magnetic interaction occurring between the nuclear spins of adjacent atoms. These interactions arise due to the magnetic dipole moments of the nuclei, which can align with or against each other depending on their relative orientations. The dipole moments of neighbouring nuclei can interact with each other, leading to a coupling of their spin states. This coupling can cause the energy levels of the nuclei to split into multiple levels. The strength of these interactions depends on the distance between the interacting nuclei, as well as their orientation relative to each other and hence, yields line broadening for powder.

2.4.4 J-Coupling

The J coupling interaction, also known as scalar coupling or spin-spin coupling, is an internal interaction between nuclear spins, mediated by the electrons within chemical bonds. In principle, this interaction can establish bond connectivity in a studied material. This is due to the magnetic field generated by one nucleus, affecting the resonance frequency of another nucleus in its vicinity. This causes the energy levels of the two nuclei to split into multiple levels. The resulting splitting is then directly proportional to the strength of the coupling interaction, which in turn is dependent on the distance between the two nuclei and the dihedral angle between their bonds. In terms of solid-state NMR, J couplings are only rarely observed due to other anisotropic interactions, described above, having greater effect in broadening the resulting spectral resonances.

2.4.5 Quadrupolar Interaction

Quadrupolar nuclei possess a spin, I , greater than $\frac{1}{2}$ hence, $2I+1$ energy levels. Therefore, they have a non-spherical distribution of nuclear charge, leading to an electric quadrupolar moment (eQ) which couples with the surrounding local electric field gradient (EFG). This is known as the quadrupolar interaction and lifts the degeneracy of the $2I$ allowed NMR transitions. The EFG is defined by three components (V_{XX} , V_{YY} , V_{ZZ}) in its principal axis system and provided by an asymmetric distribution of nuclei electron density surrounding the nucleus. Therefore, in highly symmetric materials (e.g., featuring cubic symmetry) or isotropic liquids, the EFG and quadrupolar interaction are vanishing components. The quadrupolar interaction is anisotropic, and described by two parameters:

2.4 Nuclear Magnetic Resonance

- The quadrupolar coupling constant (C_Q) which quantifies its magnitude in MHz, and is defined as

$$C_Q = eQV_{ZZ}/h \quad (2.12)$$

Where h is Planck's constant.

- The asymmetry parameter of the EFG tensor, which value lies between 0 and 1, describing the signal shape and is defined as

$$\eta_Q = (V_{XX} - V_{YY})/V_{ZZ} \quad (2.13)$$

The value of the C_Q varies from a few Hz to hundreds of MHz depending on the nucleus and material being studied. Typically in NMR experiments, the quadrupolar interaction is considered a perturbation of the Zeeman interaction, which is usually the dominant effect. The perturbation can be divided into two perturbation terms: first-order and second-order. Figure 2.7 shows the Zeeman-only energy levels for nuclei with spin $5/2$, along with both first and second order perturbations.

The first-order quadrupolar effect splits the NMR signal into $2I$ allowed transitions and shifts the energy levels. The first-order quadrupolar splitting also depends on the crystal orientation and hence, NMR spectra of quadrupolar nuclei in powder are broadened by quadrupolar interaction. In half-integer quadrupolar nuclei, the central transition (CT) occurs between the $m_I = +\frac{1}{2}$ and $m_I = -\frac{1}{2}$ levels, while the satellite transitions (ST) occur between the energy levels m_{I+1} and $m_I \neq -1/2$. The resonance frequency of the STs depends on both orders of the quadrupolar interaction. The strength of the first order interaction typically exceeds the magic angle spinning (MAS) frequency, meaning that this interaction cannot be removed by MAS alone. As a result, several spinning sidebands caused by the STs are present in the spectrum. However,

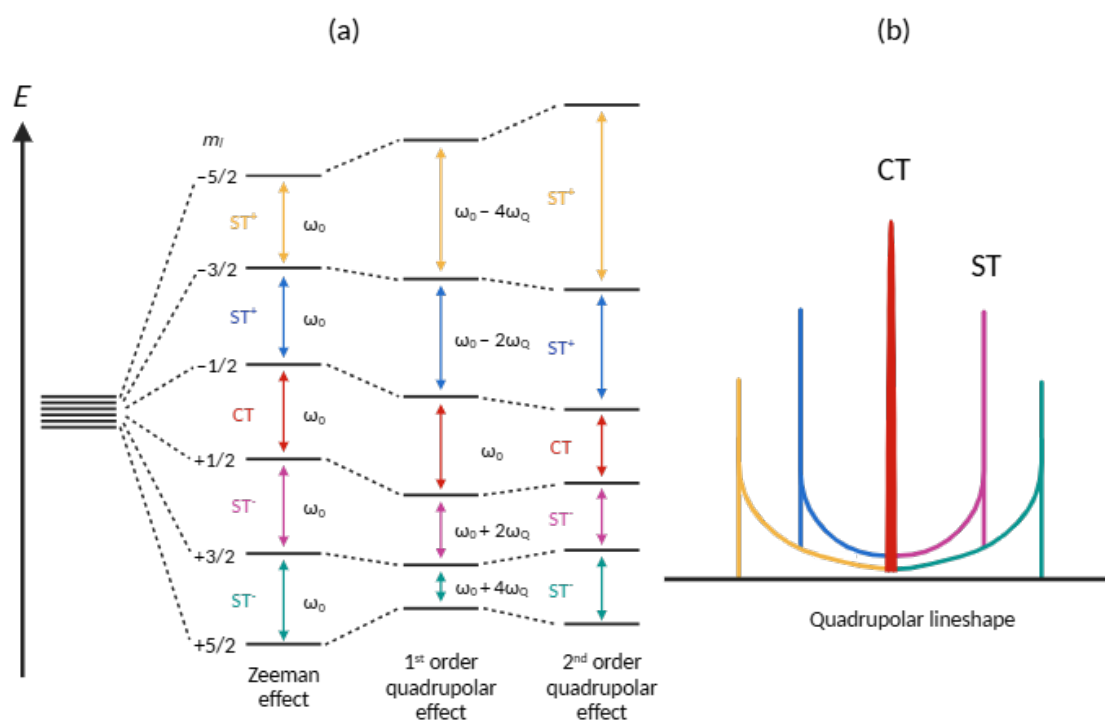


Figure 2.7 Diagram displaying the effect of quadrupolar splitting for an $I = 5/2$ nucleus upon application of a magnetic field. Along with a schematic showing the central and satellite transitions forming the quadrupolar lineshape.

2.5 Nuclear Quadrupole Resonance

the CT remains unaffected by first-order quadrupolar interaction and can be the only transition observed in the spectrum at this stage.

All the transitions are further shifted by the second-order quadrupolar interaction, including the CT. The second-order quadrupolar interaction depends on the crystallite orientation. As the angular dependence of the second-order quadrupolar interaction is more complex than those of other anisotropic interactions, MAS technique does not fully average out the second-order quadrupolar interaction. Furthermore, the signal broadening that occurs is inversely proportional to the strength of the magnetic field. So in most cases, spectral resolution can be improved at higher magnetic fields.

For certain nuclei, however, the C_Q is so large that the CT cannot be easily detected even at high magnetic fields. In such cases, NMR may not be the most appropriate technique to study these nuclei.

2.5 Nuclear Quadrupole Resonance

2.5.1 General background of NQR

Nuclear Quadrupole Resonance (NQR) represents a solid-state radio frequency technique, first introduced by Dehmelt and Kruger in 1949.[10] This method is specifically tailored for the examination of nuclei with spins $I > 1/2$. While NQR bears certain resemblances to its counterpart, NMR, it distinguishes itself by embracing the quadrupolar interaction, a factor that often contributes to line broadening in certain NMR experiments. In the case of NQR, however, this interaction is leveraged to advantage, as it enables transitions to occur autonomously, eliminating the need for an external magnetic field.[11] NQR has found widespread applications across various

2.5 Nuclear Quadrupole Resonance

fields, including chemistry, physics, and materials science. It serves as a valuable tool for investigating the properties of materials and molecules containing quadrupolar nuclei. One prominent application is in the study of compounds containing nitrogen-14, a nucleus abundant in most explosive, toxic, or narcotic substances. Nitrogen-14 boasts a natural abundance of 99.63% and possesses a spin equal to 1, making it an ideal candidate for NQR investigations.

NQR is characterised by its exceptional specificity, owing to the pronounced influence of a material's crystal structure on its resonance frequencies, as opposed to being closely aligned with the Larmor frequency unique to individual nuclei. This distinctive feature enables the NQR signal to function as a distinct "fingerprint" for each substance it encounters. Consequently, it becomes possible to measure and compile numerous substance standards into a comprehensive database, serving as a valuable point of reference when analysing unknown samples. This database, encompassing thousands of substances, greatly enhances the precision and reliability of NQR in the identification of unknown materials.[12] In theory, NQR has the potential to analyse any quadrupolar nuclei within solid powders or crystalline substances, thus opening up a wide range of applications. This versatility extends beyond its well known applications in screening for illegal substances and conducting pharmaceutical analyses, showcasing the extensive utility of NQR in various applications.

2.5.2 Basic NQR Theory

The major difference between NMR and NQR is when it comes to inducing the splitting of the spin energy states, as demonstrated schematically by Figure 2.8. For NMR, it is the Zeeman interaction that causes different spin energies with the application of an external magnetic field. However, NQR does not require the application of an

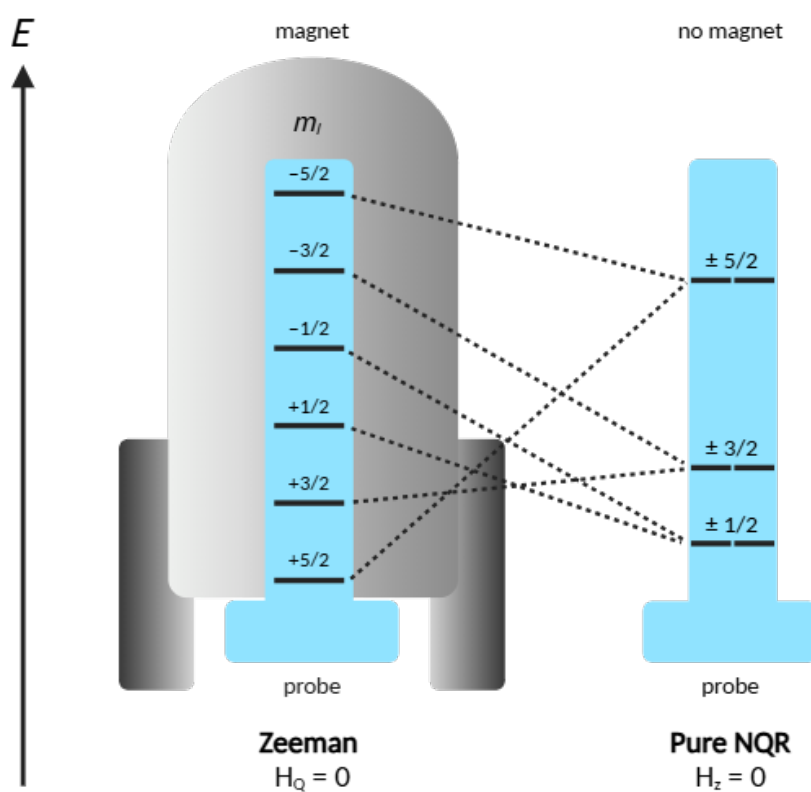


Figure 2.8 Energy level splitting and allowed transitions for a spin-5/2 nucleus in NQR. The six m_I sublevels ($\pm 5/2, \pm 3/2, \pm 1/2$) are split by quadrupolar interactions. Dashed lines indicate allowed transitions ($\Delta m_I = \pm 1$), corresponding to measurable NQR frequencies.

2.5 Nuclear Quadrupole Resonance

external magnetic field due to the EFG at the quadrupolar nucleus being sufficient enough to split the spin states. Both NMR and NQR are equally sensitive to changes in quadrupolar interaction and so the structural and dynamic information provided by the EFG is the same for both techniques. The quadrupolar parameters C_Q and η_Q , which are defined above as parameterising the EFG, can fairly simply be deduced from the lineshape of an NMR spectrum, although it usually involves lineshape simulations to do so. In NQR it is the resonance frequency values that carry this information on the quadrupolar parameters. For $I = 1$, the NQR frequencies are given by the analytical expressions below.

$$\nu_{\pm} = \frac{3}{4}C_Q\left(1 \pm \frac{\eta_Q}{3}\right) \quad (2.14)$$

$$\omega_0 = \frac{1}{2}C_Q\eta_Q \quad (2.15)$$

Whereas spin-3/2 nuclei exhibit a single transition at

$$\nu = \frac{C_Q}{2}\left(1 + \eta_Q^{\frac{2}{3}}\right)^{\frac{1}{2}} \quad (2.16)$$

However for spin $I > 3/2$, the transition frequencies cannot be expressed in a closed-form analytical expression.[13] With all except $I = 3/2$ nuclei, the C_Q and η_Q parameters can be determined experimentally from the measurement of at least two resonance frequencies. QUEST software has shown to be very useful when doing just this.[14]

In the simplest NQR experiment, a sample is placed in a static probe outside of a magnet, and a radio frequency pulse is applied to the sample. If the frequency of the pulse matches the NQR frequency of the studied material, the nuclei with a quadrupolar moment will undergo a transition to a higher energy state. This transition

is detected by measuring the emitted signal as the nuclei return to their lower energy state. The frequency of this emitted signal corresponds to the quadrupole resonance frequency and provides information about the local environment of the atomic nuclei.

2.5.3 Further complexities in NQR detection

In the realm of perovskite research, the application of halide NQR has gained increasing popularity. This is primarily because all halides exhibit quadrupolar nuclei characteristics with relatively large C_Q values, which causes the issue of MHz wide signal broadening often encountered in halide NMR spectroscopy.

Halide NQR serves as a powerful tool for gaining deeper insights into halide distribution and bonding within perovskite materials, particularly for researcher focused in multi-halide doping for phase stabilisation purposes.[15–17] Additionally, it complements temperature-dependent structural phase identification due to the resonance frequencies' sensitivity to temperature variations.[18, 19] As a result, this method can be seamlessly integrated with other structural characterisation techniques such as diffraction, facilitating a comprehensive understanding of perovskite materials' properties and behavior.

However, it is essential to acknowledge that NQR experiments introduce a layer of complexity. This complexity arises from the need to search for specific resonance frequencies, and even minor alterations in the crystal structure can result in significant shifts in the transition frequency for NQR. Additionally, the resonance frequencies exhibit temperature dependency, requiring careful consideration to ensure the proper excitation of substances. To mitigate these challenges, researchers often employ precise temperature monitoring and control as an experimental compensation method.

2.5 Nuclear Quadrupole Resonance

In cases where prior information about carrier frequencies for a new material is unavailable and necessitates experimental determination, researchers may find themselves searching over a range spanning hundreds of megahertz, whereas the pulse excitation bandwidth is typically limited to hundreds of kilohertz, akin to searching for a pearl in the ocean. Furthermore, NQR experiments may contend with a low signal-to-noise (SNR) ratio, particularly when the response amplitude falls below the thermal noise level of electronic components. This susceptibility to low SNR makes the substance's response vulnerable to radio frequency interference, as well as piezoelectric and magneto-acoustic ringing caused by the presence of piezoelectric materials or metals within the sample.

References

- [1] V. Garcia Sakai, *Quasi-Elastic Neutron Scattering*, ISIS, 13th Oxford School of Neutron Scattering, 2-13 September 2013, Retrieved from: <https://www.oxfordneutronschool.org/2013/Lectures/GarciaSakai-QENS.pdf>, 2013.
- [2] M. T. Dove, *Structure and Dynamics: An Atomic View of Materials*, Oxford University Press, 2013.
- [3] R. A. Young, *International union of crystallography*, 1993, **5**, 1–39.
- [4] *Inorganic Crystal Structure Database (ICSD)*, *Physical Sciences Data Science Service*, www.psds.ac.uk/icsd.
- [5] M. Bee, *Quasielastic Neutron Scattering, Principles and Applications in Solid State Chemistry, Biology and Materials Science*, CRC Press, 1988.
- [6] National Institute of Standards and Technology (NIST), *X-Ray Form Factor, Attenuation, and Scattering Tables*, Accessed: 2024-08-20, 2024.
- [7] J. J. Keeler, *Understanding NMR Spectroscopy*, Wiley, 2012.
- [8] P. J. Hore, *Nuclear Magnetic Resonance*, Oxford University Press, 2015.
- [9] B. C. Sanctuary and M. S. Krishnan, *Z. Naturforsch. A*, 1994, **49**, 71–79.
- [10] H. G. Dehmelt and H. Krüger, *Naturwissenschaften*, 1950, **37**, 111–112.
- [11] T. Das and E. Hahn, *Nuclear Quadrupole Resonance Spectroscopy*, Springer, 1958.
- [12] L. Cardona, J. Jiménez and N. Vanegas, *Ingeniare. Revista chilena de ingeniería*, 2015, **23**, 458–472.
- [13] G. K. Semin, *Russ. J. Phys. Chem.*, 2007, **81**, 38–46.
- [14] F. A. Perras, C. M. Widdifield and D. L. Bryce, *Solid State Nucl. Magn. Reson.*, 2012, **45–46**, 36–44.
- [15] T. A. Doherty, S. Nagane, D. J. Kubicki and et al., *Science*, 2021, **374**, 1598–1605.
- [16] M. Aebli, N. Porenta, N. Aregger and M. V. Kovalenko, *Chem. Mat.*, 2021, **33**, 6965–6973.

- [17] L. Piveteau, M. Aebli, N. Yazdani and et al., *ACS Cent. Sci.*, 2020, **6**, 1138–1149.
- [18] K. Yamada, S. Hino, S. Hirose and et al., *Bull. Chem. Soc. Jpn.*, 2018, **91**, 1196–1204.
- [19] A. Senocrate, I. Moudrakovski, G. Y. Kim and et al., *Angew. Chem. Int. Ed.*, 2017, **129**, 7863–7867.

Chapter 3

Probing the Influence of Post-Synthetic Treatments on MAPI Structures through Scattering and Diffraction Techniques

3.1 Introduction

In recent years, hybrid organic-inorganic perovskites, particularly methylammonium lead iodide (MAPI) have gained significant attention in the field of photovoltaics due to their remarkable optoelectronic properties. MAPI exhibits a bandgap located between 1.5 and 1.6 eV which is close to the optimum value predicted by the Shockley-Queisser

limit for single-junction solar cells [1]. According to this theoretical limit, the maximum efficiency for a material with a bandgap of approximately 1.4 eV is around 33.7%. In comparison, MAPI achieves power conversion efficiencies (PCE) in the range of 30% to 32%, demonstrating its potential as a competitive material for solar energy conversion [2]. Additionally, the high absorption coefficient of MAPI, with just 280 nm of the material capable of absorbing approximately 80% of incident sunlight below the bandgap, further solidifies its candidacy for use in highly efficient thin-film solar cells [3]. These qualities highlight the promise of the material for advancing the development of next-generation photovoltaic devices, necessitating a deeper understanding of its physical and chemical properties, both from practical and fundamental perspectives.

To harness the full potential of hybrid perovskites, particularly MAPI, and enable them to compete effectively with traditional silicon-based solar cells, much of the research has focused on optimising thin-film fabrication techniques. The efficiency and performance of perovskite solar cells are highly dependent on the quality of the thin films, as the morphology, crystallinity, and grain size of the films directly influence charge transport, defect density, and overall PCE [4–6]. Thus, the method of thin film deposition and the post-deposition treatments, particularly thermal annealing, play pivotal roles in determining the final device efficiency. Understanding the interplay between these techniques is essential for optimising the fabrication process, especially as PSCs move from small-area lab devices toward large-scale production [4, 7, 8].

Several deposition methods are available for the scalable production of perovskite thin films, each offering distinct advantages and limitations. These methods differ in how they control the nucleation and growth of perovskite crystals, which in turn impacts the uniformity, grain size, and defect density of the thin film — key factors influencing the photovoltaic performance of PSCs [4, 9]. A few of these methods are

briefly discussed below.

3.1.1 Thin Film Deposition

Spin coating is commonly employed for lab-scale perovskite solar cells, where a precursor solution is deposited onto a spinning substrate to create uniform films. This technique allows precise control over film thickness and has achieved record PCEs exceeding 25% for small-area devices [10]. However, its scalability is limited, as maintaining uniformity in large-area films can lead to efficiency losses.

To enhance crystallisation, anti-solvent techniques have been introduced. This involves drenching the perovskite precursor film with a non-polar solvent, like chlorobenzene, to promote rapid nucleation and crystallisation. While the use of anti-solvent is effective for producing dense, homogeneous films in small devices, scaling this method for larger areas remains a challenge, although variations such as anti-solvent bathing show promise for larger-scale applications [8, 11].

Hot casting is another method that involves heating the substrate or precursor solution during deposition to accelerate solvent evaporation and facilitate uniform crystal growth. This technique can yield films with larger grains, reducing defect density and improving charge transport. However, the high temperatures required can volatilise the organic components, potentially introducing defects that compromise long-term stability. Despite these issues, hot casting has achieved PCEs above 20% in large-area PSCs [12].

3.1.2 Role of Thermal Annealing

Regardless of the deposition technique used, thermal annealing is a critical post-deposition treatment that significantly influences the quality of perovskite thin films [6]. During annealing, the perovskite precursor undergoes crystallisation, with grain size and morphology being controlled by the rate of solvent evaporation and the temperature of the process [5].

In traditional thermal annealing, moderate temperatures (around 100 °C) are applied for up to an hour to promote crystallisation and grain growth. Fast solvent evaporation during this process increases supersaturation, leading to rapid nucleation [8]. While this can result in smaller grains, extended annealing times can trigger Ostwald ripening, where smaller grains dissolve and redeposit onto larger grains, thus increasing grain size and improving film quality. However, prolonged annealing can lead to the degradation of volatile organic components in perovskites, reducing film stability [9]. Solvent-assisted annealing is a variation where solvent vapors, such as DMF or alcohol, are introduced around the film during the annealing process. This technique encourages larger grains and improves film uniformity by allowing the precursor components to diffuse more effectively [11]. The slow evaporation of solvent in a controlled environment promotes uniform crystallisation, reducing defects such as pinholes. However, careful control of the solvent environment is required, as excessive solvent exposure can damage the film or result in incomplete crystallisation. Vacuum-assisted thermal annealing combines the benefits of rapid solvent removal and controlled crystallisation. By placing the wet film under vacuum, solvent is rapidly extracted, leading to fast supersaturation and uniform crystal growth. This method has been shown to produce pinhole-free, smooth films with excellent surface coverage [10]. Moreover, vacuum-assisted annealing at low temperatures helps maintain the stability

of the perovskite, making it an attractive option for large-scale PSC production [13].

3.1.3 Addressing Inconsistencies in Annealing Parameters for Optimal Perovskite Performance

The interplay between deposition techniques and thermal annealing processes is crucial in determining the quality of perovskite thin films, which directly affects the photovoltaic performance of perovskite solar cells. High-quality films characterised by larger grain sizes and fewer defects exhibit enhanced charge carrier mobility, reduced recombination losses, and improved overall efficiency [10]. Optimising annealing in conjunction with deposition methods is essential for achieving films with uniform morphology.

Table 3.1 Comparing the reported PCE’s and thermal treatment undertaken for several different studies of MAPI. Solvents are GBL (γ -butyrolactone), DMF (dimethylformamide), and DMSO (dimethyl sulfoxide).

Annealing Temperature (°C)	Time (min)	Annealing Environment	PCE (%)	Ref.
150	0, 30, 60, 90, 120	Air	0.66, 6.64, 12.0, 10.59, 7.17	[14]
45, 65, 85	720	O ₂	9.2, 12.0, 8.6	[15]
60 - 100	Not Specified	Vacuum	14.5	[16]
105, 115, 125	45	N ₂	6.7, 10.7, 8.5	[17]
100	30	N ₂ , H ₂ O, GBL, DMF, DMSO	7.39, 7.50, 11.50, 10.47, 11.89	[18]

Despite the recognised importance of thermal annealing, many studies fail to adequately control the environmental conditions during this process, resulting in inconsistencies and non-reproducible results. Numerous investigations have examined the effects of annealing on perovskite thin films, focusing on parameters such as temperature, duration, and atmosphere. However, a significant gap in the literature exists concerning the arbitrary selection of these parameters. Often, fixed annealing

temperatures and durations are employed with little explanation, despite their profound impact on device performance. For instance, the doctoral thesis by Jake Minns presents a comparative study on the effects of annealing on the ferroelectric properties of MAPI, highlighting the critical need for optimising these conditions [19]. Furthermore, discrepancies in the literature, with reported annealing temperatures ranging from 45 to 150 °C and durations from 0 to 720 min, complicate comparisons of average PCE across different studies. This lack of consistency and insufficient justification for the chosen parameters raise serious concerns regarding the reproducibility and reliability of the reported results in perovskite solar cell research.

3.1.4 Purpose of this Chapter

Building on the foundational work conducted by our research group at the University of Kent, this chapter aims to further investigate the effects of post-synthetic annealing treatments on the structural, dynamic, and optoelectronic properties of MAPI. This exploration will be achieved through a combination of scattering and diffraction techniques, enabling a comprehensive understanding of how these treatments influence the material's characteristics and performance.

3.2 Experimental

3.2.1 Precursor Synthesis

The precursor material methylammonium iodide ($\text{CH}_3\text{NH}_3\text{I}$ or MAI) was used in all sample preparation methods for the synthesis of $\text{CH}_3\text{NH}_3\text{PbI}_3$. To begin a dropwise

addition of hydroiodic acid (57 wt% in water, Sigma Aldrich) was added into an equimolar amount of methylamine (40% in methanol, Sigma Aldrich) in a flask with constant stirring that was cooled to 0 °C in a water-ice bath. Stirring was continued for around an hour after addition to ensure mixing and gas evolution was complete, leaving a pale yellow solution. The solvent was then evaporated by placing the flask of solution in a bead bath at 80 °C over several days. The resulting precipitate was recovered and purified by washing in diethyl ether (anhydrous 99.0%, Sigma Aldrich) and filtered using a vacuum filtration system and left to dry white crystals of $\text{CH}_3\text{NH}_3\text{I}$.

3.2.2 Solution Synthesis of $\text{CH}_3\text{NH}_3\text{PbI}_3$

This synthesis was adapted from that reported in the literature [20]. The rapid precipitation of $\text{CH}_3\text{NH}_3\text{PbI}_3$ from solution starts with dissolving PbO powder (5 mmol) in a boiling solution of hydroiodic acid (38 mmol) and phosphoric acid (7.75 mmol) while magnetic stirring for 5 minutes, the result is a bright yellow liquid. The precursor MAI (5 mmol) is then added to the solution, immediately precipitating a black powder. The stirring is then stopped and the solution is left to cool down to ambient temperature resulting in a black crystalline powder. The precipitate was filtered using a vacuum filtration system and left to dry the black powder of $\text{CH}_3\text{NH}_3\text{PbI}_3$.

3.2.3 Solution Synthesis of NH_4PbI_3

Precipitation of NH_4PbI_3 began with the dissolution of PbO powder (5 mmol) in a boiling solution of hydroiodic acid (38 mmol) and phosphoric acid (7.75 mmol) while magnetic stirring for 5 minutes, the resulting in a bright yellow liquid. NH_4I (5 mmol) was dissolved into the solution with stirring which allowed for the precipitation of a

yellow precipitate. The precipitate filtered using a vacuum filtration system and left to dry in a vacuum oven overnight, producing a yellow powder of NH_4PbI_3 .

3.2.4 Quasi Elastic Neutron Scattering Measurements

The Quasi-Elastic Neutron Scattering (QENS) experiments were conducted using the OSIRIS high flux time-of-flight spectrometer at the ISIS pulsed neutron and muon source, Rutherford Appleton Laboratory, UK. In this setup, the energy of the scattered neutrons is analysed via Bragg scattering with a PG002 crystal analyser array, which has an effective energy of 1.84 meV. The instrument was configured to measure energy transfers in the range of -0.55 to 0.55 meV, with a resolution of 25.4 meV, representing the minimum detectable full width at half maximum (FWHM). The momentum transfer range investigated spans from 0.18 to 1.8 \AA^{-1} . Samples were subjected to temperatures ranging from 7 to 400 K.

High-statistics measurements (300 mAh) were conducted at temperatures of 7, 100, 160, 220, 270, 285, 300, and 365 K. This strategy was implemented to ensure reliable data for investigating the dynamics of the MA^+ cation, taking into account that additional time is necessary to stabilise the temperature within the cryostat for each measurement. The data was fitted using the Mantid software, [21, 22] in a similar manner to that reported in [23].

3.2.5 Synchrotron Powder Diffraction

For most bulk powder data collection, the in-house X'pert3 PANalytical diffractometer was used. This spectrometer uses Bragg-Brentano setup and operates in Reflection-Transmission mode, with a Cu source operating at 40 kV and 40 mA, measuring $K_{\alpha 1} =$

3.3 Probing cation dynamics with Quasi-elastic Neutron Scattering

1.5405 Å and $K_{\alpha 2} = 1.5444$ Å. Phase identification was performed utilising the Malvern Panalytical Highscore software which allowed comparison of patterns to structural databases. Rietveld refinement was performed using the Fullprof software suite.

Variable temperature powder synchrotron X-ray diffraction experiments were conducted at both the ESRF and Diamond facilities.

Synchrotron X-ray powder diffraction data was collected at the High Resolution Powder Diffraction beamline I11 at Diamond Light Source, UK [24]. The energy was specified as 15 keV, with the wavelength calculated to be $\lambda = 0.826870$ Å (15.0 keV) and the angular zero-error to be $+ 0.002003^\circ$ in 2θ by using a NIST silicon standard. Samples were loaded into borosilicate capillaries of diameter 0.5 mm, and analysed by Debye-Sherrer geometry using a multi-analyser crystal (MAC) diffractometer.

At the Swiss Norwegian Beamline (SNBL), the PILATUS@SNBL based single-crystal diffractometer (see figure 3.1) was used with a focusing double-crystal Si(111) monochromator [25]. Unless otherwise stated, an X-ray wavelength of $\lambda = 0.64114$ Å was used for all measurements. An Oxford Cryostream 700+ nitrogen blower was used at both facilities to maintain experimental temperatures between 80 K and 500 K.

3.3 Probing cation dynamics with Quasi-elastic Neutron Scattering

Continuing from the previous work conducted within our research group, which focused on two developed post-synthetic treatments and associated diffraction measurements as outlined in references [19] and [26], this study further investigates the dynamics of MA^+ ions within the crystal lattice of MAPI using Quasi-Elastic Neutron Scattering

3.3 Probing cation dynamics with Quasi-elastic Neutron Scattering

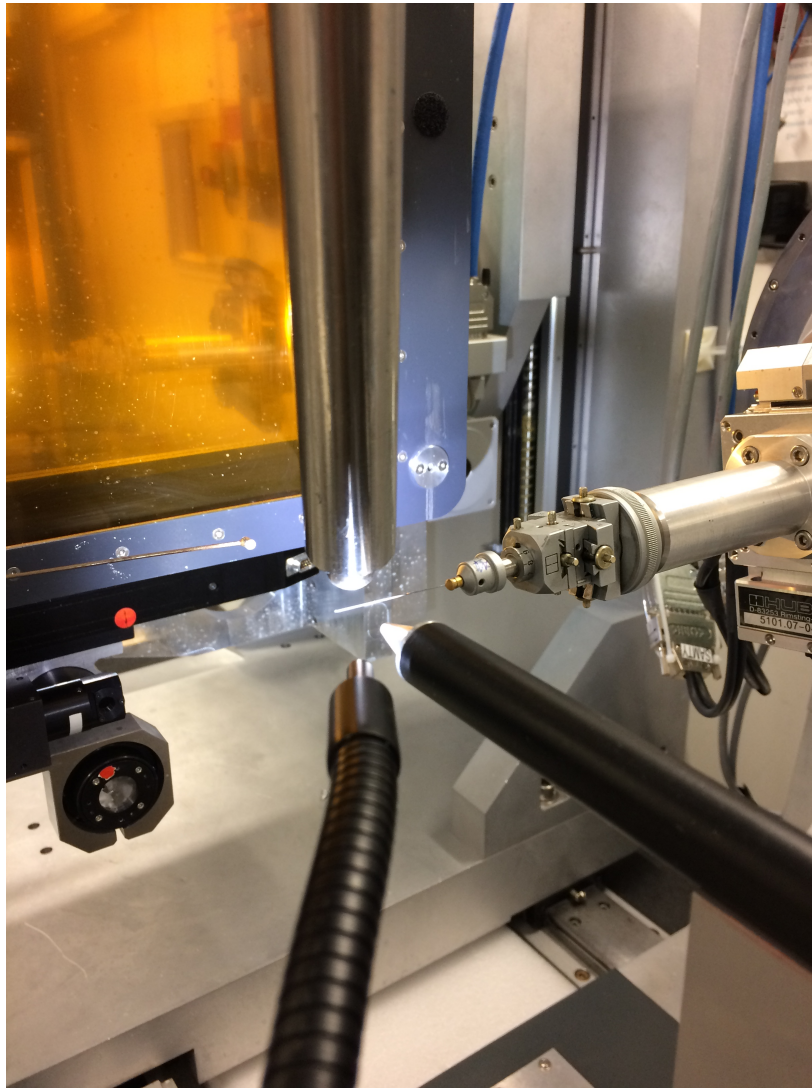


Figure 3.1 Photograph of the SNBL based diffractometer during a powder diffraction experiment. Photo captured by Dr Charlie McMonagle for purpose of this thesis.

3.3 Probing cation dynamics with Quasi-elastic Neutron Scattering

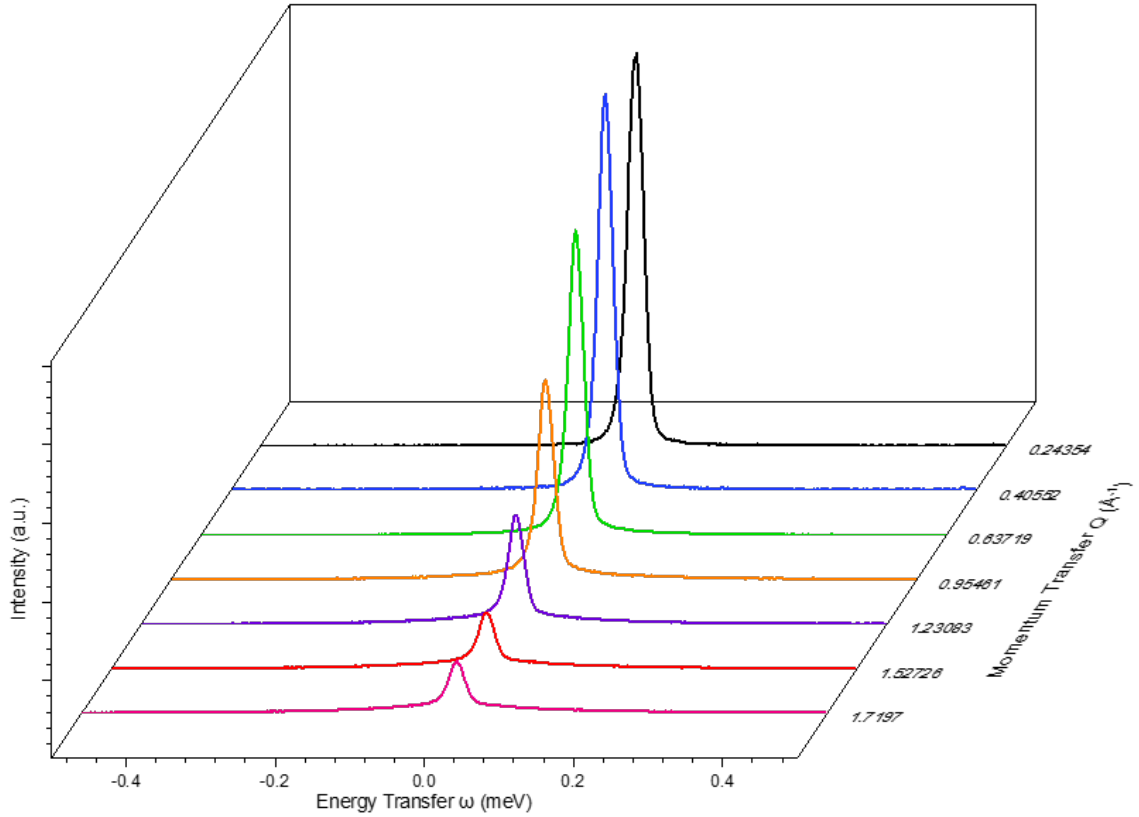


Figure 3.2 Representative QENS measurements of pristine MAPI indicating scattering intensity against energy transfer ω (meV) measured at 270 K plotted for groups of 7 detectors corresponding to different momentum transfers, Q . Values are 0.24354, 0.40552, 0.63719, 0.95461, 1.23083, 1.52726, and 1.7197 \AA^{-1} .

(QENS). The samples for this investigation were synthesised at the University of Kent by Rhianna Day, and the measurements were performed by Dr. Jake Minns using the high-flux time-of-flight spectrometer OSIRIS at the ISIS pulsed neutron source, Rutherford Appleton Laboratory, UK.

The incident energy of the instrument was configured to measure energy transfers ranging from -0.55 to 0.55 meV, achieving a resolution of $25.4 \mu\text{eV}$, which corresponds to the minimum detectable full width at half maximum (FWHM). The full Q -range examined varied from 0.18 to 1.8\AA^{-1} as depicted in Figure 3.2, while the sample temperature was systematically increased from 100 to 400 K. This comprehensive

3.3 Probing cation dynamics with Quasi-elastic Neutron Scattering

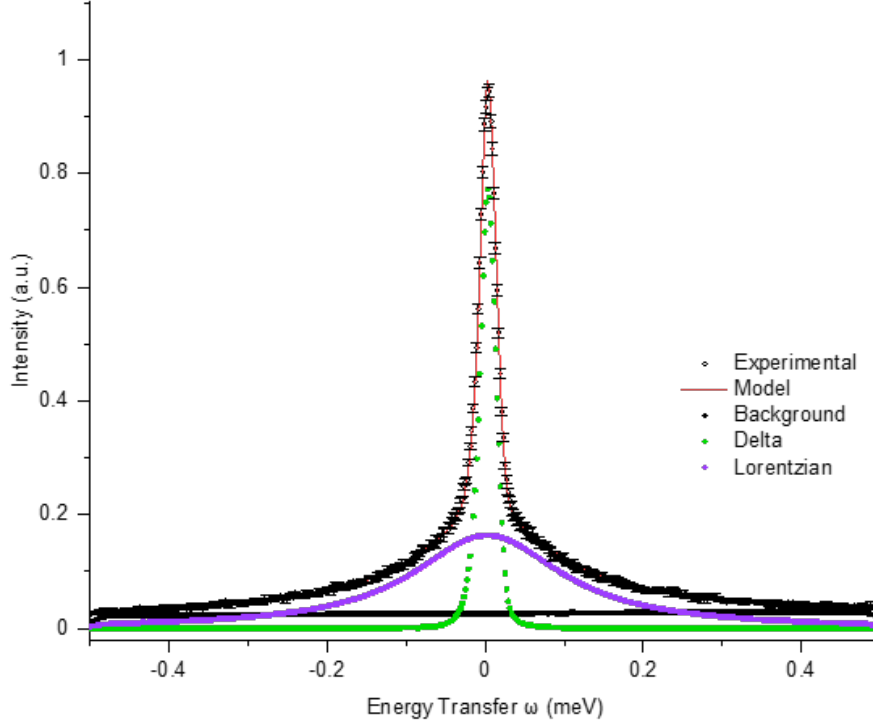


Figure 3.3 Representative QENS spectrum of pristine MAPI corresponding to $Q = 1.72 \text{ \AA}^{-1}$ measured at 270 K. Experimental data are represented by hollow circles with associated error bars. The solid red curve corresponds to the fit of $S(Q, \omega)$ model. The elastic part is simulated with a delta function (green) and the quasielastic part is simulated with a single Lorentzian function (purple).

approach enables a detailed understanding of the dynamic behavior of MA^+ ions and their influence on the properties of MAPI.

The three samples measured in this study included untreated/pristine MAPI (UT), vacuum-annealed MAPI (VAC), and MAPI exposed to iodine partial pressure (I_2). Illustrative quasielastic scattering spectra for the UT sample is presented in Figure 3.2, showing the scattered intensity as a function of energy transfer (ω) to or from the neutron beam, which is a result of the movement of hydrogen nuclei. The spectra are plotted for various momentum transfer (Q) values, which are determined by the

3.3 Probing cation dynamics with Quasi-elastic Neutron Scattering

scattering angle. Figure 3.3 illustrates the fitting process applied to each dataset of all studied samples, where the scattering function is modeled by an elastic peak (represented as a delta function) convolved with the instrument resolution function. Additionally, a single Lorentzian function is used to denote the quasielastic broadening associated with the dynamics of the MA^+ ions. For each sample environment, the FWHM of each Lorentzian was extracted and plotted against Q^2 across the temperature range, as shown in Figures 3.4, 3.5, and 3.6. Data collected at low temperature (100 K) were excluded from the analysis due to difficulties in establishing a suitable model for the quasielastic scattering observed at that temperature. This challenge is likely due to the pronounced change in the dynamics of MAPI below 160 K, where a phase transition occurs, shifting the structure to the orthorhombic phase. This transition reduces the rotational cavity within the ionic lattice, slowing down the motion of the MA^+ cation [27]. Unlike the gradual increase in cationic dynamics seen in the transition from tetragonal to cubic phases—where the cationic cavity expands, allowing more rotational freedom—the shift to the orthorhombic phase involves a more abrupt restriction of MA^+ dynamics, which complicates the fitting process. Similar difficulties in analysing these low-temperature dynamics have been reported in previous studies [23].

Figure 3.4 illustrates that for untreated (UT) MAPI, the width of the Lorentzians remains approximately invariant with Q^2 at low temperatures (160 – 220 K). When compared with similar studies from literature, [23], this observation suggests that localised motions are occurring, indicating that the MA^+ cation is becoming ordered as UT MAPI transitions between the orthorhombic and tetragonal phases at these temperatures.

As the temperature is increased to the range of 280 – 300 K, the Lorentzian widths

3.3 Probing cation dynamics with Quasi-elastic Neutron Scattering

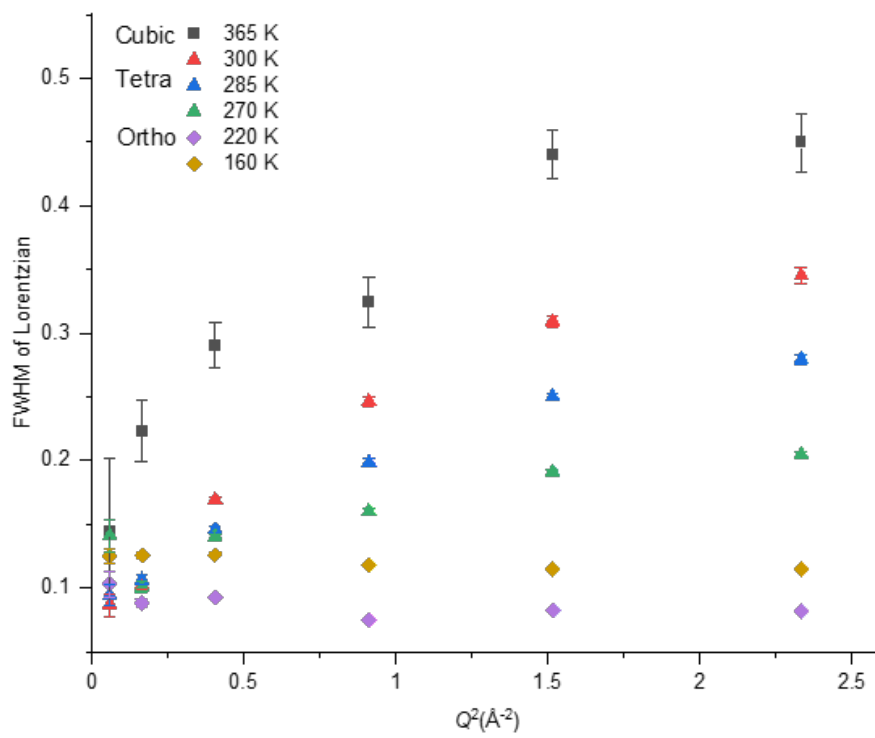


Figure 3.4 FWHM of Lorentzian *vs.* momentum transfer (Q^2) for QENS data ranging from 365 to 160 K for pristine MAPI.

3.3 Probing cation dynamics with Quasi-elastic Neutron Scattering

begin to exhibit a dependence on Q^2 , implying that the MA^+ cation is becoming more disordered within the tetragonal phase. By 365 K, the FWHM shows a significant dependence on Q^2 , with broader Lorentzians appearing as Q^2 increases. This behaviour indicates a diffusive-like motion of the MA^+ cation in the cubic phase.

Overall, these results demonstrate observable changes in the dynamics of the MA^+ cation that correlate with the three transition phases of UT MAPI and highlight the intricate relationship between the cationic motion and the structural transitions in MAPI.

Specifically, the transition from the tetragonal to cubic phases is associated with a gradual increase in the cation's mobility, while the orthorhombic phase imposes restrictions on its motion. However, the findings for untreated MAPI contrast with previous studies [23], which suggest that localised motions in the orthorhombic and tetragonal phases are not consistent with the expected diffusive dynamics observed in the cubic phase. This discrepancy is particularly surprising, as it is generally anticipated that in the high-temperature cubic phase, the cation's rotational cavity expands, allowing for less restricted motion. Moreover, at elevated temperatures, the system gains additional energy, which typically promotes more diffusive cation motions, as seen in other QENS literature [28–30]. These inconsistencies highlight the complexity of cation dynamics in halide perovskites and point to the need for further investigation to reconcile the differing interpretations of these behaviours, particularly in relation to the original method of material preparation. This aspect seems to have a significant effect on the results obtained for MAPI, especially at elevated temperatures, as indicated in a variety of studies.

When comparing the temperature dependence of Lorentzian widths for untreated (UT) and vacuum-annealed (VAC) MAPI samples, as shown in Figure 3.5, it is observed

3.3 Probing cation dynamics with Quasi-elastic Neutron Scattering

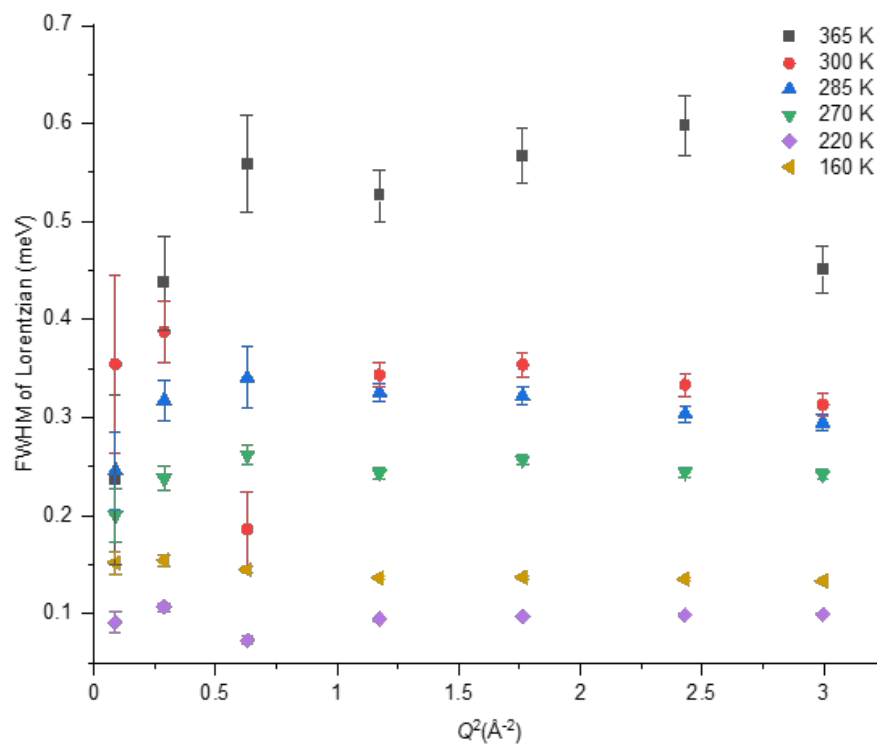


Figure 3.5 FWHM of Lorentzian vs Q for QENS data ranging from 365 to 160 K for vacuum-annealed MAPI.

3.3 Probing cation dynamics with Quasi-elastic Neutron Scattering

that for the VAC sample, the FWHM remains approximately constant from 160 K to 300 K, except for an anomalous value at $Q^2 \approx 0.6 \text{ \AA}^{-2}$ at 300 K. This anomaly is likely due to the significant contribution of elastic scattering at low Q^2 values, which can overlap with the quasielastic signal. Such overlap complicates the accurate separation of quasielastic broadening from the strong elastic peak, resulting in larger uncertainties in the fit and, consequently, larger error bars. Furthermore, at lower Q^2 values, the system probes more complex collective motions, which produce broader and more diffuse features, adding to the challenges in fitting and increasing the uncertainty in the quasi-elastic width.

Similarly, for the iodine-treated (I_2) sample, as shown in Figure 3.6, the FWHM remains independent of Q^2 across the entire temperature range, suggesting that the MA^+ cation remains in an ordered state and undergoes localised motions, akin to those observed in untreated MAPI during the orthorhombic phase. These results indicate that annealing in the presence of iodine significantly modifies the behaviour of the cation over a range of temperatures.

At 365 K, the MA^+ cation in the I_2 sample exhibits behaviour that deviates slightly from the UT sample, showing less diffusive motion at high temperatures and a slight dependence of the FWHM on Q^2 . This is accompanied by increased error bars in the fit, which can be attributed to the faster atomic and molecular motions at elevated temperatures. The increased motion leads to broader quasielastic peaks, making precise fitting and characterisation of the quasielastic width more difficult.

The QENS data analysis provides strong evidence that post-synthetic treatments, such as vacuum annealing and iodine exposure, have a profound impact on the structural properties of MAPI. These treatments lead to significant changes in the dynamics and structural behaviour of the material, influencing the organisation and motion of the

3.3 Probing cation dynamics with Quasi-elastic Neutron Scattering

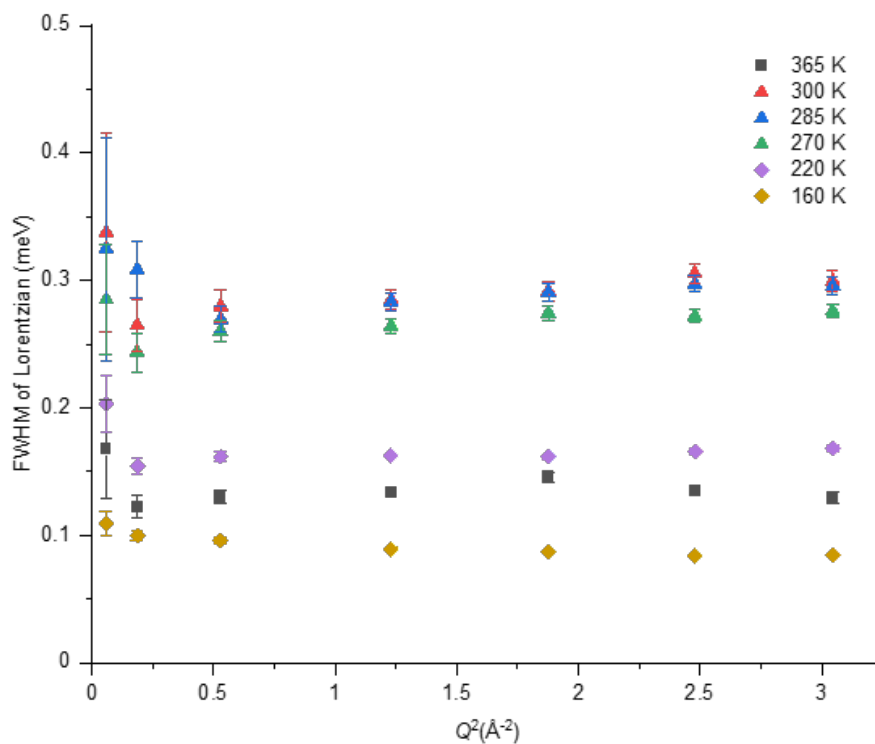


Figure 3.6 FWHM of Lorentzian vs Q for QENS data ranging from 365 to 160 K for MAPI exposed to I_2 vapour in the post-synthetic annealing treatment.

molecular components within the framework. As a result, the behaviour of the MA^+ cation within the crystal lattice is notably altered, suggesting that such treatments could be used to tailor the optoelectronic properties of MAPI for various applications.

3.4 Optimising Vacuum Annealing through Variable Temperature and Time

3.4.1 Purpose of this study

This study extends the research previously reported by our group by systematically investigating the relationship between annealing conditions—specifically temperature and annealing time—and the resulting structural changes, as measured through diffraction techniques. By further investigating and refining the understanding of the annealing process, the aim is to identify optimal and reproducible conditions. A follow-up investigation into the temperature effects of vacuum annealing on MAPI was conducted to compare the results with previous studies from the group. To explore the impact of high-temperature vacuum annealing on this prototypical perovskite material, pristine MAPI was synthesised using the low-temperature solution-based method described in Section 3.2.2 and the vacuum annealing treatment was performed post-synthesis.

For the initial phase of the study, each sealed tube was positioned in the center of a furnace and subjected to annealing for 1 hour and 30 minutes at temperatures ranging from 280 to 360 °C. Each sample was assigned a sample ID number based on its specific annealing temperature, with a summary of the sample conditions provided in Table 3.2. After annealing, the tubes were carefully broken to retrieve the samples, which were then ground and prepared for subsequent analysis.

3.4 Optimising Vacuum Annealing through Variable Temperature and Time

Table 3.2 Vacuum annealing conditions applied post-synthesis to a series of samples, each annealed for 90 minutes and identified by a unique ID indicating the annealing temperature.

Sample ID	Annealing Temperature (°C)
Vac280	280
Vac290	290
Vac300	300
Vac310	310
Vac320	320
Vac330	330
Vac340	340
Vac350	250
Vac360	360

3.4.2 Initial Investigation into Reproducibility of Variable Temperature Annealing

The initial characterisation of the samples listed in Table 3.2 was conducted using PXRD. These measurements were performed at room temperature with the Panalytical X'Pert diffractometer. Each sample was mounted on a zero-background silicon wafer, and data were collected over a 2θ range of 5 to 50° with a step size of 0.001°. The dual-source beam setup utilised both Cu-K $_{\alpha 1}$ and Cu-K $_{\alpha 2}$ radiations, with an incident wavelength ratio of Cu-K $_{\alpha 1}$ /Cu-K $_{\alpha 2}$ = 0.5. Structural characterisation of the resulting diffraction patterns was performed through Rietveld refinement using the Fullprof software suite, allowing for analysis of the crystalline phases and lattice parameters.

Figure 3.7a compares the X-ray diffraction pattern of MAPI annealed at different temperatures. All diffraction patterns were indexed assuming a tetragonal crystal system, with approximate unit cell dimensions of $a \approx b \approx 8.8 \text{ \AA}$ and $c \approx 12.6 \text{ \AA}$, consistent with the values reported for room temperature pristine MAPI.

As the annealing temperature rises, a noticeable shift occurs in the diffraction

3.4 Optimising Vacuum Annealing through Variable Temperature and Time

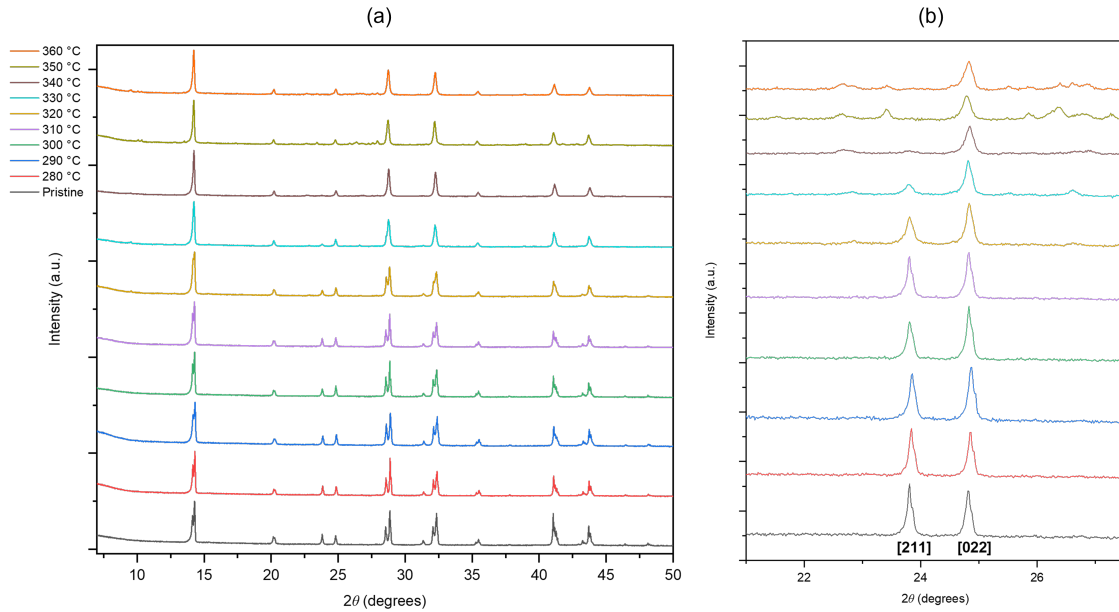


Figure 3.7 Powder X-ray diffraction patterns for MAPI samples annealed under vacuum at various temperatures for 90 minutes. (b) Expanded view of the tetragonal phase reflections at [211] and [022].

pattern, with the previously observed peak splitting at around 28 and 32 2θ merges into single peaks. This trend, along with the suppression of the [211] reflection (as shown in Figure 3.7b), suggests a structural transition from the tetragonal phase to the high-temperature cubic phase observed in pristine MAPI. This suggests some stabilisation of the cubic phase in these post-synthetically treated materials, when the sample is brought back to room temperature. By 340 °C, the [211] reflection is suppressed, indicating a complete phase transition. However, at higher temperatures, the appearance of additional peaks at around 22.5, 23.5, and 26 2θ , suggest the formation of impurity phases, which could not be conclusively identified using structural databases.

At 340 °C, the diffraction pattern can be indexed using a simple cubic crystal system, aligning with the expected high-temperature phase of MAPI. Nonetheless, due to the resolution limitations of the measurements using the in-house diffractometer, distinguishing between the tetragonal and cubic phases is challenging. Higher resolution

3.4 Optimising Vacuum Annealing through Variable Temperature and Time

Table 3.3 Room temperature refined lattice parameters for variable temperature vacuum-annealed samples.

Sample ID	a (Å)	b (Å)	c (Å)	Volume (Å) ³
Vac280	8.7199(2)	8.7199(2)	12.4607(3)	947.470
Vac290	8.7357(6)	8.7357(6)	12.4792(9)	952.318
Vac300	8.7374(6)	8.7374(6)	12.4748(8)	952.353
Vac310	8.7247(1)	8.7247(1)	12.4559(2)	948.144
Vac320	8.7313(2)	8.7313(2)	12.4491(3)	949.056
Vac330	8.7539(3)	8.7539(3)	12.4340(4)	952.827
Vac340	8.7644(7)	8.7644(7)	12.4005(9)	952.541
Vac350	8.7570(3)	8.7570(3)	12.4236(10)	952.704
Vac360	8.7476(2)	8.7476(2)	12.3979(8)	948.694

PXRD would have been preferable to use in-house, however this was not available. To address this, each pattern was refined using a tetragonal structural model with the space group $I4/mcm$, to extract the unit cell parameters. The sequential refinements are presented in Figures 3.8 and 3.9 and lattice parameters are shown in Table 3.3.

This study shows that the phase transition occurs at a higher annealing temperature than the previously reported value of 315 °C in reference [19]. The discrepancy may be attributed to various factors; the annealing conditions, such as the furnace type, heating rate, and atmosphere, which can also shift the transition temperature. Furthermore, differences in the sensitivity and resolution of diffraction measurements may lead to varying detection thresholds for phase transitions. These factors highlight the complexity of accurately determining the phase transition temperature and suggest that minor variations in experimental procedures could significantly affect the results.

3.4.3 Further Investigating the Impact of Annealing Time

Based on these findings, a time-dependent investigation on synthesis was conducted in which samples were annealed at 340 °C, following the same post-synthetic annealing

3.4 Optimising Vacuum Annealing through Variable Temperature and Time

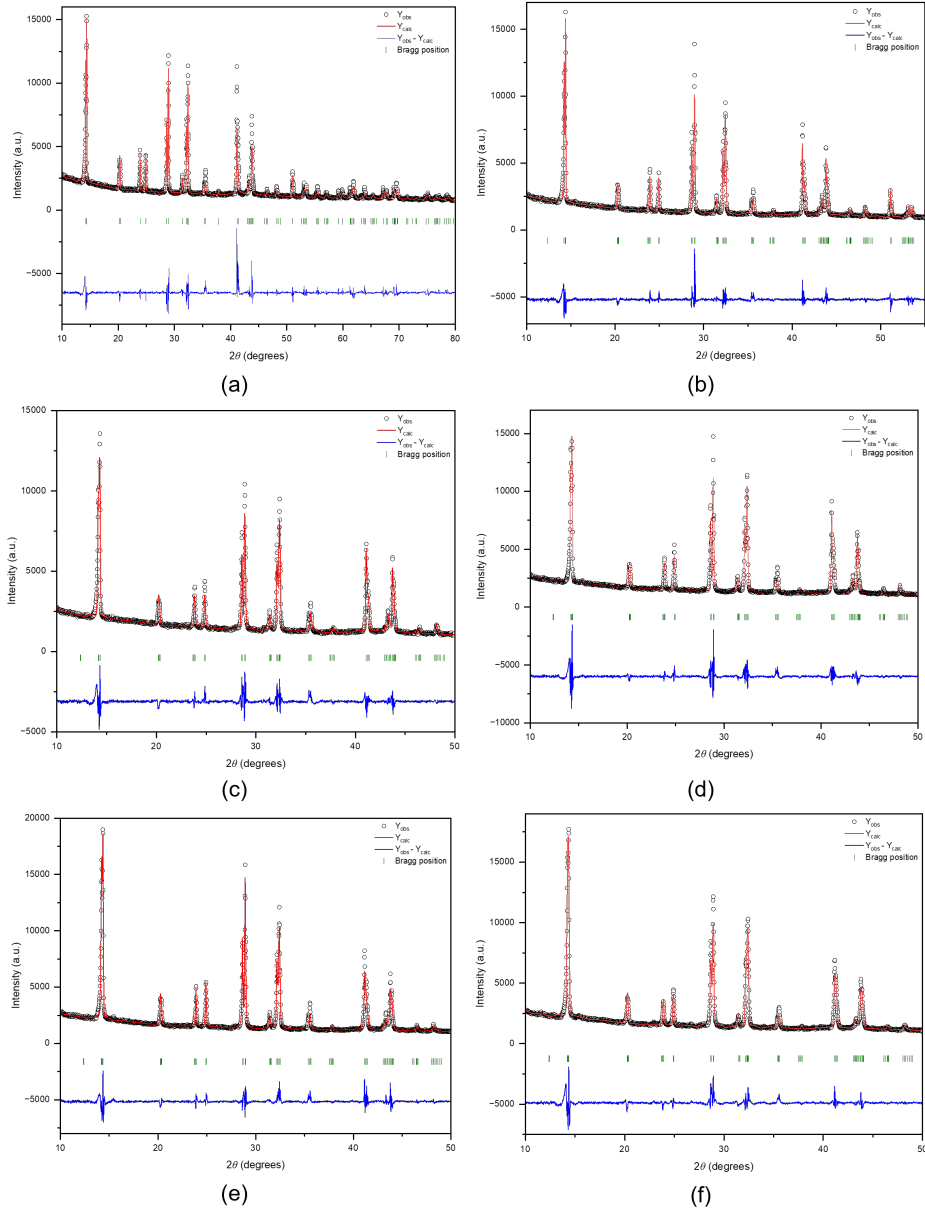


Figure 3.8 X-ray powder diffraction profile from Rietveld refinement for the MAPI samples annealed under vacuum at temperatures ranging from 280 to 320 K. Measurements were collected at room temperature. (a) Pristine MAPI $R_p = 4.32\%$ and $R_{wp} = 6.42\%$, (b) Vac280 $R_p = 4.32\%$ and $R_{wp} = 6.42\%$, (c) Vac290 $R_p = 5.22\%$ and $R_{wp} = 7.54\%$, (d) Vac300 $R_p = 6.30\%$ and $R_{wp} = 9.19\%$, (e) Vac310 $R_p = 5.62\%$ and $R_{wp} = 7.79\%$ and (f) Vac320 $R_p = 5.04\%$ and $R_{wp} = 7.25\%$.

3.4 Optimising Vacuum Annealing through Variable Temperature and Time

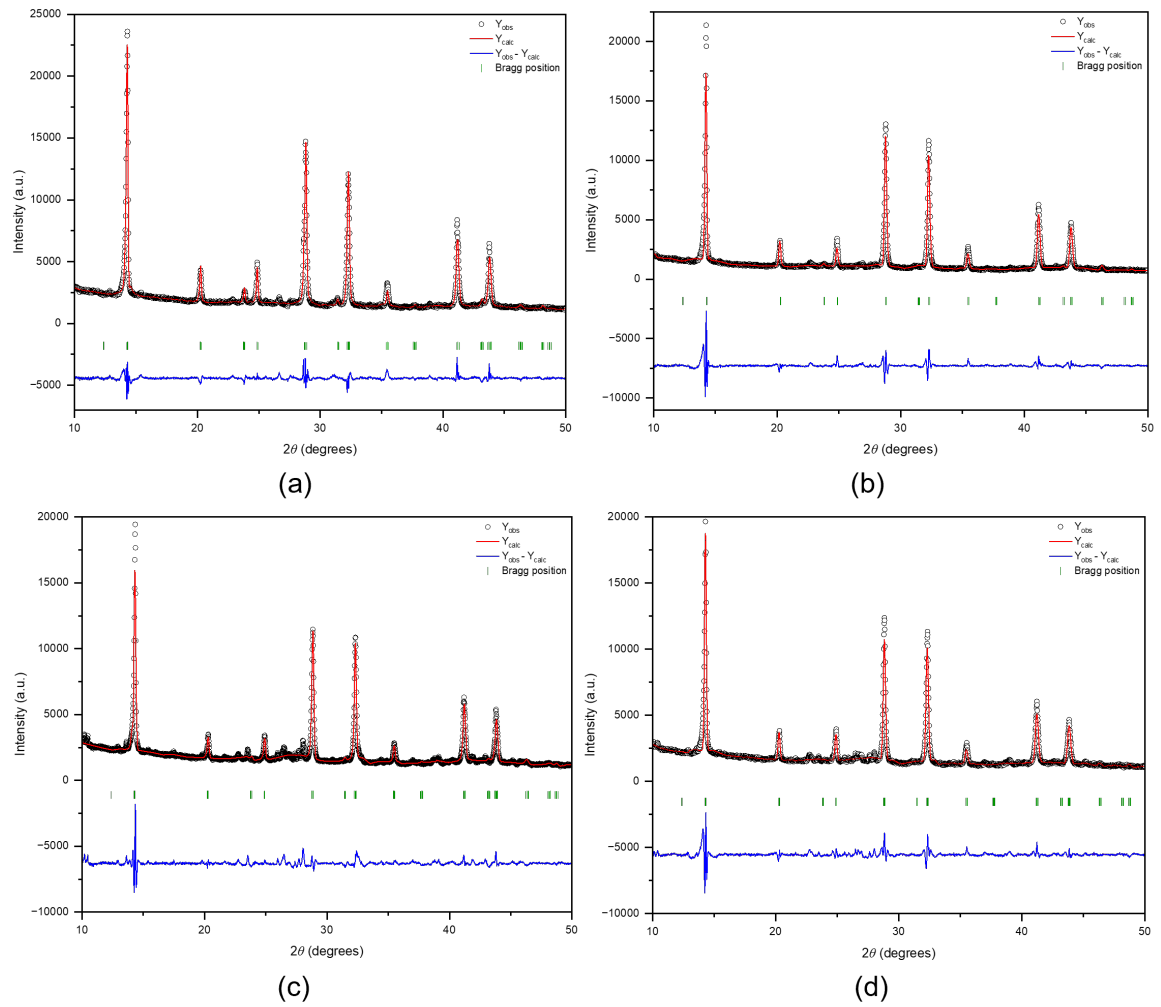


Figure 3.9 X-ray powder diffraction profile from Rietveld refinement for the MAPI samples annealed under vacuum at temperatures ranging from 320 to 360 K. The measurements were collected at room temperature. (a) Vac330 $R_p = 4.45\%$ and $R_{wp} = 6.03\%$, (b) Vac340 $R_p = 6.55\%$ and $R_{wp} = 9.37\%$, (c) Vac350 $R_p = 5.19\%$ and $R_{wp} = 7.38\%$, (d) Vac360 $R_p = 5.44\%$ and $R_{wp} = 7.66\%$.

3.4 Optimising Vacuum Annealing through Variable Temperature and Time

Table 3.4 Post synthesis vacuum annealing conditions undertaken for a range of samples annealed at 340 °C identified by a unique ID, specifying the annealing time.

Sample ID	Annealing Time (min)
Vac 0h 15	15
Vac 0h 30	30
Vac 1 h	60
Vac 1 h 30	90
Vac 2 h	120

procedure as previously described, but for varying duration. The unique sample IDs assigned to each of these time-annealed samples are listed in Table 3.4.

The room temperature X-ray diffraction patterns for the vacuum-annealed variable time samples are presented in Figure 3.10. As the annealing time increases, the characteristic doublet peaks in the diffraction patterns progressively merge into single peaks. Additionally, as shown in Figures 3.10(b) and (c), the intensity of the [211] reflection and the ratio between the [211] and [022] reflections decrease linearly with increasing annealing time. These observations suggest a continued structural transition with extended annealing.

Although the patterns from samples annealed above 330 °C can be indexed using a simple cubic phase for MAPI, initial refinements were carried out assuming a tetragonal crystal system with the space group $I4/mcm$. The results of these refinements are displayed in Figure 3.11.

Further analysis of the Vac 1 h and Vac 2 h samples was conducted using high-resolution variable temperature powder diffraction measurements at the I11 beamline of the Diamond Light Source facility (Figures 3.12, 3.13, and 3.14). The experiments employed the MAC diffraction detector with a fixed standard energy of 15 keV and a standard Debye-Scherrer (capillary) geometry. A Cryostream Plus system, with an

3.4 Optimising Vacuum Annealing through Variable Temperature and Time

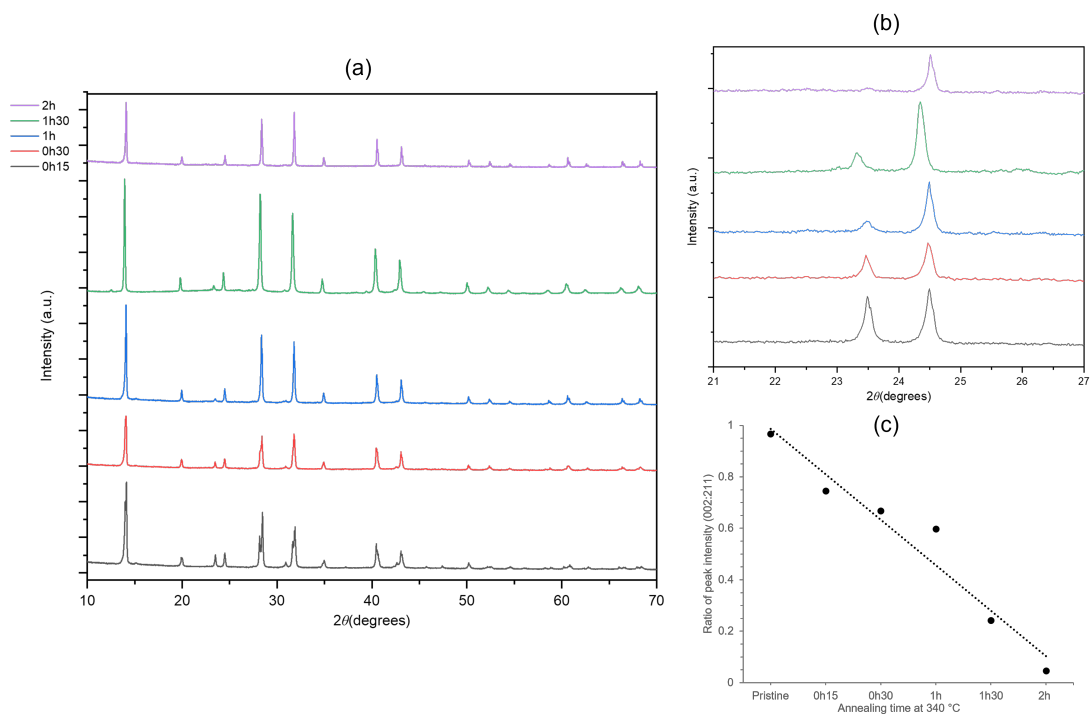


Figure 3.10 Powder X-ray diffraction patterns for MAPI samples annealed under vacuum at 340 °C for various lengths of time. (b) Magnified view of the tetragonal phase reflections at (211) and (022). (c) The ratio of the intensity of these two peaks as a function of annealing time.

3.4 Optimising Vacuum Annealing through Variable Temperature and Time

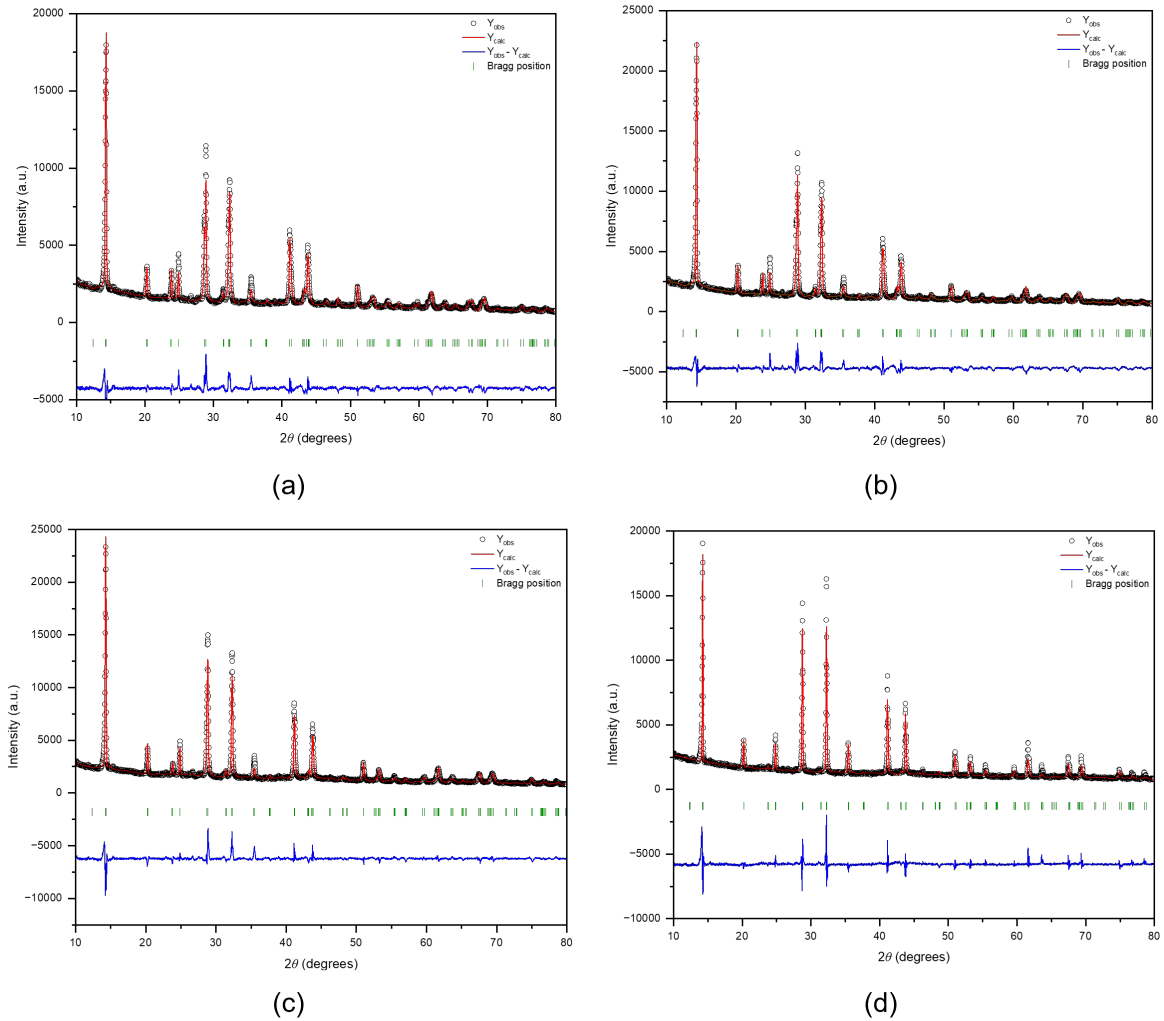


Figure 3.11 X-ray powder diffraction profile from Rietveld refinement for the samples performed at room temperature. (a) Vac 0h30 $R_p = 6.31\%$ and $R_{wp} = 8.22\%$, (b) Vac 1 h $R_p = 5.51\%$ and $R_{wp} = 8.38\%$, (c) Vac 1 h 30 $R_p = 6.09\%$ and $R_{wp} = 8.50\%$, (d) Vac 2 h $R_p = 6.03\%$ and $R_{wp} = 9.26\%$.

3.4 Optimising Vacuum Annealing through Variable Temperature and Time

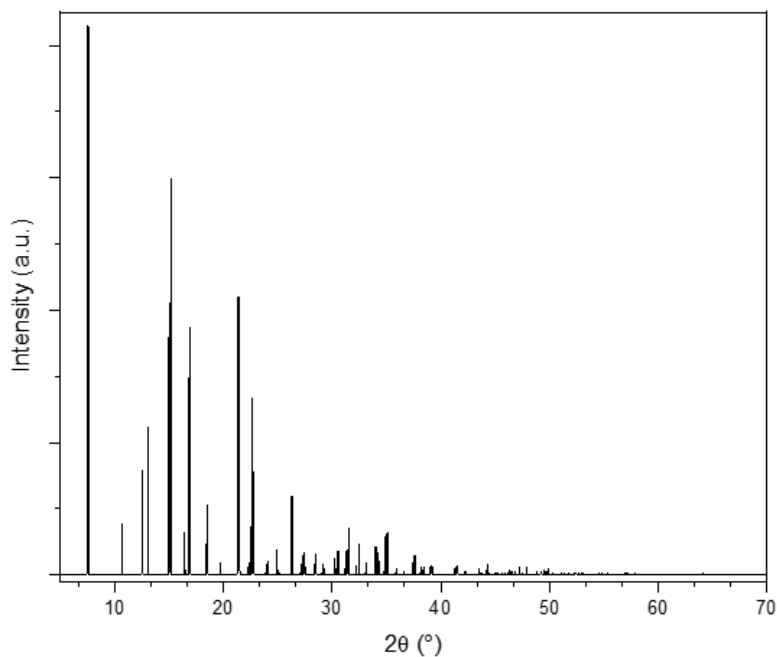


Figure 3.12 I11 synchrotron powder diffraction profile of Pristine MAPI measured at 297 K.

operational range of 295–400 K, was used to control the heating and cooling cycles during the measurements.

Sequential refinements were performed across the temperature range for both samples. The structural model used for these refinements was the tetragonal space group $I4/mcm$ which is commonly reported in literature [27, 31], and the refined parameters are provided in Tables 3.5, 3.6, and 3.7.

The high-resolution data revealed that, despite undergoing vacuum annealing for over two hours, the samples were not fully cubic at room temperature as seen by the existing presence of the [211] reflection (Figure 3.14). This subtle structural difference could only be detected with the advanced resolution available at Diamond. However, it is clear that the room temperature structure of MAPI has been significantly altered by the post-synthetic treatments as this reflection has been significantly decreased.

3.4 Optimising Vacuum Annealing through Variable Temperature and Time

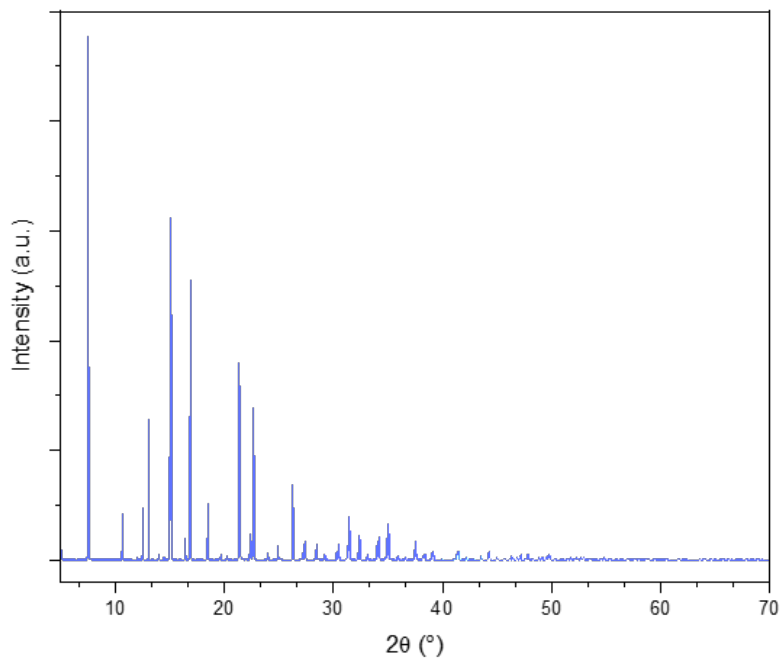


Figure 3.13 I11 synchrotron powder diffraction profile of Vacuum Annealed 1 h measured at 297 K.

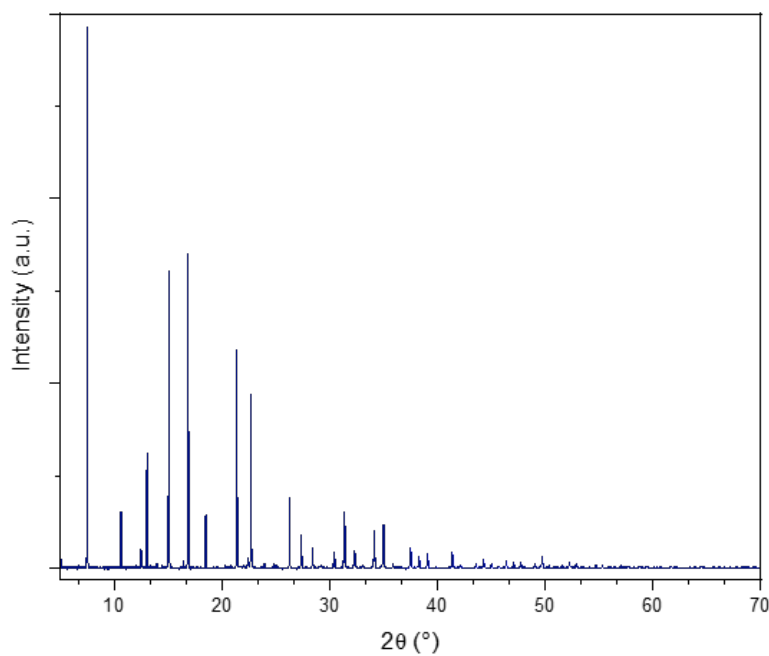


Figure 3.14 I11 synchrotron powder diffraction profile of Vacuum Annealed 2 h measured at 297 K.

3.4 Optimising Vacuum Annealing through Variable Temperature and Time

Table 3.5 Refined structural parameters for Pristine MAPI derived from Rietveld refinement of synchrotron powder diffraction data measured at 297 K. Lattice parameters $a = 8.8705 \text{ \AA}$, $b = 8.8705 \text{ \AA}$, $c = 12.6678 \text{ \AA}$ and a cell volume of 996.771 \AA^3 .

Pristine MAPI - Powder Diffraction Atomic Coordinates at 297 K				
Site	$x \text{ (\AA)}$	$y \text{ (\AA)}$	$z \text{ (\AA)}$	Occupancy
C1	0.9030	-0.4030	0.1356	0.27
I1	0.2142	0.2858	0.5000	0.95
I2	0.5000	0.5000	0.7500	0.97
N1	0.4485	0.0515	0.2144	0.61
Pb1	0.5000	0.5000	0.5000	1.00

Table 3.6 Refined structural parameters and occupancies for Vac 1 h derived from Rietveld refinement of synchrotron powder diffraction data measured at 297 K. Lattice parameters $a = 8.8817 \text{ \AA}$, $b = 8.8817 \text{ \AA}$, $c = 12.6493 \text{ \AA}$ and a cell volume of 997.820 \AA^3 .

Vac 1 h - Powder Diffraction Atomic Coordinates at 297 K				
Site	$x \text{ (\AA)}$	$y \text{ (\AA)}$	$z \text{ (\AA)}$	Occupancy
C1	0.8300	-0.3300	0.1356	0.26
I1	0.2189	0.2811	0.5000	0.94
I2	0.5000	0.5000	0.7500	0.97
N1	0.4345	0.0655	0.2072	0.62
Pb1	0.5000	0.5000	0.5000	1.00

Table 3.7 Refined structural parameters and occupancies for Vac 2 h derived from Rietveld refinement of synchrotron powder diffraction data measured at 297 K. Lattice parameters $a = 8.8926 \text{ \AA}$, $b = 8.8926 \text{ \AA}$, $c = 12.6238 \text{ \AA}$ and a cell volume of 998.274 \AA^3 .

Vac 2 h - Powder Diffraction Atomic Coordinates at 297 K				
Site	$x \text{ (\AA)}$	$y \text{ (\AA)}$	$z \text{ (\AA)}$	Occupancy
C1	0.8689	-0.3689	0.1356	0.29
I1	0.2249	0.2751	0.5000	0.91
I2	0.5000	0.5000	0.7500	0.95
N1	0.4478	0.0522	0.1869	0.59
Pb1	0.5000	0.5000	0.5000	1.00

3.4 Optimising Vacuum Annealing through Variable Temperature and Time

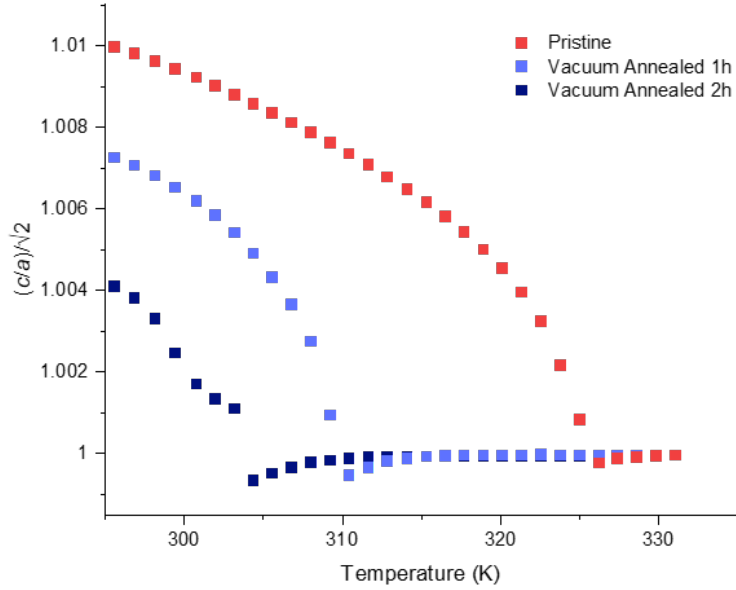


Figure 3.15 The ratio of a and c lattice parameters $(c/a)\sqrt{2}$ plotted as a function of temperature for pristine MAPI, Vac 1 h, and Vac 2 h.

As shown in Figures 3.17 and 3.16, both the cell volume and the Pb–I–Pb bond angle increased with prolonged annealing time. For pristine MAPI at 295 K, the cell volume is measured at 996.621 \AA^3 , and the Pb–I–Pb bond angle is 163.432° . After annealing for 60 min at 340°C (Vac 1 h), the cell volume increases to 997.637 \AA^3 , with a corresponding bond angle of 165.912° . For the Vac 2 h sample, these values further increase, with a cell volume of 998.159 \AA^3 and a bond angle of 168.307° . These observations indicate a gradual alteration in the tilting of the PbI_6^{4-} octahedra as the annealing time increases, suggesting significant structural changes induced by the post-synthetic thermal treatment.

The high-resolution diffraction analysis further revealed that increasing the annealing time results in a significant reduction in the tetragonal-to-cubic phase transition temperature. For pristine MAPI, the phase transition occurs at 327 K. However, for

3.4 Optimising Vacuum Annealing through Variable Temperature and Time

the Vac 1 h and Vac 2 h samples, this transition temperature drops to 310 K and 305 K, respectively. This trend is depicted in Figure 3.15, where the ratio of the c and a lattice parameters from the sequential refinements of each sample is plotted against temperature. The plot clearly pinpoints the temperature at which the phase transition occurs for each material.

For pristine MAPI, the c/a ratio decreases gradually in a logarithmic manner as the temperature rises, becoming more pronounced near the phase transition temperature. Once the transition occurs, the ratio stabilises at approximately 1, indicating the structural shift from a tetragonal to a cubic phase. This behaviour is also observed in the Vac 1 h and Vac 2 h samples, but as previously noted, the phase transition occurs at lower temperatures for these vacuum-annealed samples.

Additionally, a positive linear relationship between cell volume and temperature is observed across all samples, including pristine MAPI and the vacuum-annealed variants. Importantly, as seen in Figure 3.16 the post-synthetic treatment does not alter this linear relationship, indicating that the thermal expansion behaviour of the material remains consistent despite the annealing-induced changes in the phase transition temperature. This increase in the unit cell volume upon annealing is most likely due to the change in coordination environments of the ions within the structure. It was previously proposed that vacuum annealing causes some of the MA^+ cation to leave the structure, leading to a structural defect [32]. This introduction of a vacancy within the structure will influence a change in the hydrogen bonding between the cation and the ionic lattice cage and therefore affect the distances between the ions, altering the unit cell dimensions. The rearrangement of atoms to relieve the defect is also possible, leaving a more stable and expanded lattice. As it is proposed that vacuum annealing has triggered a stabilisation of the material between the tetragonal and cubic phase,

3.4 Optimising Vacuum Annealing through Variable Temperature and Time

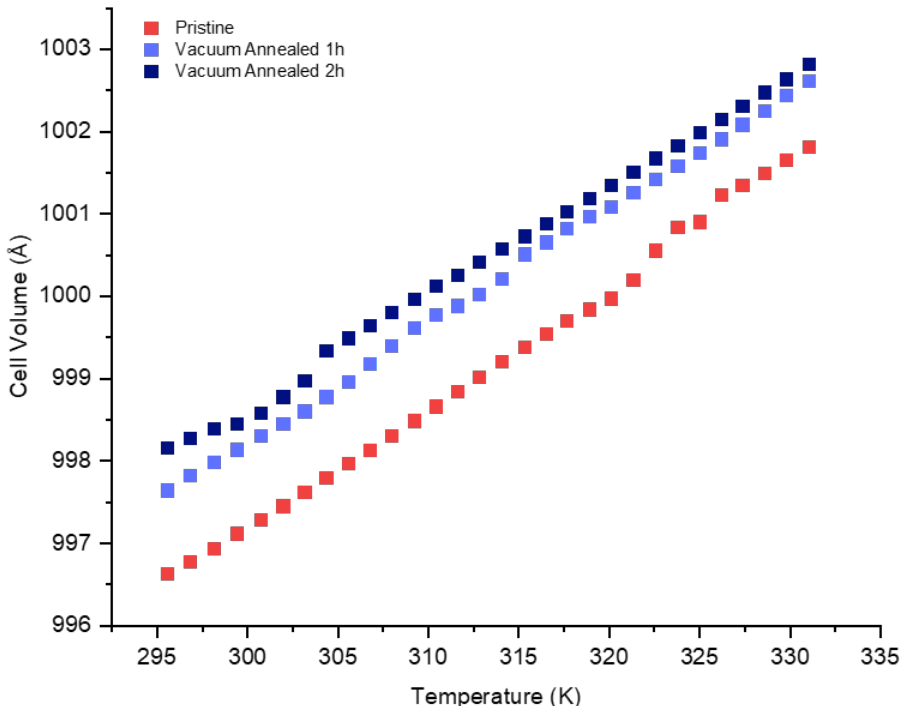


Figure 3.16 Unit cell volume for the Pristine, Vac 1 h, and Vac 2 h MAPI samples derived from Rietveld refinement of powder X-ray diffraction measurements performed at variable temperature.

this difference in structure will have altered the arrangement of the atoms and the volume of the unit cell to be increased. Finally with the introduction of defects as described in [32], the mobility of the cation may have changed, allowing the adoption of more favourable positions and potentially leading to an increase in the overall volume of the unit cell.

This analysis also highlights how the lattice cavity, in which the MA^+ cation rotates, expands due to increased octahedral tilting, allowing for greater rotational freedom of the cation within the structure. The most pronounced effect of the annealing treatments, however, is observed in the behaviour of the Pb–I–Pb bond angle with respect to temperature.

For pristine MAPI, the bond angle gradually increases as the temperature rises (seen

3.5 Attempt to optimise Iodine Annealing post synthetic treatment

in Figure 3.17), becoming more pronounced near the phase transition temperature. Beyond the transition, the bond angle increases rapidly, eventually stabilising at approximately 174° . In the case of Vac 1 h, a similar trend is observed up to around 310 K, after which the bond angle starts to linearise at about 173° . For Vac 2 h, the change in bond angle is less defined, with a more rapid stabilisation beyond 330 K, where it remains relatively constant. These observations suggest that the post-synthetic vacuum annealing treatment alters the range of motion of the octahedra within the temperature range studied. This is evidenced by the decreased variation in the Pb–I–Pb bond angle, indicating that the structural flexibility of the material has been altered by the annealing process, with increasing annealing time allowing for decreased flexibility of the structure. The change in the tilting of the octahedra could be responsible for the altered phase transition behaviour and overall structural stability at lower temperatures.

3.5 Attempt to optimise Iodine Annealing post synthetic treatment

As detailed in the theses by J. Minns and R. Day, the development of an iodine post-synthetic treatment aimed to address the interstitial iodine sites reported within the MAPI structure and to elucidate the mechanism of iodine mobility within this hybrid perovskite material [19, 33]. The primary objective of this treatment was to enhance the flexibility and disorder of MAPI, with the potential to synthesise new structural phases. This section focuses on optimising the iodine annealing process to further investigate its effects on the overall structure of MAPI.

To initiate this investigation, varying amounts of iodine (0.025 g, 0.05 g, and 0.1 g)

3.5 Attempt to optimise Iodine Annealing post synthetic treatment

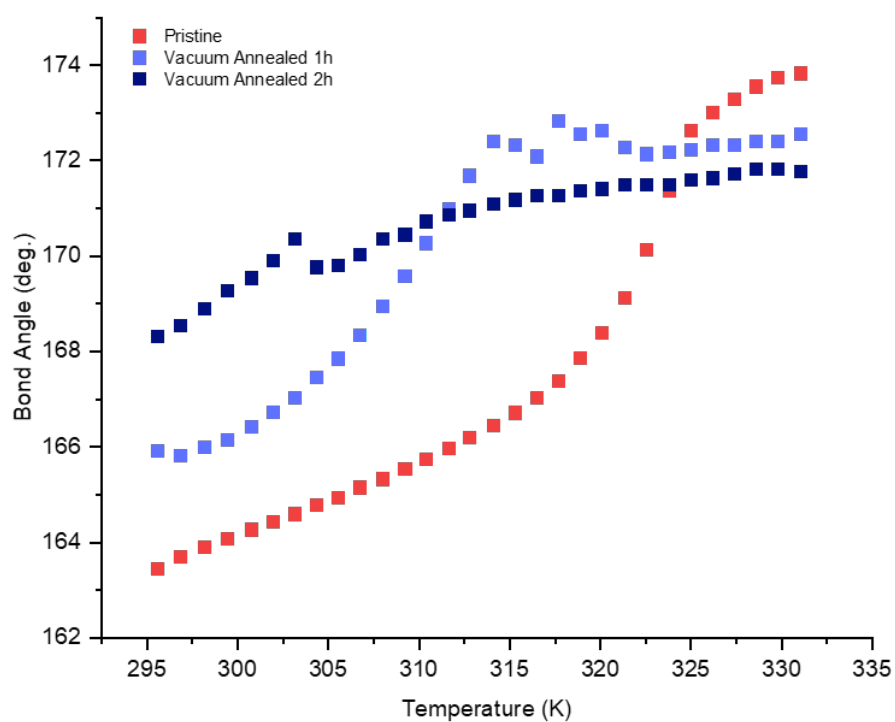


Figure 3.17 P–I–Pb bond angle for the Pristine, Vac 1 h, and Vac 2 h MAPI samples derived from Rietveld refinement of powder X-ray diffraction measurements performed at variable temperature.

3.5 Attempt to optimise Iodine Annealing post synthetic treatment

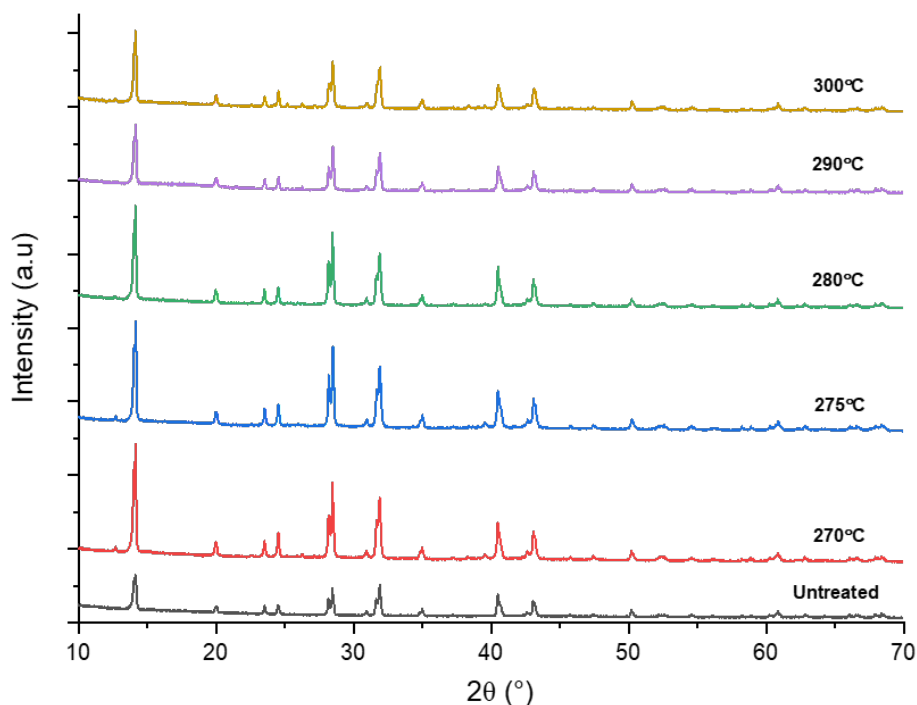


Figure 3.18 Powder X-ray diffraction patterns for MAPI samples annealed with 0.025 g of iodine at various temperatures for 90 min.

were introduced into a quartz tube containing 0.05 g of MAPI. For clarity, the terms "low iodine exposition," "moderate iodine exposition," and "high iodine exposition" will refer to the addition of 0.025 g, 0.05 g, and 0.1 g of iodine, respectively. Following the addition of iodine, the tubes were evacuated and sealed before being placed in a furnace for 90 minutes at varying temperatures. The results of these initial investigations were obtained using the X'pert diffractometer for all PXRD measurements, and are presented in the following sections.

Figure 3.18 presents the diffraction patterns of various MAPI samples that were annealed at temperatures ranging from 270 to 300 °C in the presence of a low iodine concentration (0.025 g). The results indicate no significant structural changes in the samples, suggesting that either the treatment was ineffective or that any alterations in

3.5 Attempt to optimise Iodine Annealing post synthetic treatment

the overall structure of MAPI resulting from low iodine exposition are too subtle to be detected through conventional diffraction analysis.

In contrast, increasing the iodine concentration to a moderate level (0.05 g), as shown in Figure 3.19, reveals observable changes in the X-ray diffraction (XRD) patterns at elevated temperatures. Notable alterations occur between $2\theta = 22^\circ$ and 34° , particularly the suppression of peaks at $2\theta = 23.5^\circ$ and 33° as the temperature rises. However, this treatment also leads to increased sample degradation, which is evidenced by the increase in the peak intensity at approximately 12° , corresponding to the formation of PbI_2 . Additionally, the emergence of new peaks between 22° and 27° may indicate the release of CH_3NH_3 from the MAPI structure. Despite these observations, attempts to identify these new reflections using the Highscore pattern matching software and relevant crystallographic databases yielded no satisfactory matches.

Finally, the samples with high iodine content (0.10 g) are presented in Figure 3.20. In these samples, a similar trend is observed, with nearly complete degradation occurring at 300°C . This degradation at elevated temperatures likely indicates the collapse of the perovskite structure, primarily resulting in the formation of PbI_2 alongside some residual organic components from the cation. Furthermore, identifying the reflections that appear between 22° and 27° proved challenging due to the absence of matching reflections in the crystallographic database. Additionally, these peaks were not well defined compared to the pronounced peaks associated with MAPI or its degradation products.

A comparative analysis of different iodine exposures (0.025 g, 0.05 g, 0.075 g, and 0.1 g) at a constant temperature of 290°C is presented in Figure 3.21. The samples heated at 290°C exhibited the best quality for assessing the effects of increasing

3.5 Attempt to optimise Iodine Annealing post synthetic treatment

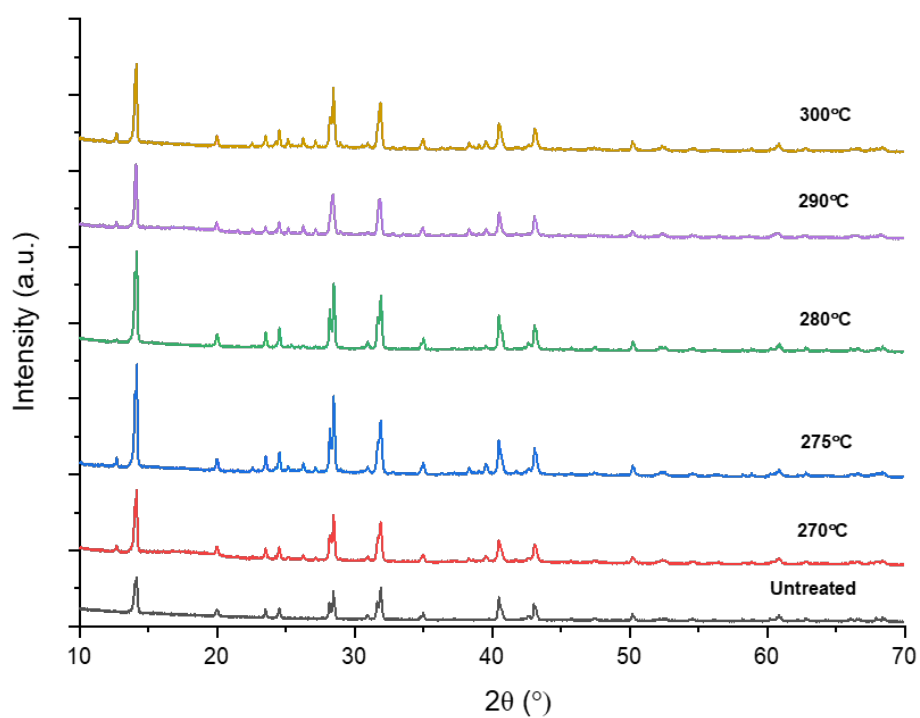


Figure 3.19 Powder X-ray diffraction patterns for MAPI samples annealed with 0.05 g of iodine at various temperatures for 90 minutes.

3.5 Attempt to optimise Iodine Annealing post synthetic treatment

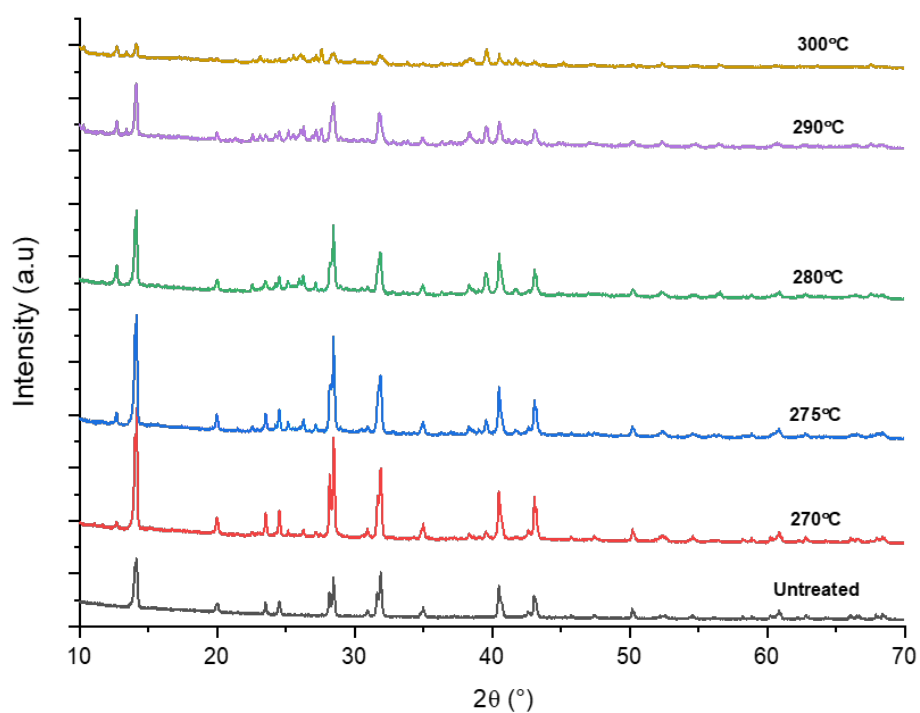


Figure 3.20 Powder X-ray diffraction patterns for MAPI samples annealed with 0.1 g of iodine at various temperatures for 90 minutes.

3.5 Attempt to optimise Iodine Annealing post synthetic treatment

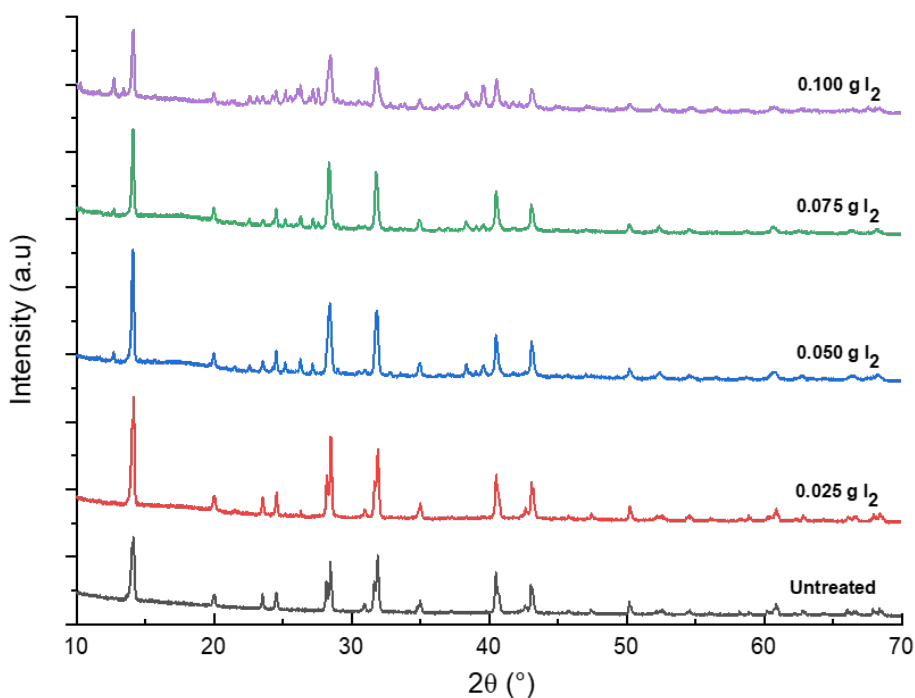


Figure 3.21 Powder X-ray diffraction patterns for MAPI samples annealed with variable amounts of iodine at 290 °C for 90 minutes.

iodine content on the structure of MAPI. As the amount of iodine increased, there was evidence to suggest that the structure transitions into a new cubic phase, which remains stable at room temperature. However, it is important to note that this observation of structural transition is accompanied by an increase in sample degradation. The optimal iodine exposure was determined to be between 0.075 g and 0.1 g when annealed at temperatures ranging from 280 to 290 °C. Exceeding 0.1 g of iodine or applying temperatures above 300 °C led to significant degradation of the samples. Consequently, achieving consistent and reproducible tuning of the structure and properties of MAPI through this treatment has proven increasingly challenging.

Due to the limited laboratory time available as a result of the extenuating circumstances caused by the COVID-19 pandemic, only one sample was successfully

3.5 Attempt to optimise Iodine Annealing post synthetic treatment

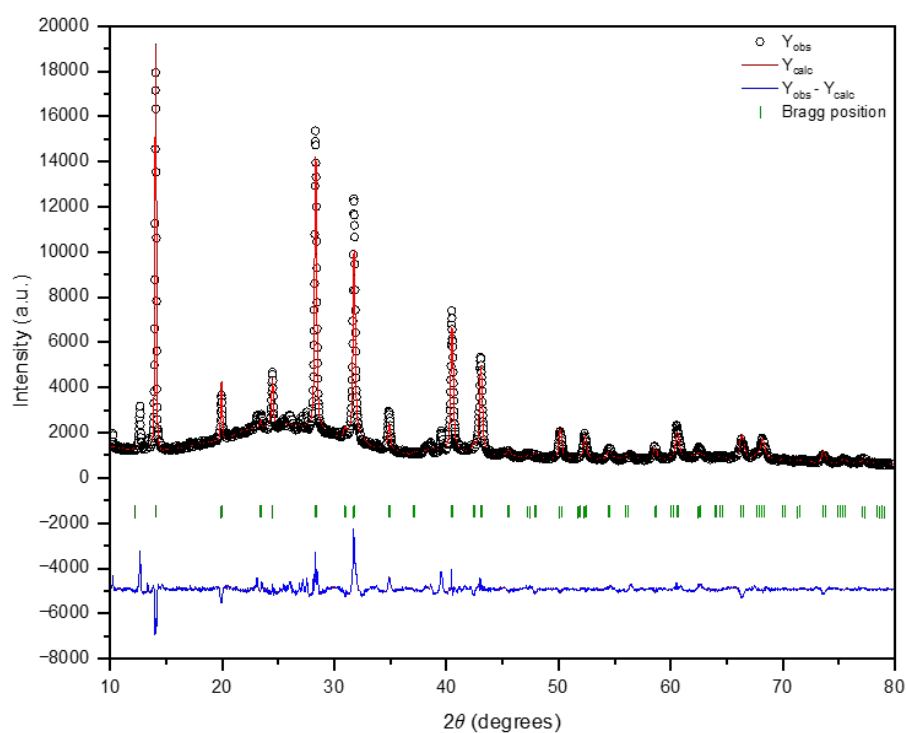


Figure 3.22 X-ray powder diffraction profile from Rietveld refinement for I₂-Annealed performed at room temperature using I/4mcm space group. Lattice parameters were refined to $a = 8.9096(3)$ Å, $b = 8.9096(3)$ Å, $c = 12.5989(2)$ Å. $R_p = 6.06\%$ and $R_{wp} = 8.69\%$.

3.5 Attempt to optimise Iodine Annealing post synthetic treatment

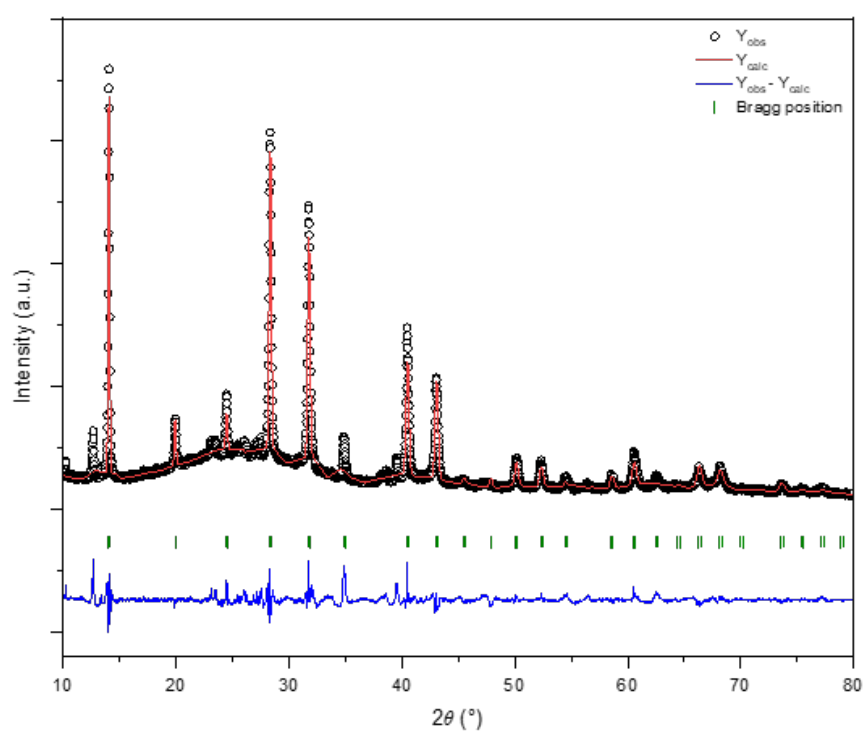


Figure 3.23 X-ray powder diffraction profile from Rietveld refinement for I₂-Annealed performed at room temperature using Pm-3m space group. Lattice parameters were refined to $a = 6.3005(0)$ Å, $b = 6.3005(0)$ Å, $c = 6.3005(0)$ Å. $R_p = 6.38\%$ and $R_{wp} = 8.63\%$.

3.5 Attempt to optimise Iodine Annealing post synthetic treatment

Table 3.8 Refined structural parameters for I₂-Annealed derived from Rietveld refinement of synchrotron powder diffraction data measured at 297 K.

Site	x (Å)	y (Å)	z (Å)	Occupancy
C1	0.7536	-0.2535	0.0330	2.62
I1	0.2017	0.2983	0.5000	0.52
I2	0.5000	0.5000	0.7500	0.81
N1	0.4465	0.0536	0.2995	0.58
Pb1	0.5000	0.5000	0.5000	1.00

post-synthetically treated to induce a phase change with minimal phase degradation. This sample of MAPI was iodine-annealed at 280 °C using 0.1 g (further referred to as I₂-Annealed) of iodine, resulting in the PXRD pattern presented. The diffraction pattern could be indexed with a simple cubic crystal system for MAPI, and refinement was performed twice using either a tetragonal crystal structure with the space group $I4/mcm$ (Figure 3.22) or a cubic crystal structure with the space group $Pm-3m$ (Figure 3.23). Despite the challenges posed by the restricted time, this sample provided valuable insights into the phase stability and structural changes of MAPI following iodine annealing. Interestingly, when attempting a refinement with an alternative crystallographic model, the goodness of fit was fairly similar for each refinement. This potentially suggests that neither of these models alone provide a completely correct interpretation of this sample. It is possible that a coexistence of these phases may exist in the sample, and so an additional model may also be required.

This sample was also measured at room temperature using the PILATUS detector at the Swiss-Norwegian Beam Line (SNBL) of the European Synchrotron Radiation Facility, with a wavelength of $\lambda = 0.64114$ Å. The resulting single-phase refinement from this measurement is presented in Figure 3.24, showing an additional impurity phase is present in the diffraction pattern. However, numerous attempts to perform a multiphase refinement were unsuccessful due to the complexity of the impurity which

3.5 Attempt to optimise Iodine Annealing post synthetic treatment

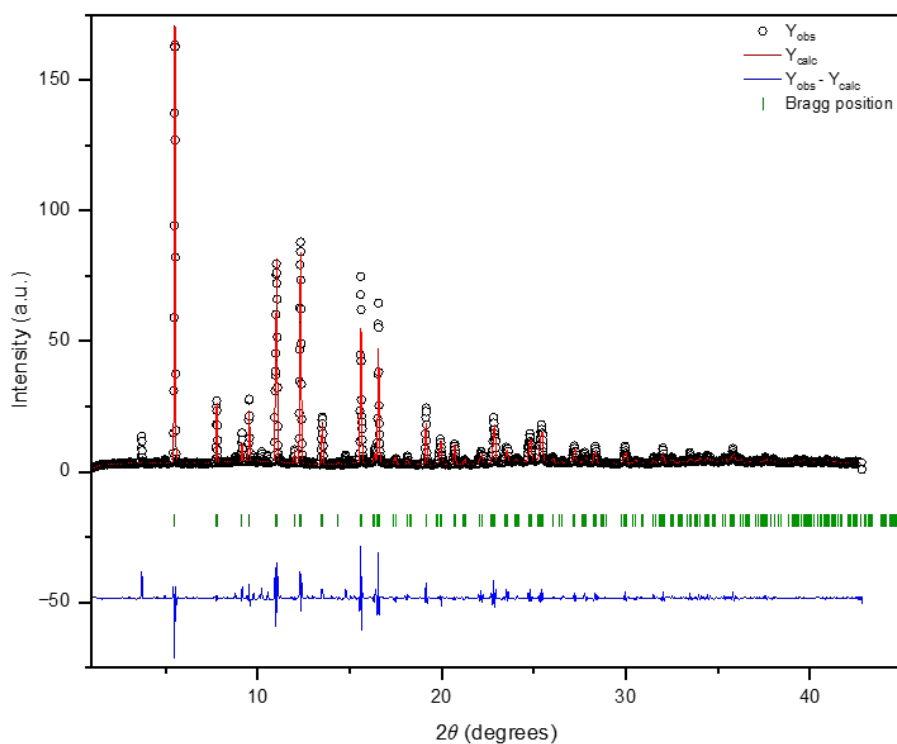


Figure 3.24 Synchrotron powder diffraction profile from Rietveld refinement for I₂-Annealed performed at 297 K. Lattice parameters were refined to $a = 8.8909(3) \text{ \AA}$, $b = 8.8909(3) \text{ \AA}$, $c = 12.6457(5) \text{ \AA}$. $R_p = 8.98\%$ and $R_{wp} = 10.6\%$.

3.5 Attempt to optimise Iodine Annealing post synthetic treatment

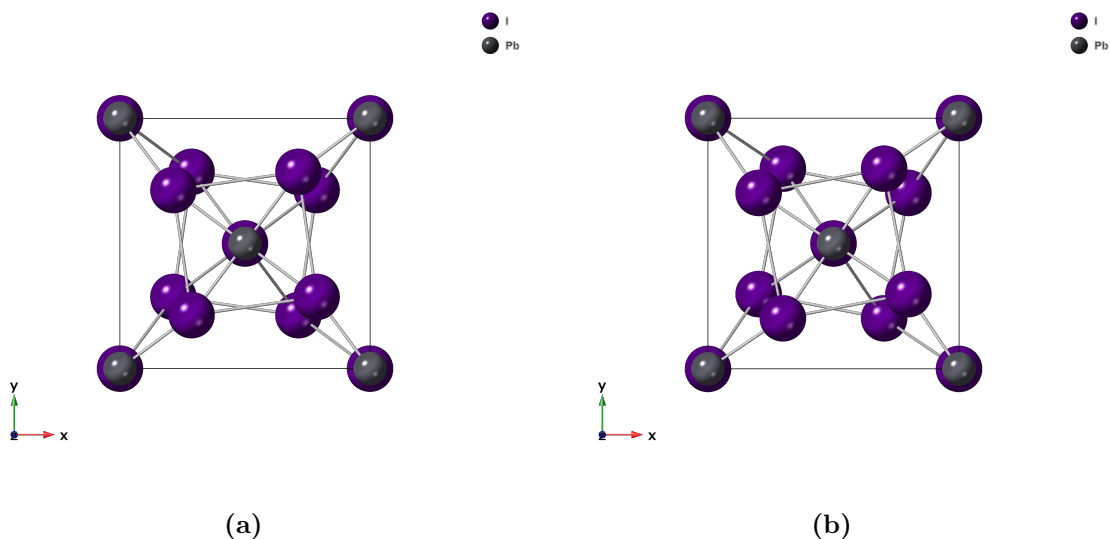


Figure 3.25 (a) Structural model for pristine MAPI with lattice parameter $a = 8.8696 \text{ \AA}$ and $c = 12.6685 \text{ \AA}$, and a cell volume of 996.621 \AA^3 . (b) Structural model for iodine treated MAPI with lattice parameter $a = 8.8909 \text{ \AA}$ and $c = 12.6458 \text{ \AA}$, and a cell volume of 999.626 \AA^3 .

did impact the overall goodness of fit. Further discussion regarding this impurity phase is provided in Section 3.6. As observed from the diffraction pattern, the 211 reflection is much more pronounced than seen in with in-house diffraction measurements. It was found most appropriate to continue to refine this sample using a tetragonal phase crystal structure, details of crystallographic parameters can be found in Table 3.8.

When comparing the crystal structure of pristine MAPI with that of the iodine-treated sample, a noticeable difference in the octahedral tilting can be observed (Figure 3.25b). Additionally, the room temperature cell volume of the iodine-treated material has increased significantly from 996.621 \AA^3 (pristine MAPI) to 999.626 \AA^3 . This represents a larger expansion in cell volume than that seen in the vacuum-annealed samples discussed earlier.

The increase in cell volume and the altered tilting of the octahedra correspond to an elongation of the Pb-I bond length, a phenomenon also reported in previous

3.6 Addressing Impurity Phase Formation in the Optimisation of MAPI Treatments

single-crystal structural determinations. [19] It is possible that this iodine treatment has resulted in the successful occupation of small interstitial sites, which were observed in work performed previously in the group. [34] This then leads to a larger perovskite cavity size, as evidenced by the increased unit cell volume. This could, in turn, reduce the interaction between the MA⁺ cations and the iodine anions within the octahedral framework. However, this interpretation is based on a limited set of measurements, and a more thorough investigation is required to fully understand the implications of the iodine treatment on the crystal structure and should be a focus of future work.

3.6 Addressing Impurity Phase Formation in the Optimisation of MAPI Treatments

One thing that has plagued this investigation is the appearance of an unknown secondary impurity phase with both vacuum and iodine annealing treatments. Initially, it was thought just to be the presence of lead iodide as this is a commonly reported decomposition product of MAPI during thermal treatments. However, the reflections observed in several treated MAPI XRD patterns never matched perfectly with the reflections of lead iodide and thus an unknown phase was produced. Additionally, in the vacuum annealing treatments, the reflections produced by this secondary phase were so small, they were undetectable using conventional in-house PXRD, and reflections were only revealed during a high resolution beamtime experiment at the I11 beamline in Diamond facility as seen in Figure 3.26.

In the thesis precursing this there was identification of a NH₄PbI₃ phase through single crystal measurements [19]. A review of the literature of this material revealed that one research group investigated a different vacuum annealing treatment of pellets

3.6 Addressing Impurity Phase Formation in the Optimisation of MAPI Treatments

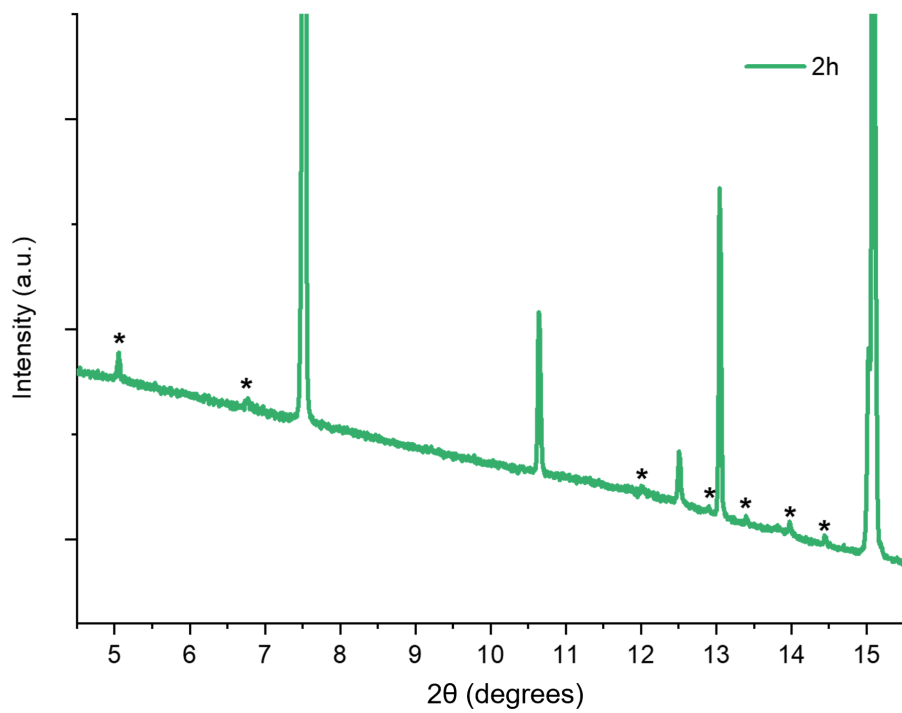


Figure 3.26 Very small presence of secondary phase reflections in vacuum-annealed 2 h sample, indicated by asterisks. Diffraction pattern was collected on the I11 beamline.

3.6 Addressing Impurity Phase Formation in the Optimisation of MAPI Treatments

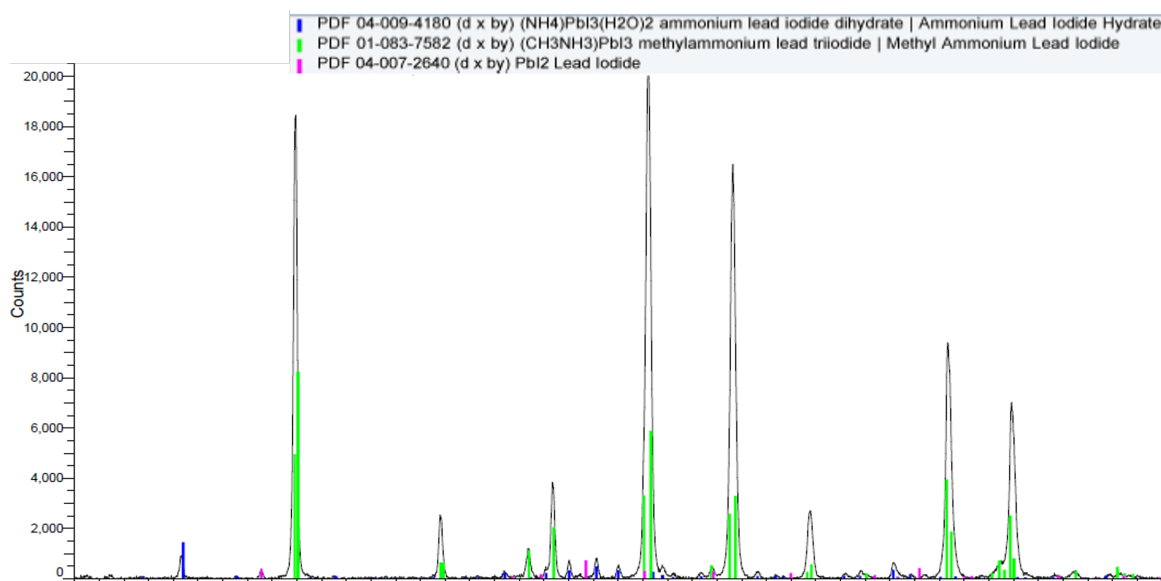


Figure 3.27 Pattern matching of MAPI annealed with iodine was performed using the Diffrac.Eva software. The green reflections correspond to the main phase of pristine MAPI, the blue reflections match those of $\text{NH}_4\text{PbI}_3(\text{H}_2\text{O})_2$, and the pink reflections are consistent with PbI_2 .

of MAPI over longer periods of time and found that during this, they would also experience a secondary phase impurity of NH_4PbI_3 up to 4.4 wt% when annealed for 40 hours [35]. Access to a different XRD pattern matching database was available (utilising DiffracEva Software) and through the regular analysis of the iodine-annealed sample before NMR experiments, a correct match for these small impurity reflections was found, corresponding to $\text{NH}_4\text{PbI}_3(\text{H}_2\text{O})_2$. This is demonstrated in Figure 3.27. However, multiphase rietveld refinements still continued to be unsuccessful due to some limitations of the available refinement software.

Instead, an alternative method was considered to attempt to synthesise NH_4PbI_3 using the same solution based procedure as MAPI (described in Figure 3.28) and systematically mix pure phases of pristine MAPI with NH_4PbI_3 to potentially artificially simulate PXRD patterns that bear resemblance to those of impure treated materials previously studied.

3.6 Addressing Impurity Phase Formation in the Optimisation of MAPI Treatments

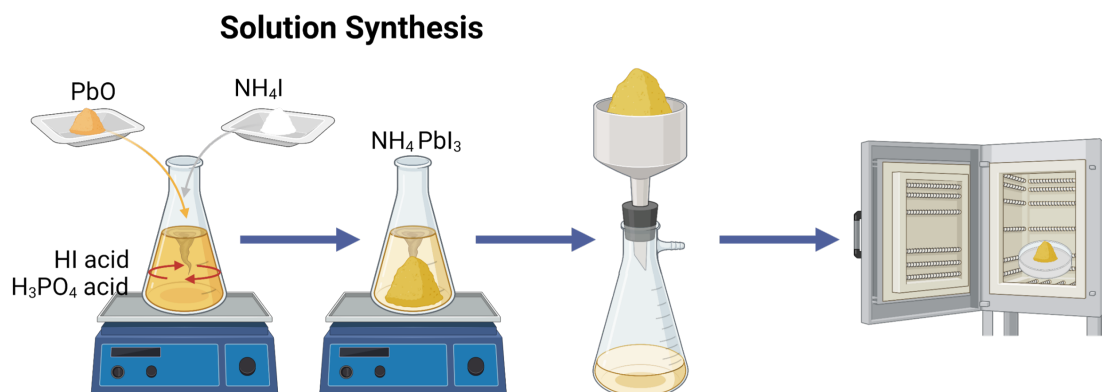


Figure 3.28 Schematic of solution synthesis protocol for preparation of NH_4PbI_3 .

3.6.1 Synthesis and determination of NH_4PbI_3

A schematic overview of the synthesis of NH_4PbI_3 is shown in Figure 3.28. While most literature describes the mechanochemical synthesis of NH_4PbI_3 , a solution-based synthesis was employed in this study to facilitate accurate comparison with methylammonium lead iodide (MAPI) [36, 37]. This approach is a modified version of the synthesis of MAPI initially reported by Stoumpos *et al.* [38]. During synthesis, it was observed that the resulting yellow powder of NH_4PbI_3 was significantly wetter than the black precipitate of MAPI prepared by the same procedure. Standard filtration and vacuum drying were insufficient to remove the excess moisture, necessitating an overnight drying step in a vacuum oven, which yielded a dry yellow powder.

The phase purity of the dried NH_4PbI_3 was assessed using room-temperature powder X-ray diffraction. However, attempts to match the experimental pattern to known patterns using Highscore software were unsuccessful. Instead, simulated diffraction patterns from literature were used for comparison. As illustrated in Figure 3.29, there was minimal agreement between the experimental diffraction peaks and the simulated pattern for NH_4PbI_3 as reported by Prisinzano *et al.* [39]. This indicated that the synthesised powder could not be definitively identified as NH_4PbI_3 .

3.6 Addressing Impurity Phase Formation in the Optimisation of MAPI Treatments

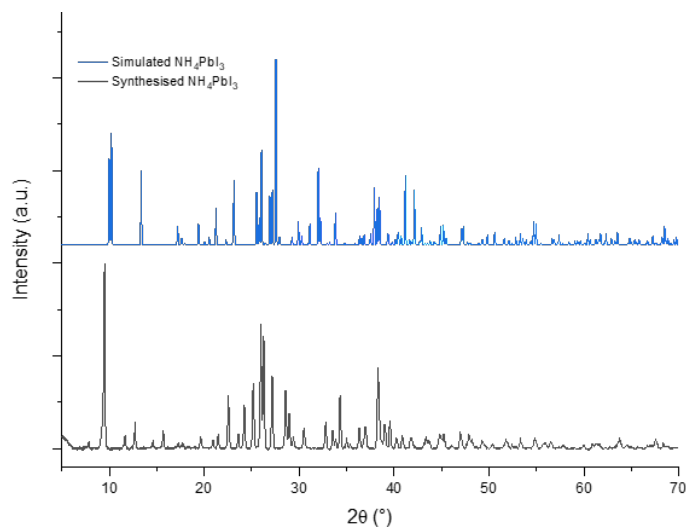


Figure 3.29 Comparison of synthesised NH_4PbI_3 with simulated diffraction pattern from CIF available in literature from reference [39].

A closer match was observed when comparing the experimental diffraction pattern to the simulated pattern of the hydrated phase $\text{NH}_4\text{PbI}_3(\text{H}_2\text{O})_2$, as reported by Fan *et al.* [40] (see Figure 3.30). The similarity between these patterns suggested that the synthesised material was likely $\text{NH}_4\text{PbI}_3(\text{H}_2\text{O})_2$, with the additional non-matching reflections attributed to residual PbI_2 in the sample. This interpretation aligns with the synthesis observations, specifically the material's increased hygroscopicity compared to MAPI, which necessitated extensive drying. To confirm this phase assignment, a Rietveld refinement of the PXRD data was performed using the space group $Pnma$ and structural data from the literature [40].

The refinement, detailed in Figure 3.31 and Table 3.6, yielded lattice parameters of $a = 10.2266(2) \text{ \AA}$, $b = 4.6049(1) \text{ \AA}$, $c = 22.6850(4) \text{ \AA}$, and a cell volume of 1068.286 \AA^3 . The refinement quality was satisfactory, with $R_p = 4.96\%$ and $R_{wp} = 7.06\%$, supporting the conclusion that the synthesised yellow powder is indeed $\text{NH}_4\text{PbI}_3(\text{H}_2\text{O})_2$. The final refined crystal structure is presented in Figures 3.32a and 3.32b.

3.6 Addressing Impurity Phase Formation in the Optimisation of MAPI Treatments

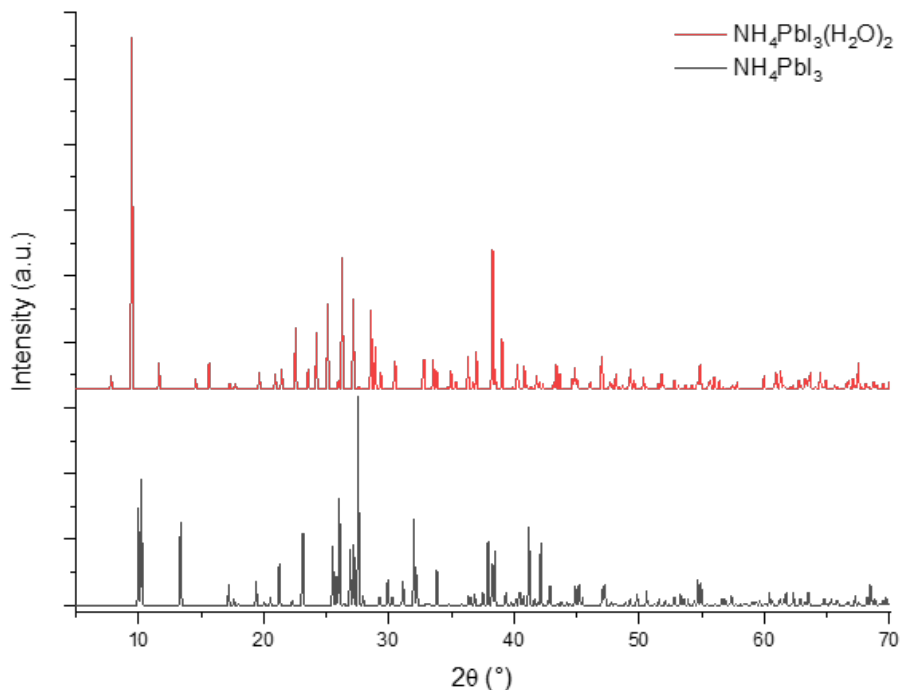


Figure 3.30 Comparison of synthesised $\text{NH}_4\text{PbI}_3(\text{H}_2\text{O})_2$ with simulated diffraction pattern from CIF available in literature from reference [40].

Table 3.9 Refined structural parameters for NH_4PbI_3 derived from Rietveld refinement of in-house powder diffraction data measured at room temperature. Lattice parameters $a = 10.2266(2) \text{ \AA}$, $b = 4.6049(1) \text{ \AA}$, $c = 22.6850(4) \text{ \AA}$ and a cell volume of 1068.286 \AA^3

Site	$x \text{ (\AA)}$	$y \text{ (\AA)}$	$z \text{ (\AA)}$	Occupancy
I1	0.4150	0.2500	0.2846	0.97
I2	0.7522	0.2500	0.8716	0.99
I3	0.6639	0.2500	0.5495	0.99
N1	0.1658	0.7500	0.2869	2.68
O1	0.0263	0.2500	0.3703	1.80
O2	0.0387	0.2500	0.4906	2.08
Pb1	0.5475	0.2500	0.4059	1.00

3.6 Addressing Impurity Phase Formation in the Optimisation of MAPI Treatments

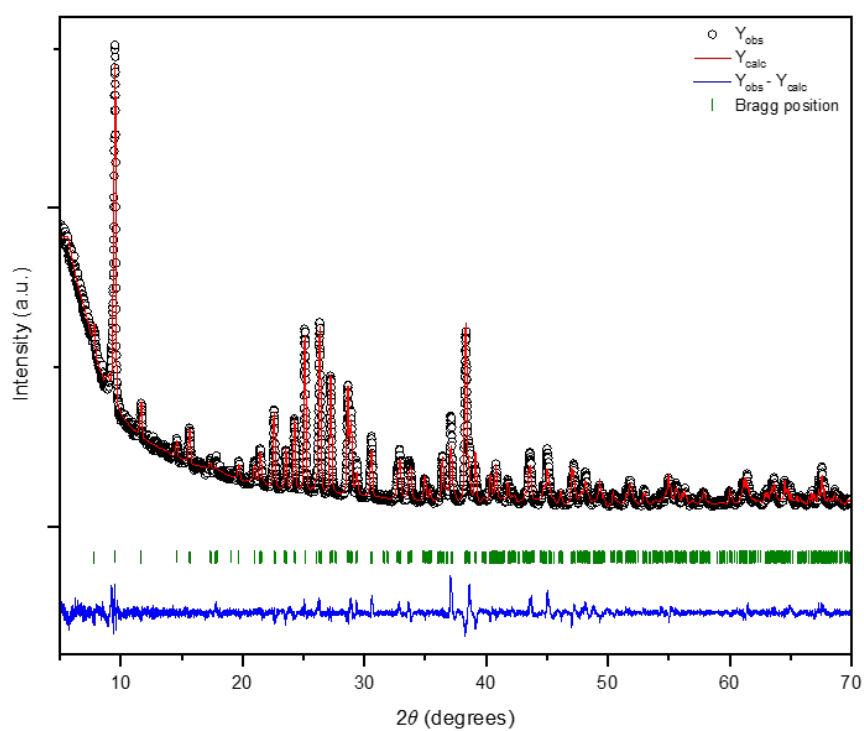
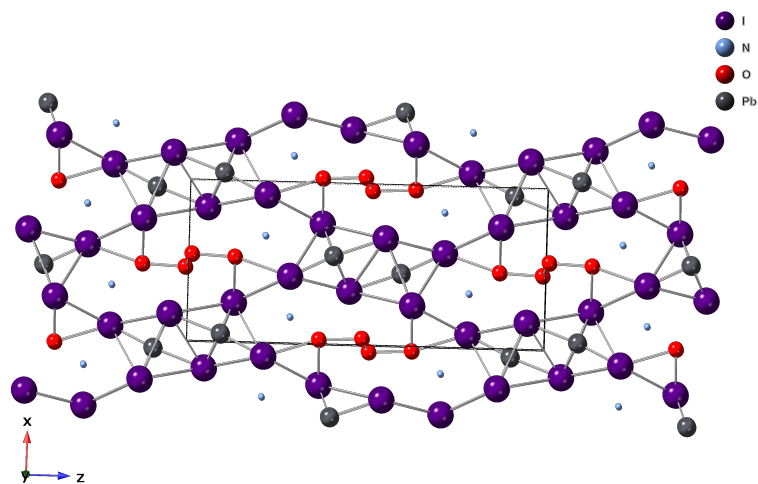
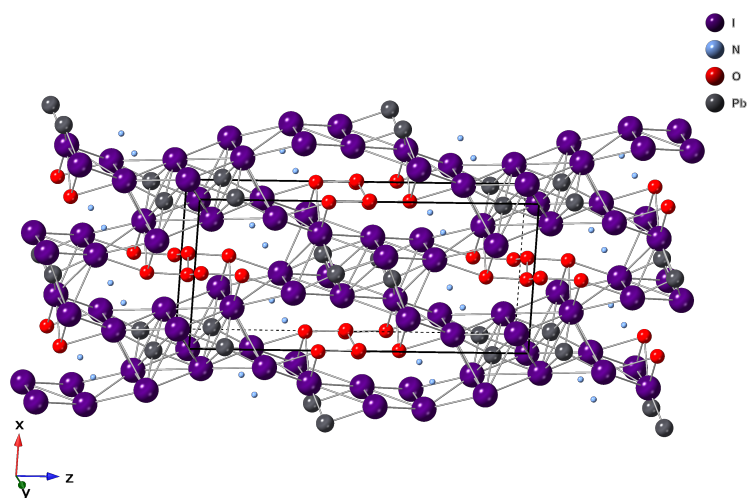


Figure 3.31 X-ray powder diffraction profile from Rietveld refinement for $\text{NH}_4\text{PbI}_3(\text{H}_2\text{O})_2$ performed at room temperature. $R_p = 4.96\%$ and $R_{wp} = 7.06\%$.

3.6 Addressing Impurity Phase Formation in the Optimisation of MAPI Treatments



(a)



(b)

Figure 3.32 Different views of the refined crystal structure of $\text{NH}_4\text{PbI}_3(\text{H}_2\text{O})_2$ using the space group Pnma . The unit cell is described with a black cuboid.

3.7 NH_4PbI_3 as a Decomposition Product in the Annealing of MAPbI_3

To further validate the identification of $\text{NH}_4\text{PbI}_3(\text{H}_2\text{O})_2$ as an impurity phase arising from post-synthetic treatment of MAPI, a systematic approach of comparison between experimental work and literature data was conducted. Initial annealing experiments had revealed only trace amounts of the impurity phase when samples were annealed for up to 2 hours, insufficient for confident phase identification through powder X-ray diffraction. To enhance the visibility of this impurity phase, extended annealing times of 6 and 7 hours under vacuum conditions were applied to new MAPI samples, anticipating an increase in the intensity of impurity reflections.

Figure 3.33 presents the diffraction patterns for these extended vacuum-annealed MAPI samples (Vac 6 h and Vac 7 h) alongside the diffraction pattern for $\text{NH}_4\text{PbI}_3(\text{H}_2\text{O})_2$ synthesised and identified in prior experiments. The dotted lines in figure 3.33 highlight regions where impurity phase reflections in the annealed MAPI samples align with those of the synthesised $\text{NH}_4\text{PbI}_3(\text{H}_2\text{O})_2$, particularly in the 20 to 30° 2θ range. This region demonstrates the strongest overlap, supporting the hypothesis that $\text{NH}_4\text{PbI}_3(\text{H}_2\text{O})_2$ forms as a decomposition product during prolonged annealing.

These findings add significant weight to the argument that the impurity phase in vacuum-annealed MAPI corresponds to $\text{NH}_4\text{PbI}_3(\text{H}_2\text{O})_2$. Additionally, the increasing intensity of these reflections with longer annealing times supports a progressive formation of this phase, suggesting that specific annealing conditions directly influence impurity formation in MAPI.

3.7 NH_4PbI_3 as a Decomposition Product in the Annealing of MAPbI_3

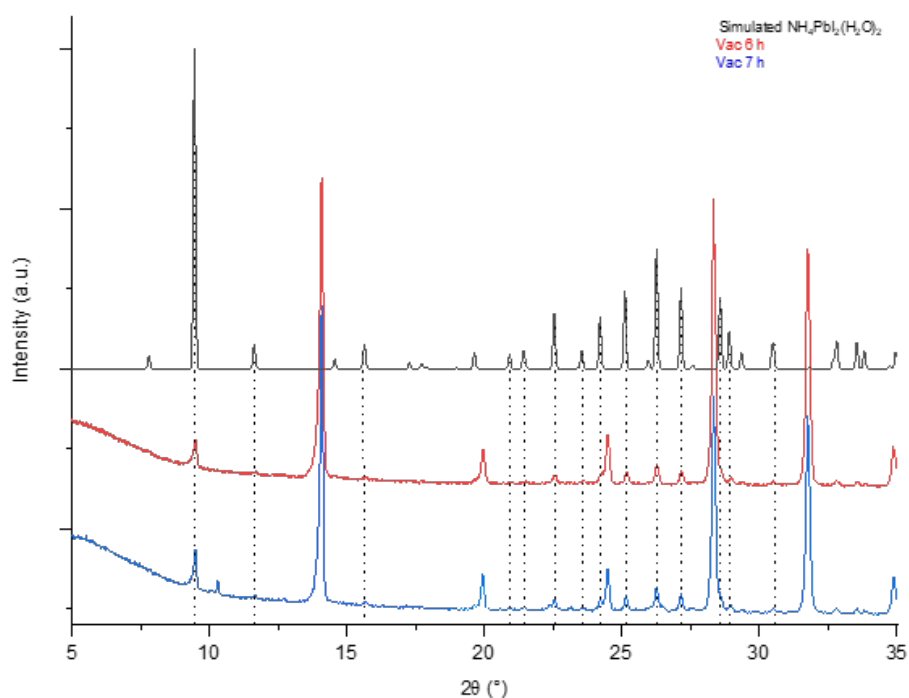
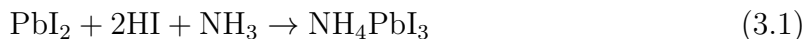


Figure 3.33 Comparison of the simulated diffraction pattern of $\text{NH}_4\text{PbI}_3(\text{H}_2\text{O})_2$ with experimental diffraction patterns of MAPI subjected to extended post-synthesis vacuum-annealing for 6 h (red) and 7 h (blue), highlighting the increased presence of secondary phases for comparison with observed reflections. Dotted lines are used to guide the eye towards matching reflections.

3.7.1 Thermal Decomposition of MAPbI₃

As discussed in Chapter 1, MAPI exhibits relatively low thermal stability, with decomposition typically occurring at temperatures exceeding 150 °C. The decomposition process often initiates with the volatilisation of methylammonium (CH₃NH₃⁺) cations, which results in the formation of lead iodide (PbI₂) as a primary degradation product. During this decomposition, methylammonium iodide (MAI) can break down into methylamine (CH₃NH₂) and hydrogen iodide (HI). The byproducts, namely NH₃ and HI, may further react with PbI₂ to generate ammonium lead iodide (NH₄PbI₃). This reaction occurs due to the presence of NH₃, which can protonate to form NH₄⁺, thus stabilising the ammonium form of the perovskite as shown in Equation 3.1.



The phenomenon of NH₄PbI₃ formation has been documented in the literature during the synthesis of both MAPI and formamidinium lead iodide (FAPbI₃), where yellow crystals of NH₄PbI₃ are produced [36, 38, 41, 42]. Schaefer *et al.* described a mechanism for this degradation in FAPbI₃, highlighting successive condensation reactions of formamidine that release ammonia, eventually leading to the formation of a linear trimer that cyclises into the *sym*-triazine molecule [37].

However, most studies report this degradation pathway in the context of material synthesis, often in the presence of hydrated phases of MAPbI₃ or FAPbI₃, which can trigger the degradation reactions. In contrast, annealing under high-temperature vacuum conditions generally excludes residual water species. Nevertheless, it is clear that NH₃ plays a crucial role in this mechanism. Huang *et al.* utilised X-ray photoelectron spectroscopy to demonstrate that MAPbI₃ undergoes direct cation substitution with

3.7 NH_4PbI_3 as a Decomposition Product in the Annealing of MAPbI_3

NH_4^+ , leading to the formation of NH_4PbI_3 . This transformation was observed under both low and high pressures of NH_3 gas [41].

3.7.2 Formation of NH_4PbI_3 During Annealing

The formation of NH_4PbI_3 is particularly pronounced when annealing occurs in iodine-rich environments or within sealed systems (such as quartz tubes) where decomposition gases cannot escape. In these scenarios, NH_4PbI_3 can crystallise as a secondary phase, competing with the formation of PbI_2 . The presence of NH_4PbI_3 can be detected in X-ray diffraction patterns from iodine-annealed samples, indicated by characteristic reflections that differ from those of MAPbI_3 and PbI_2 . However, its prevalence diminishes significantly during vacuum annealing. Therefore, it is likely that iodine enhances the degradation of MAPbI_3 when subjected to vacuum-sealed environments, similar to findings reported in studies conducted in air [43]. Once the vacuum is disrupted by opening the quartz tube, the sample is immediately exposed to moisture in the air. Given the hygroscopic nature of these materials, this exposure accounts for the observed formation of the hydrated phase of ammonium lead iodide, specifically $\text{NH}_4\text{PbI}_3(\text{H}_2\text{O})_2$, in the post-synthetically treated samples.

3.7.3 Impact on Material Properties and Challenges

The formation of NH_4PbI_3 during the thermal degradation of MAPbI_3 has not been shown to be detrimental to optoelectronic device performance. Although NH_4PbI_3 possesses distinct band gap and optoelectronic properties compared to MAPbI_3 , which could theoretically hinder charge transport and reduce device efficiency, several reports indicate that the presence of NH_4PbI_3 as a minority phase does not significantly impair

the optoelectronic properties of MAPbI₃ thin films [36, 44].

Mitigating the formation of NH₄PbI₃ during annealing poses challenges, as it closely resembles the chemical structure of MAPbI₃. Some studies suggest that exposure to methylamine gas can revert NH₄PbI₃ back to MAPbI₃ [41, 45], presenting a potential post-processing strategy for annealed materials. Furthermore, controlling the annealing environment is crucial in minimising the transformation from MAPbI₃ to NH₄PbI₃. Strategies may include conducting the annealing process in a more open system under a controlled atmosphere (e.g., nitrogen or vacuum), which facilitates the escape of volatile byproducts and thus reduces the likelihood of secondary phase formation. The materials would then additionally need to be continuously handled under inert atmosphere during characterisation in order to avoid the formation of the hydrated phase and therefore probe the structural changes in absence of air.

3.8 Final Discussion

This chapter has provided an exploration of the structural and dynamic changes in MAPI induced by various post-synthetic treatments. The focus on scattering and diffraction techniques has allowed a comprehensive assessment of how annealing parameters, such as temperature, time, and atmospheric conditions, influence both the material's phase stability and the presence of impurity phases. These insights are critical for understanding the pathways of decomposition and transformation in hybrid perovskites, which bear significant implications for their optoelectronic applications, particularly in photovoltaics.

A key outcome of this study is the identification of NH₄PbI₃(H₂O)₂ as an impurity phase that emerges first as NH₄PbI₃ under vacuum annealing of MAPI, and

is then hydrated when exposed to the air. Comparative X-ray diffraction patterns and simulation-based matching confirm that this hydrated ammonium lead iodide phase forms as a secondary product, likely due to the evolution of ammonia and its subsequent reaction with PbI_2 . The systematic increase in impurity reflections with longer annealing durations supports a progressive formation process, underlining that specific thermal conditions play a crucial role in promoting this decomposition pathway. This observation aligns with existing literature, which reports similar secondary phase formations under high-temperature annealing of perovskites, though these findings extend this understanding to controlled vacuum conditions.

The study also highlights the complex thermal decomposition behaviour of MAPI. The primary degradation route involves the loss of methylammonium cations and the formation of PbI_2 , with potential side reactions that yield NH_4PbI_3 . The results from iodine-annealed samples further suggest that sealed environments enhance this degradation process, as NH_4PbI_3 can crystallise alongside PbI_2 . This behaviour is critical in scenarios where the material's exposure to iodine or ammonia byproducts cannot be effectively managed, as in closed-loop annealing systems.

Furthermore, QENS measurements provided insights into the impact of post-synthetic treatments on the dynamic behaviour of the methylammonium (MA^+) cation within MAPI's crystal lattice. As observed, vacuum annealing alters the rotational freedom of MA^+ , potentially due to subtle structural modifications. The QENS data demonstrate that treated samples exhibit distinct changes in cation mobility, with annealing conditions directly influencing the dynamic environment of the cation, likely contributing to phase stabilisation at lower temperatures. These findings underscore the importance of precise control over annealing conditions, not only to mitigate impurity formation but also to preserve the intrinsic structural and dynamic properties essential

for device performance.

In conclusion, this chapter has established a robust understanding of the structural and dynamic transformations in MAPI subjected to post-synthetic treatments. The identification of $\text{NH}_4\text{PbI}_3(\text{H}_2\text{O})_2$ as a decomposition product provides a valuable insight into impurity phase behaviour, with practical implications for optimising perovskite processing techniques. Future work should focus on refining annealing protocols to balance phase stability with minimal impurity formation, as well as exploring alternative environments (e.g., nitrogen or controlled humidities) that could further stabilise the perovskite structure. These advancements could enhance the reproducibility and durability of MAPI-based devices, contributing to the broader goal of sustainable and high-performance perovskite photovoltaics.

References

- [1] W. Shockley and H. J. Queisser, *J. Appl. Phys.*, 1961, **32**, 510–519.
- [2] National Renewable Energy Laboratory (NREL), *Best Research-Cell Efficiency Chart*, <https://www.nrel.gov/pv/cell-efficiency.html>, Accessed: 2024-07-19, 2024.
- [3] C. Roldan-Carmona, O. Malinkiewicz, R. Betancur, G. Longo, C. Momblona, F. Jaramillo, L. Camacho and H. J. Bolink, *Energy Environ. Sci.*, 2014, **7**, 2968–2973.
- [4] M. Abbas, L. Zeng, F. Guo, M. Rauf, X.-C. Yuan and B. Cai, *Materials*, 2020, **13**.
- [5] S. D. Stranks, G. E. Eperon, G. Grancini, C. Menelaou, M. J. Alcocer, T. Leijtens, L. M. Herz, A. Petrozza and H. J. Snaith, *Science*, 2013, **342**, 341–344.
- [6] D. Shi, V. Adinolfi, R. Comin, M. Yuan, E. Alarousu, A. Buin, Y. Chen, S. Hoogland, A. Rothenberger, K. Katsiev et al., *Science*, 2015, **347**, 519–522.
- [7] S. Wang, L. K. Ono, M. R. Leyden, Y. Kato, S. R. Raga, M. V. Lee and Y. Qi, *J. Mater. Chem. A*, 2015, **3**, 14631–14641.
- [8] L.-L. Gao, C.-X. Li, C.-J. Li and G.-J. Yang, *J. Mater. Chem. A*, 2017, **5**, 1548–1557.
- [9] X. Zhao, W. Hu, H. Xu, Y. Liu, J. Yao, W. Wu, J. Wang, Z. Lu, C. Liu, Z. Su et al., *Nano Energy*, 2016, **28**, 351–358.
- [10] M. Kim, G.-H. Kim, K. S. Oh, Y. Jo, H. Yoon, K.-H. Kim, H. Lee, J. Y. Kim and D. S. Kim, *ACS Nano*, 2017, **11**, 6057–6064.
- [11] N. J. Jeon, J. H. Noh, Y. C. Kim, W. S. Yang, S. Ryu, J. Seo and S. I. Seok, *Nat. Mater.*, 2014, **13**, 897–903.
- [12] H. Zhang, J. Cheng, D. Li, F. Lin, J. Mao, C. Liang, A. K. Jen, M. Grätzel and W. C. Choy, *Adv. Mater.*, 2017, **29**, 1604695.
- [13] A. Amir, M. F. Ahmed, P. Subramanian, H. El-Tanany, G. Salvatore, X. Guo and J. P. Correa-Baena, *Solar Energy Mater. Solar Cells*, 2020, **217**, 110737.
- [14] Q. Chen, H. Zhou, T.-B. Song, S. Luo, Z. Hong, H.-S. Duan, L. Dou, Y. Liu and Y. Yang, *Nano Letters*, 2014, **14**, 4158–4163.

- [15] Z. Ren, A. Ng, Q. Shen, S. H. Cheung, H. C. Gokkaya, A. B. Djurišić and C. Surya, *Sci. Reports*, 2014, **4**, 6752.
- [16] F. X. Xie, D. Zhang, H. Su, X. Ren, K. S. Wong, M. Grätzel and W. C. H. Choy, *ACS Nano*, 2015, **9**, 639–646.
- [17] S. R. Raga, M.-C. Jung, M. V. Lee, M. R. Leyden, Y. Kato and Y. Qi, *Chem. Mater.*, 2015, **27**, 1597–1603.
- [18] J. Liu, C. Gao, X. He, Q. Ye, L. Ouyang, D. Zhuang, C. Liao, J. Mei and W. Lau, *ACS Appl. Mater. Interfaces*, 2015, **7**, 24008–24015.
- [19] J. L. Minns, Ph.D. Thesis, University of Kent, 2021.
- [20] C. C. Stoumpos, D. H. Cao, D. J. Clark, J. Young, J. M. Rondinelli, J. I. Jang, J. T. Hupp and M. G. Kanatzidis, *Chem. Mater.*, 2016, **28**, 2852–2867.
- [21] O. Arnold and et al., *Nucl. Instrum. Methods Phys. Res. A*, 2014, **764**, 156–166.
- [22] M. Project, *Mantid: Manipulation and Analysis Toolkit for Instrument Data*, <http://dx.doi.org/10.5286/SOFTWARE/MANTID>, 2013.
- [23] A. M. A. Leguy, J. M. Frost, A. P. McMahon, V. G. Sakai, W. Kochelmann, C. Law, X. Li, F. Foglia, A. Walsh, B. C. O’Regan, J. Nelson, J. T. Cabral and P. R. F. Barnes, *Nat. Commun.*, 2019, **6**, 7124.
- [24] *I11 Beamline at the DLS, Oxford, UK*, www.diamond.ac.uk/Instruments/Crystallography/I11.
- [25] SNBL at the ESRF, Grenoble, France, www.esrf.fr/UsersAndScience/Experiments/CRG/BM01.
- [26] R. Day, (KAR id:94069), Master of Science by Research (MScRes) thesis, University of Kent, 2022.
- [27] M. T. Weller, O. J. Weber, P. F. Henry, A. M. Di Pumpo and T. C. Hansen, *Chem. Commun.*, 2015, **51**, 4180–4183.
- [28] T. Chen, B. J. Foley, B. Ipek, M. Tyagi, J. R. D. Copley, C. M. Brown, J. J. Choi and S. H. Lee, *Phys. Chem. Chem. Phys.*, 2015, **17**, 31278–31286.
- [29] A. A. Bakulin, O. Selig, H. J. Bakker and et al., *J. Phys. Chem. Lett.*, 2015, **6**, 3663–3669.
- [30] V. K. Sharma, R. Mukhopadhyay, A. Mohanty, V. G. Sakai, M. Tyagi and D. D. Sarma, *J. Phys. Chem. C*, 2021, **125**, 13666–13676.
- [31] P. S. Whitfield, N. Herron, W. E. Guise, K. Page, Y. Q. Cheng, I. Milas and M. K. Crawford, *Sci. Rep.*, 2016, **6**, 1–16.
- [32] J. L. Minns, Ph.D. Thesis, University of Kent, 2021.
- [33] R. Day, Ph.D. Thesis, University of Kent, 2022.
- [34] J. L. Minns, P. Zajdel, D. Chernyshov, W. Van Beek and M. A. Green, *Nat. Commun.*, 2017, **8**, 1–5.

-
- [35] A. Bonadio, C. A. J. Escanhoela, F. P. Sabino, G. Sombrio, V. G. de Paula, F. F. Ferreira, A. Janotti, G. M. Dalpiana and J. A. Souza, *J. Mater. Chem. A*, 2021, **9**, 1089.
- [36] W. T. M. Van Gompel, R. Herckens, G. Reekmans, B. Ruttens, J. D'Haen, P. Adriaensens, L. Lutsen and D. Vanderzande, *J. Phys. Chem. C*, 2018, **122**, 4117–4124.
- [37] F. C. Schaefer, I. Hechenbleikner, G. A. Peters and V. P. Wystrach, *Russ. Chem. Bull.*, 1959, **81**, 1466–1470.
- [38] C. C. Stoumpos, C. D. Malliakas and M. G. Kanatzidis, *Inorg. Chem.*, 2013, **52**, 9019–9038.
- [39] L. Prisinzano, D. Delmonte, K. C. Ravaglia, V. Vit and L. Righi, *Mater. Res. Express*, 2020, **7**, 115503.
- [40] L. Fan and et al., *Acta Crystallograph. E*, 2007, **63**, i189.
- [41] W. Huang, J. S. Manser, S. Sadhu, P. V. Kamat and S. Ptasinska, *J. Phys. Chem. Lett.*, 2016, **7**, 5068–5073.
- [42] R. O. Agbaoye, G. A. Adebayo and S. Kenmoe, *J. Phys. Chem. Sol.*, 2021, **151**, 109860.
- [43] A. Senocrate, I. Moudrakovski, G. Y. Kim and et al., *Angew. Chem. Int. Ed.*, 2017, **129**, 7863–7867.
- [44] H. Si, Q. Liao, Z. Kang, Y. Ou, J. Meng, Y. Liu, Z. Zhang and Y. Zhang, *Adv. Func. Mat.*, 2017, **27**, 1701804.
- [45] Y. Zong, Y. Zhou, M. Ju, H. F. Garces, A. R. Krause, F. Ji, G. Cui, X. C. Zeng, N. P. Padture and S. Pang, *Angew. Chem. Int. Ed.*, 2016, **128**, 14943–14947.

Chapter 4

Investigating Cation Dynamics in MAPI Using Solid-State NMR Techniques

4.1 Introduction

Building upon the findings presented in the previous chapter, this section focuses on utilising solid-state NMR (ssNMR) to measure the impact of post-synthetic treatments on MAPI. The soft ionic lattice of MAPI is known for its susceptibility to degradation due to external factors such as moisture, temperature, and light [1–3]. As a result, there is a pressing need to develop treatments that stabilise and potentially enhance the material's properties in both bulk and thin film forms.

Various analytical techniques have been employed to assess the structure and dynamics of MAPI and other organic cation based perovskites. Techniques such

as XRD, thermogravimetry, mass spectrometry, and microscopy provide valuable information on crystallinity, morphology, and structural changes [4–8]. However, XRD and other long range techniques often struggle to elucidate the effects on the organic cations due to their lower intensity compared to the dominant inorganic components.

To address this limitation, ssNMR has emerged as a powerful tool. Unlike XRD, ssNMR is adept at probing atomic level interactions and can specifically characterise the organic cations in isolation from the surrounding inorganic lattice [9–20]. This chapter leverages ssNMR to explore the effects of post-synthetic treatments on the dynamics of the organic cations within MAPI. By examining the intricate variations in the NMR spectra of treated samples, we aim to provide critical insights into the dynamic changes induced by these treatments, demonstrating the unique value of ssNMR in understanding the subtle yet significant alterations in perovskite materials subjected to post-synthetic modifications.

4.2 Experimental

4.2.1 Solid-state ^1H NMR Spectroscopy

Solid-state MAS NMR experiments were performed on pristine MAPI and post-synthetically treated samples (Vacuum-Annealed 1 h, Vacuum-Annealed 2 h, and I_2 -Annealed). Two different spectrometers were used for the experiments:

- **9.4 T Spectrometer:** Samples were packed into 2.5 mm zirconia rotors, and the experiments were conducted on a Bruker AVANCE-NEO 9.4 T NMR spectrometer (^1H Larmor frequency of 400 MHz) equipped with a 2.5 mm HXY probe in double resonance mode. The MAS frequency was set to 25 kHz. Optimised parameters

used include a pulse length of 3.74 μs , and an rf field amplitude, ν_1 of 66.8 kHz. The 1D spectra resulted from averaging with 4 scans with a recovery delay of 20 s. The T_1 relaxation times were measured using saturation recovery experiments, with 1 scan per measurement, a recovery delay of 3 seconds, and a saturation pulse train consisting of 5 pulses with a 0.005 s delay between pulses. The relaxation curve was fitted to a single exponential model. Adamantane ($\text{C}_{10}\text{H}_{16}$) was used as the external reference for chemical shift calibration at 1.87 ppm.

- **18.8 T Spectrometer:** Samples were packed into 1.3 mm zirconia rotors and experiments were carried out using a Bruker AVANCE-NEO 18.8 T NMR spectrometer (^1H Larmor frequency of 800 MHz) equipped with a 1.3 mm HXY probe in double mode. A MAS frequency of 40 kHz was applied. Experiments were performed using a DEPTH pulse sequence to suppress background signals, with 16 scans, pulse length of 1.19 μs , ν_1 of 210.5 kHz, and a recycle delay of 60 s. The T_1 relaxation times were measured using saturation recovery experiments, with 2 scans per measurement, a recovery delay of 2 seconds, and a saturation pulse train consisting of 11 pulses with a 0.03 s delay between pulses. The relaxation curve was fitted to a single exponential model. Adamantane was again used as the external chemical shift reference at 1.87 ppm.

4.2.2 Solid-state ^{13}C NMR Spectroscopy

For solid-state ^{13}C MAS NMR, pristine and treated MAPI samples were packed into 2.5 mm zirconia rotors. Experiments were conducted using a Bruker AVANCE-NEO 9.4 T NMR spectrometer (^1H Larmor frequency of 400 MHz) equipped with a 2.5 mm HXY probe in double mode, operating at a MAS frequency of 25 kHz. The 1D ^{13}C NMR spectra were acquired using single-pulse experiment with 912 scans, a pulse

length of 3.3 μs , ν_1 of 75.8 kHz, and a recovery delay of 40 s. ^1H decoupling sequence was applied during the acquisition utilising a SPINAL-64 decoupling pulse with a pulse length of 5.6 μs . Adamantane was used as the external standard for chemical shift calibration at 37.77 ppm.

4.2.3 Solid-state ^{14}N NMR Spectroscopy

Solid-state ^{14}N MAS NMR measurements were performed on both pristine and annealed MAPI samples packed into 4 and 3.2 mm zirconia rotors, using two different spectrometers:

- **9.4 T Spectrometer:** Experiments were conducted using a Bruker AVANCE-NEO 9.4 T NMR spectrometer (^1H Larmor frequency of 400 MHz) with a 4 mm WVT triple-resonance probe and a 25–32 MHz insert to tune the probe to 28.9 MHz. The MAS frequency was 5 kHz. The 1D ^{14}N NMR spectra were acquired using single-pulse experiment. The pulse parameters included a pulse length of 10.48 μs , ν_1 of 23.9 kHz, 1024 scans, and a recovery delay of 0.25 s. ^1H decoupling sequence was applied during the acquisition utilising a SPINAL64 decoupling pulse with a pulse length of 19.5 μs . Probe temperature was controlled and calibrated using $\text{Pb}(\text{NO}_3)_2$ and variable temperature measurements were conducted at several temperatures between 295 - 350 K. Ammonium chloride (NH_4Cl) was used as the external standard for chemical shift calibration.
- **18.8 T Spectrometer:** Additional experiments were conducted on a Bruker AVANCE-NEO 18.8 T NMR spectrometer (^1H Larmor frequency of 800 MHz) using a 3.2 mm probe with a MAS frequency of 5 kHz. The 1D ^{14}N NMR spectra were acquired using single-pulse experiment. ^1H decoupling sequence

4.3 Investigation of MA⁺ Cation Dynamics and Impurities in Post-Synthetically Treated MAPI via ¹H NMR

was applied during the acquisition. A pulse length of 6.25 μs , ν_1 of 40 kHz, 1024 scans, and a recovery delay of 0.5 s. ¹H decoupling sequence was applied during the acquisition utilising a SPINAL-64 decoupling pulse with a pulse length of 16.67 μs . Temperature control and calibration were performed using $\text{Pb}(\text{NO}_3)_2$, and ammonium chloride was used as the external standard for chemical shift calibration.

Topspin SOLA with the QUADALL model was used to simulate the ¹⁴N MAS NMR spectra.

4.3 Investigation of MA⁺ Cation Dynamics and Impurities in Post-Synthetically Treated MAPI via ¹H NMR

Proton NMR (¹H NMR) spectroscopy is particularly useful for investigating the MA⁺ cation in MAPI, as it provides direct insight into the hydrogen atoms within the cation. This allows for a detailed examination of changes in the local cation environment and its interactions with the inorganic framework following post-synthetic treatments. By focusing on the hydrogen nuclei, ¹H NMR can reveal information about the dynamics of the cation, hydrogen bonding interactions, and structural modifications. In the tetragonal phase of pristine MAPI, Whitfield *et al.* describes the dynamic disorder of the MA⁺ cation, which can adopt multiple configurations [21]. The cation may either be disordered across eight possible orientations or ordered into four distinct orientations. While earlier models typically assumed a four-fold order, recent studies indicate that the MA⁺ cation actually exhibits eight-fold disorder at lower temperatures within the

4.3 Investigation of MA⁺ Cation Dynamics and Impurities in Post-Synthetically Treated MAPI via ¹H NMR

tetragonal phase. Furthermore, an alternative model suggests that the nitrogen atom remains ordered, while the methyl group exhibits disorder [21]. However, distinguishing between these models is challenging due to the rapid reorientation of the cation at room temperature; thus, the majority of 1D NMR measurements tend to reflect an average of these orientations rather than providing specific details about individual configurations.

Following this, investigating the impact of post-synthetic treatments on the organic cation, solid-state NMR experiments were conducted to better understand how these treatments influence the dynamics and orientations of the MA⁺ cation. By examining the changes in the NMR spectra, the aim is to elucidate the structural and dynamical modifications that occur in MAPI as a result of various post-synthetic processes. This approach will provide insights into the interplay between the organic cation and the inorganic framework, shedding light on the effects of treatments such as vacuum annealing and iodine doping on the overall material properties.

4.3.1 Results from ¹H NMR

Initially, a 1D NMR spectrum was obtained for pristine MAPbI₃, revealing characteristic signals at 6.3 and 3.3 ppm, attributed to the NH₃⁺ and CH₃ groups of the methylammonium cation, respectively (Figure 4.1). The corresponding spectrum for the MAI precursor exhibited similar signals; however, with notable linewidth broadening due to higher density of protons and more restricted motions.

Comparative analysis was performed on selected post-synthetically treated samples; vacuum-annealed 1 h, vacuum-annealed 2 h, and annealed in the presence of iodine. Synthesis and post-synthetic treatments are described in Chapter 3. All materials

4.3 Investigation of MA⁺ Cation Dynamics and Impurities in Post-Synthetically Treated MAPI via ¹H NMR

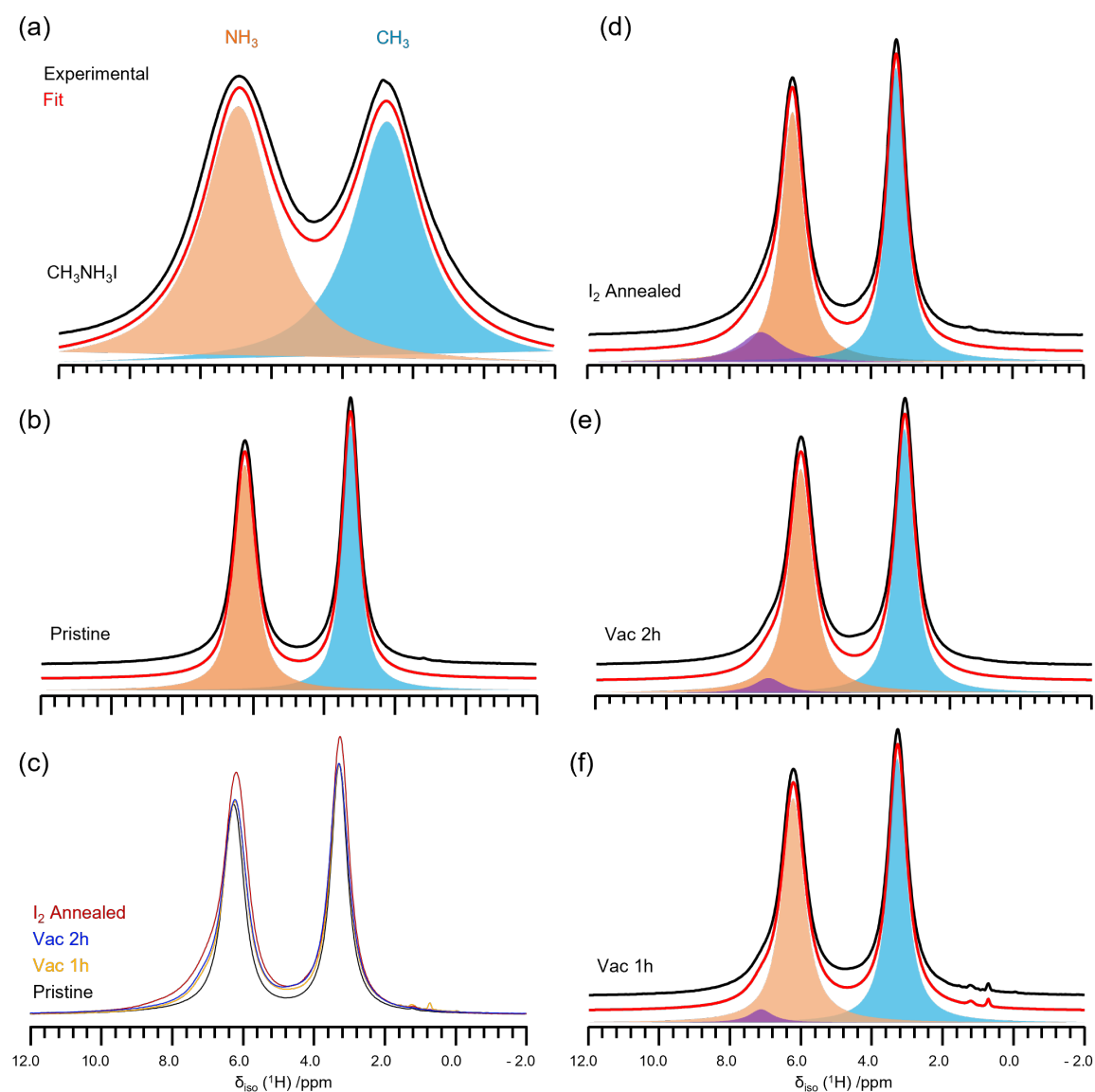


Figure 4.1 Experimental (black) and simulated (red) ¹H MAS NMR spectra at 9.4 T with a MAS frequency of 25 kHz for (a) MAI precursor, (b) pristine MAPbI₃, (d) vacuum-annealed for 1 h, (e) vacuum-annealed for 2 h, and (f) iodine-annealed samples. Spectra were collected at room temperature and simulated as the sum of the signals of three species: CH₃ (blue), NH₃⁺ (orange) and NH₄⁺ (purple). Panel (c) shows an overlay of the four spectra to highlight the broadening of the NH₃ signal.

4.3 Investigation of MA⁺ Cation Dynamics and Impurities in Post-Synthetically Treated MAPI via ¹H NMR

display NH₃ and CH₃ signals at 6.2 and 3.3 ppm, respectively. Minimal changes are seen in the methyl region of the spectrum between pristine and treated samples, except for a slight decrease in signal intensity, suggesting potential changes in sample crystallinity. Intriguingly, a slight broadening of the signal associated with the ammonium side of the cation was observed in all samples, but this is most noticeable in the iodine-annealed sample. Additionally, simulation of the lineshape for each spectrum hinted at the presence of a third signal, which was not visible experimentally due to the broad nature of the proton signals. However, due to its close proximity to the region in which ammonium resonates, it is likely to be caused by a similar ammonium containing species within these samples.

To delve deeper into the characterisation of this third signal, additional 1D proton experiments were conducted at 18.8 T using faster magic angle spinning (MAS) to enhance signal resolution. Figure 4.2 illustrates the obtained spectra, revealing the characteristic NH₃ and CH₃ signals around 6.2 and 3.2 ppm, respectively. Notably, a distinct third signal at 7.0 ppm is observed in the spectra of all treated materials, indicating successful signal separation. The simulation results detailed in Tables 4.2, 4.3, and 4.4, attribute a 5% molar fraction to this third signal in the vacuum-annealed samples, and up to 11% in the iodine-annealed sample. Its close chemical shift to NH₃ suggests its origin as a similar cation species. It is likely that this signal is caused by the presence of an NH₄⁺ cation, stemming from NH₄PbI₃ impurities within the vacuum treated samples, demonstrating these ¹H NMR studies are consistent with results obtained from synchrotron diffraction and as reported in literature [22]. Interestingly, while NMR easily detected this impurity, XRD struggled to identify and refine it using in-house facilities alone, leveraging the importance of NMR to study these kinds of systems and overall why the use of multicharacterative techniques is important when studying tuned and potentially new materials.

4.3 Investigation of MA⁺ Cation Dynamics and Impurities in Post-Synthetically Treated MAPI via ¹H NMR

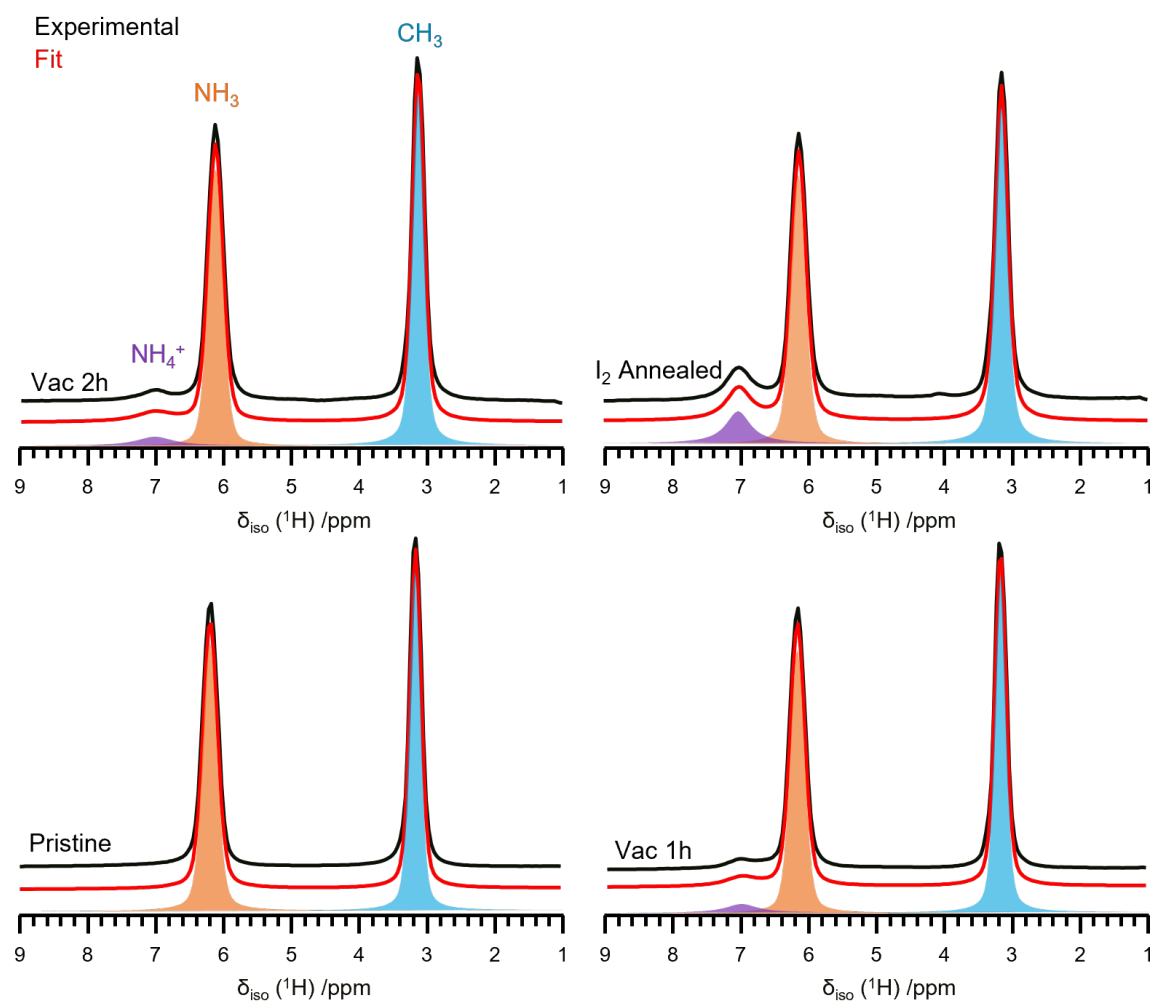


Figure 4.2 Experimental (black) and simulated (red) 1D ¹H MAS NMR spectra of MAPbI₃, vacuum-annealed during 1 h or 2 h, or annealed in the presence of iodine acquired at 18.8 T with a MAS frequency of 40 kHz. Spectra were collected at room temperature simulated as the sum of the signals of three species: CH₃ (blue), NH₃⁺ (orange), and NH₄⁺ (purple).

Table 4.1 Isotropic chemical shift (δ_{iso}) and FWHM values for different proton environments in pristine MAPI, obtained from ¹H NMR measurements at 18.8 T.

Proton Environment	δ_{iso} (ppm)	FWHM (ppm)	Rel. Intensity %
CH ₃	3.18	0.19	50
NH ₃	6.20	0.25	50

4.3 Investigation of MA⁺ Cation Dynamics and Impurities in Post-Synthetically Treated MAPI via ¹H NMR

Table 4.2 Isotropic chemical shift (δ_{iso}) and FWHM values for different proton environments in Vac 1 h, obtained from ¹H NMR measurements at 18.8 T.

Proton Environment	δ_{iso} (ppm)	FWHM (ppm)	Rel. Intensity %
CH ₃	3.19	0.19	48
NH ₃	6.19	0.25	47
NH ₄ ⁺	7.02	0.57	5

Table 4.3 Isotropic chemical shift (δ_{iso}) and FWHM values for different proton environments in Vac 2 h, obtained from ¹H NMR measurements at 18.8 T.

Proton Environment	δ_{iso} (ppm)	FWHM (ppm)	Rel. Intensity %
CH ₃	3.16	0.21	49
NH ₃	6.14	0.26	46
NH ₄ ⁺	7.04	0.64	5

Table 4.4 Isotropic chemical shift (δ_{iso}) and FWHM values for different proton environments in I₂-Annealed, obtained from ¹H NMR measurements at 18.8 T.

Proton Environment	δ_{iso} (ppm)	FWHM (ppm)	Rel. Intensity %
CH ₃	3.17	0.22	42
NH ₃	6.15	0.26	47
NH ₄ ⁺	7.02	0.44	11

4.3 Investigation of MA⁺ Cation Dynamics and Impurities in Post-Synthetically Treated MAPI via ¹H NMR

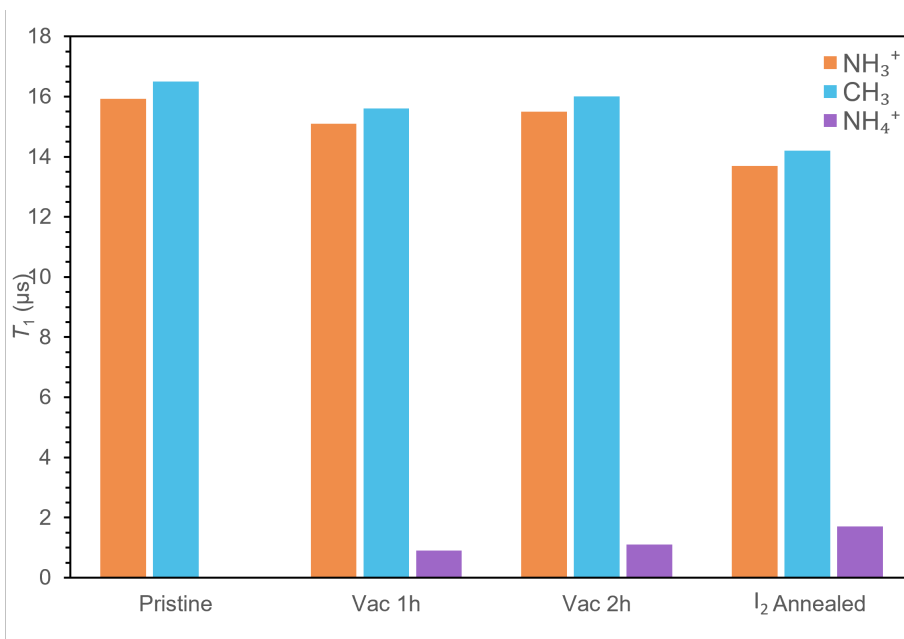


Figure 4.3 Room temperature T_1 relaxation times of CH₃, NH₃⁺, and NH₄⁺ protons for each material measured at 18.8 T with a MAS frequency of 40 kHz.

Figure 4.3 presents the measured longitudinal (or spin lattice) relaxation times (T_1), showing that all measured times fall within the data previously reported literature [23, 24]. Vacuum-annealed samples exhibit faster T_1 relaxation than the pristine MAPI. The recorded relaxation times for the iodine-annealed materials is even shorter than for the vacuum-annealed samples. The potential alterations in cation dynamics observed in these materials following post-synthetic treatments can be linked to several structural changes. These treatments modify the crystal structure by altering the size and symmetry of the perovskite cage, influencing cation mobility. Additionally, changes in hydrogen bonding and octahedral tilting can affect cation movement, while iodine vacancies may reduce restrictions and impact MA⁺ dynamics. However, more precise control over the synthetic procedures is necessary to confirm these hypotheses.

4.4 Analysing Carbon Environments in Treated MAPI Using ^{13}C NMR

Using ^{13}C NMR spectroscopy, the carbon component of the MA^+ cation can be effectively probed to investigate changes in the local cation environment and its interactions with the inorganic framework as a result of post-synthetic treatments. Despite its utility, ^{13}C NMR is not the most time efficient method due to the low natural abundance (1.1%) of the ^{13}C isotope, requiring extended acquisition times to obtain sufficient signal to noise ratios. As previously discussed, the MA^+ cation in MAPI can adopt four distinct orientations within the cavities of the perovskite structure [21]. Each of these orientations potentially experiences a different chemical shift at the ^{13}C nucleus, theoretically resulting in four separate resonances in the ^{13}C NMR spectrum. However, due to the rapid reorientation of the organic cation at temperatures above 160 K, the observed spectrum (see Figure 4.4) reflects an averaged isotropic chemical shift, yielding a single resonance corresponding to the average environment of the four possible orientations. This dynamic averaging is a significant phenomenon that can be explored using NMR spectroscopy. By lowering the sample temperature, thereby reducing the frequency of reorientational hops, it is possible to slow down the dynamic averaging. At sufficiently low temperatures, the individual resonances corresponding to the four orientations of the MA^+ cation could, in principle, be resolved. Nonetheless, given the fast reorientation time of the cation in both the tetragonal and cubic phases, accurately monitoring phase transitions using ^{13}C NMR alone presents significant challenges. Despite this, alterations in the cation environment due to phase changes or other factors can still be detected through shifts in chemical shift values and changes in signal linewidths in the ^{13}C spectrum [25].

4.4 Analysing Carbon Environments in Treated MAPI Using ^{13}C NMR

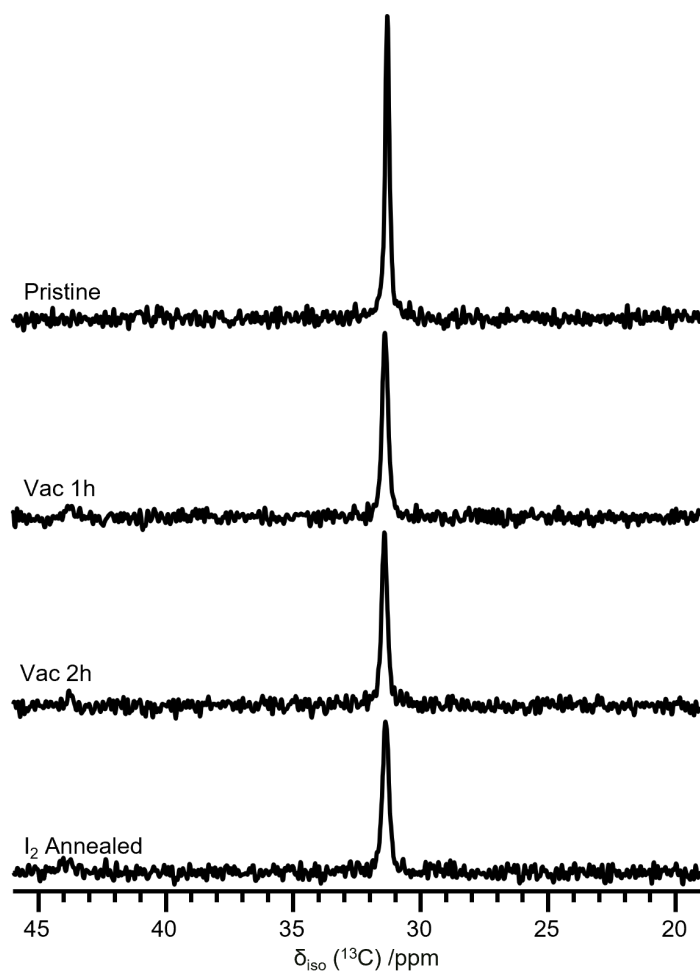


Figure 4.4 Room temperature 1D ^{13}C MAS NMR spectra of pristine and post-synthetically treated MAPI at 9.4 T with a MAS frequency of 25 kHz.

4.4 Analysing Carbon Environments in Treated MAPI Using ^{13}C NMR

Table 4.5 Summary of ^{13}C isotropic chemical shifts, FWHM, and relative intensities for pristine and post-synthetically treated MAPI

Material	δ_{iso} /ppm	Linewidth /Hz	Relative Intensity (%)
Pristine	31.31	18.2	100
Vac 1 h	31.39	23.3	63
Vac 2 h	31.42	23.5	58
I ₂ -Annealed	31.39	25.6	50

Figure 4.4 shows the ^{13}C MAS NMR spectra of pristine MAPI alongside those of three treated materials. The spectra reveal a single peak corresponding to the carbon in the MA^+ cation, with no other carbon-containing compounds detected in the samples. Notably, this includes the synthetic precursor methylammonium iodide, which would typically resonate at around 29.1 ppm. The observed chemical shifts in each sample are consistent with those reported in the literature [26–28].

Upon closer examination, some differences among the treated samples become apparent, as detailed in Table 4.5. Firstly, there is a very small observed increase in chemical shift, potentially indicating a change in the carbon environment of the MA^+ cation. Secondly, there is a noticeable broadening of the signal linewidth, from 18 Hz in the pristine sample to approximately 23 Hz in the vacuum-annealed samples, and further to 26 Hz in the iodine-annealed sample. This broadening could suggest alterations in the cation’s reorientational dynamics, potentially linked to increased disorder within the material and a decrease in crystallinity. However as the broadening is relatively minimal, it is difficult to conclude this from these measurements and the ^{13}C linewidth alone.

Furthermore, the observed signal broadening is accompanied by a decrease in relative intensity, which could suggest decomposition of the organic cation. This occurs despite the absence of detectable carbon containing decomposition products in the

4.5 Structural and Dynamic Insights from Variable Temperature ^{14}N NMR

^{13}C NMR spectra. It is plausible that such impurities exist at concentrations below the detection threshold of ^{13}C NMR, given the isotope's low natural abundance. To enhance detection sensitivity and confirm the presence of these impurities, longer experimental durations would be necessary.

However, as outlined in Section 4.4 of reference [29], it has been observed that during the thermal treatment process, the cation volatilises at high temperatures under vacuum conditions, leaving behind a black residue that deposits on the interior of the tube. Subsequent SEM, EDX, and XRD analyses identified this residue as a long chain hydrocarbon species, implying that the cation decomposition pathway may involve the recombination of carbon containing radicals to form a different organic paraffin species. Since this residue typically deposits in the upper section of the tube, it remains physically separate from the bulk of the sample and, consequently, would not appear in the ^{13}C NMR spectra. Additionally, no other carbon containing decomposition products, such as iodomethane, were detected, raising further questions about the exact decomposition pathway of methylammonium lead iodide under these conditions.

To elucidate the full mechanism of decomposition, particularly the formation of NH_4PbI_3 as identified in the ^1H NMR study, further controlled decomposition experiments would be necessary.

4.5 Structural and Dynamic Insights from Variable Temperature ^{14}N NMR

The use of ^{14}N isotope is highly advantageous for investigating the symmetry of the A site cation lattice in hybrid perovskites due to its high natural abundance and its nature

4.5 Structural and Dynamic Insights from Variable Temperature ^{14}N NMR

as a quadrupolar nucleus ($I = 1$). However, ^{14}N isotope does not produce a central transition, necessitating the acquisition of the entire quadrupolar spectrum to obtain comprehensive data [15]. Notably, the width of a ^{14}N spectrum can be significantly narrower than expected based on structural asymmetry. This phenomenon occurs because the interaction between the quadrupole moment and the electric field gradient (EFG) makes ^{14}N spectra highly sensitive to lattice distortions and cation motions. Changes in asymmetry can lead to either narrower or broader spectral linewidths [14]. As a result of these intertwined effects, it can be challenging to separate the contributions of lattice distortions and cation dynamics.

In hybrid perovskites, ^{14}N NMR provides sensitivity to the reorientation dynamics of cations within the material. However, in MAPI, this sensitivity can be practically limited within the fast motion regime (corresponding tetragonal and cubic phases), as outside this range, the spectral linewidths become prohibitively broad [14]. In this study, variable temperature ^{14}N NMR measurements were employed to investigate potential differences in the dynamics of the organic cation within MAPI resulting from post-synthetic treatments.

At 297 K, pristine MAPI exhibits a characteristic double-horned splitting pattern with a small-intensity centerband, indicative of the tetragonal phase and consistent with observations by Franssen et al. [26]. This splitting pattern, commonly seen in quadrupolar NMR, arises from the ^{14}N nuclear transitions (-1 to 0 and 0 to 1), with each horn corresponding to a distinct transition. The presence of a non-zero ERF, caused by the anisotropic local environment, leads to this splitting. In contrast, at 350 K, the splitting pattern collapses into a single peak, signaling the transition to the cubic phase. This occurs due to the increased symmetry of the nitrogen environment and the surrounding cation cage, which effectively reduces the EFG around the nitrogen

4.5 Structural and Dynamic Insights from Variable Temperature ^{14}N NMR

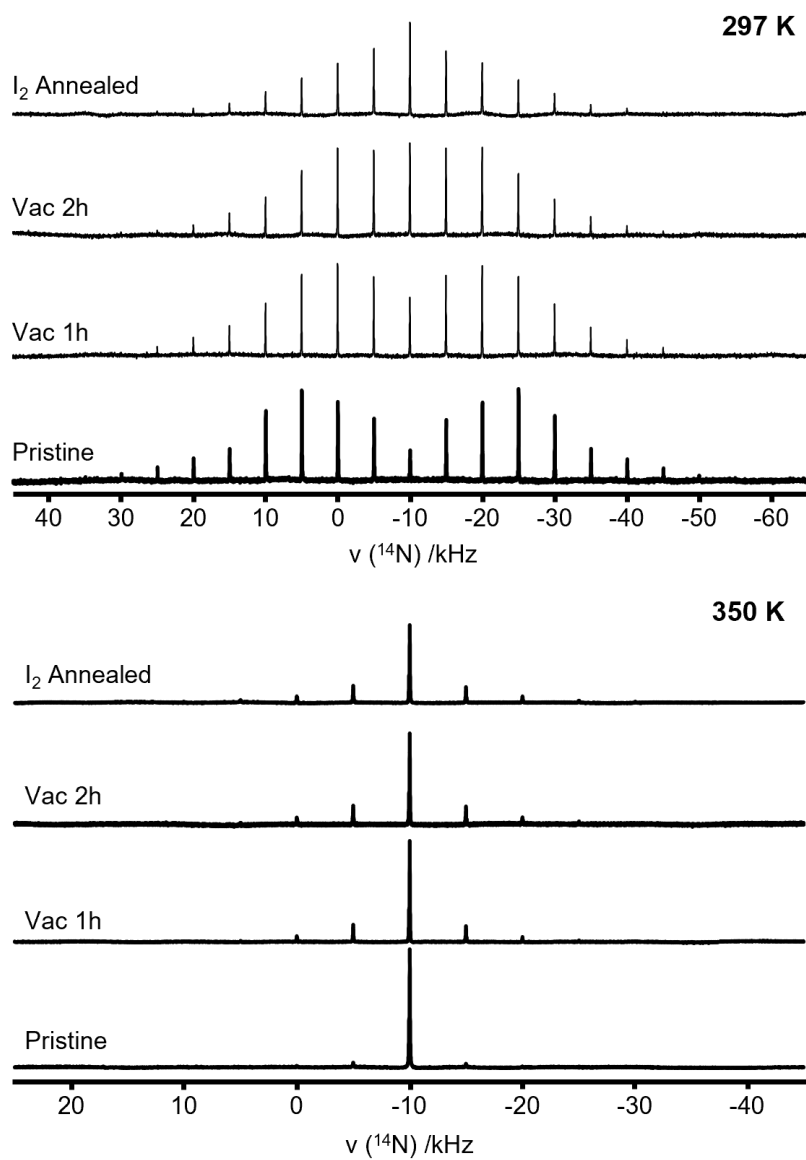


Figure 4.5 1D ^{14}N NMR spectra of pristine and post-synthetically treated MAPI collected at 297 (top) and 350 K (bottom) using a 9.4 T magnetic field and a MAS frequency of 5 kHz.

4.5 Structural and Dynamic Insights from Variable Temperature ^{14}N NMR

nuclei to near zero.

When comparing the pattern of the pristine material to post-synthetically treated samples at room temperature, an obvious observation is the increasing intensity of the centreband. This suggests an altered symmetry of the cation environment at room temperature, allowing for enhanced reorientation of the nitrogen within the lattice cage. Such an alteration could also indicate a change in the octahedral structure to a non-tetragonal configuration, facilitating this difference in reorientation. Specifically, in samples subjected to vacuum annealing (Vac 1 h and Vac 2 h), increased annealing time correlates with increased symmetry of the nitrogen environment, while treatment with iodine results in the most significant alteration.

However, at elevated temperatures, none of the post-synthetically treated samples experience a complete collapse of the spinning sideband pattern, suggesting that these materials do not achieve a transition to a fully cubic phase at this temperature. This incomplete phase transition implies altered nitrogen dynamics within the treated samples. Although the presence of NH_4PbI_3 is identified by ^1H NMR in these samples, it is unlikely that this compound significantly affects the spinning sideband pattern due to its fundamentally different lattice structure. Furthermore, at high temperatures, the central peak intensity for pristine MAPI remains quite large, whereas it decreases across the treated samples.

4.5 Structural and Dynamic Insights from Variable Temperature ^{14}N NMR

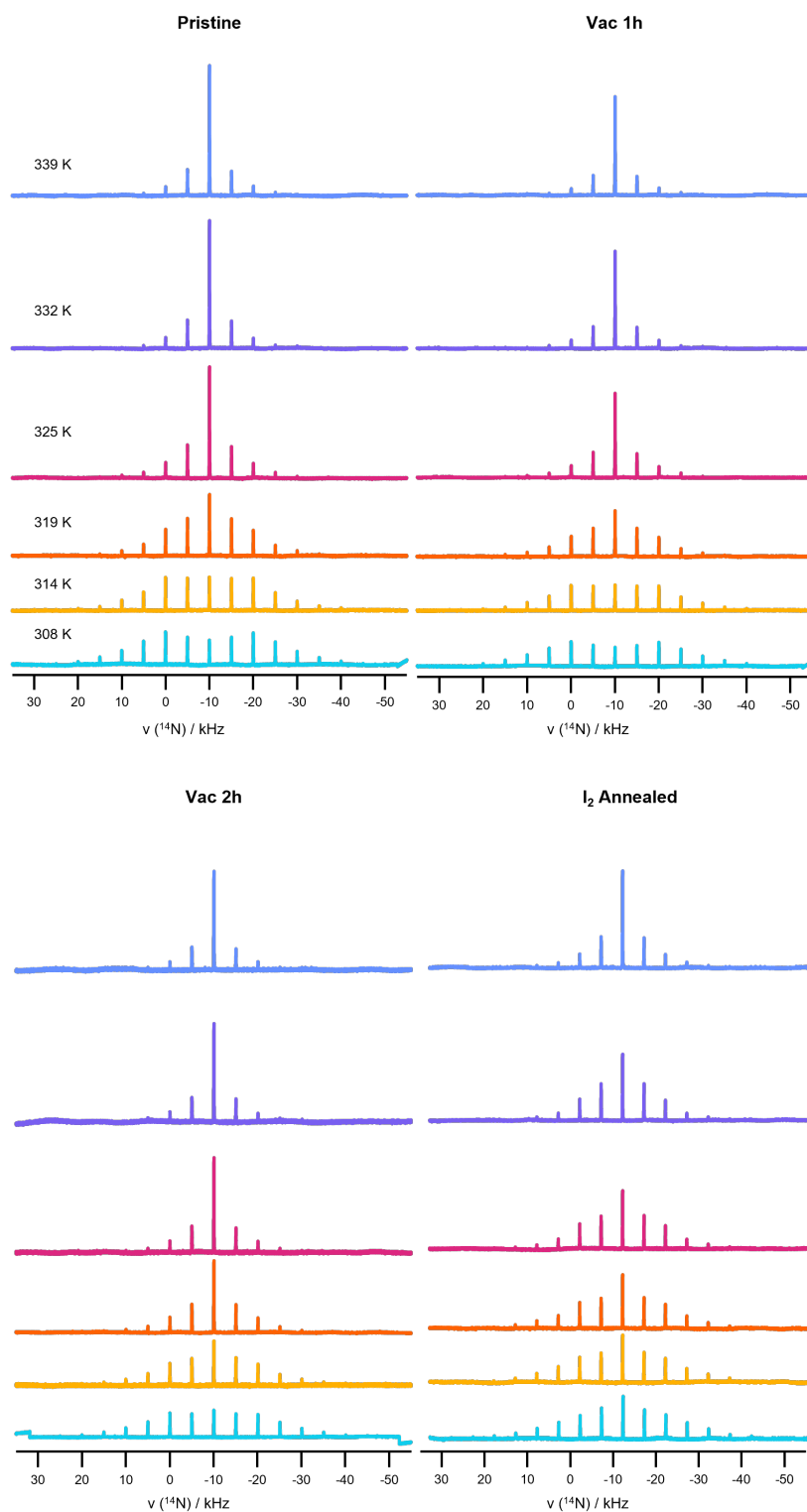


Figure 4.6 1D variable temperature ^1H -decoupled ^{14}N NMR spectra of pristine and post-synthetically treated MAPI collected using a 9.4 T magnetic field and a MAS frequency of 5 kHz.

4.5.1 Temperature Dependent Variations in Quadrupolar Coupling Constant (C_Q) and Their Implications for Phase Transitions in MAPI

By simulating the ^{14}N NMR spectra at various temperatures, as shown in Figure 4.7, key parameters such as the relative intensities of the centerband, spinning sidebands, and the quadrupolar coupling constant (C_Q) can be extracted. These parameters offer critical insights into the local nitrogen environment and its temperature-dependent evolution. When plotted against temperature, they reveal the temperature dependence of the nitrogen quadrupolar interaction, shedding light on structural and dynamic changes such as phase transitions and cation reorientations.

For example, variations in the relative intensities of the centerband and spinning sidebands reflect changes in local symmetry, with higher temperatures typically increasing symmetry, leading to a shift in intensity toward the centerband. Conversely, variations in C_Q signal alterations in the electric field gradient (EFG), helping track transitions from distorted, lower-symmetry phases (such as tetragonal) to higher-symmetry cubic phases. These NMR parameters serve as powerful tools for linking microscopic behaviour to macroscopic structural changes over a range of temperatures.

Figure 4.8 illustrates the variation of C_Q , measured from 295 to 360 K, capturing the tetragonal-to-cubic phase transition of MAPI. These values were extracted from simulations of ^{14}N spectra for four samples: Pristine, Vacuum-Annealed 1 h, Vacuum-Annealed 2 h, and Iodine-Annealed. Monitoring C_Q offers valuable insights into the local environment and motions surrounding the nitrogen atoms as a function of temperature.

Phase transitions typically involve changes in crystal symmetry. In MAPI, a tran-

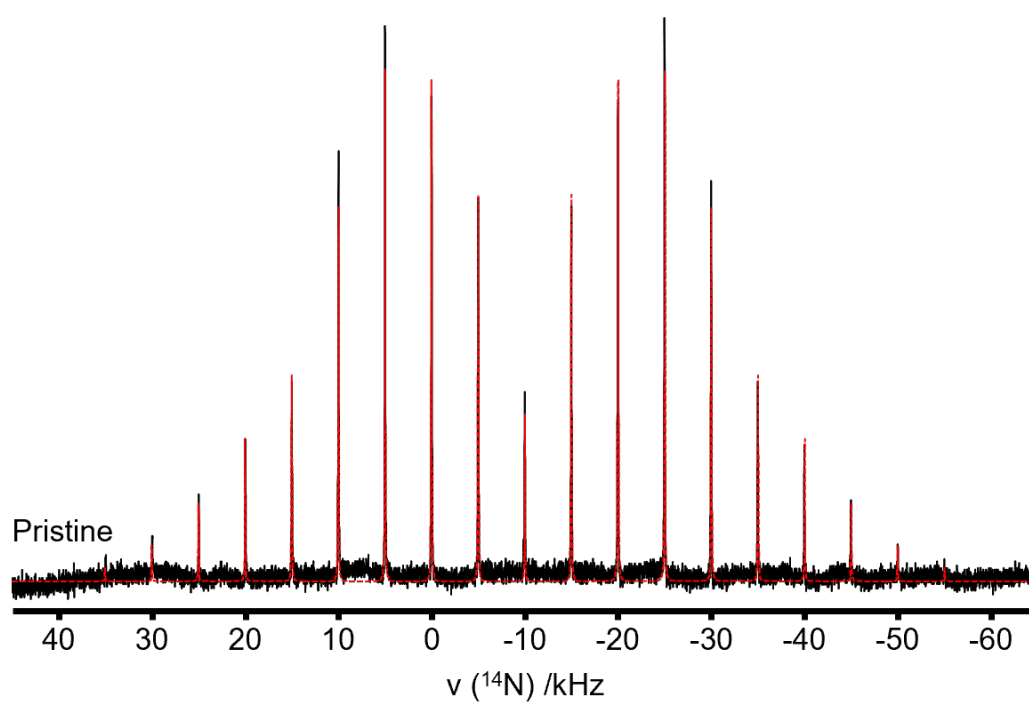


Figure 4.7 1D ^1H -decoupled ^{14}N MAS NMR experimental spectrum of pristine MAPI (black) compared with a spectral simulation (red dashed). The experimental spectrum was recorded at 295 K using a 9.4 T magnetic field and a MAS frequency of 5 kHz. The simulation, generated using the Topspin sola QUADALL model, represents the spectrum as a sum of the centreband (isotropic component) and a series of spinning sidebands (anisotropic component).

4.5 Structural and Dynamic Insights from Variable Temperature ^{14}N NMR

sition from the high-symmetry cubic phase to lower-symmetry phases (e.g., tetragonal or orthorhombic) alters the local environment, which in turn affects the EFG and C_Q . As the temperature rises, atoms may gain greater freedom of motion, leading to dynamic averaging of the EFG and a reduction in C_Q . This temperature dependence is reflected in both gradual and abrupt changes in C_Q , which help distinguish between second-order and first-order phase transitions.

The study of C_Q as a function of temperature provides critical insights into phase transitions, revealing the temperatures at which these occur and shedding light on the nature of the involved phases. Significant changes in C_Q at specific temperatures typically indicate transitions from more symmetric high-temperature phases to less symmetric low-temperature phases. Lower C_Q values are often associated with high-symmetry phases, while higher C_Q values indicate low-symmetry or distorted phases.

In addition, changes in phase transition temperature can also be monitored by comparing the relative intensities of the centerband and/or spinning sideband as a function of temperature, as shown in Figures 4.9 and 4.10.

Pristine MAPI

At lower temperatures, pristine MAPI exhibits high C_Q values, associated with a low centerband intensity and moderate spinning sideband intensity. In contrast, vacuum-annealed and I_2 -annealed samples show lower initial C_Q values, with an increased centerband intensity. This indicates a more symmetric nitrogen environment resulting from post-synthetic treatments. Vacuum annealing, for instance, increases sideband intensity, while I_2 annealing slightly decreases it, suggesting distinct impacts on cation dynamics.

4.5 Structural and Dynamic Insights from Variable Temperature ^{14}N NMR

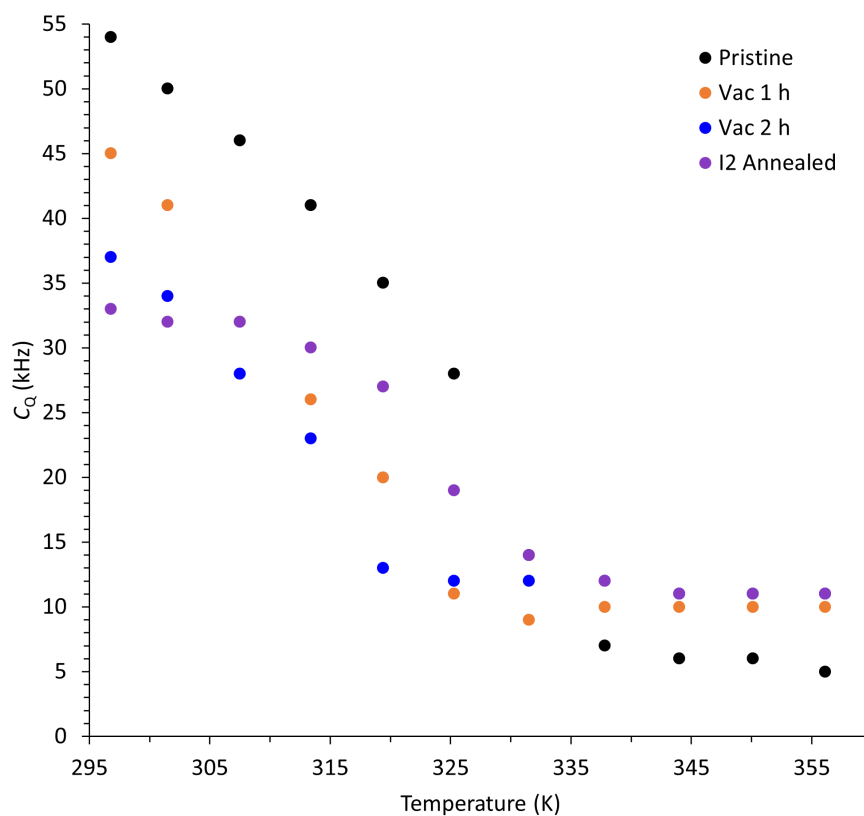


Figure 4.8 Plot of C_Q versus temperature for pristine MAPI (black), vac 1 h (orange), vac 2 h (blue), and I_2 -annealed (purple) samples, illustrating the evolution of the ^{14}N nucleus interaction with the EFG as a function of temperature. The differences in C_Q reflect variations in local symmetry and cation dynamics across the samples due to different post-synthetic treatments.

4.5 Structural and Dynamic Insights from Variable Temperature ^{14}N NMR

As temperature increases, C_Q values generally decrease, reflecting enhanced dynamics and symmetry as MAPI transitions from the tetragonal to cubic phase. The Vacuum-Annealed 1 h sample shows the most rapid decline in C_Q , suggesting more dynamic behaviour and symmetry, whereas the I_2 -annealed sample retains higher C_Q values, indicating persistent structural disorder at elevated temperatures. These results underscore the influence of annealing on the nitrogen environment and MA^+ cation mobility.

In the cubic phase, MAPI's high symmetry leads to a small EFG, reducing C_Q . As temperature decreases, the material transitions to lower-symmetry phases, increasing C_Q values due to lattice distortions. Between 297 and 325 K, the gradual decline in C_Q suggests a second-order phase transition, while between 325 and 337 K, the more abrupt decline points to a first-order transition. In the cubic phase, C_Q plateaus at higher temperatures, indicating a stable, high-symmetry structure.

The centerband intensity increases with temperature, peaking after 325 K, which aligns with the tetragonal-to-cubic phase transition. After 335 K, the intensity levels off, correlating with the stabilization of the cubic phase. The spinning sideband intensity follows a similar trend, increasing until 320 K before sharply dropping at the phase transition temperature, indicating a shift in cation dynamics.

Overall, the analysis of C_Q and relative intensities reveals crucial insights into phase transitions and the dynamic behaviour of MAPI. The observed changes highlight the effects of temperature on symmetry, cation mobility, and overall structure, influenced by post-synthetic treatments.

4.5 Structural and Dynamic Insights from Variable Temperature ^{14}N NMR

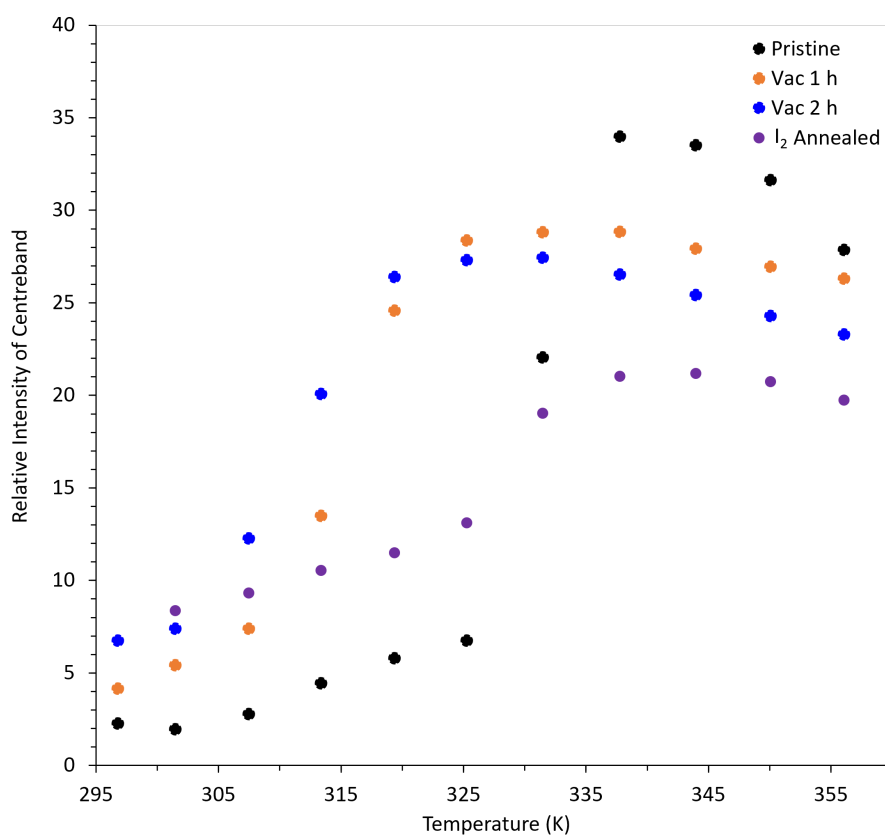


Figure 4.9 Plot of relative intensity of the centreband versus temperature for pristine MAPI (black), vac 1 h (orange), vac 2 h (blue), and I₂ annealed (purple) samples.

4.5 Structural and Dynamic Insights from Variable Temperature ^{14}N NMR

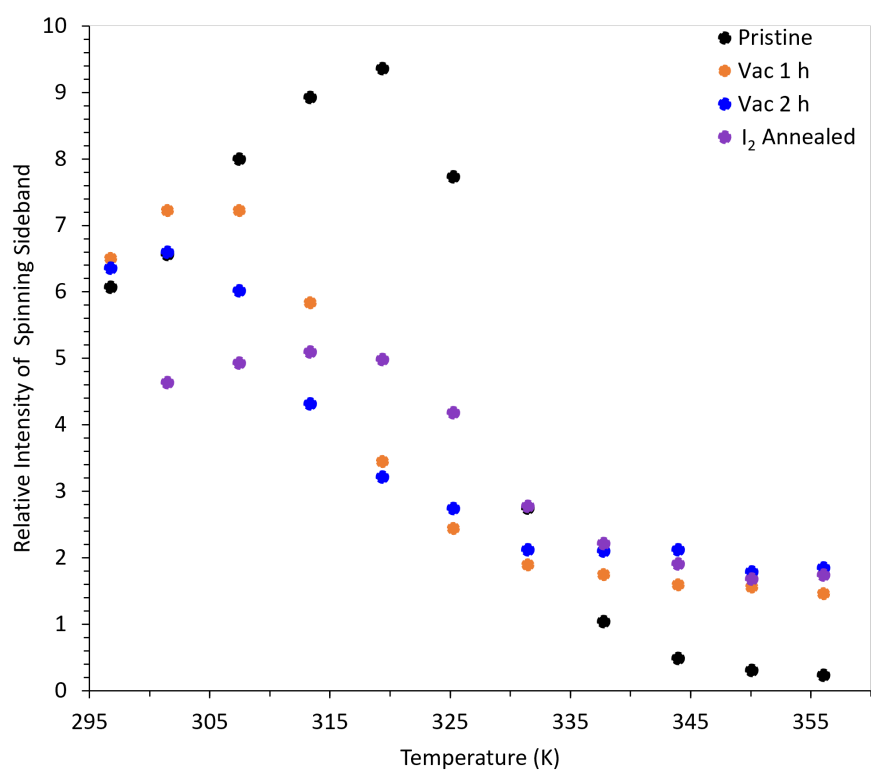


Figure 4.10 Plot of relative intensity of the second spinning sideband versus temperature for pristine MAPI (black), vac 1 h (orange), vac 2 h (blue), and I₂-annealed (purple) samples.

4.5 Structural and Dynamic Insights from Variable Temperature ^{14}N NMR

Vacuum-Annealed MAPI

The vacuum-annealed MAPI samples exhibit significant changes in C_Q compared to pristine MAPI, reflecting modifications in the nitrogen environment and cation dynamics induced by the annealing process. For the Vacuum-Annealed 1 h sample, C_Q is lower at 297 K (45 kHz), suggesting an environment with increased symmetry, consistent with XRD data indicating structural rearrangements. As temperature increases, C_Q decreases more sharply than in pristine MAPI, reaching a plateau (10 kHz) around 325 K. This accelerated decline suggests that vacuum annealing promotes an earlier transition from the tetragonal to cubic phase.

In the Vacuum-Annealed 2 h sample, C_Q is even lower at 297 K (37 kHz) and declines more rapidly, stabilising at 12 kHz by 320 K. The earlier onset and completion of the transition suggest that prolonged annealing increases defect density, leading to a narrower transition range. Notably, post-transition C_Q values remain higher than in pristine MAPI, indicating persistent disorder in the cubic phase, likely due to the partial removal of methylammonium, as discussed in Section 4.4 and Section 4.4 of reference [29]. This removal disrupts intermolecular forces between the organic cation and inorganic framework, impacting phase stability.

Both vacuum-annealed samples show notable trends in centreband and spinning sideband intensities. In the Vacuum-Annealed 1 h sample, centreband intensity increases gradually until a sharp rise at 305 K, stabilising around 29 beyond 325 K. In the 2 h sample, this increase begins earlier (300 K) and levels off after 315 K. Meanwhile, spinning sideband intensity increases slightly before dropping after 305 K, remaining nonzero at higher temperatures, indicating residual disorder. These trends further highlight the impact of vacuum annealing on cation mobility and phase transition behaviour, where increased symmetry is achieved at the cost of defect-induced

4.5 Structural and Dynamic Insights from Variable Temperature ^{14}N NMR

instability in the cubic phase.

I₂-Annealed MAPI

The I₂ -Annealed sample exhibits distinct behaviour compared to both pristine and vacuum-annealed MAPI, with a higher initial C_Q at 297 K (50 kHz), indicating a more distorted nitrogen environment, likely due to structural modifications from iodine exposure. As temperature increases, C_Q decreases gradually, following a trend similar to pristine MAPI but with a less pronounced drop near the phase transition. The plateau value in the cubic phase remains higher (15 kHz), suggesting persistent asymmetry even at elevated temperatures.

The centerband intensity increases with temperature but does not reach the same maximum as in pristine MAPI, suggesting that local distortions hinder complete dynamic averaging of the quadrupolar interaction. The spinning sideband intensity follows a similar pattern, decreasing at the phase transition but remaining more pronounced at higher temperatures than in vacuum-annealed samples. These observations suggest that iodine annealing stabilises structural distortions, suppressing the full transition to a highly symmetric cubic phase.

Similar to vacuum annealing, the defects introduced by iodine treatment likely arise from either the partial removal of methylammonium iodide or the filling of interstitial iodine sites with additional iodine, as proposed in reference [30]. Both mechanisms alter cation-lattice interactions, particularly hydrogen bonding, affecting octahedral tilting in the room-temperature structure and shifting phase transition temperatures.

4.6 Summary of Structural and Dynamic Insights from Solid-State NMR

This chapter underscores the power of solid-state NMR in elucidating structural and dynamic changes induced by post-synthetic treatments in MAPI, particularly concerning the organic cation.

^1H NMR revealed subtle but significant modifications in the local environment of the MA^+ cation, including signal broadening and an additional resonance at 7.0 ppm, suggesting the formation of NH_4^+ impurities. These observations, corroborated by synchrotron diffraction, highlight the importance of complementary techniques in characterising perovskite structural modifications.

Further analysis via ^{13}C NMR spectroscopy identified minor chemical shift variations and increased signal broadening in treated samples, indicative of changes in cation mobility and crystallinity. Additionally, variable-temperature ^{14}N NMR provided insight into the tetragonal-to-cubic phase transition, with C_Q trends revealing distinct responses to post-synthetic treatments. Vacuum annealing enhanced nitrogen environment symmetry, facilitating cation mobility and accelerating the phase transition, albeit introducing defects affecting phase stability. In contrast, iodine annealing preserved structural distortions, suppressing the full transition to the cubic phase by altering cation-lattice interactions.

Overall, these findings illustrate how post-synthetic treatments subtly yet significantly influence MAPI's structural integrity, cation dynamics, and phase stability. The ability of C_Q NMR to track temperature-dependent symmetry and disorder changes makes it a valuable tool for understanding the intricate behaviour of hybrid perovskites

and optimising their performance.

4.7 Overview on the Impact of Phase Transition Behaviour of Post-synthetic treatments

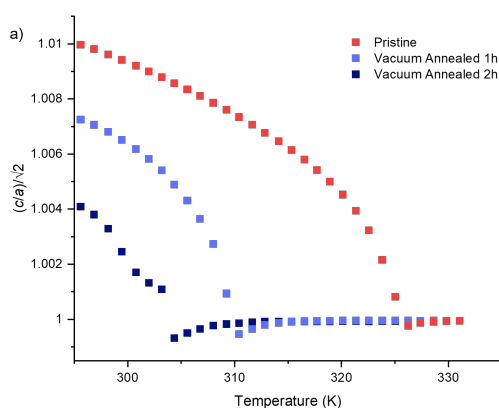
The combined analysis of XRD, QENS, and NMR provides a comprehensive picture of how post-synthetic treatments affect phase transitions in MAPI perovskites. X-ray diffraction (Section 3.4) highlights abrupt structural changes in the inorganic lattice, particularly octahedral tilting, as the material undergoes phase transitions. Figure 4.11a shows synchrotron diffraction data demonstrating reduced transition temperatures and structural modifications with increased annealing time.

Conversely, NMR (presented in Chapter 4) reveals a more gradual evolution in structural parameters, associated with the progressive rotational dynamics of the MA⁺ cation. This is evident from plots of C_Q and relative centerband intensity in Figure 4.11b and c. Some correlations in transition temperatures can be drawn when considering both techniques, as shown in Table 4.6. Differences in reported transition temperatures arise due to varying sensitivities to structural and rotational dynamics.

Additionally, QENS results, though not directly comparable due to differences in timescale sensitivity, provide further evidence of altered hydrogen dynamics, particularly in the tetragonal-to-cubic phase transition region above 270 K (Figures 3.5 and 3.6, Chapter 3.3). While QENS captures collective hydrogen motions on the picosecond-to-nanosecond scale, NMR probes local motions on the nanosecond-to-microsecond scale, offering complementary insights.

4.7 Overview on the Impact of Phase Transition Behaviour of Post-synthetic treatments

VT Synchrotron diffraction – probing inorganic lattice



VT ^{14}N ss-NMR – probing organic cation behaviour

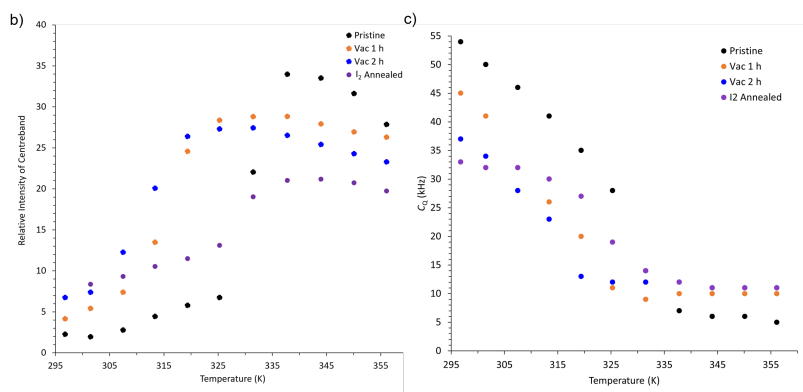


Figure 4.11 Plot of relative intensity of the second spinning sideband versus temperature for pristine MAPI (black), vac 1 h (orange), vac 2 h (blue), and I_2 -annealed (purple) samples. Dashed lines serve only as a guide for the eyes.

Together, these results demonstrate that post-synthetic treatments introduce modifications not only in lattice distortions but also in the dynamic behaviour of the organic cation. These findings reinforce the necessity of using multiple complementary techniques to fully understand phase stability and transition mechanisms in MAPI perovskites.

Table 4.6 Comparison of phase transition temperatures for different MAPI samples as determined by diffraction and solid-state NMR techniques. Variations in transition temperatures highlight the impact of vacuum and iodine annealing on structural stability and phase behaviour.

Sample	Transition Temp. (Diffraction, K)	Transition Temp. (ss-NMR C_Q , K)	Transition Temp. (ss-NMR centreband, K)
Pristine	327	325 - 336	325
Vac 1 h	310	310 - 325	307
Vac 2 h	305	307 - 317	301
I ₂ Annealed	-	320 - 330	325

4.8 MAPI and the Magic Angle

During initial investigations, some unusual behaviour was observed during the acquisition of ^{14}N NMR spectra of MAPI for room temperature comparisons with post-synthetically treated samples. When performing a standard acquisition using a proton-decoupled pulse sequence, the resulting spectrum of pristine MAPI exhibited an unexpected splitting of the centreband as shown in Figure 4.12. This phenomenon is typically attributed to ^1H - ^{14}N coupling, which can affect lineshapes. However, since the pulse sequence employed effective decoupling, it was clear that such coupling could not be influencing the lineshape.

Furthermore, the spinning sideband patterns observed were non uniform, displaying a variance in lineshape that had not been previously reported in the literature [26]. The centreband also proved to be unfittable when simulation attempts were made, complicating the analysis further. To address this anomaly, several spectrometer parameters were systematically checked to ensure the disturbance in the signal was not due to instrumental misalignment.

One critical parameter checked was the magic angle, which was adjusted by

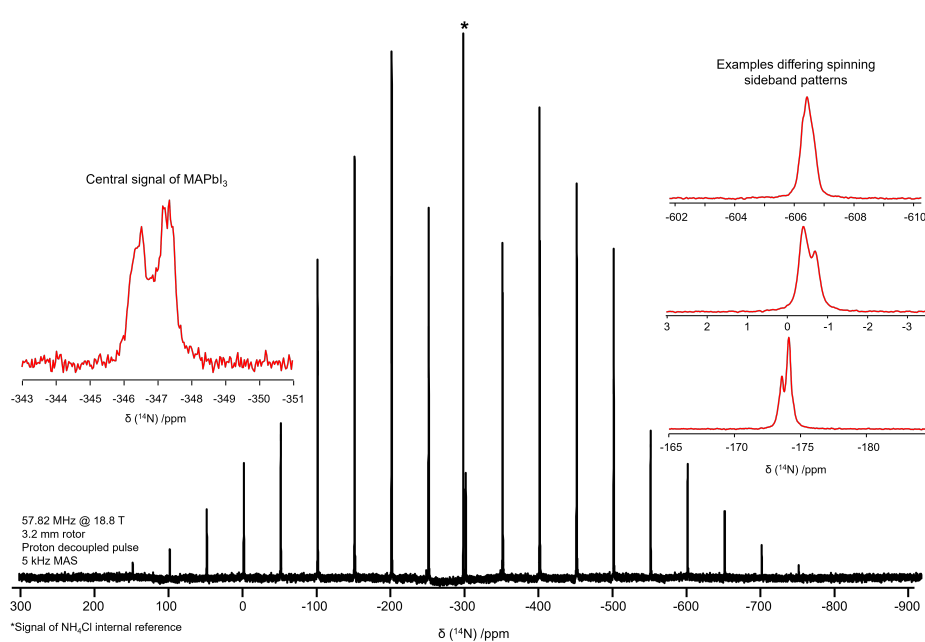


Figure 4.12 1D ^{14}N NMR spectrum with ^1H decoupling of pristine MAPI obtained at room temperature at 9.4 T with a MAS frequency of 5 kHz. The overall spectrum (black) is presented alongside expanded views of the centreband and various lineshapes of the spinning sidebands (red), offering detailed insight into the spectral characteristics. The asterisk indicates a contamination of NH_4Cl reference in the sample.

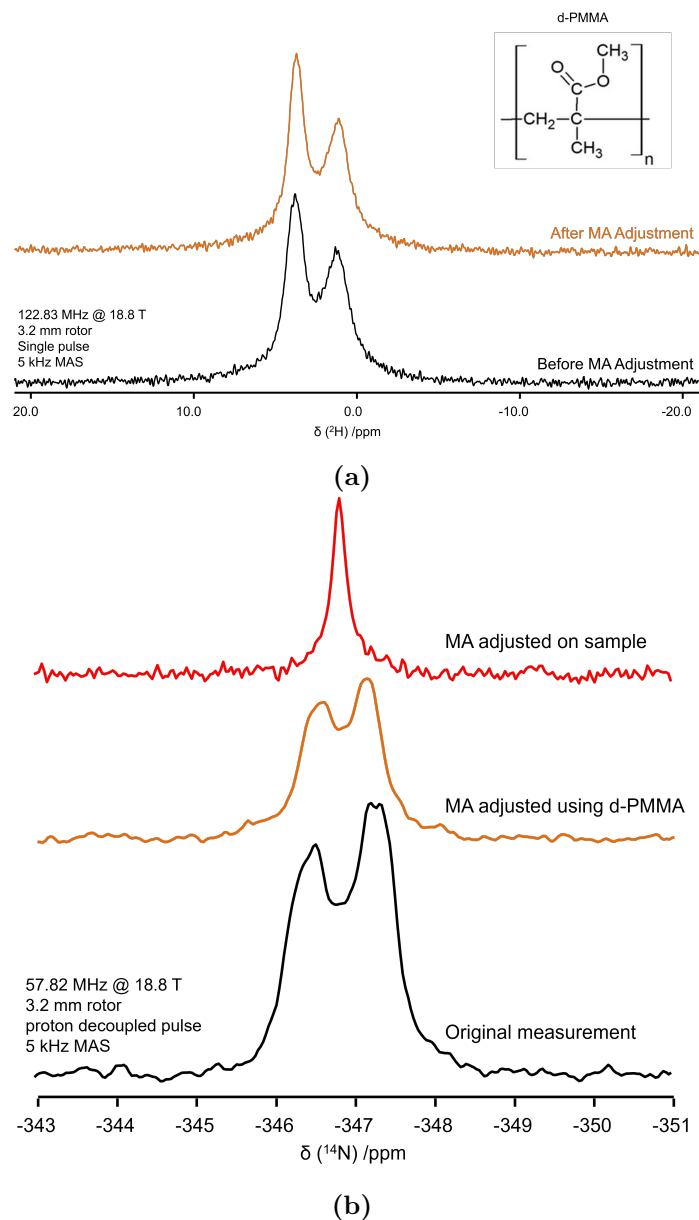


Figure 4.13 (a) ^2H signal of PMMA before (black) and after (orange) magic angle adjustment. (b) 1D ^{14}N NMR spectra of pristine MAPI recorded at room temperature using a 18.8 T magnetic field and a MAS frequency of 5 kHz. The spectrum includes the initial centreband signal without magic angle adjustment (black), the signal after adjustment using PMMA (orange), and the final resulting signal after applying magic angle adjustment directly to the MAPI sample (red).

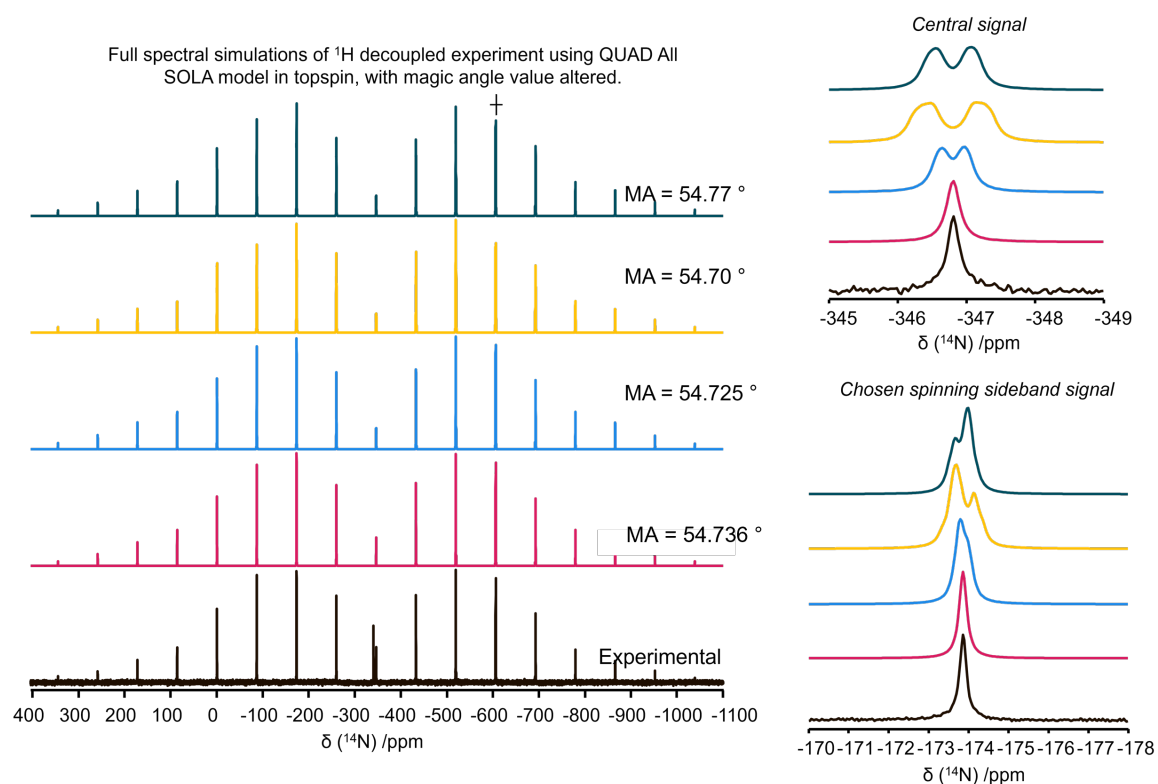


Figure 4.14 Spectral simulations aimed at determining the effect of deviations in the magic angle on the lineshape distortion observed in MAPI. These simulations illustrate how variations in the magic angle influence the spectral characteristics, providing insights into the underlying causes of the observed lineshape alterations. Chosen spinning sideband is denoted with † on full spectra.

acquiring a ^2H NMR spectrum of deuterated polymethylmethacrylate (PMMA) (Figure 4.13a). This adjustment resulted in a small narrowing of the lineshape, yet a similar narrowed splitting of the centreband persisted in subsequent ^{14}N spectra of pristine MAPI. The magic angle was then readjusted directly using the material itself (Figure 4.13b), which immediately led to the collapse of the centreband into a single peak. This indicated a direct relationship between the magic angle precision and the observed spectral pattern for MAPI.

Spectral simulations (as shown in Figure 4.14) confirmed that even a slight deviation from the magic angle, as small as 0.01° , could cause the observed signal splitting.

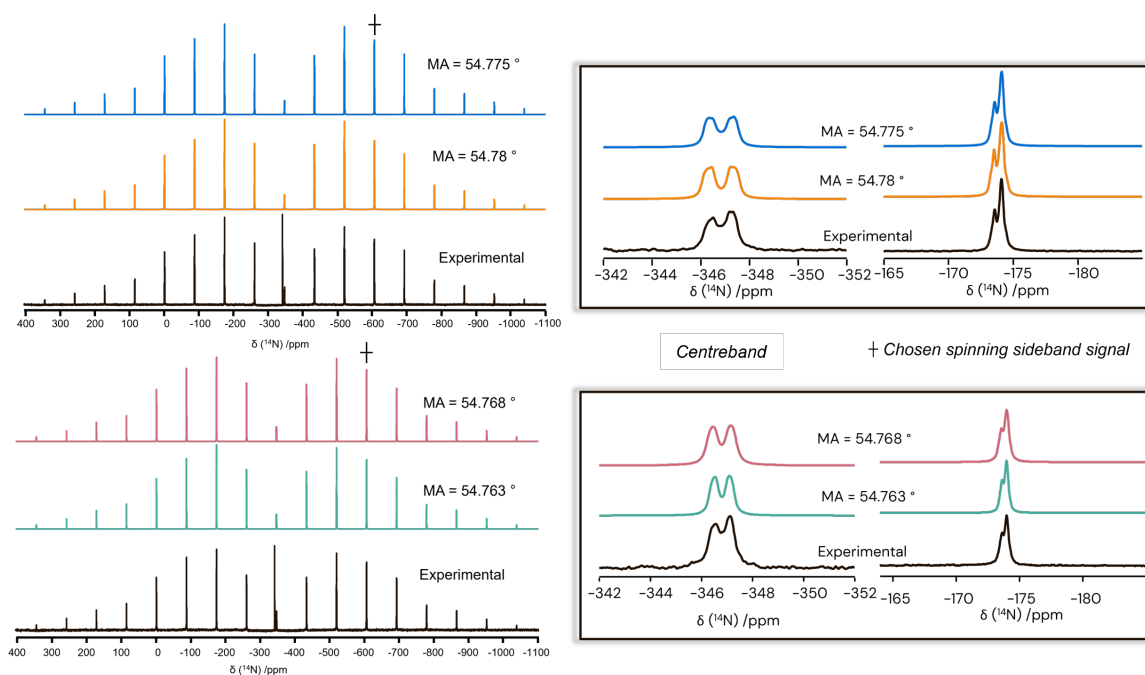


Figure 4.15 Simulations of the initially acquired spectra, facilitating the back calculation of the magic angle, enabling a more accurate understanding of its influence on the spectral lineshape of MAPI.

Further simulations of the initially acquired spectra (Figure 4.15) allowed for back calculation of the magic angle, revealing an unexpected and valuable finding: the magic angle can be precisely measured using ^{14}N NMR, providing an alternative to the commonly utilised ^{79}Br experiment on KBr. This is because the satellite transitions of quadrupolar nuclei are highly sensitive to the precision of the magic angle due to the broad breadth of the satellite transitions in the absence of MAS.

Therefore, this material offers a novel alternative use in monitoring the magic angle on NMR instruments, enhancing the precision of ^{14}N NMR measurements and contributing to the broader understanding and characterisation of hybrid perovskite materials.

References

- [1] D. Bryant, N. Aristidou, S. Pont, I. Sanchez-Molina, T. Chotchunangatchaval, S. Wheeler, J. R. Durrant and S. A. Haque, *Energy Environ. Sci.*, 2016, **9**, 1655–1660.
- [2] L. Ma, D. Guo, M. Li, C. Wang, Z. Zhou, X. Zhao, F. Zhang, Z. Ao and Z. Nie, *Chem. Mater.*, 2019, **31**, 8515–8522.
- [3] G. Niu, X. Guo and L. Wang, *J. Mater. Chem. A*, 2015, **3**, 8970–8980.
- [4] F. X. Xie, H. Chen, X. Yang, M. L. Mao, T. Zhang, Z. Li and L. Han, *ACS Nano*, 2015, **9**, 639–646.
- [5] S. Wang, H. Huang, W. Ren, J. Chen, Y. Deng, X. Wan and X. Zhang, *Nature Energy*, 2016, **2**, 1–6.
- [6] Z. Ren, A. Ng, Q. Shen, S. H. Cheung, H. C. Gokkaya, A. B. Djurišić and C. Surya, *Sci. Reports*, 2014, **4**, 6752.
- [7] J. Padchasri and R. Yimnirun, *J. Alloys and Compd.*, 2017, **720**, 63–69.
- [8] B. Dänekamp, C. Müller, M. Sendner, P. P. Boix, M. Sessolo, R. Lovrincic and H. J. Bolink, *J. Phys. Chem. Lett.*, 2018, **9**, 2770–2775.
- [9] C. J. Dahlman, D. J. Kubicki and G. N. M. Reddy, *J. Mater. Chem. A*, 2021, **9**, 19206–19244.
- [10] P. Raval, M. Dhennin, H. Vezin, T. Pawlak, P. Roussel, T.-Q. Nguyen and G. N. M. Reddy, *Electrochim.*, 2022, **424**, 140602.
- [11] D. Sarkar, R. W. Hooper, A. Karmakar, A. Bhattacharya, A. Pominov, V. V. Terskikh and V. K. Michaelis, *ACS Mater. Lett.*, 2022, **4**, 1255–1263.
- [12] R. W. Hooper, D. Sarkar and V. K. Michaelis, *Curr. Opin. Colloid Interface Sci.*, 2022, **101631**.
- [13] A. Mishra, M. A. Hope, M. Almalki, L. Pfeifer, S. M. Zakeeruddin, M. Grätzel and L. Emsley, *J. Am. Chem. Soc.*, 2022, **144**, 15175–15184.
- [14] D. Kubicki, D. Prochowicz, A. Hofstetter, S. Zakeeruddin, M. Grätzel and L. Emsley, *J. Am. Chem. Soc.*, 2017, **139**, 14173–14180.

-
- [15] D. J. Kubicki, S. D. Stranks, C. P. Grey and L. Emsley, *Nat. Rev. Chem.*, 2021, **5**, 624–645.
- [16] J. H. Lee, N. C. Bristowe, J. H. Lee, S. H. Lee, P. D. Bristowe, A. K. Cheetham and H. M. Jang, *Chem. Mater.*, 2016, **28**, 4259–4266.
- [17] A. M. A. Leguy, J. M. Frost, A. P. McMahon, V. G. Sakai, W. Kochelmann, C. Law, X. Li, F. Foglia, A. Walsh, B. C. O'Regan, J. Nelson, J. T. Cabral and P. R. F. Barnes, *Nat. Commun.*, 2019, **6**, 7124.
- [18] A. M. Leguy, Y. Hu, M. Campoy-Quiles, M. I. Alonso, O. J. Weber, P. Azarhoosh, M. van Schilfgaarde, M. T. Weller, T. Bein, J. Nelson and et al., *Chem. Mater.*, 2015, **27**, 3397–3407.
- [19] L. Piveteau, M. Aebli, N. Yazdani and et al., *ACS Cent. Sci.*, 2020, **6**, 1138–1149.
- [20] L. Piveteau, V. Morad and M. V. Kovalenko, *J. Am. Chem. Soc.*, 2020, **142**, 19413–19437.
- [21] P. S. Whitfield, N. Herron, W. E. Guise, K. Page, Y. Q. Cheng, I. Milas and M. K. Crawford, *Sci. Rep.*, 2016, **6**, 1–16.
- [22] H. Si, Q. Liao, Z. Kang, Y. Ou, J. Meng, Y. Liu, Z. Zhang and Y. Zhang, *Adv. Func. Mat.*, 2017, **27**, 1701804.
- [23] A. Senocrate, I. Moudrakovski, G. Y. Kim and et al., *Angew. Chem. Int. Ed.*, 2017, **129**, 7863–7867.
- [24] A. Senocrate, I. Moudrakovski and J. Maier, *Phys. Chem. Chem. Phys.*, 2018, **20**, 20043–20055.
- [25] R. E. Wasylshen, O. Knop and J. B. Macdonald, *Solid State Commun.*, 1985, **56**, 581–582.
- [26] W. M. J. Franssen, C. M. M. van Heumen and A. P. M. Kentgens, *Inorg. Chem.*, 2020, **59**, 3730–3739.
- [27] W. T. M. Van Gompel, R. Herckens, G. Reekmans, B. Ruttens, J. D'Haen, P. Adriaensens, L. Lutsen and D. Vanderzande, *J. Phys. Chem. C*, 2018, **122**, 4117–4124.
- [28] A. M. Askar, G. M. Bernard, B. Wiltshire, K. Shankar and V. K. Michaelis, *J. Phys. Chem. C*, 2017, **121**, 1013–1024.
- [29] J. L. Minns, Ph.D. Thesis, University of Kent, 2021.
- [30] J. L. Minns, P. Zajdel, D. Chernyshov, W. Van Beek and M. A. Green, *Nat. Commun.*, 2017, **8**, 1–5.

Chapter 5

Optimisation of NQR echo for MAPbI₃

5.1 The Application of Halide NMR and NQR to Study Hybrid Perovskites

To enhance the efficiency and stability of hybrid halide perovskite, it becomes imperative to gain a profound understanding of the local structure and dynamic behaviour of halide ions within these compounds. However, the immediate environment surrounding these nuclei significantly influences the spectral lineshape, chemical shift, and quadrupolar interaction offering a unique insight into the structural composition and phase behaviour of these materials within the solid state, across a range of temperatures. Numerous studies have explored a wide range of A-site (¹H [1–3], ¹³C, ¹⁴N, ¹⁵N [3–6], ¹¹³Cs [7–10], ⁸⁷Rb, ³⁹K [7, 11]) and B-site (²⁰⁷Pb [10, 12–14], ¹¹⁹Sn [15], ²⁰⁹Bi, ¹¹⁵In [10]) cation nuclei, yielding valuable insights into domain structure, phase transition behavior,

5.1 The Application of Halide NMR and NQR to Study Hybrid Perovskites

Table 5.1 NMR properties of the half-integer-spin quadrupolar halogen nuclei, adapted from Szell *et al.* (2020).[16]

Nucleus	Spin	N.A. (%)	γ (10^7 rad s $^{-1}$ T $^{-1}$)	Q (fm 2)
^{35}Cl	3/2	75.78	2.6241991	-8.17
^{37}Cl	3/2	24.22	2.1843688	-6.44
^{79}Br	3/2	50.69	67.25619	31.33
^{81}Br	3/2	49.31	72.49779	26.15
^{127}I	5/2	100.0	53.8957	-69.61

and dynamic properties. However, a significant challenge arises when attempting to record magnetic resonance spectra of halide X-site nuclei, including $^{35/37}\text{Cl}$, $^{79/81}\text{Br}$, and ^{127}I . These nuclei possess spin $I = 3/2$ or $5/2$ and substantial quadrupole moments as displayed in Table 5.1, leading to interactions with EFGs at the position of the nucleus. While the quadrupolar interaction provides rich information due to its high sensitivity to geometric and chemical coordination, it also introduces difficulties during spectral acquisition. The highly asymmetrical environment of halogen atoms in hybrid perovskites results in large EFGs, and hence, large C_Q constants, notably for $^{79/81}\text{Br}$ and ^{127}I isotopes featuring large electric quadrupolar moments. As a result, the C_Q parameter of these nuclei can reach tens of megahertz. Hence, their quadrupolar interaction is comparable to the Zeeman interaction, which usually determines the resonance frequencies in NMR spectra. The significant C_Q value results in extensive broadening of halide spectra, reaching breadths of several megahertz, as illustrated in Figure 5.1. Furthermore, this broadening decreases the intensity of the signal since the total integrated intensity is spread over a broad frequency region. Conventional line-narrowing techniques, such as increasing magnetic field strength and sample rotation about the magic angle (MAS), offer limited solutions to this issue. Therefore, it is not surprising that acquiring halide NMR spectra in perovskite-based materials poses a substantial challenge. Various techniques already exist to acquire extremely wide spectra. One common approach involves the acquisition of step-wise sub-spectra with

5.1 The Application of Halide NMR and NQR to Study Hybrid Perovskites

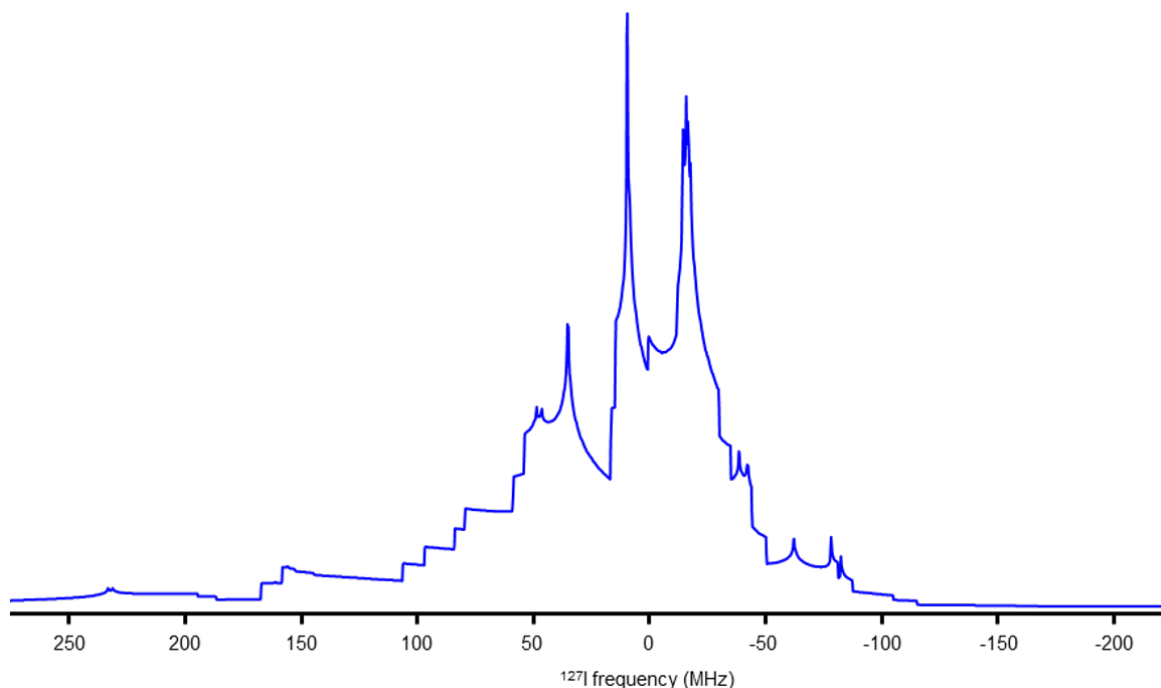


Figure 5.1 Simulation of the ^{127}I NMR spectrum of MAPI at 28.2 T using QUEST software.[17] The spectrum highlights the intricate and broad nature of the signals, rendering it indecipherable due to its complexity.

varying offsets during static experiments. Variable offset cumulative frequency stepping (VOCS) is frequently employed in halide NMR experiments.[18] As the wide spectra are associated with having short free-induction decay (FID) with length comparable to pulse transients, they are often acquired using echo pulse sequences or trains of echoes by applying a series of CT-selective pulses, a sequence called quadrupolar Carr-Purcell Meiboom-Gill (QCPMG).[18] Furthermore, adiabatic pulses can be employed to increase the excitation bandwidth of QCPMG scheme which is well described by Schurko.[19] The combination of a WURST-QCPMG scheme with VOCS method has already been demonstrated as effective by Piveteau *et al.* and other groups for acquiring ^{35}Cl and ^{79}Br spectra in inorganic perovskites.[20, 21] However, there are no reports regarding the success of this method in acquiring ^{127}I perovskite spectra. This absence of data is likely attributed to the substantially larger quadrupolar interaction of ^{127}I nuclei compared to its lighter halide counterparts, making it considerably more

5.1 The Application of Halide NMR and NQR to Study Hybrid Perovskites

challenging to mitigate.[16]

In situations like these, NQR emerges as a more suitable technique. As elucidated earlier in Chapter 2, NQR has the capacity to yield analogous information to NMR concerning the quadrupole interaction, while also providing valuable insights into a material's structure and dynamics. Both techniques can offer insights into the symmetry, fluctuations, and strength of the EFG. In NMR, this is accomplished through lineshape analysis, while in NQR, resonance frequency values provide information regarding the C_Q and η_Q parameters. Furthermore, parameters such as linewidth and the T_1 and T_2 relaxation times can furnish greater insights into dynamics due to their dependence on nuclear motion.

This wide array of information offered by NMR and NQR elucidates the rationale behind the abundance of studies that employ one or both of these techniques in the investigation of halide perovskites. These studies aim to explore halide-induced octahedral tilting, phase transitions, and structural variations through mixed cation and anion doping, contributing to a comprehensive understanding of these materials.[6, 19–31]

Within the existing body of literature, the prevalent approach in perovskite NQR studies involves the utilisation of pulse sequences originally optimised for NMR. [22, 24] When the expected resonance frequencies for a material have been previously documented, as is the case for MAPI, initial experiments can be conducted by utilising pulse lengths optimised for nuclei with Larmor frequencies that are in close proximity to the anticipated NQR carrier frequencies of the material. For ^{127}I NQR in MAPI, this approach could involve employing pulse lengths that are optimised for ^{207}Pb NMR, which resonates at 83.710 MHz in a 9.4 T magnetic field, to target the lower carrier frequency. Similarly, pulse lengths optimised for ^{31}P NMR, resonating at 161.976 MHz

5.2 Current Status of NQR Optimisation

at 9.4 T, can be utilised to address the higher carrier frequency. However, this reliance on pulse optimisation tailored for spin-1/2 NMR nuclei raises a critical concern whether these assumptions are actually directly transferable to NQR nuclei.

Another notable open question in perovskite NQR literature pertains to the limited exploration of variable probe diameters and the optimisation of RF pulses. A majority of experiments are conducted using the largest available wide-bore probe, typically 4 mm in diameter, while certain groups opt for custom-built probes for NQR acquisition. Although these practices enable groups to obtain satisfactory signals for their specific materials, they lack universal accessibility and reproducibility across the field. Drawing insights from NMR, it is evident that smaller sample coils can produce larger RF field and hence, excite broader spectral width at the expense of lower sample volume, which results in lower sensitivity. This improvement could allow for easier detection of NQR resonances with a smaller number of probe re-tuning steps. As the field of perovskite NQR seeks expansion and refinement, it becomes imperative to gain a clearer understanding of the nature of optimisation in NQR, coupled with an exploration of the impact of probe diameter on the acquisition of NQR spectra.

5.2 Current Status of NQR Optimisation

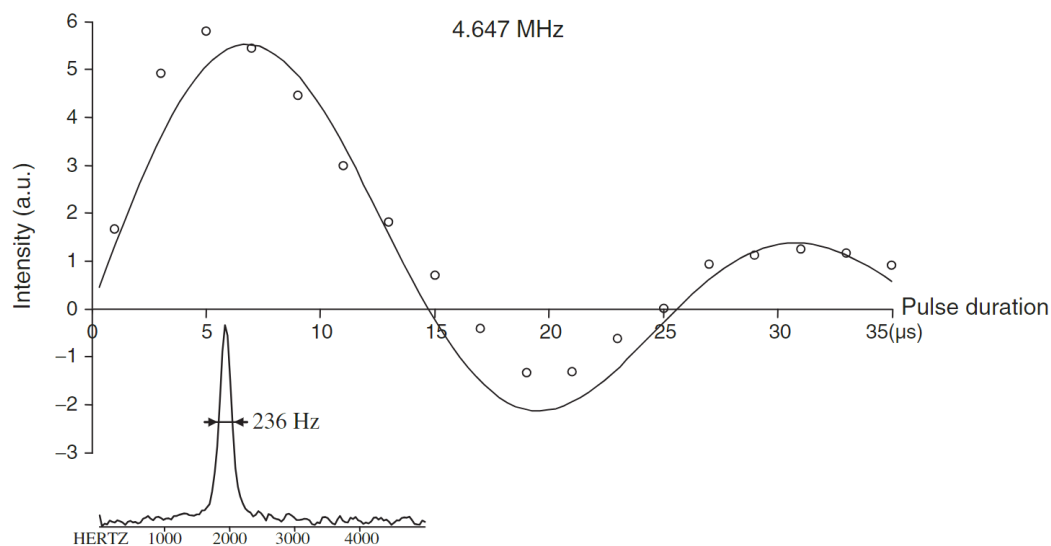
The endeavour of NQR optimisation is not a new one. There have been many previous investigations into one and multi-pulse optimisation of NQR. This has been carried out most comprehensively on ^{14}N nuclei, due to the wide applications NQR has in the detection of narcotics and explosives as mentioned earlier in Chapter 2.

Canet has pioneered discussions through a series of papers delving into the intricacies surrounding the application of RF pulses in NQR theory. An inherent complexity lies

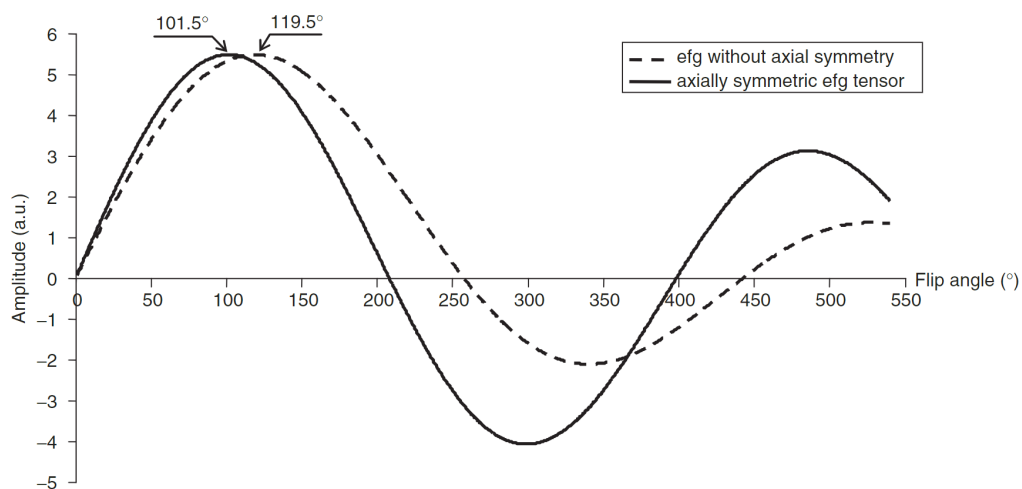
5.2 Current Status of NQR Optimisation

in the fact that the direct transposition of NMR sequences to NQR, especially for powdered samples, is far from straightforward. This complication arises primarily due to the absence of a Zeeman term in pure NQR, eliminating any preferential direction. The concept of the rotating frame, which is invaluable in NMR for predicting the effects of radiofrequency pulses, becomes inapplicable. The second challenge stems from the lack of a preferential direction and the random orientation of microcrystallites constituting the powdered sample. This renders RF pulses corresponding to the first maximum and first zero of a nutation curve as not true 90° and 180° pulses.[32]

Canet *et al.* conducted a thorough assessment of the NMR $\pi/2$ pulse and computed the accurate NQR flip angle for the ^{14}N nucleus, which possesses either a symmetric or non-symmetric EFG tensor, as illustrated in Figure 5.2b. Their experimental observations revealed that not only is the flip angle for an $I = 1$ spin system longer than observed in NQR, but also the symmetry of the EFG can further influence this angle.[33, 34] The conclusion drawn is that perfect sine functions do not characterise NQR nutations, with maxima, zero and minima occurring at multiples of $\pi/2$. Instead, damped sine functions with maxima, zero, and minima occurring at values larger than multiples of $\pi/2$ tend to be more representative.[35] Consequently, true 90° or 180° pulses do not exist in NQR, as they do in NMR. Instead, pseudo 90° and 180° pulses can be defined, corresponding to the first maximum and zero of nutation curves, respectively.[32] This underscores that pseudo pulses can differ based on the symmetry of the EFG. Optimal pulse lengths for single-pulse and echo NQR experiments were also calculated for spin-1 nuclei when the recycle delay is shorter than $5T_1$ with T_1 the longitudinal relaxation time, i.e., under steady-state conditions.[32, 36] Furthermore, composite pulses have been designed to broaden the excitation bandwidth of NQR pulse sequences for spin-1 nuclei.[37, 38] While these findings have been demonstrated to be applicable to NQR of spin-1 nuclei, there is a noticeable gap in the literature



(a)



(b)

Figure 5.2 (a) The evolution of the NQR signal as a function of RF pulse length for one resonance frequency of sodium nitrate. Below the nutation curve is the observed signal. Figure adapted from reference [33] and reprinted with permission. (b) Nutation curves for NQR signal of ^{14}N nucleus with $\eta_Q = 0$ (solid line) and $\eta_Q \neq 0$ (dashed line). Figure adapted from reference [33] and reprinted with permission.

concerning the confirmation or dismissal of the extension of these concepts into spin-3/2 and -5/2 nuclei.

Advancements in optimising NQR for spin-3/2 nuclei have been explored in research conducted by C. Odin. He notably calculated the nutation curve and the excitation bandwidth of single-pulse NQR experiment and different variants of echo schemes for spin-3/2 nuclei.[39, 40]

Like for spin-1 nuclei, composite pulses have been designed for spin-3/2 nuclei, in order to broaden the excitation bandwidth of NQR pulse sequences.[37, 41, 42] Amplitude and frequency-modulated pulses have also been applied to increase the excitation bandwidth of NQR experiments.[43, 44] However, it is important to note that there is currently no evidence supporting the extension of these findings to other quadrupolar nuclei with spin $I \geq 5/2$. Consequently, a notable gap exists in the literature addressing the optimisation of NQR for spin-5/2 nuclei.

5.3 Purpose of Present Study

The objective of this chapter is to outline an optimisation of the NQR technique when applied to ^{127}I in pristine MAPI. This optimisation is achieved through a series of experiments employing different probe diameters and RF pulse sequences. The study aims to assess the impact of these variations on the overall signal and excitation bandwidth at two distinct carrier frequencies. Simultaneously, simulations were conducted to provide a comparative analysis with observed findings. The intention behind this approach is to offer valuable insights into the optimisation of NQR experiments, specifically targeting spin-5/2 nuclei, in the context of studying halide perovskite materials.

5.4 Experimental Section

5.4.1 Material Synthesis

To prepare pristine MAPI, procedures similar to that of reference [45] and [46] were followed. Full synthesis details can be found in Chapter 3.

5.4.2 Characterisation

X-ray Diffraction

Prior to NQR measurements, PXRD patterns were collected by using a small amount of each sample ground using a pestle and mortar, before being transferred to a Rigaku zero background holder. A Rigaku Miniflex 600 powder diffractometer (Cu $K_\alpha = 1.54$ Å) in transmission mode (Debye-Scherrer geometry) was used, with each measurement consisting of a 2θ range of 5° to 80° and step size of 0.02° .

NMR RF calibration

Experiments were recorded at 400 MHz for ^1H , 83 MHz for low NQR carrier frequency (close to ^{207}Pb), and 167 MHz for high NQR carrier frequency (close to ^{31}P). A wide-bore magnet ($B_0 = 9.4$ T) equipped with a Bruker AVANCE II console was used, in conjunction with both 4 mm and 2.5 mm triple-resonance HXY MAS probes operated in double resonance mode. A sample of solid silicon was placed into zirconium rotors and spun at a MAS rate of 451 or 20 kHz. In all cases the Bloch-Siegert effect was measured using 4 scans of a ^1H spin-echo ($\pi/2 - \tau_e - \pi - \text{de} - \text{acq}$) with a pulse length

of 3.1 μs , an echo delay, τ_e , of 5 ms, a deadtime, d_e , of 6.5 μs , and a recovery delay of 1 s.

NQR Spectroscopy

Solid-state ^{127}I NQR static measurements were recorded on a Bruker Avance II 2.35 T spectrometer equipped with either a Bruker 4.0 mm WVT triple resonance probe or a Bruker 2.5 mm Wide-Bore Triple resonance probe, that was placed outside of the magnet and temperature was monitored and controlled. All optimisation experiments were performed at 295 K to ensure MAPI adopted its room temperature tetragonal structure. A Hahn echo sequence, with an echo delay of 12 μs , and a recycle delay of 0.02 s were used. Different RF field amplitudes were employed, with a maximum strength of 160 kHz for high carrier frequency measurements (> 100 MHz) and 74 kHz for low carrier frequency measurements (< 100 MHz), with pulse lengths optimised for each condition. For investigations into excitation bandwidth, and offset value of 100 kHz per experiment was used.

Simulation and Data Processing

All simulations were carried out for an isolated ^{127}I spin and were performed using MATLAB with the Spinach software package, using the in-built *shaped pulse af* function.

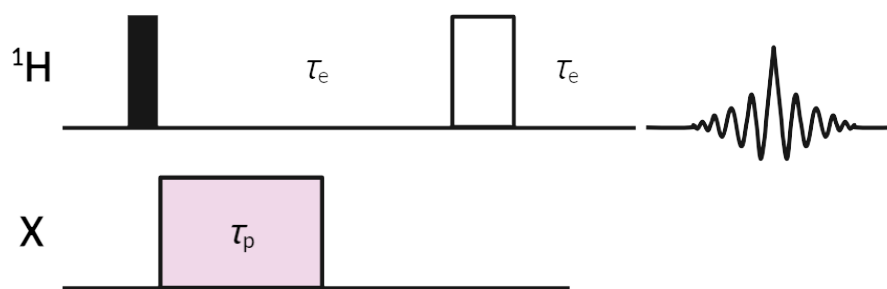


Figure 5.3 Pulse sequence utilised to measure the Bloch-Siegert shift of protons for the calibration of rf field strength.[47]

5.5 Results and Discussion

5.5.1 Initial RF calibration with 400 MHz NMR Spectrometer

In order to determine the RF power supplied to the probes, The Bloch-Siegert shift effect was used for indirect RF calibration via proton detection.[47] Bloch-Siegert shifts are able to describe the differences in frequency seen between NMR signals measured in the presence or absence of an RF field that is applied during acquisition. Such shifts can occur because the RF field alters the effective magnetic field experienced by nearby resonances. The observed shift is inversely related to the difference between the resonance frequency and the irradiation frequency, and is most commonly observed when homonuclear decoupling is applied during experiments.

The advantage of using this method is that RF field calibration can be achieved without directly observing the nuclei of interest. Moreover, it can be executed using simple ${}^1\text{H}$ detection and applied for calibration across virtually any nucleus or RF channel available on a probe. A further comprehensive explanation of this indirect calibration technique is provided in reference.[47] During these experiments, a silicon sample was placed into a rotor size corresponding to the probe being studied. Due to potential sample imbalance in the rotor, only a low MAS rate could be employed with

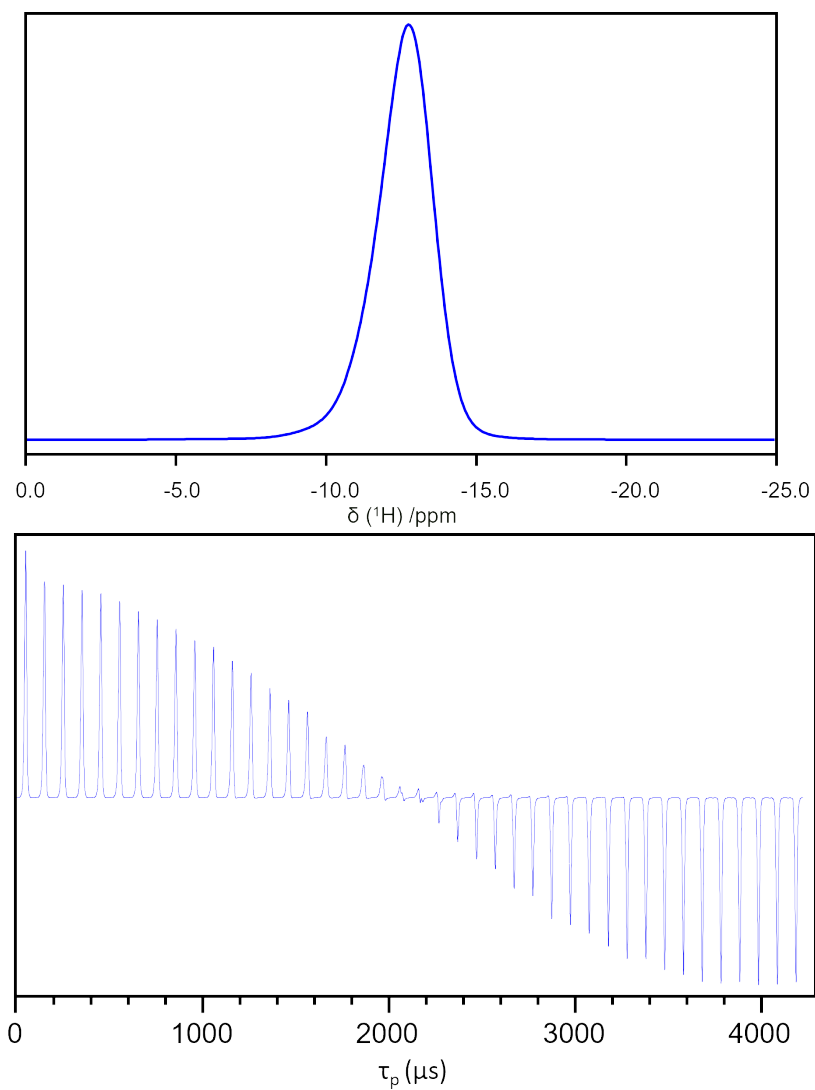


Figure 5.4 Example of a 1D spectrum of silicon acquired (top). An example of a ^1H -detected Bloch-Siegert shift nutation spectrum depicted as a function of the pulse length τ_p (bottom).

Table 5.2 Parameters for Bloch-Siegert experiments used to calibrate the RF field at relevant carrier frequencies for MAPI. Here, ν_R denotes the MAS frequency, ν_{0X} represents the carrier frequency, ν_{1X} indicates the RF field amplitude, and p_{90} is the pulse length.

	4.0 mm		2.5 mm	
ν_R (Hz)	416	416	20,000	20,000
ν_{0X} (MHz)	167.0	83.1	83.1	167.0
$\Delta\tau_p$ (μ s)	1400	1505	530	455
ν_{1X} (kHz)	101.38	52.38	88.26	177.84
p_{90} (μ s)	2.47	4.77	2.83	1.41

the 4 mm probe. These calibrations established the RF value being sent, close to two of the 4 expected carrier frequencies exhibited by MAPI, serving as a basis for calculating RF levels at each power. Detailed parameters resulting from these calibrations are presented in Table 5.2. The RF field for the X channel and p_{90} (90-degree ($\pi/2$) pulse) are calculated using Equations 5.1 and 5.2 respectively, where $\nu_{0H} = 400.104996$ MHz.

$$\nu_{1X} = \frac{\nu_{0X}}{\nu_{0H}} \sqrt{\frac{\nu_{0H}}{4\Delta\tau_p} \left(1 - \left(\frac{\nu_{0X}}{\nu_{0H}} \right)^2 \right)} \quad (5.1)$$

$$p_{90} = \frac{250,000}{\nu_{1X}} \quad (5.2)$$

5.5.2 Experimental NQR Measurements

Once the RF field was calibrated relative to the potential carrier frequencies of MAPI, NQR experiments could proceed using these results as a guideline. Simulations of potentially observable NQR signals for MAPI in the room temperature tetragonal phase were conducted using the QUEST software,[17] based on literature data. As depicted in Figure 5.5, it is expected that four possible signals can be observed, corresponding to the two allowed transitions at the two different iodine sites. At low frequencies, two

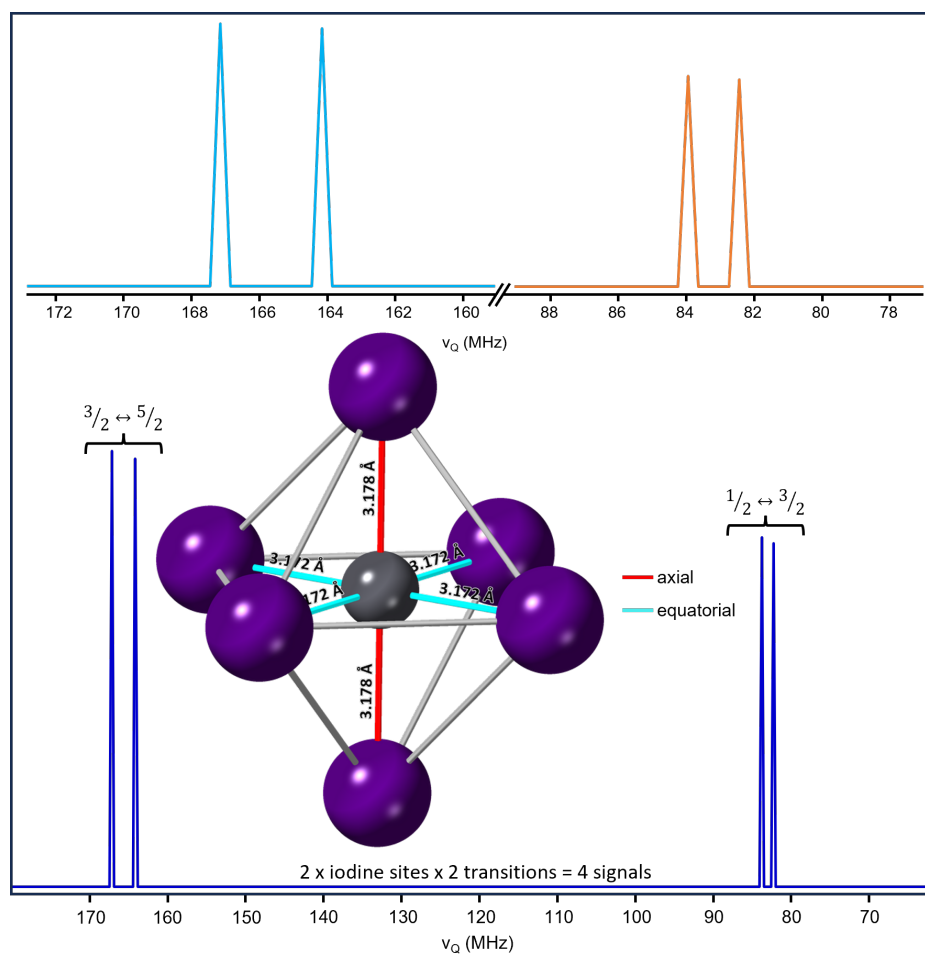


Figure 5.5 QUEST simulation [17] of NQR spectra of tetragonal MAPbI₃ using C_Q and η_Q values reported in reference [24]. An expansion of the spectra corresponding to $3/2 \leftrightarrow 5/2$ and $1/2 \leftrightarrow 3/2$ transitions are provided above.

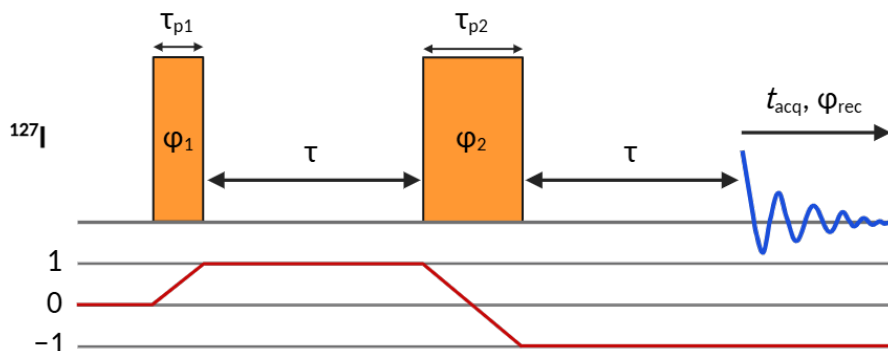


Figure 5.6 Illustration of the Hahn echo pulse sequence and corresponding coherence pathway for NQR experiments.

signals around 82 and 84 MHz are observable, corresponding to the transitions between energy levels 1/2 and 3/2. At higher frequencies, two further signals around 164 and 167 MHz are observable, corresponding to the transitions between energy levels 3/2 and 5/2. The calculated frequencies from this simulation served as a guideline when searching for signals experimentally. Initial experiments were conducted using a 4 mm probe, commonly utilised in perovskite NQR literature. A Hahn echo pulse was employed throughout (see Figure 5.6), and the temperature was carefully controlled at 295 K since temperature influences the quadrupolar interaction and hence, the frequencies of NQR transitions. Four signals for MAPI were detected at 82.062, 83.447, 164.101, and 166.909 MHz, which are in good agreement with previously reported NQR spectra of this sample.[24, 25, 27, 48]

Following these initial observations, the first and second pulses of Hahn echo experiment were optimised at one high carrier frequency and one low carrier frequency, specifically 166.91 and 83.45 MHz, respectively. This optimisation was not performed for the two transitions at 82.06 and 164.10 MHz since their frequencies are close to

Table 5.3 Optimal experimental parameters for the observation of NQR transitions of MAPI at 83.45 and 166.91 MHz using 2.5 and 4.0 mm probes.

	4.0 mm		2.5 mm	
$\nu_{0,X}$ (MHz)	83.45	166.91	83.45	166.91
$\nu_{1,X}$ (kHz)	74	160	125	251
τ_{p1} (μ s)	1.2	1.7	0.8	1.0
τ_{p2} (μ s)	2.1	2.7	1.4	1.6

the investigated transitions and optimal experimental parameters are expected to be similar for close transitions.

Several experimental NQR spectra are depicted in Figure 5.7, where the RF field amplitude was systematically varied using each probe. For each RF field value, the lengths of the first and second pulses in Hahn echo experiment were optimised to maximize the sensitivity. From these experiments, it was observed that at 83.45 MHz, a minimum RF field of 50 kHz is required to excite the $\frac{1}{2} \leftrightarrow \frac{3}{2}$ transition of MAPI. Similarly, at 166.9 MHz, a minimum RF field of 160 kHz is necessary to excite the $\frac{3}{2} \leftrightarrow \frac{5}{2}$ NQR transition of MAPI. This suggests that a greater RF field improves the excitation bandwidth of Hahn echo experiment. However, when comparing the spectral linewidths observed while employing the maximum allowed RF field for each probe, both probe diameters exhibited similar capabilities in enabling the full excitation of the NQR transitions. The optimisation results of τ_{p1} and τ_{p2} for each probe are presented in Table 5.3. As discussed earlier, there appears to be no straightforward relationship between these two pulse lengths, contrary to what is commonly observed in traditional NMR Hahn echoes. Instead, it is noted that optimal τ_{p2} is always shorter than $2\tau_{p1}$. Overall, for both probe diameters, the optimal pulse lengths follow a relationship as described in Equations 5.3, 5.4, and 5.5. This finding deviates from what is typically observed in both NMR and NQR of spin-3/2 nuclei.[39] These observations may provide additional evidence suggesting that pulse evolutions in NQR studies of $I = \frac{5}{2}$ spin

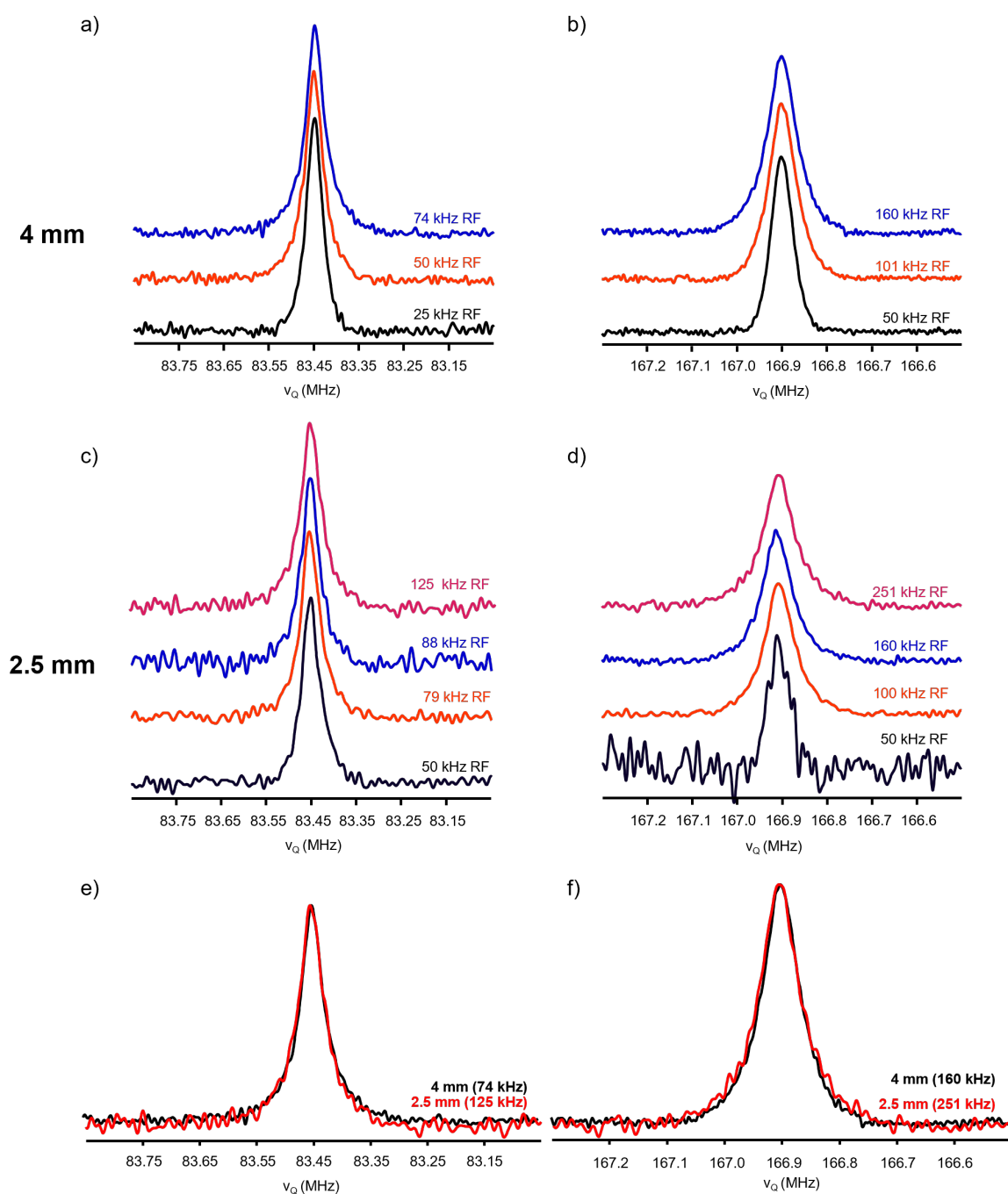


Figure 5.7 Influence of RF field on NQR transitions of MAPI resonating at (a, c, e) 83.45 and (b, d, f) 169.91 MHz detected using Hahn echo experiment and (a, b) 4 and (c, d) 2.5 mm MAS probes. For each RF field amplitude, the lengths of the first and second pulses were optimised. Panels (e, f) displays a comparison of the transitions at (e) 83.45 and (f) 169.91 MHz detected using 2.5 (red) and 4 (black) mm MAS probes.

systems may differ substantially from those of $I = \frac{1}{2}$, and $I = \frac{3}{2}$ spin systems.

$$\text{Traditional NMR: } \tau_{p2} = 2\tau_{p1} \quad (5.3)$$

$$I = \frac{5}{2} \text{ NQR at 83.45 MHz: } \tau_{p2} = 1.75\tau_{p1} \quad (5.4)$$

$$I = \frac{5}{2} \text{ NQR at 166.9 MHz: } \tau_{p2} = 1.60\tau_{p1} \quad (5.5)$$

Subsequently, an investigation into the excitation bandwidth of each probe at different NQR carrier frequencies was conducted. It is known that the smaller diameter probe can produce greater RF field, thus could provide a broader range of excitation and reducing the need for manual tuning during NQR experiments when searching for a signal. For each probe at each carrier frequency, a series of experiments were conducted using the optimised parameters in Table 5.3, with the carrier frequency offset altered by 100 kHz each time to explore the range of the excitation bandwidth. The overall results have been illustrated in Figure 5.8. For the two transitions, the higher RF field amplitude produced by the 2.5 mm probe yields a broader excitation bandwidth, which can be useful to detect NQR transitions.

5.5.3 Investigating the effect of shorter second pulse

Furthermore, an exploration was conducted to assess whether employing a shorter-than-optimal duration for the second pulse of the Hahn echo could augment the excitation bandwidth. At the outset, the investigation focused on the lower carrier frequency (83.45 MHz), where a second pulse duration of 2 μs was selected for comparison with the optimised pulse duration of 2.4 μs , (as detailed in the preceding section 5.5.2). The excitation profiles obtained for the two different lengths of the second pulse are compared in Figure 5.9. Notably, the on-resonance signal exhibited no

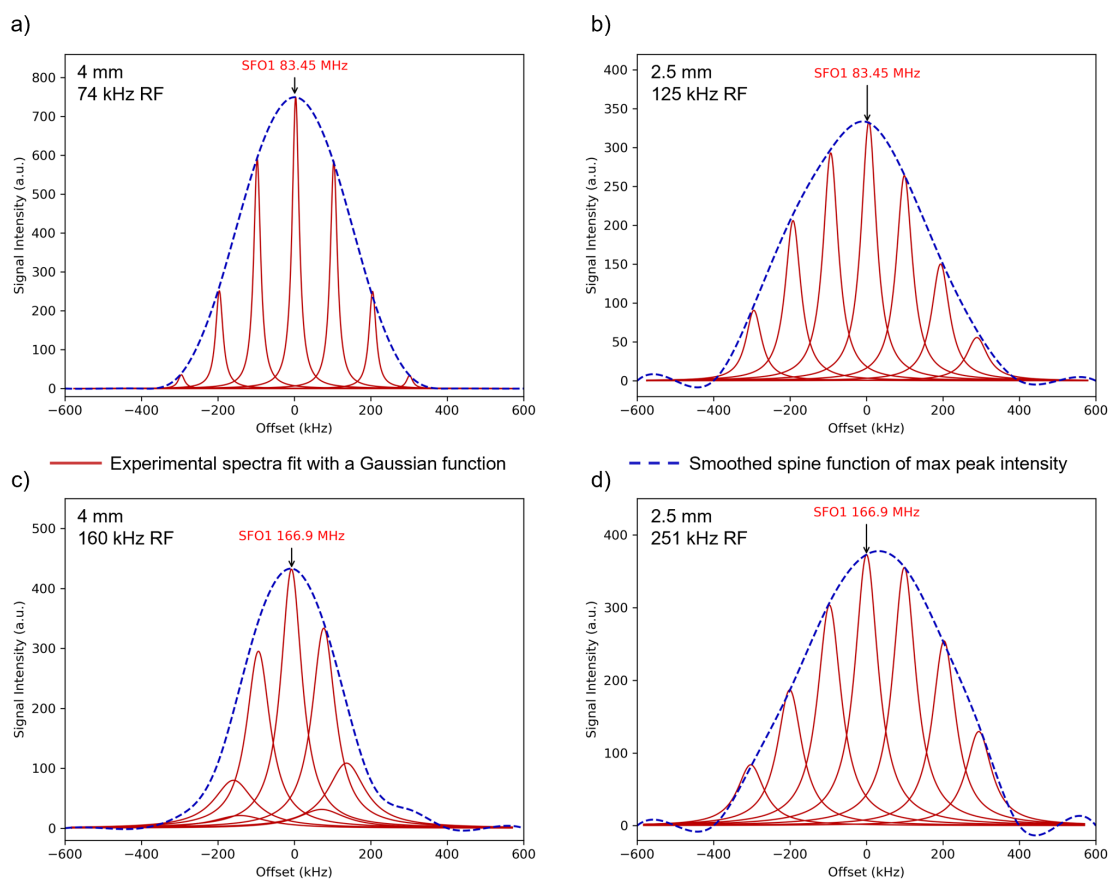


Figure 5.8 Comparison of excitation bandwidth of each probe at various carrier frequencies. (a) 4 mm probe, 74 kHz RF field amplitude, (b) 2.5 mm probe, 125 kHz RF field amplitude, (c) 4 mm probe, 160 kHz RF field amplitude, and (d) 2.5 mm probe, 251 kHz RF field amplitude. Each experimentally measured signal is fitted with a Gaussian function (red) and plotted relative to the carrier frequency offset. The maximum intensity of each peak is depicted as a function of the offset and fitted with a smooth spline function (blue) to aid in overall comparisons.

discernible difference in the spectral linewidth upon shortening the duration of the second pulse; however, a slight decrease in signal intensity was observed. Conversely, when comparing with the off-resonance signals, no variation in the spectral linewidth was evident. Instead, there was an observable increase in signal intensities when employing a shorter duration for the second pulse.

Subsequently, an assessment of the NQR excitation profile was undertaken, as depicted in Figure 5.9. Overall, it was observed that while intensity was diminished in the on-resonance signal with a shorter duration for the second pulse, the excitation bandwidth was increased as expected. This phenomenon is likely attributed to the inherent robustness of the NQR echo pulse sequence to frequency offsets when employing a shorter pulse duration.

Again the result of using a shorter length for the second pulse was then investigated for the transition resonating at 166.9 MHz. This time, two shorter pulse lengths of 2.3 μs and 2.1 μs were chosen to compare with the optimised length at 2.7 μs . As shown in Figure 5.10 again there is the same trend as with the transition at 83.45 MHz, that a shorter second pulse reduces the intensity of the on resonance signal. Meanwhile, the off resonance signals experience an increase in signal intensity and the overall linewidth of all signals are unchanged. Moving onto look at the excitation bandwidth as shown in Figure 5.10, we again see this trend of signal enhancement at off resonance frequencies and a damping of the signal on resonance. Using a shorter second pulse length, either lasting 2.3 μs or 2.1 μs , increases the overall excitation bandwidth. Comparing Figure 5.10a to Figure 5.10b shows a 100 kHz increase in the bandwidth when using a shorter pulse length. This shows that shortening the length of second pulse increases the excitation bandwidth at the expense of lower intensity signal when on resonance.

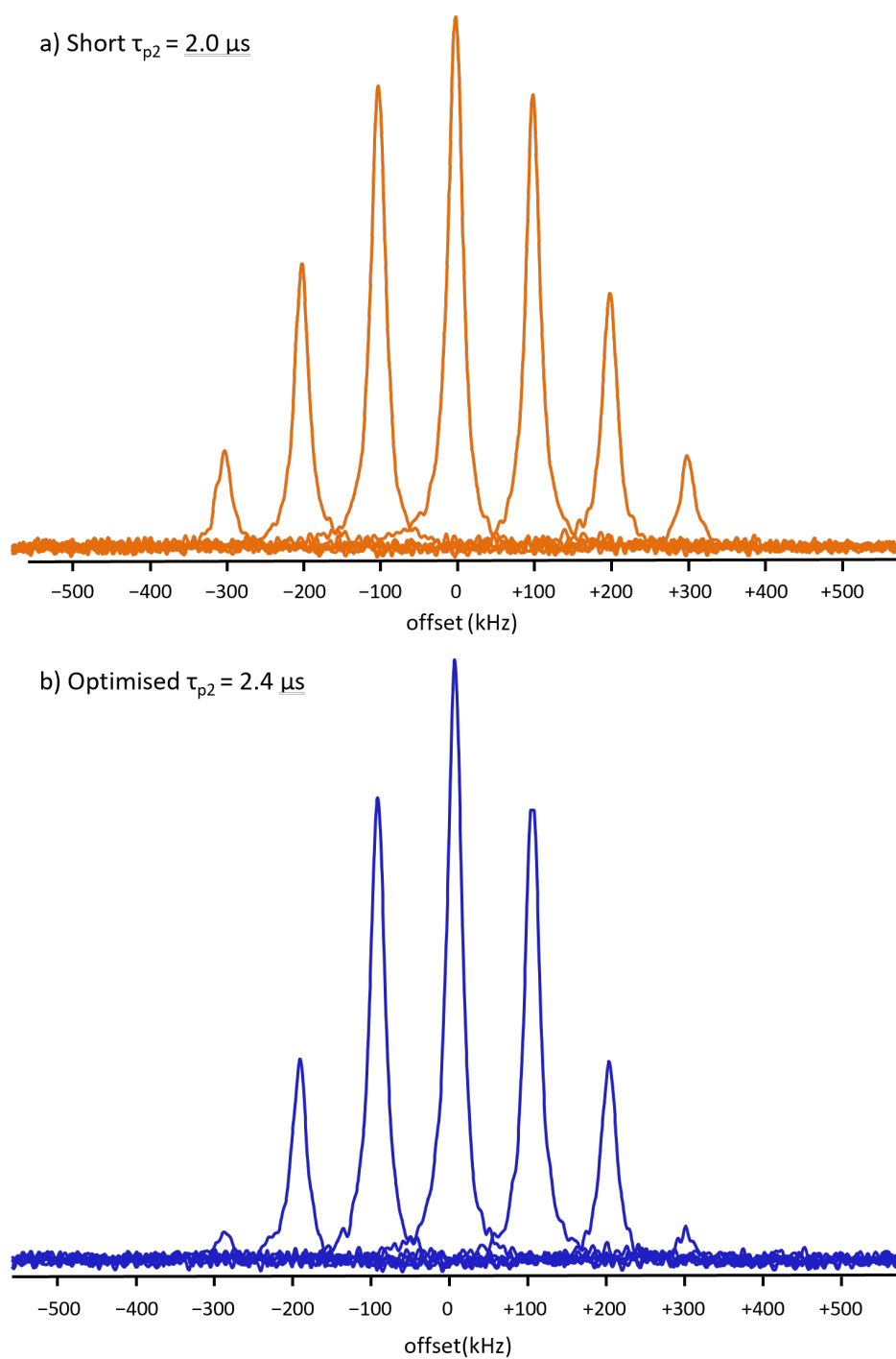


Figure 5.9 NQR excitation profile at 83.45 MHz using both shortened (a) and optimised (b) second pulse lengths with 4 mm probe.

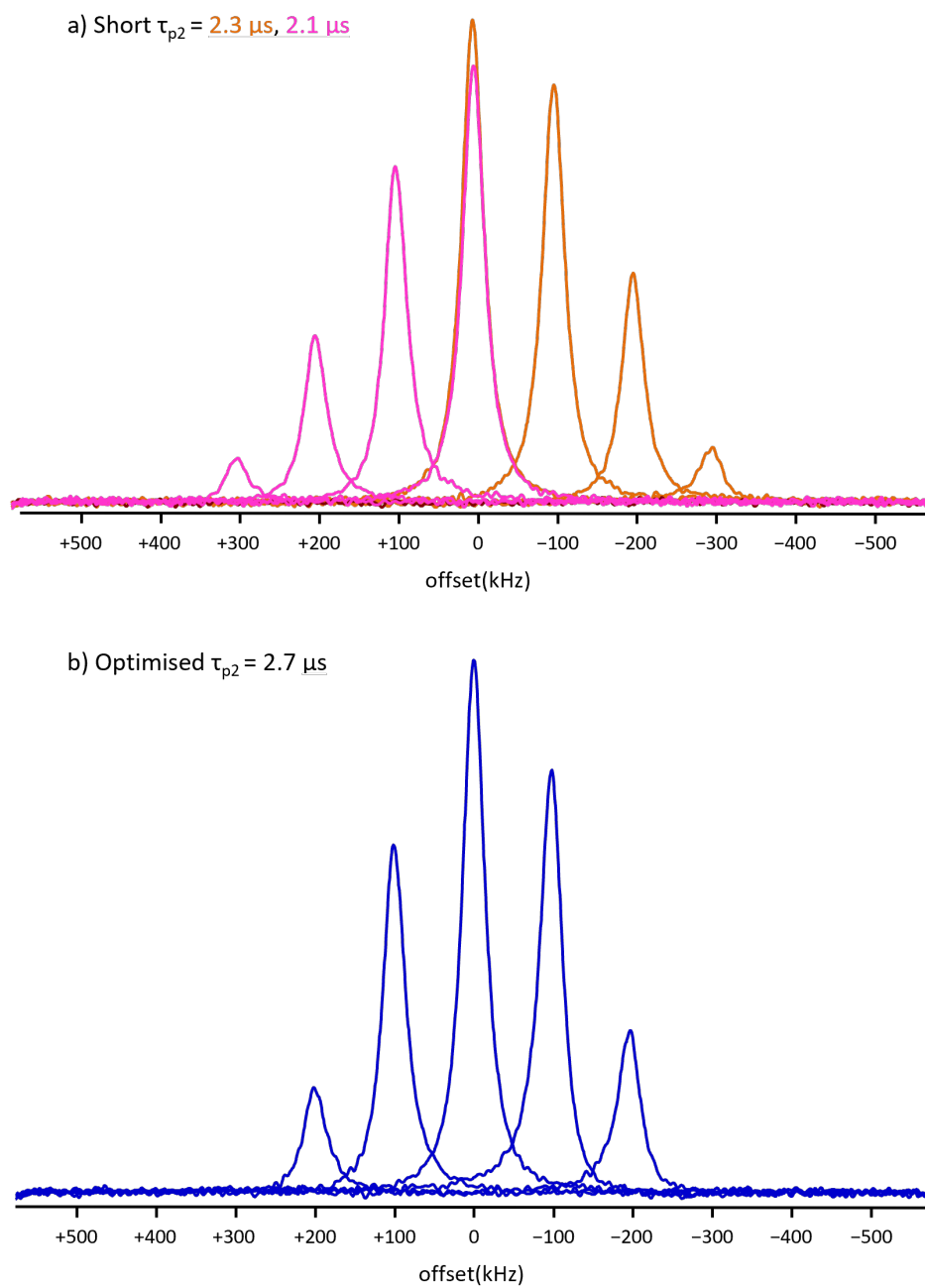


Figure 5.10 NQR excitation profile for transition resonating at 166.9 MHz using both shortened (a) and optimised (b) second pulse lengths with 4 mm probe.

Table 5.4 Optimised pulse lengths and FWHM from NQR simulations at two different carrier frequencies, with two values of RF field.

Simulation	83.45 MHz		166.9 MHz	
$\nu_{1,X}$ (kHz)	100	50	100	50
τ_{p1} (μ s)	1.25	2.25	1.50	2.75
τ_{p2} (μ s)	2.25	4.50	3.00	5.50
FWHM (kHz)	350	150	250	150

5.5.4 Spinach Simulations of echo pulse nutations

Moving on, simulations using Spinach software were conducted, to attempt to simulate the pulse optimisations parallel to experimental work. This was done by a series of simulated pulse nutations and followed by a simulation of the excitation bandwidths. Firstly, the length of the first pulse was varied at 0.5 μ s intervals while the length of second pulse was fixed at a nominal value. Once the simulation produced an optimum value for first pulse, this length was fixed and the length of the second pulse was varied at 0.5 μ s intervals. In the final stage of the simulation, both pulse lengths remained fixed, while the frequency offset value was systematically varied at 50 kHz intervals to simulate the excitation bandwidth at each carrier frequency. As anticipated and illustrated in Figures 5.11 and 5.12, it was observed for both transitions that the optimised pulse lengths were shorter and the excitation bandwidths were larger when applying an RF field with an amplitude of 100 kHz, instead of 50 kHz. However, contrary to expectation, it was noted that at half the supplied RF field, the pulse lengths did not precisely double. Upon comparing the simulation and experimental results, as presented in Tables 5.4 and 5.5, several noteworthy observations emerged. Specifically, the simulation outcomes obtained at 83.45 MHz with a 100 kHz RF field revealed a τ_{p1} length of 1.25 μ s and a τ_{p2} length of 2.25 μ s, demonstrating reasonable agreement with the experimental results obtained using the 2.5 mm probe and 79 kHz RF field amplitude. In this case, the experimental pulse lengths were measured

Table 5.5 Optimised pulse lengths from NQR experiments using both 2.5 and 4 mm probes, at different RF field amplitudes.

Experimental	83.45 MHz				166.9 MHz			
Probe diameter (mm)	4.0		2.5		4.0		2.5	
RF (kHz)	74	50	79	50	101	50	100	50
τ_{p1} (μs)	1.2	1.9	1.4	2.5	2.3	5.0	1.5	-
τ_{p2} (μs)	2.1	3.5	2.3	4.3	4.4	9.4	2.8	-

at 1.4 μs for τ_{p1} and 2.3 μs for τ_{p2} . Moreover, for RF field strength of 50 kHz, the simulations also predict optimal τ_{p1} and τ_{p2} lengths (2.25 and 4.50 μs , respectively) similar with those measured for the same RF field value using 2.5 mm probe (2.50 and 4.30 μs , respectively). Transitioning to the results obtained at 166.9 MHz, a close correspondence is also evident between these simulations and the experimental observations recorded with the 2.5 mm probe using 100 kHz RF amplitude. However, no definitive conclusions can be drawn experimentally using 50 kHz RF due to the inadequate signal-to-noise ratio achieved with the 2.5 mm probe, thereby precluding accurate pulse nutation experiments. Conversely, the experimental results obtained using the 4 mm probe exhibit considerable deviation from the simulated pulse lengths. Specifically, only measurements conducted at 83.45 MHz using 74 kHz RF amplitude demonstrate reasonable concordance with the simulated pulse lengths at 100 kHz RF amplitude. In contrast, all other comparisons display substantial misalignment. These significant disparities in the optimisation of pulse lengths with the 4 mm probe may stem from RF field inhomogeneity within the probe.

5.6 Conclusions and Outlook

The optimisation of NQR techniques for studying ^{127}I in pristine MAPI has been the focal point of this study. Through a series of meticulously designed experiments

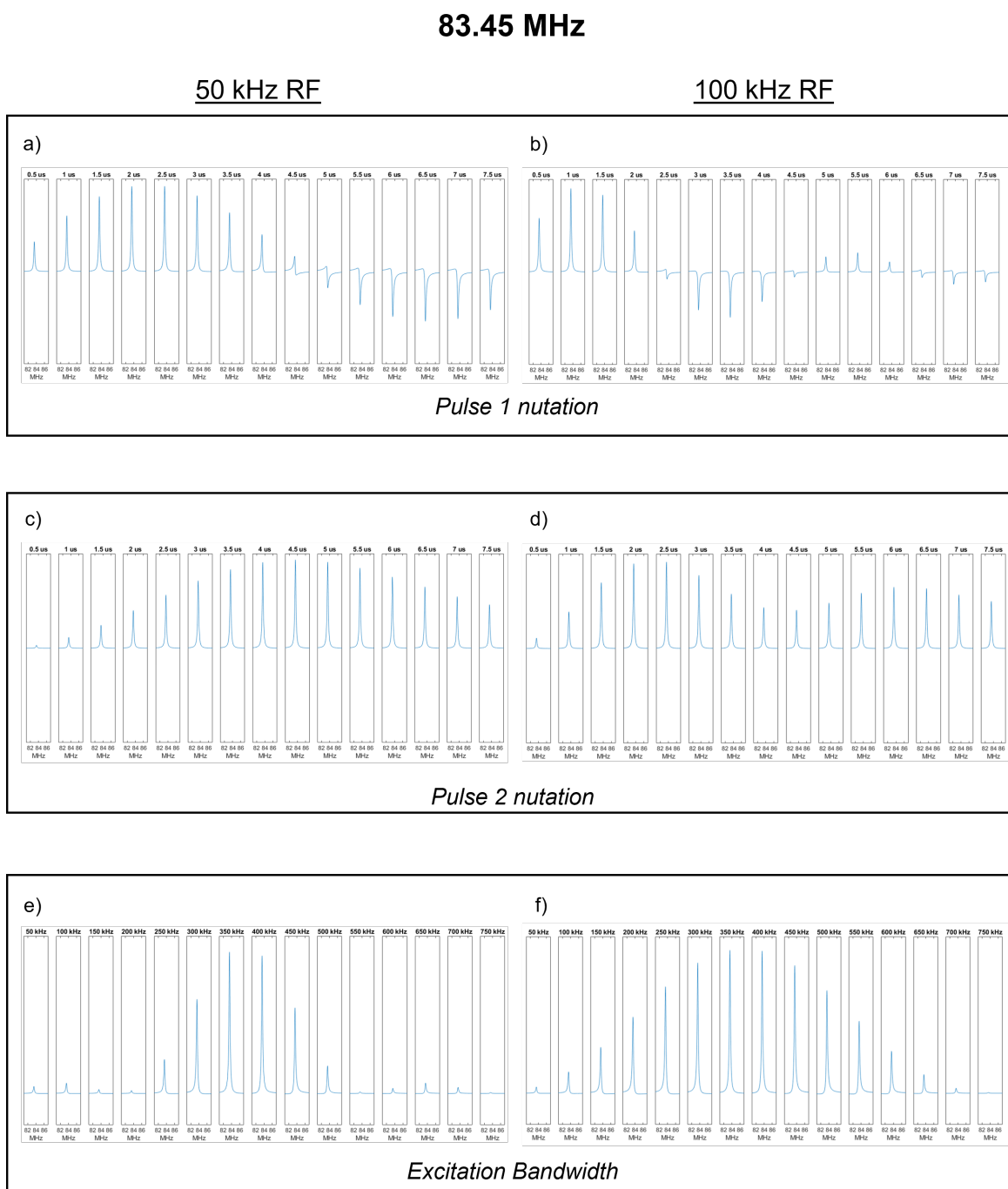


Figure 5.11 Simulated nutation during (a, b) first and (c, d) second pulses of Hahn echo experiment along with (e, f) excitation profiles for the detection of NQR transition at 83.45 MHz using RF field amplitude of 50 (a, c, e) and 100 (b, d, f) kHz.

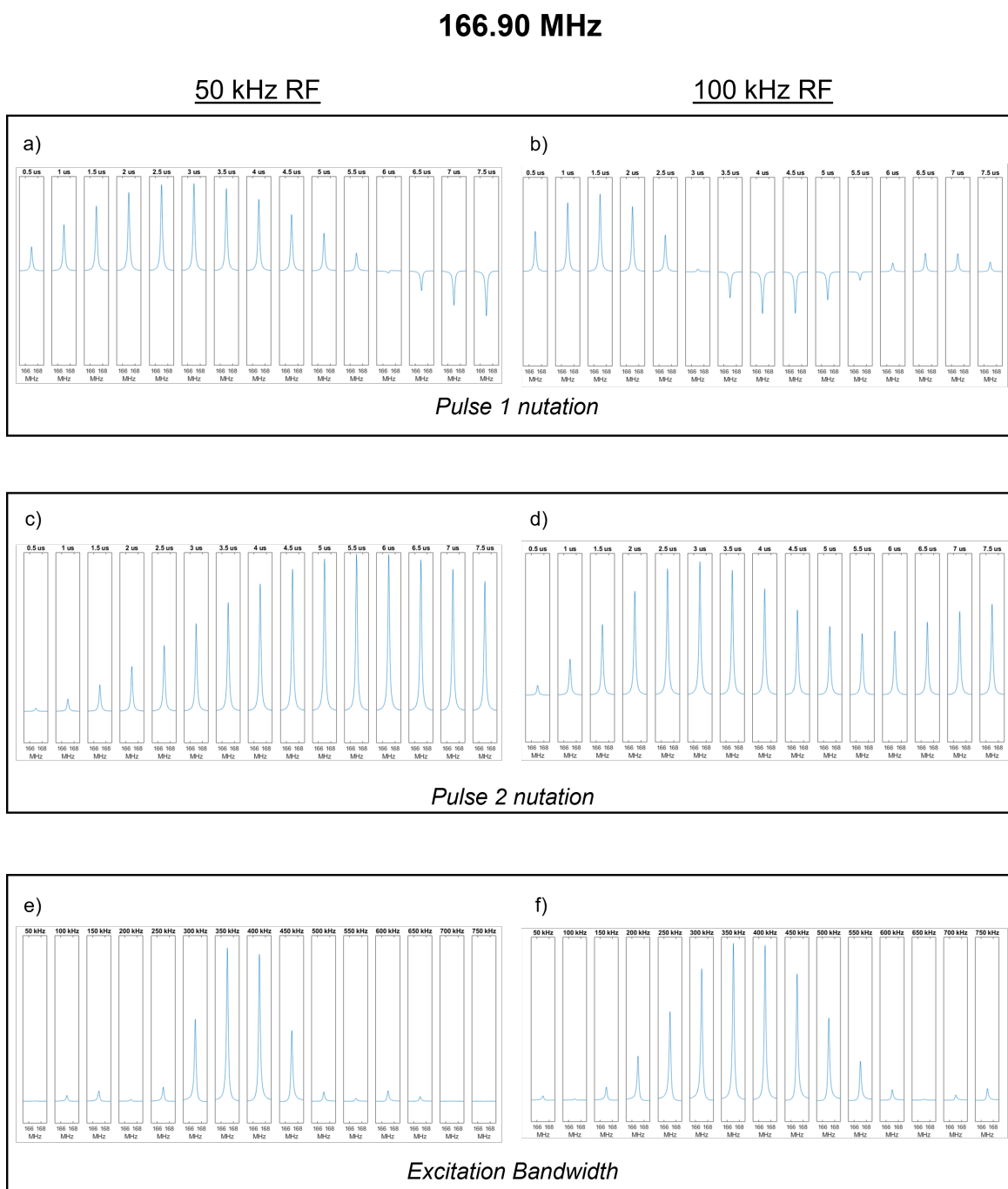


Figure 5.12 Simulated nutation during (a, b) first and (c, d) second pulses of Hahn echo experiment along with (e, f) excitation profiles for the detection of NQR transition at 166.90 MHz using RF field amplitude of 50 (a, c, e) and 100 (b, d, f) kHz.

employing different probe diameters and RF pulse sequences, we aimed to elucidate the impact of these variations on the overall signal quality and excitation bandwidth at two distinct carrier frequencies. Complementing these experimental endeavors, simulations were conducted to provide a comparative analysis, adding depth to our understanding of the observed phenomena. Our investigation was motivated by the prospect of enhancing the efficiency and effectiveness of NQR experiments, particularly for studying spin-5/2 nuclei in perovskite materials.

By utilising the Bloch-Siegert shift method, calibration of the RF power supplied to the probes enabled precise control over the RF field. Furthering this, NQR experiments were guided by QUEST simulations to identify potential signals corresponding to different iodine sites in MAPI. The agreement between experimental observations and simulations provided confidence in the experimental setup and paved the way for further optimisation.

Subsequent experiments focused on optimising the τ_{p1} and τ_{p2} pulse lengths at selected carrier frequencies. Surprisingly, findings revealed a departure from conventional pulse sequence optimisation observed in NMR studies, suggesting unique characteristics in NQR experiments involving $I = \frac{5}{2}$ spin systems. Additionally, an exploration of excitation bandwidths at different carrier frequencies highlighted the potential advantages of using smaller probe diameters, particularly at higher frequencies.

An intriguing aspect of the investigation was the exploration of the effect of pulse duration on excitation bandwidth and signal intensity. It was observed that shortening the pulse duration for τ_{p2} led to an increase in excitation bandwidth at the expense of reduced signal intensity on resonance, providing valuable insights into trade-offs inherent in pulse sequence design and NQR acquisition.

Simulations conducted in parallel with experimental work further corroborated findings, indicating good agreement between simulated and experimental outcomes, particularly with the 2.5 mm probe. However, notable disparities were observed in experiments involving the 4 mm probe, potentially attributable to RF field inhomogeneity within the probe.

Looking ahead, this study lays the groundwork for further refinements in NQR techniques for studying perovskite materials. Future research could explore additional pulse sequence optimisation strategies, including the investigation of alternative sequences that may offer improved performance or sensitivity. Additionally, simulations with SPINACH software can enhance the optimisation of NQR pulse sequences. Moreover, expanding the scope of probe configurations beyond those examined in this study could provide valuable insights and overcome limitations encountered in this work. By leveraging a diverse array of probe designs, researchers can enhance the robustness and versatility of NQR techniques for probing challenging nuclei such as ^{127}I , enabling deeper insights into the properties and behaviour of perovskite materials. Ultimately, these advancements will contribute to a more comprehensive understanding of perovskite materials, facilitating their development for various applications in areas such as energy harvesting, optoelectronics, and beyond.

References

- [1] W. Franssen, B. Bruijnaers, V. Portengen and A. Kentgens, *Phys. Chem. Chem. Phys.*, 2018, **19**, 3107–3115.
- [2] E. A. Alharbi, A. Y. Alyamani, D. J. Kubicki, A. R. Uhl et al., *Nat. Commun.*, 2019, **10**, 3008.
- [3] D. J. Kubicki, D. Prochowicz, A. Hofstetter, P. Péchy, S. M. Zakeeruddin, M. Grätzel and L. Emsley, *J. Am. Chem. Soc.*, 2017, **139**, 10055–10061.
- [4] D. J. Kubicki, D. Prochowicz, A. Hofstetter, M. Sasaki et al., *J. Am. Chem. Soc.*, 2018, **140**, 3345–3351.
- [5] J. V. Milić, J.-H. Im, D. J. Kubicki, A. Ummadisingu et al., *Adv. Energy Mater.*, 2019, **9**, 1900284.
- [6] E. M. Mozur, M. A. Hope, J. C. Trowbridge and et al., *Chem. Mat.*, 2020, **32**, 6266–6277.
- [7] D. Mitzi, C. Feild, W. Harrison and A. Guloy, *Nature*, 1994, **369**, 467–469.
- [8] W. Xiang, Z. Wang, D. J. Kubicki, W. Tress et al., *Joule*, 2019, **3**, 205–214.
- [9] D. J. Kubicki, D. Prochowicz, A. Pinon, G. Stevanato, A. Hofstetter, S. M. Zakeeruddin, M. Grätzel and L. Emsley, *J. Mater. Chem. A*, 2019, **7**, 2326–2333.
- [10] A. Karmakar, A. M. Askar, G. M. Bernard, V. V. Terskikh, M. Ha, S. Patel, K. Shankar and V. K. Michaelis, *Chem. Mater.*, 2018, **30**, 2309–2321.
- [11] D. J. Kubicki, D. Prochowicz, A. Hofstetter, S. M. Zakeeruddin, M. Grätzel and L. Emsley, *J. Am. Chem. Soc.*, 2018, **140**, 7232–7238.
- [12] B. A. Rosales, M. P. Hanrahan, B. W. Boote, A. J. Rossini, E. A. Smith and J. Vela, *Chem. Mater.*, 2016, **28**, 6848–6859.
- [13] A. M. Askar, A. Karmakar, G. M. Bernard, M. Ha, V. V. Terskikh, B. D. Wiltshire, S. Patel, J. Fleet, K. Shankar and V. K. Michaelis, *J. Phys. Chem. Lett.*, 2018, **9**, 2671–2677.
- [14] C. Roiland, G. Trippé-Allard, K. Jemli, B. Alonso et al., *Phys. Chem. Chem. Phys.*, 2016, **18**, 27133–27142.

-
- [15] D. J. Kubicki, D. Prochowicz, E. Salager, A. Rakhmatullin, C. P. Grey, L. Emsley and S. D. Stranks, *J. Am. Chem. Soc.*, 2020, **142**, 7813–7826.
- [16] P. M. Szell and D. L. Bryce, in Academic Press, 2020, vol. 100, ch. 3, pp. 97–152.
- [17] F. A. Perras, C. M. Widdifield and D. L. Bryce, *Solid State Nucl. Magn. Reson.*, 2012, **45–46**, 36–44.
- [18] F. Larsen, H. Jakobsen, P. Ellis and N. Nielsen, *J. Phys. Chem. A*, 1997, **101**, 8597–8606.
- [19] R. W. Schurko, *Acc Chem Res.*, 2013, **46**, 1985–1995.
- [20] L. Piveteau, M. Aebli, N. Yazdani and et al., *ACS Cent. Sci.*, 2020, **6**, 1138–1149.
- [21] D. Sarkar, R. W. Hooper, A. Karmakar, A. Bhattacharya, A. Pominov, V. V. Terskikh and V. K. Michaelis, *ACS Mater. Lett.*, 2022, **4**, 1255–1263.
- [22] M. Aebli, N. Porenta, N. Aregger and M. V. Kovalenko, *Chem. Mat.*, 2021, **33**, 6965–6973.
- [23] T. A. Doherty, S. Nagane, D. J. Kubicki and et al., *Science*, 2021, **374**, 1598–1605.
- [24] A. Senocrate, I. Moudrakovski, G. Y. Kim and et al., *Angew. Chem. Int. Ed.*, 2017, **129**, 7863–7867.
- [25] K. Yamada, S. Hino, S. Hirose and et al., *Bull. Chem. Soc. Jpn.*, 2018, **91**, 1196–1204.
- [26] L. Piveteau, V. Morad and M. V. Kovalenko, *J. Am. Chem. Soc.*, 2020, **142**, 19413–19437.
- [27] A. Senocrate, I. Moudrakovski and J. Maier, *Phys. Chem. Chem. Phys.*, 2018, **20**, 20043–20055.
- [28] P. M. Szell, L. Grébert and D. L. Bryce, *Angew. Chem. Int. Ed.*, 2019, **58**, 13479–13485.
- [29] Q. Xu, T. Eguchi, H. Nakayama, N. Nakamura and M. Kishita, *Z. Naturforsch. A*, 1991, **46**, 240–246.
- [30] E. A. Kravchenko, A. A. Gippius, A. V. Tkachev, M. V. Mastryukov and M. N. Brekhovskikh, *Mendeleev Commun.*, 2023, **33**, 282–284.
- [31] S. Sharma, N. Weiden and A. Weiss, *Z. Naturforsch. A*, 1991, **46**, 329–336.
- [32] M. Ferrari and D. Canet, *Mol. Phys.*, 2009, **107**, 2419–2430.
- [33] D. Canet, L. Merlat, B. Cordier, D. Grandclaude, A. Retournard and M. Ferrari, *Mol. Phys.*, 2006, **104**, 1391–1399.
- [34] B. Cordier, D. Grandclaude, A. Retournard, L. Merlat and D. Canet, *Mol. Phys.*, 2005, **103**, 2593–2598.
- [35] A. R. M. Ferrari, N. Hiblot and D. Canet, *Mol. Phys.*, 2007, **105**, 3005–3012.
- [36] C. Odin, *Solid State Nucl Magn Reson.*, 2017, **84**, 73–82.

-
- [37] A. Ramamoorthy and P. Narasimhan, *J. Mol. Struct.*, 1989, **192**, 333–344.
- [38] A. Ramamoorthy, *Mol. Phys.*, 1998, **93**, 757–766.
- [39] C. Odin, *J. Magn. Reson.*, 1999, **141**, 239–255.
- [40] C. Odin, *J. Magn. Reson.*, 2000, **143**, 299–310.
- [41] A. Ramamoorthy and P. Narasimhan, *Mol. Phys.*, 1991, **73**, 207–219.
- [42] A. Ramamoorthy, N. Chandrakumar, A. Dubey and P. Narasimhan, *J. Magn. Reson. A*, 1993, **102**, 274–286.
- [43] C. Schurrer and S. C. Pérez, *Appl. Magn. Reson.*, 1999, **16**, 135–146.
- [44] A. J. Rossini, H. Hamaed and R. W. Schurko, *J. Magn. Reson.*, 2010, **206**, 32–40.
- [45] J. L. Minns, P. Zajdel, D. Chernyshov, W. Van Beek and M. A. Green, *Nat. Commun.*, 2017, **8**, 1–5.
- [46] C. C. Stoumpos, D. H. Cao, D. J. Clark, J. Young, J. M. Rondinelli, J. I. Jang, J. T. Hupp and M. G. Kanatzidis, *Chem. Mater.*, 2016, **28**, 2852–2867.
- [47] I. Hung, P. Gor'kov and Z. Gan, *J. Magn. Reson.*, 2020, **310**, 106636.
- [48] W. M. J. Franssen, S. G. D. van Es, R. Dervişoğlu, G. A. de Wijs and A. P. M. Kentgens, *J. Phys. Chem. Lett.*, 2017, **8**, 61–66.

Chapter 6

Final Conclusions and Outlook

6.1 Conclusions

This thesis identifies the intrinsic instability of MAPI as a core challenge for its use in commercial solar cells, largely due to its sensitivity to environmental conditions like moisture, oxygen, and heat. To address this, the research explores compositional modifications that show significant promise in stabilising the perovskite structure that can better withstand environmental stressors without sacrificing efficiency. Furthermore, the examination of structural phase transitions reveals that targeted material adjustments can effectively counteract UV- and heat-induced degradation. This insight is crucial in developing perovskite solar cells that perform reliably under real-world conditions, marking a significant advancement in compositional engineering for commercial photovoltaic applications.

The research also delves into post-synthetic treatments, notably iodine and vacuum annealing, which led to fascinating structural and dynamic changes in MAPI. Chapter

3 focuses on the structural characterization of these materials using synchrotron X-ray diffraction and QENS. The synchrotron diffraction studies offered insight into temperature-dependent transformations in the perovskite lattice as influenced by post-synthetic treatments, revealing shifts in lattice constants and phase stability. High-resolution synchrotron facilities such as ESRF and Diamond Light Source enabled precise measurements of these transformations across different phases, while neutron scattering studies highlighted atomic-level dynamics, particularly in how organic cations reorient within the perovskite framework—an essential aspect of understanding molecular motion and its impact on structural stability and performance.

These structural studies provided foundational data on the stability of treated perovskites under variable environmental conditions, a key factor for photovoltaic applications. Critical findings include the correlation between temperature-induced symmetry changes and lattice robustness, both of which are directly relevant to achieving long-term solar cell performance. The vacuum annealing treatment, in particular, induced notable alterations in the lead-iodine octahedral framework, creating defects in the lattice structure observable through diffraction measurements. Meanwhile, QENS and NMR studies revealed shifts in cation motion in these annealed systems, reflecting a modified relationship between the organic and inorganic framework components. By systematically analysing different annealing temperatures and durations, this research contributes a detailed understanding of how these treatments impact perovskite structure at the atomic level, supporting the development of optimised post-treatment processes towards for the commercial scalability and durability of perovskite solar cells.

Advanced techniques like QENS and NMR played a crucial role in uncovering the dynamics of organic cations within MAPI structures. Understanding these dynamics is vital, as the movement of methylammonium ions significantly influences both the

stability and performance of the material by affecting its structural integrity and charge transport mechanisms.

Two innovations in magnetic resonance techniques were introduced. First, MAPI was identified as highly sensitive to the magic angle when studying ^{14}N nuclei, even more so than materials traditionally used to adjust the magic angle, suggesting a novel application for MAPI in NMR studies. Additionally, an NQR echo pulse sequence was optimised for investigating iodine perovskites, enhancing the ability to study halide behavior and its impact on perovskite stability and performance. This study thus highlights NQR as a potentially powerful diagnostic tool for future research, enabling precise detection of structural defects and guiding material improvements in real time. This technique is especially useful in assessing the effects of iodine vacancies and other halide-related defects on charge-carrier lifetimes and transport efficiency.

6.2 Outlook

This research has demonstrated the potential of combining scattering, diffraction, and nuclear resonance techniques to deeply explore the impact of post-synthetic treatments on MAPI perovskite powders in the bulk. Building on these findings, several promising paths for future work could further enhance understanding and application of MAPI.

One primary avenue for continued exploration is the refinement of post-synthetic vacuum annealing. Expanding the range of annealing temperatures tested would help clarify subtle annealing effects on MAPI's structural behavior, potentially enabling more precise control of lattice dynamics and phase stability. This fine-tuning could also improve control over iodine annealing, which currently shows unpredictable variability that may stem from uncontrollable factors like iodine partial pressure and tube volume.

Achieving greater consistency in iodine partial pressure and tube environment might allow for the production of more finely tunable MAPI structures with enhanced stability.

Understanding the formation of secondary NH_4PbI_3 phases is another key area for future study, as reducing this phase could yield purer, more efficient perovskite materials. In-situ studies focusing on the mechanisms behind secondary phase formation would provide insights into minimising this byproduct, potentially leading to more consistent MAPI synthesis protocols.

A logical next step would be to apply these treatments to thin-film perovskites. Thin films are more commercially relevant, and the structural changes observed in the bulk may manifest differently at the nanoscale. Investigating the impact of vacuum and iodine annealing on thin films could provide crucial information about potential improvements in device efficiency and stability. If these treatments successfully enhance thin-film properties, examining their effects on device performance could reveal new pathways to optimize perovskite solar cells.

The suite of techniques employed in this work — scattering, diffraction, and magnetic resonance — would be invaluable in characterising these novel thin-film treatments. Systematic analysis with these tools could provide a comprehensive picture of structural changes across both lattice and cation behaviors, deepening understanding of perovskite chemistry and optimizing these materials for photovoltaic applications. Additionally, using optimized NQR acquisition to study iodine distribution would link lattice structure insights from diffraction with localized iodine behavior. This would aid in refining knowledge of halide dynamics and provide insights into iodine-related defects and their impact on stability and performance.

Additionally, one of the next significant steps in the field will be the integration of

perovskite solar cells with existing technologies, such as silicon-based solar cells, to create tandem devices. Tandem solar cells, which combine perovskites with silicon to capture a broader spectrum of sunlight, could dramatically increase the efficiency of solar energy conversion. This work will support these efforts by advancing the understanding of perovskite material behavior at multiple levels, ensuring that perovskite-based devices can not only compete with but also complement existing technologies.

The ongoing investigation into the fundamental material properties of perovskites, from bulk powders to thin films, will continue to drive improvements in the efficiency and longevity of these materials. With each incremental advancement, perovskite solar cells are poised to make an even greater impact in the global effort to harness renewable energy. By advancing both the understanding and the practical application of perovskite materials, this research contributes to the continued growth and commercialisation of perovskite photovoltaics, paving the way for more efficient, durable, and scalable solar energy solutions.

In conclusion, the insights gained from this thesis not only contribute to a more nuanced understanding of the molecular dynamics and stability of MAPI, but also provide a framework for future research to address the challenges that remain. These findings provide an additional essential basis of understanding as the field moves toward developing the further potential of perovskite solar cells in the coming years, with the aim of achieving greater adoption and improving the efficiency of global solar energy generation.

